A NUMERICAL STUDY OF INCOMPRESSIBLE VISCOUS FLOW AROUND AIRFOILS

A THESIS

Presented to

The Faculty of the Division of Graduate Studies and Research

By

SARANGAN SAMPATH

In Partial Fulfillment

of the Requirements for the Degree of

Doctor of Philosophy

in the School of Aerospace Engineering

Georgia Institute of Technology

September, 1977

A NUMERICAL STUDY OF INCOMPRESSIBLE VISCOUS

FLOW AROUND AIRFOILS

Approved:

James C. Wu, Chairman

Robin B. Gray

Louis H. Bangert

Date approved by Chairman 8/29/77

ACKNOWLEDGMENTS

The author wishes to express his sincere appreciation to his thesis advisor, Dr. J. C. Wu, for encouragement and assistance throughout the course of this work. Working with Dr. J. C. Wu has been a stimulating and pleasant experience. The author is thankful to his reading committee members, Dr. R. B. Gray, Dr. L. H. Bangert and Dr. G. A. Pierce for their useful suggestions.

The author is grateful to Ms. Gloria Larson for typing the thesis. The financial support by the National Aeronautics and Space Administration under Grant No. NSG 1004 is acknowledged.

Finally the author is indebted to his father for his constant encouragement and understanding.

TABLE OF CONTENTS

LIST OF ILLUSTRATIONS

SUMMARY

An integro-differential formulation for the numerical solution of the two-dimensional incompressible Navier-Stokes equations is developed and presented. This formulation utilizes vorticity and stream function as dependent variables in the governing equations. In contrast to the prevailing finite difference techniques, the present formulation has the unique capability of confining the computations to the region of non-negligible vorticity. This feature offers a significant reduction in the computer time requirements for the study of external viscous flow problems. Furthermore, for external flow problems, this procedure enables the exact boundary condition on velocity to be satisfied truly at infinity. Based on the integral representation for stream function, a new method for the determination of vorticity on the solid surface is also presented. With this method the physical process of vorticity generation on the solid surface is correctly simulated and the principle of conservation of total vorticity is satisfied. Additionally it becomes possible to compute surface vorticity distribution without having to know in advance the stream function values at adjacent grid points.

The present formulation is applied to the numerical study of time dependent incompressible viscous flow past a 9% thick symmetric airfoil. The airfoil is impulsively started from rest at an angle of attack of 15^{o} and a Reynold's number, based on chord length, of 1000. In the numerical application the flow field that is confined to the non-negligible vorticity region is further divided into several compartments and each one

is treated as a fluid domain with its own boundaries. The advantages of such block division and the resultant computational efficiency are demonstrated.

The numerical results of flow past the airfoil are presented through time histories of loads, separation and reattachment points and through instantaneous values of field variables at selected time levels. The flow pattern around the airfoil is indicated through contour maps of equi-vorticity lines and instantaneous streamlines at various time levels. The equi-vorticity contours indicate the appearance of a "starting vortex" after the impulsive start. The "starting vortex" is observed to move at a constant velocity equal approximately to two thirds of free stream velocity before it is diffused through viscous effects. With progress in time, a clockwise separation bubble appears on the upper surface of the airfoil. The bursting of this bubble is followed by the appearance of other smaller bubbles. The variations in the force coefficients with time and their relation to the nature of separation bubbles are discussed. It is found that the lift increases when the strength of attached clockwise bubble increases; lift decreases when anti-clockwise bubbles grow. The separation on the airfoil surface is shown to occur at the location where the rate of change of vorticity along the surface is zero. The formation of separation bubble is also shown to be preceded by an adverse pressure gradient on the surface.

Numerical results of the present formulation are compared with available finite difference results and the improvements achieved in computational efficiency are pointed out.

NOMENCLATURE

a	radius of the circle to which airfoil is transformed; also characteristic length scale
B	boundary of fluid domain; coefficient in finite difference equation
b	element in lower triangular matrix - defined in Eq. 69
c	Constant in Joukowski's Transformation; also element in lower triangular matrix - defined in Eq. 70
D	coefficient in finite difference equation
D_N	distance along normal grid line from airfoil surface in the physical plane
d	element in lower triangular matrix - defined in Eq. 71
e	element in upper triangular matrix - defined in Eq. 72
F	coefficient in finite difference equation
f	a function defined in Eq. 21; also element in upper triangular matrix;
G_1	geometric coefficient for surface vorticity computation
G_2, G_3	geometric coefficients for stream function calculations
H	scale factor of transformation defined by Eq. 22; also coefficient in finite difference equation
i	node point in θ-direction
J	Jacobian of transformation
R_1, R_2	Constants defined in Eq. (18)
$[L]$	lower triangular matrix
L	non-dimensional chord length, ℓ/a
ℓ	airfoil chord length
$[M]$	coefficient matrix of finite difference equation

$\vec{n}_o$	outward unit normal vector
p	pressure
Q	inhomogeneous term in finite difference equation
$\{R\}$	column vector of residues
r'	relative distance between two points in the field
r	coordinate of the κ-plane
S	Strouhal Number
t	non-dimensional time, a/V
$[U]$	upper triangular matrix
u	velocity component along free stream direction in physical plane; velocity component along x-axis in Appendix
V	matrix defined in Eq. (80)
V_∞	magnitude of free stream velocity
v	velocity component normal to free stream direction in physical plane; velocity component along y-axis in Appendix
x	coordinate in z-plane
y	coordinate in z-plane
z	complex physical plane, x + iy
α	angle of attack
α_p	cyclic iteration parameter
β_1, β_2 β_3, β_4	relaxation parameters
γ	complex distance through which origin of coordinate system is shifted in transformation, $\gamma = \zeta_o + i\eta_o$
δ	parameter controlling radius of curvature at trailing edge
ζ	surface vorticity sheet strength
η	Cartesian coordinate of κ-plane
θ	coordinate of κ-plane

κ working plane, $re^{i\theta}$ or $\zeta + i\eta$

ξ Cartesian coordinate of κ-plane

ρ density; also coordinate $\rho = \rho(r)$

$\vec{\Psi}$ vector function

Ψ stream function

$\vec{\omega}$ vorticity vector

ω vorticity component normal to z-plane

Infrequently used symbols and symbols used in the derivation of equations in the Appendix are locally defined as needed.

Subscripts

B denotes block boundary

C refers to distance measured along airfoil chord

i refers to a grid point in θ-direction

j refers to a grid point in ρ-direction

L indicates lower surface of airfoil

U denotes upper surface of airfoil

κ refers to the κ-plane

Superscripts

k refers to iteration

n indicates time level

Operators

$\vec{\nabla}$ vector del operator

∇^2 Laplacian operator

Δ indicates an increment or a difference

Abbreviations

C_D drag coefficient

C_{DF}	friction drag coefficient
C_{DP}	pressure drag coefficient
C_L	lift coefficient
C_{LF}	friction lift coefficient
C_{LP}	pressure lift coefficient
C_M	moment coefficient
C_{MF}	friction moment coefficient
C_{MP}	pressure moment coefficient
C_N	normal force coefficient
C_T	tangential force coefficient
FSP	forward stagnation point
LE	leading edge
RP	reattachment point
RSP	rear stagnation point
SP	separation point
TE	trailing edge

CHAPTER I

INTRODUCTION

Solutions to many practical problems of interest in the realm of fluid mechanics in the past have been obtained by using various simplifying approximations to the governing equations. The major reason for this is the fact that in many instances of viscous flow the appropriate governing equations are the Navier-Stokes equations and the complexity of these equations preclude in general the possibility of obtaining direct analytical solutions. An alternative to the usage of simplifying approximations is to treat the Navier-Stokes equations numerically.

The extent to which numerical procedures can be successfully employed is dependent both on the nature of the problem and on the available computational facilities. For the numerical solution of external flow problems a major computational obstacle is the necessity of dealing with infinite fluid domain. In such cases very high demands are placed both on computer memory storage requirements and on the speed of computation. Consequently, before the introduction of the present generation of large electronic computers, potential flow approximations and boundary layer approximations have been very popular. Procedural details for these approaches are well established and they have been sucessfully and extensively employed whenever the flow phenomena permit such approximations. However there are many instances when these approximations are not valid and in such cases one has to treat the complete Navier-Stokes

equations or employ experimental procedures. In this context Chapman et al. (1) make several interesting observations on the comparative efficiency and economy of computers against wind tunnels for aerodynamic flow simulations. They observe that both the cost of wind tunnel testing and the tunnel test time have been steadily increasing in the past and that these might continue to do so. On the other hand the computation cost has been decreasing, while the computational speed has been increasing. Chapman et al. (1) believe that, if the present trend of improvements in computer technology continues to increase, fully three-dimensional flows of practical interest could be numerically simulated using computers in about a decade or so. They also expect that sophisticated computers in the future will eventually displace wind tunnel as the principal facility for providing aerodynamic flow simulation. Even though these projections may be too optimistic, the importance of computational fluid dynamics cannot be over-emphasized. In making these projections, Chapman et al. (1) also assume that the efficiency of numerical procedures will continue to improve in the future. Thus the development of efficient numerical procedures for solving Navier-Stokes equations has come to be an important aspect of fluid mechanics, and a part of the present work is directed towards this effort.

With the computer facilities currently available, numerical solution of Navier-Stokes equations is retricted mostly to two-dimensional laminar flows. The flow could be either steady or unsteady. In the former case the governing partial differential equations are elliptic in character while in the later case they are parabolic. Forward marching techniques used for the time dependent parabolic equations have numerical

advantages over iterative techniques needed for elliptical problems. In fact an iterative procedure for the steady state problem can be viewed as equivalent to solving the time dependent problem, each time step solution being equivalent to an iteration. Thus the difficulties associated with the numerical solution of steady state Navier-Stokes equations can be avoided by treating it as the asymptotic form of a time dependent problem [2]. Additionally one does not always know in advance whether a given problem has a steady state solution or not. For example, considering the viscous flow past a circular cylinder at high Reynolds numbers, the periodic shedding of vorticity causes the flow to reach a cyclic state and all variables are necessarily to be treated as functions of time. In view of these facts, one finds the treatment of transient Navier-Stokes equations to be more common in the literature.

A comprehensive survey of existing numerical methods for the numerical solution of Navier-Stokes equations is presented by Roache [3]. A large portion of this work is devoted to the solution of Navier-Stokes equations for incompressible flows in terms of the derived variables, stream function and vorticity. For incompressible flows, Navier-Stokes equations formulated in terms of the derived variables (like stream function-vorticity or velocity-vorticity) have certain specific advantages over the use of primitive variables, namely velocity components and pressure. The elliptic equation for pressure takes longer computer time [3] than the elliptic equation for stream function. The treatment of the pressure boundary condition is relatively more complex. Also, compared to the vorticity transport equation, the momentum transport equations encountered with primitive variables are more complicated [3]. Unless the

pressure values are required in the entire flow field, the usage of derived variables seem to be the most advantageous approach for two-dimensional incompressible flow problems.

In external flows past finite bodies at moderate and high Reynolds numbers there is in general a region containing separated flow as well as an attached boundary layer. In this region the viscous effects are important and the gradients of field variables are usually large. This small viscous region is embedded in an infinite region of essentially inviscid potential flow with much smaller gradients of field variables. A fine grid spacing is necessary in the viscous region to obtain proper resolution, while such a spacing is wasteful in the potential flow region. Because of the vastly different length scales it becomes exceedingly difficult to construct a data grid that provides a sufficient resolution for the viscous region and yet does not contain large number of data points in the potential flow region. In the current literature some form of coordinate stretching is found to be the only popular method to overcome this difficulty (see for example [3], [4]). This still does not offer significant reduction in the number of data points to be used since the potential flow region extends to infinity. With conventional finite-difference approaches the kinematic part of the computation must be carried out in the whole fluid region inclusive of the potential flow region. Consequently to preserve accuracy the grid spacings even in farfield region must be kept within acceptable limits and this restricts the extent to which coordinates can be stretched.

In view of these facts, it becomes apparent that a method which could confine the solution field to the viscous region of the flow would

offer a significant reduction in computer time.

There are two other difficulties associated with the conventional finite difference approaches available in the literature. These pertain to the enforcement of boundary conditions. The first of these difficulties is associated with external flows and arises due to the fact that the flow region is infinite in extent. Consequently boundary conditions at infinity are imposed on a finite boundary during the computational procedure. Wu [5] has demonstrated that this results in significantly inaccurate results for even a problem involving the simple geometry of a flat plate at zero angle of attack. Additionally when one chooses to impose the far stream boundary conditions at a finite distance there exists an uncertainty about the acceptable location of such a boundary. A possible approach is to repeat the computations for several different locations successively away from the surface and to choose a location in such a way that varying the location beyond that point will have no significant effect on the solution. One then has to solve the same problem several times over and because of the prohibitively large computer time involved one rarely attempts such a procedure.

An anomaly in applying uniform velocity boundary conditions at finite distances is pointed out by Roache [3]. Consider the viscous flow past a finite body solved by using the boundary condition that velocity and pressure attain free stream values at an outer boundary located at a finite distance away from the surface. A finite difference momentum integral around the outer boundary will then show the body to have zero drag. Nevertheless, such conditions have been specified in the past [10, 11, 12] even though they are incompatible from the above point of

view. In some instances [13], instead of a uniform velocity condition, the potential flow solution based on body shape is also found to have been used. Since the potential flow solution implies zero drag it is doubtful if even this approach is compatible.

A refinement found in the literature on this approach is to require some auxillary condition based in general on physical intuition and on heuristic arguments, be satisfied at the outer boundary [14, 15, 16]. A most commonly used condition at the downstream part of outer boundary is to require that the gradient of normal velocity in the downstream direction be zero. Mehta [17] neglected pressure gradient in one of the coordinate directions at the outer boundary and used the component of Navier-Stokes equation in that direction to compute velocity. For another approximate method of determining conditions at a finite outer boundary, Leal et al. [18] have shown that it is essentially equivalent to applying uniform conditions farther out. Roache [3] cites an example from literature showing that an error of 18% could result in the drag calculation for flow past a sphere when "infinity" conditions on velocity are applied at ten radii away. Cheng [19] compares the solutions of flow past a sphere for different far away boundary conditions and finds them to be significantly different. It could then be stated that there is no uniquely defined valid approximation for enforcing the far stream boundary conditions and that it is very much desirable that they be satisfied truly at infinity.

Another difficulty associated with conventional finite difference approaches exists for both external and internal flow problems. This is due to the fact that the vorticity transport equation contains both

vorticity and velocity vectors as unknowns whereas boundary conditions are specified on only one of them, namely velocity vector. But, to initiate and perpetuate the solution, the values of vorticity must be known on the boundary. Various one sided finite difference formulae are available in the literature and these determine vorticity values on the surface using the no slip condition and the values of stream function or velocity at adjacent grid points. There are considerable uncertainties regarding the choice of correct formula.

An integro-differential formulation which overcomes the difficulties associated with finite difference solution procedures was developed by Wu and Thompson [6]. This approach is used in conjunction with the vorticity-velocity formulation of the Navier-Stokes equations. It was demonstrated [5-8] that using this approach (i) the solution field can be confined to the viscous region of the flow (ii) the solution field can be segmented into compartments and the kinematic computations in each compartment can be performed independently of the other compartments (iii) the vorticity boundary conditions on the solid surface can be established correctly through kinematic considerations alone (iv) for external flows, the far stream boundary conditions are satisfied truly at infinity.

Instead of the velocity-vorticity formulation that was employed in the previous integro-differential approaches [5-8], in the present study a stream function-vorticity formulation is used, and an integral representation for stream function is employed. This formulation is shown to possess all the advantages of the integral formulation for velocity. One additional advantage is that computations need be done for one dependent

variable, namely the stream function, whereas in the previous integral formulation for velocity the two components of velocity had to be computed.

In the previous integro-differential formulation the vorticity on the solid surface was obtained by numerically solving a Fredholm integral equation with the boundary vorticity distribution as the unknown function [5]. Instead of such an implicit numerical procedure, an explicit formula for the computation of surface vorticity distribution is developed and used in the present study. The new explicit procedure is restricted to circular geometries or to bodies that could be transformed into a circle, so that the values of scale factor of transformation are known at points where vorticity values are to be computed. This is not a severe restriction since any two-dimensional body can be transformed into a circle (either analytically or numerically) and the corresponding scale factors established. The new approach is also shown to conserve the total vorticity in the flow field and hence one does not have to employ special differencing schemes to ensure that the principle of conservation of total vorticity is satisfied.

The field values of vorticity are obtained by solving the vorticity transport equation using finite differences. Significant reduction in computer time is achieved by dividing the flow field into several blocks and applying a rapidly converging iterative procedure in each block.

The objectives of the present work are as follows: (1) to develop an integro-differential formulation when stream function and vorticity are used as dependent variables in the Navier-Stokes equations. The far stream boundary conditions will be incorporated in such a formulation and

they will be satisfied truly at infinity. (2) to develop an accurate method of determining surface vorticity (3) to incorporate refinements to available finite difference methods for solving the vorticity transport equation with a view to improve the computational speed. (4) to develop a computer program that could yield solution to the viscous flow past any Joukowski profile after an impulsive start. (5) Finally, detailed numerical results are to be obtained for a 9% thick Joukowski airfoil set into motion impulsively at an angle of attack of 15^{o} and a Reynold's number of 1000. These results will be compared with existing difference solutions (17).

CHAPTER II

MATHEMATICAL FORMULATION

The required governing equations for initiating and perpetuating the solution are presented in this section. The boundary conditions associated with these equations are stated and the importance of their accurate specification or evaluation is also discussed. To preserve readability, algebraically involved derivations are omitted here and instead they are given in an Appendix at the end.

General Form of Governing Equations

The time-dependent Navier-Stokes and continuity equations for a fluid with constant density ρ and kinematic viscosity ν, and subject to negligible body forces are expressible in terms of the velocity $\vec{v}$ and pressure p as

$$\frac{\partial \vec{v}}{\partial t} + (\vec{v}\cdot\vec{\nabla})\vec{v} = -\frac{1}{\rho}\vec{\nabla} p + \nu\nabla^2\vec{v} \tag{1}$$

$$\vec{\nabla}\cdot\vec{v} = 0 \tag{2}$$

where t represents the time coordinate. Choosing the characteristic velocity as the free stream velocity V_∞, a characteristic length 'a', the characteristic time T given by the ratio a/V_∞ and normalizing Eqs. (1) and (2), one obtains the form

$$\frac{\partial \vec{v}}{\partial t} + (\vec{v}\cdot\vec{\nabla})\vec{v} = -\vec{\nabla}p + \frac{L}{Re}\nabla^2\vec{v} \tag{3}$$

$$\vec{\nabla}\cdot\vec{v} = 0 \tag{4}$$

where $Re \equiv V_\infty \ell/\nu$, and $L \equiv \ell/a$. The Reynolds number, Re, is based on the length, ℓ, of the body, the viscous flow over which is under investigation. Thus L represents the nondimensional length of this body.

Alternate forms of equations (3) and (4) can be written in terms of the velocity and the vorticity, $\vec{\omega}$, or in terms of the vector potential $\vec{\Psi}$ and the vorticity. In the present study the vector potential-vorticity formulation is used for reasons that are explained later.

Equation (4) implies that a vector potential exists which is related to the velocity vector through the relation

$$\vec{v} = \vec{\nabla} \times \vec{\Psi} \tag{5}$$

Defining the vorticity vector using

$$\vec{\omega} \equiv \vec{\nabla} \times \vec{v}, \tag{6}$$

one obtains from (3), (4) and (5) the following set of vector differential equations

$$\frac{\partial \vec{\omega}}{\partial t} = \vec{\nabla} \times \left[(\vec{\nabla}\times\vec{\Psi}) \times \vec{\omega}\right] + \frac{L}{Re}\nabla^2\vec{\omega} \tag{7}$$

and

$$\vec{\nabla} \times \vec{\nabla} \times \vec{\Psi} = \vec{\omega} \tag{8}$$

The present study deals with two-dimensional flow past a finite body immersed in an infinite fluid medium. For two-dimensional flows the non-zero component of vorticity vector and that of vector potential are directed perpendicular to the plane of flow. By the definition of vorticity (Eq. 6), counter-clockwise rotation implies positive vorticity. The vector potential reduces to the stream function Ψ . Choosing Cartesian coordinates, denoted by x and y in the plane of the flow, equations (7) and (8) reduce to

$$\frac{\partial \omega}{\partial t} = -\frac{\partial \Psi}{\partial y}\frac{\partial \omega}{\partial x} + \frac{\partial \Psi}{\partial x}\frac{\partial \omega}{\partial y} + \frac{L}{Re}\left[\frac{\partial^2 \omega}{\partial x^2} + \frac{\partial^2 \omega}{\partial y^2}\right] \tag{9}$$

and

$$\nabla^2 \Psi = \frac{\partial^2 \Psi}{\partial x^2} + \frac{\partial^2 \Psi}{\partial y^2} = -\omega \tag{10}$$

which are scalar equations.

The unknowns in equations (9) and (10) are the vorticity ω and the stream function Ψ . The set of equations (9) and (10) partitions the problem conveniently into a kinetic part and a kinematic part. The kinetic part of the problem, described by Eq. (9), deals with the change of the vorticity with time through convection and diffusion. That is, it deals with the transport of vorticity. The kinematic aspect relates the distribution of stream function at any given instant of time to the vorticity

distribution at that instant. This is done by the Poisson's equation (10) together with prescribed boundary conditions.

The vorticity transport equation (9) is parabolic in its time-space relation and the Poisson's equation (10) for stream function is elliptic. Together with properly specified initial and boundary conditions, these two equations permit the numerical solution of ω and Ψ as functions of the space and time coordinates. The general numerical procedure to advance the solution by one time step is to solve the vorticity transport equation (9), using known distributions of ω and Ψ at a given instant of time, to establish a new vorticity distribution at the next time level. This is the kinetic part of the solution procedure. With the new vorticity distribution, Eq. (10) is solved to obtain the new stream function values. This is the kinematic part. Note that the convective terms of the vorticity transport equation (9) are non-linear. Thus if the non-linear character of this equation were to be preserved in the solution procedure, alternate application of the kinetic and the kinematic calculations at the same time level is necessary until convergence occurs. If, instead, the values of stream function are allowed to lag by one time step, equations (9) and (10) are solved only once at each time level.

An examination of the vorticity transport equation shows that it is necessary to know the vorticity and the stream function only in the region of non-negligible vorticity at any given time in order to compute the vorticity values at a subsequent instant of time. This region is identical to the viscous region and the remainder of the flow field, being practically free of vorticity, is essentially inviscid. But prevailing finite difference and finite element procedures for the kinematic part of the

problem lack the ability to confine the solution of Ψ to this viscous region. Because of the elliptic nature of equation (10) computation of Ψ at any given point requires the knowledge of the values of Ψ at neighboring grid points. Thus the computations using prevailing finite difference methods require an implicit, and in general, iterative procedure. Additionally, for external flow problems the domain of integration of equation (10) is, in a theoretical sense at least, infinite in extent since the boundaries where Ψ values are known (namely the surface and the far stream boundary) are infinitely far apart. Consequently the conventional numerical methods must compute values of Ψ over this entire region inclusive of both viscous and inviscid regions.

Integral Representation for the Stream Function

The difficulties associated with conventional approaches for the kinematic aspect of the problem are eliminated by using an integral representation for the stream function. Such an integral representation for the velocity values was developed by Wu et al.[6] when the solution procedure uses vorticity and velocity as dependent field variables. In this section it is shown that the integral representation for Ψ retains all the advantages of the integral representation for velocity, and the relative merits between these two formulations are discussed.

Equation (10) can be recast (See Appendix) into an integral representation for the dependent variable Ψ by the use of Green's theorem and a principal solution of the Laplace's equation. Such a representation is

$$\Psi(\vec{r},t) = \frac{1}{2\pi}\int_R \omega_o \ln\frac{|\vec{r}|}{|\vec{r}_o-\vec{r}|}\,dR_o + \frac{1}{2\pi}\int_B \frac{\Psi_o(\vec{r}_o-\vec{r})\cdot\vec{n}_o}{|\vec{r}_o-\vec{r}|^2}\,dB_o$$

$$+ \frac{1}{2\pi}\int_B (\vec{\nabla}_o\Psi_o)\cdot\vec{n}_o \ln\frac{1}{|\vec{r}_o-\vec{r}|}\,dB_o \qquad (11)$$

where R is the domain of integration of Eq. (10) bounded by the closed boundary B; $\vec{r}$ is the position vector and $\vec{n}$ is a unit normal vector directed outward from R. The subscript 'o' denotes that the variables, their differentiations and integrations are performed in the $\vec{r}_o$ space.

On the boundary B, which for external flow problems consists of the body boundary and a boundary infinitely far from the body, the velocity boundary conditions are known. Consequently values of $\vec{\nabla}_o\Psi_o$ are known on B. The stream function Ψ_o on boundary B is again known to within an arbitrary constant. Thus the integrals over B in Equation (11) can be evaluated. For viscous flow exterior to a body, the no-slip condition prevails on the body surface and a return of the velocity to its freestream value is required on the boundary infinitely away from surface. Using these conditions, the combined contributions of the two contour integrals over B in Eq. (11) is found to be Ψ_∞, the stream function that would prevail in the absence of the solid body. If the freestream velocity vector is inclined by an angle α to the x-axis, then

$$\Psi_\infty = V_\infty\,(y\,\mathrm{Cos}\alpha - x\,\mathrm{Sin}\alpha)$$

where V_∞ is the magnitude of freestream velocity. Equation (11) then simplifies to:

$$\Psi(\vec{r},t) = \frac{1}{2\pi}\int_R \omega_o \ln\frac{|\vec{r}|}{|\vec{r}_o - \vec{r}|}\, dR_o + V_\infty (y\,\mathrm{Cos}\alpha - x\,\mathrm{Sin}\alpha) + C \quad (12)$$

The arbitrary constant, C, in the above expression can be set to zero to give $\Psi = 0$ inside the solid body.

In the numerical computations Eq. (12) would be written as a numerical quadrature formula of the form

$$\Psi_m = \sum_{n=1}^{N} G_{m,n}\omega_n + \Psi_{\infty m} \quad (13)$$

where 'm' refers to the data point at which the value of Ψ is to be computed, "n" refers to a non-negligible vorticity point and "N" is the total number of such non-negligible vorticity points. $G_{m,n}$ are geometric functions depending on the relative positions of the data points m and n. These geometric coefficients are time-independent and therefore are pre-computed and stored.

When the vorticity distribution in the region R is known, the integral in Eq. (12) can be numerically evaluated to obtain the value of stream function at any chosen point $\vec{r}$. Note that the no-slip boundary condition on the surface of the solid, as well as the far stream boundary conditions are incorporated in Eq. (12). The value of Ψ at any chosen point $\vec{r}$ can be obtained independent of its value at any other point. That is, the computation is explicit and point by point. As a result, if one chooses to restrict the computation of stream function values to the viscous region alone it can easily be accomplished. The entire solution procedure, including the kinetic and kinematic parts, can therefore be confined to the viscous region.

A further advantage of the integral representation is that it permits the viscous region to be divided into segments of arbitrary shape and size, and the computations to be performed within each segment independent of stream function values in other segments. Using the velocity formulation, Wu et al. [7] demonstrated that the flow field segmentation technique leads to further substantial improvement in solution speed and accuracy. This advantage is retained in the stream function formulation also. To implement this technique the generalized integral expression given by Eq. (11) is used. In Eq. (11) one considers the region R to be any segment of the fluid domain bounded by B. The values of Ψ on the boundary B and on two adjacent grid lines are evaluated first using Eq. (12). This renders the integrals over B in Eq. (11) to be known. Then, for the interior points in that segment the stream function values are evaluated using the vorticity values of that segment only. The advantage of employing the segmentation technique is easily seen by considering the number of algebraic operations involved through an example.

For numerical computations Eq. (11) would be written as

$$\Psi_m = \sum_{n=1}^{Q} G_{m,n}\omega_n + \sum_{k=1}^{P} F_{m,k}\Psi_k + \sum_{k=1}^{P} E_{m,k}(\Delta\Psi)_k \qquad (14)$$

where $E_{m,k}$ and $F_{m,k}$ are geometric coefficients depending upon the relative locations of the point m and the point k which is located on the segment boundary; Q is the number of non-negligible vorticity points in the compartmentalized region R; and P is the number of points on the

boundary, B, of the region R. Consider for example a rectangular flow field with total number of grid points being, say, 99 x 40 = 3960, where stream function values are to be computed. If no segmentation is employed Eq. (13) would be used to compute these values. The computation for each point would require the multiplication of 3960 values of vorticity with 3960 values of geometric coefficients and the addition of these products. The total number of multiplications required is 1.4×10^7. Now consider the flow field to have been divided into, say, eight segments. The lines i = 2, 14, 26,...86, 98 form the vertical boundaries of these segments and the lines j = 2 and j = 39 form the horizontal boundaries. To apply segmentation technique the stream function values and normal derivatives of stream function at the boundary points must be known. If the derivatives are evaluated using central differences, then stream function values are needed on two lines adjacent to these boundary lines. For the example chosen, the total number of boundary points turn out to be 1512. To compute stream function at these points Eq. (13) has to be used which results in 5.6×10^6 multiplications. For the interior points in each segment, however, Eq. (14) would be employed. In Eq. (14), Q = 306 and P = 98 for the example chosen, and the computation of Ψ for the interior points of all eight segments require 0.75×10^6 multiplications. Thus the total number of multiplications with segmentation procedure for this example is 6.4×10^6. This is about 45% of the effort required for the case where no segmentation of flow field is employed.

The above discussion also indicates the possible existence of an optimum number of segments that could be used. As the number of segments is increased, the number of boundary points increases while the number of

interior points in each segment decreases. In the extreme case, almost all data points of the entire flow field could become boundary points of segments. Since the computation of Ψ at these points involve the vorticity points of the whole flow field as per equation (13), such an extreme case would degenerate to the procedure where no segmentation is used. Thus there is in general an optimum number of segments that gives a minimum number of total operations. Such an optimum number would depend on the specific problem and can be determined by considering several different numbers of segments and their corresponding operation counts which are easily determined.

Another versatile aspect of this procedure is that, after obtaining the values of stream function on segment boundaries, one could use any finite difference implicit method or direct inversion method to obtain the solution at interior points. Many of these methods [20] have restrictions on the shape of the boundary. In such cases an irregularly shaped flow field can be divided into several blocks of required shapes and the boundary values for these blocks can be determined from the integral representation. Additionally with many of the prevailing finite difference methods (like for example Successive Relaxation and Alternating Direction Implicit procedures) the number of iterations required for convergence increases with increasing number of data points [21] In such cases again it is advantageous to subdivide the flow field into smaller blocks and use these methods to obtain the solution interior to these blocks. The usage of integral representation for such applications is termed as block subdivision technique in the present work to distinguish it from the segmentation technique described earlier, where integral

representation is used for both block boundary and interior points. The block subdivision has been successfully used in the present study and the details of its application are presented in the next chapter.

The advantages of the integral representation that have been described so far are common to both the integral representation for stream function and for velocity. With the use of stream function, however, numerical differentiation of these values must be performed since the derivatives of stream function, and not the stream function itself, appear in the convective terms of the vorticity transport equation. This results in loss of accuracy compared to the direct evaluation of the velocity components. On the other hand the integral representation for velocity (6) gives rise to two separate equations, one for each component of velocity, similar to Eq. (13). The computer time requirement as well as storage space for geometric coefficients are thus approximately doubled when the velocity formulation is used. In general, then, for problems that use fine grid spacings and hence a large number of data points the stream function formulation is preferable because of its computational efficiency. In such cases the errors due to numerical differentiation of Ψ will also be low because of the fine grid spacings. If coarse grid spacing is used and if number of grid points is relatively small then the velocity formulation is preferable. With these in consideration in the present study, where numerical solution is obtained for viscous flow past an impulsively started airfoil, the stream function formulation is chosen.

Formulation for the Study of Impulsively Started Airfoil

The integro-differential formulation discussed above is

particularized and applied to the study of incompressible viscous flow past an impulsively started airfoil. The airfoil geometry and the grid system are generated through a conformal transformation. The airfoil considered for numerical study is a 9% thick modified Joukowski airfoil with rounded trailing edge instead of a cusped one. In the numerical study time-dependent solutions are obtained for flow past such an impulsively started airfoil at an angle of 15^{o} and a Reynolds number of 1000 (based on airfoil chord length).

This problem has previously been studied by Mehta [17], who mapped the fluid domain outside the airfoil into the interior of a unit circle and used implicit finite difference procedures for both kinetic and kinematic parts of the numerical solution. In the present study the formulation for the kinematic part of solution procedure as well as the method of solving the finite difference equations of the vorticity transport equation are significantly different from those of Mehta [17]. Additionally, unlike in the study of Mehta [17], no approximations whatsoever are used to enforce the far stream boundary condition on velocity. The present study also uses a new explicit procedure for computing the boundary vorticity distribution. To facilitate an easy comparision of the results of these two significantly different procedures, the airfoil geometry as well as the grid system for the present case are kept the same as those of Mehta [17].

Coordinate Transformation

A circle of unit radius and centered at the origin is considered in the working plane defined by $\kappa = re^{i\theta}$. By choosing a coordinate system that is displaced thorugh a complex distance γ with respect to the center

of the circle and employing Joukowski's transformation, the κ-plane can be conformally mapped into the z-plane through the relation

$$z = \frac{1}{\kappa} + \gamma + \frac{\kappa c^2}{1+\gamma\kappa} \tag{15}$$

where

$$\kappa = \xi_o + i\eta_o \tag{16}$$

$$c = (\xi_o + \sqrt{1 - \eta_o}\ )\ (1-\delta) \tag{17}$$

This transformation maps the interior of the unit circle in the κ-plane to the exterior of the transformed shape in the z-plane. By proper choice of the parameters ξ_o and η_o airfoils of different thickness ratios and camber can be generated in the physical plane. In equation (17) the value of the arbitrary constant δ is close to zero and is positive. Introduction of this constant removes the singular point of the transformation at the trailing edge and yields a rounded trailing edge instead of a cusped one. For the present problem the values of these constants are chosen as $\xi_o = -0.05214$, $\eta_o = 0.0$ and $\delta = 0.025$. The resulting symmetric airfoil is 8.9998% thick and its chord length non-dimensionalized with respect to the radius of the circle is 3.7128127. The flow variables and the coordinates are normalized with respect to the radius of the circle and the free stream velocity.

The kinetic as well as the kinematic part of the computations are performed in the κ-plane by choosing discretized grid points on and inside the unit circle. When the grid points are equally spaced in the θ-

direction of the working plane (i.e., κ-plane) the conformal mapping causes the constant-θ grid lines to be more crowded near leading and trailing edges compared to their spacings around midchord of the airfoil This is a desirable feature since we expect rapid changes in the flow behavior at these locations. However equal spacing of points in the r-direction in the working plane causes the spacings between constant-r grid lines to increase rapidly in the physical plane as one moves away from the airfoil. So, to obtain a more efficient grid spacing, the radial coordinate in the working plane is stretched according to the relation (17)

$$\rho\ (r) = \frac{1}{k_1+k_2}\ \left[\tanh^{-1}(rk_3-k_4) + k_2\right] \tag{18}$$

with

$$k_3 = \left[\tanh(k_1) + \tanh(k_2)\right]\ \left[1- \frac{r_o}{r_o-1.0}\right]$$

$$k_4 = \tanh(k_2) - r_o\ \left[\tanh(k_1) + \tanh(k_2)\right]\ /\ (r_o-1.0)$$

where k_1, k_2 and r_o are constants. In addition to stretching the radial coordinate, this relation also transforms the region between $r = r_o$ and $r = 1.0$ into a region between $\rho = 0.0$ and $\rho = 1.0$. The values of the constants used are $k_1 = 2.0$, $k_2 = 2.8$ and $r_o = 0.02$, and these are the same as in the study of Mehta (17). The circle $r = r_o = 0.02$ in the working plane corresponds approximately to a circle of radius 13 times the airfoil chord length in the physical plane.

For the conformal transformation of equation (15) with $\eta_o = 0$ (which gives a symmetrical airfoil) the coordinate relations between the

physical and the working plane are

$$x = \left[1 + \frac{c^2 r^2}{f^2}\right]\left[\frac{\cos\theta}{r} + \xi_o\right] \tag{19}$$

and

$$y = \frac{\sin\theta}{r}\left[\frac{c^2 r^2}{f^2} - 1\right] \tag{20}$$

where

$$f^2 = 1 + \xi_o^2 r^2 + 2\xi_o r\cos\theta \tag{21}$$

The scale factor of the transformation is given by

$$H \equiv \left|\frac{dz}{d\kappa}\right| = \left[\left(\frac{1}{r^2} - \frac{c^2}{f^2}\right)^2 + \frac{4c^2}{r^2 f^4}\sin^2\theta\right]^{\frac{1}{2}} \tag{22}$$

where f^2 is defined by equation (21).

Governing Equations in the Working Plane

The non-dimensional vorticity transport equation transforms into the $\rho-\theta$ plane as

$$r^2H^2\frac{\partial\omega}{\partial t} = r\frac{d\rho}{dr}\left[\frac{\partial\Psi}{\partial\rho}\frac{\partial\omega}{\partial\theta} - \frac{\partial\Psi}{\partial\theta}\frac{\partial\omega}{\partial\rho}\right] + \frac{L}{Re}\left[\left(r\frac{d\rho}{dr}\right)^2\frac{\partial^2\omega}{\partial\rho^2} + r\left(\frac{d\rho}{dr} + r\frac{d^2\rho}{dr^2}\right)\frac{\partial\omega}{\partial\rho} + \frac{\partial^2\omega}{\partial\theta^2}\right] \tag{23}$$

where $\rho = \rho(r)$ represents the stretching relation defined by Eq. (18), L is the non-dimensional chord length of the airfoil and Re is the Reynold number based on airfoil chord length.

The Poisson's equation for stream function in the $r-\theta$ coordinates is

$$\nabla_{\kappa}^{2}\Psi = \frac{\partial^{2}\Psi}{\partial r^{2}} + \frac{1}{r}\frac{\partial\Psi}{\partial r} + \frac{1}{r^{2}}\frac{\partial^{2}\Psi}{\partial\theta^{2}} = -\omega H^{2} \qquad (24)$$

The use of the stretching relation (18) with the above equation yields

$$\left(\frac{d\rho}{dr}\right)^{2}\frac{\partial^{2}\Psi}{\partial\rho^{2}} + \left(\frac{d\rho}{dr}\frac{1}{r} + \frac{\partial^{2}\rho}{\partial r^{2}}\right)\frac{\partial\Psi}{\partial\rho} + \frac{1}{r^{2}}\frac{\partial^{2}\Psi}{\partial\theta^{2}} = -\omega H^{2} \qquad (25)$$

Equation (24) differs from the Poisson's Eq. (10) only in the inhomogeneous term. Thus by defining

$$\omega_{\kappa} = \omega H^{2} \qquad (26)$$

in formal analogy with the integral representation given by Eq. (11), one may write

$$\Psi(\vec{r}_{\kappa},t) = \frac{1}{2\pi}\int_{R_{\kappa}} \omega_{\kappa o}\ln\frac{|\vec{r}|}{|\vec{r}_{o}-\vec{r}|}\,dR_{\kappa o}$$

$$+ \frac{1}{2\pi}\int_{B_{\kappa}} \frac{\Psi_{\kappa}(\vec{r}_{\kappa o}-\vec{r}_{\kappa})\cdot\vec{n}_{\kappa o}}{|\vec{r}_{\kappa_{o}}-\vec{r}_{\kappa}|^{2}}\,dB_{\kappa_{o}}$$

$$+ \frac{1}{2\pi}\int_{B_{\kappa}} (\vec{\nabla}_{\kappa_{o}}\Psi_{o})\cdot n_{\kappa_{o}}\ln\frac{1}{|\vec{r}_{\kappa_{o}}-\vec{r}_{\kappa}|}\,dB_{\kappa_{o}} \qquad (27)$$

The subscript κ in the above expression refers to the κ-plane. Thus R_{κ} refers to the rotational region in the κ-plane corresponding to the region

R in the z-plane.

The contribution of the contour integrals over the boundaries B_K in Eq. (27) is evaluated by considering the velocity boundary conditions. Consider S' to be a circle of radius A centered about the origin in the physical plane, with $A \to \infty$. The boundary S' would then enclose the airfoil in the physical plane, and the stream function on S' is $V_\infty(y\cos\alpha - x\sin\alpha)$. In the working plane, S'_K is a circle of radius $\varepsilon \to 0$ centered about the origin. Since Ψ is a scalar and invarient in the transformation, one obtains the following conditions valid on S'_K :

$$\Psi = -\frac{1}{r} V_\infty \sin(\alpha+\theta), \text{ at } r = \varepsilon \tag{28}$$

$$\frac{\partial \Psi}{\partial n} = -\frac{\partial \Psi}{\partial r} = -\frac{1}{r^2} V_\infty \sin(\alpha+\theta), \text{ at } r = \varepsilon \tag{29}$$

Together with the no-slip boundary conditions on the surface, S_K, Eq. (27) becomes (See Appendix)

$$\Psi(r_K, t) = \frac{1}{2\pi} \int_{R_K} \omega_{K_o} \ln \frac{|\vec{r}_K|}{|\vec{r}_{K_o} - \vec{r}_K|} dR_{K_o} - \frac{1}{r} V_\infty \sin(\alpha+\theta) \tag{30}$$

Denoting the vorticity distribution on the solid surface S_K by ζ_K and separating its contribution from the rest of the region, Eq. (30) may be rewritten as

$$\Psi\ (\vec{r}_K,t) = \frac{1}{2\pi} \int_{R_K-S_K} \omega_{K_o} \ln \frac{|\vec{r}_K|}{|\vec{r}_{K_o} - \vec{r}_K|}\, dR_{K_o}$$

$$+ \frac{1}{2\pi} \int_{S_K} \zeta_K \ln \frac{|\vec{r}_K|}{|\vec{r}_{K_o} - \vec{r}_K|}\, dS_{K_o} - \frac{1}{r}\ V_\infty \sin(\alpha+\theta) \qquad (31)$$

Using Eq. (26) along with the normalized free stream velocity $V_\infty = 1$, Eq. (31) written in scalar notation is

$$\Psi(r,\theta,t) = \frac{1}{2\pi} \iint_{R_K-S_K} \omega_o H_o^2 \ln\left(\frac{r}{r'}\right) r_o\, d\theta_o\, dr_o + \frac{1}{2\pi} \int_{S_K} \zeta_K \ln \frac{r}{r'}\, d\theta_o$$

$$- \frac{1}{r} \sin(\alpha+\theta) \qquad (32)$$

where

$$r' = \left[r^2 + r_o^2 - 2rr_o\cos(\theta_o-\theta)\right]^{\frac{1}{2}} \qquad (33)$$

Eq. (32) is not re-expressed in terms of ρ and θ using the stretching relation as it can easily be evaluated in its present form during the computational procedure.

Determination of Surface Vorticity

The vorticity distribution away from the surface is determined at any instant of time by the kinetics of the problem using the vorticity transport equation (23). But in order to solve Eq. (23) the vorticity values on the surface boundary must be known. Since the generation and depletion of vorticity on the surface is not described by the kinetic processes, the surface vorticity values may not be computed using Eq. (23).

The surface vorticity distribution instead has to be determined from the kinematic restriction that $\Psi = 0$ on the surface and in the domain of the solid.

In the literature one finds that various one sided difference formulae have been used to obtain vorticity values on solid boundaries using the no-slip condition and the computed values of stream function or velocity at grid points adjacent to the solid boundary. There are considerable uncertainties regarding the choice of correct formula and the limitations of the same. In some cases formulae of first order accuracy were found to yield stable solutions while second-order formulae gave unstable results. Wu (5) has demonstrated that these anomalies are related to the principle of conservation of total vorticity, and that formulae that help conserve total vorticity, in general, give better results.

With the integral representation for the kinematics it becomes possible to determine surface vorticity values based on kinematic considerations alone. In Reference (5), using the velocity-vorticity formulation, it was demonstrated that this new approach correctly simulates the physical process of vorticity generation on the surface and that it conserves total vorticity. In Reference (5) an implicit method which requires the numerical solution of an integral equation is presented. In the present study, an explicit method, which also conserves the total vorticity is developed and used in the computations.

Refering to Eq. (31), the surface vorticity distribution ζ_K is to be determined so that the values of stream function inside the solid surface is zero. Since the differential equation describing the kinematic

relation between vorticity and stream function is linear, the method of superposition is valid. Let us consider ζ_K in two parts

$$\zeta_K = \zeta_{K\,1} + \zeta_{K\,2} \tag{34}$$

where $\zeta_{K\,1}$ is the contribution of the free stream to the surface vorticity and ζ_{K2} is the contribution due to vorticity away form the surface.

The surface vorticity distribution corresponding to a potential flow past a circular cylinder upon conformal mapping becomes

$$\zeta_{K\,1} = 2V_\infty \mathrm{Sin}(\alpha+\theta) \tag{35}$$

Using this in Eq. (31) with $\omega_K = 0$ in the region $(R_K - S_K)$, it could be shown that $\Psi = 0$ for the region $r \geq 1$, which corresponds to the domain of the airfoil in the z-plane. It is also possible to show that the integral of $\zeta_{K\,1}$ around the circle vanishes. Thus $\zeta_{K\,1}$ does not contribute to the total vorticity.

Now let $d\zeta_{K_2}$ be the contribution of the elemental vorticity $\omega_{K\,o} dR_{K_o}$ located at r_{K_o}. By the method of images one finds

$$d\zeta_{K2} = \frac{(r_o^2 - 1)\omega_{K_o} dR_{K\,o}}{2\pi\left[1 + r_o^2 - 2r_o \mathrm{Cos}(\theta_o - \theta)\right]} \tag{36}$$

Using the method of residues it can be shown that the combined contribution of $d\zeta_{K2}$ and $(\omega_{K\,o} dR_{K_o})$ to the stream function inside the airfoil is zero.

Also the integral of $d\zeta_{K2}$ around the unit circle together with $\omega_{K_o} dR_{K_o}$ do not contribute to total vorticity.

Since the principle of superposition is valid, one lets

$$\zeta_{K2} = \int d\zeta_{K2} = \frac{1}{2\pi} \int_{R_K - S_K} \frac{(r_o^2 - 1)\omega_{K_o} dR_{K_o}}{[1 + r_o^2 - 2r_o \cos(\theta_o - \theta)]} \qquad (37)$$

Finally combining the two solutions given by Eq. (35) and (37), one obtains

$$\zeta_K = \frac{1}{2\pi} \int_{R_K - S_K} \frac{(r_o^2 - 1)\omega_{K_o} dR_{K_o}}{1 + r_o^2 - 2r_o \cos(\theta_o - \theta)} + 2V_\infty \sin(\alpha + \theta) \qquad (38)$$

The surface vorticity as determined by this equation satisfies both the kinematic restriction that the stream function be zero inside the airfoil and the principle of conservation of total vorticity.

Farfield Boundary Condition

For the external flow problem the difficulty of satisfying the farfield boundary conditions is removed by the use of integral representation for the kinematics. By differentiating the expression for Ψ given by Eq. (12) with respect to $\vec{r}$, the relation for the velocity vector is obtained. As $\vec{r} \to \infty$ in the physical plane, the integral in the resulting expression becomes zero and the velocity at $\vec{r} \to \infty$ is obtained correctly as $\vec{V}_\infty$. Thus the boundary conditions are truly satisfied at infinity.

Initial Conditions

After the impulsive start, at time $t = 0^+$, the flow field

corresponds to that of non-circulatory potential flow. The corresponding vorticity singularity distribution on the surface of the airfoil is contained in the explicit relation for the determination of surface vorticity, Eq. (38) and is given by

$$\zeta_K = 2V_\infty \sin(\alpha+\theta) \tag{39}$$

Using this in Eq. (31) and setting ω_{K_0} to be zero in the region $(R_K - S_K)$ the value of stream function in the flow field is readily obtained as

$$\psi(\vec{r}, t = 0) = \sin(\alpha+\theta)\left[r - \frac{1}{r}\right] \tag{40}$$

With the initial values of both vorticity and stream function thus known, the perpetuation of the solution with time becomes possible.

Determination of Loads and Velocity

The Navier-Stokes equations in the primitive variables given by Eq. (3) when transformed to the working plane and particularized for the surface with $\vec{V} = 0$, can be written as

$$\frac{\partial p}{\partial r}\vec{e}_1 + \frac{\partial p}{\partial \theta}\vec{e}_2 = -\frac{L}{Re}\left[\frac{\partial \omega}{\partial \theta}\vec{e}_1 - \frac{\partial \omega}{\partial r}\vec{e}_2\right] \tag{41}$$

Separating the θ-momentum equation from the above and integrating it along with the usage of the stretching relation $\rho = \rho(r)$, the expression for non-dimensional surface pressure is obtained as

$$p(\theta) = \frac{L}{Re} \left.\frac{d\rho}{dr}\right|_{r=1} \int_0^{\theta} \left.\frac{\partial \omega}{\partial \rho}\right|_{\rho=1} d\theta_o + p(0) \tag{42}$$

Noting that the pressure, p, in the above expression is normalized with respect to ρV_∞^2, the equation for C_p defined by

$$C_p(\theta) \equiv \frac{\hat{p}(\theta)-\hat{p}(0)}{\frac{1}{2}\rho V_\infty^2} \tag{43}$$

where $\hat{p}$ represents dimensional pressure, is obtained as

$$C_p(\theta) = 2 \frac{L}{Re} \left.\frac{d\rho}{dr}\right|_{r=1} \int_0^{\theta} \left.\frac{\partial \omega}{\partial \rho}\right|_{\rho=1} d\theta_o \tag{44}$$

The force coefficients normal and tangential to the airfoil chord, denoted by C_N and C_T respectively, are given by

$$C_{N_p} = -\frac{1}{L} \int_0^{2\pi} Cp(\theta) \frac{\partial x}{\partial \theta} d\theta \tag{45}$$

$$C_{N_f} = -\frac{2}{Re} \int_0^{2\pi} \omega(1,\theta) \frac{\partial y}{\partial \theta} d\theta \tag{46}$$

$$C_{T_p} = \frac{1}{L} \int_0^{2\pi} Cp(\theta) \frac{\partial y}{\partial \theta} d\theta \tag{47}$$

$$C_{T_f} = -\frac{2}{Re} \int_0^{2\pi} \omega(1,\theta) \frac{\partial x}{\partial \theta} d\theta \tag{48}$$

Here the subscripts p and f denote pressure and friction parts respectively. All derivatives in the expressions are evaluated at the

surface. The lift and drag coefficients referred to the wind axes are obtained from

$$C_L = C_N \text{Cos}\alpha - C_T \text{Sin}\alpha \tag{49}$$

$$C_D = C_N \text{Sin}\alpha + C_T \text{Cos}\alpha \tag{50}$$

The equations for the moment coefficients are readily set up as

$$C_{M_p} = -\frac{1}{L^2} \int_0^{2\pi} Cp \left[x\frac{\partial x}{\partial \theta} + y \frac{\partial y}{\partial \theta} \right] d\theta \tag{51}$$

$$C_{M_f} = -\frac{2}{ReL} \int_0^{2\pi} \omega(1,\theta) \left[x \frac{\partial y}{\partial \theta} - y \frac{\partial x}{\partial \theta} \right] d\theta \tag{52}$$

In all the expressions above the forces and moments are normalized with respect to the airfoil chord length. The moment taken about the origin of the coordinate system is positive in the counterclockwise direction.

The velocity components in the physical plane are obtained by considering the derivatives of stream function. Noting that Ψ is invarient in the transformation, one has

$$\frac{\partial \Psi}{\partial r} = \frac{\partial \Psi}{\partial x}\frac{\partial x}{\partial r} + \frac{\partial \Psi}{\partial y}\frac{\partial y}{\partial r} \tag{53}$$

$$\frac{\partial \Psi}{\partial \theta} = \frac{\partial \Psi}{\partial x}\frac{\partial x}{\partial \theta} + \frac{\partial \Psi}{\partial y}\frac{\partial y}{\partial \theta} \tag{54}$$

Solving for $\frac{\partial \Psi}{\partial x}$ and $\frac{\partial \Psi}{\partial y}$, the x and y-components of velocity in the physical plane are obtained as

$$V(x) = \frac{\partial \Psi}{\partial y} = \frac{1}{J}\left[\frac{\partial \Psi}{\partial \theta}\frac{\partial x}{\partial r} - \frac{\partial \Psi}{\partial r}\frac{\partial x}{\partial \theta}\right] \tag{55}$$

$$V(y) = -\frac{\partial \Psi}{\partial x} = \frac{1}{J}\left[\frac{\partial \Psi}{\partial \theta}\frac{\partial y}{\partial r} - \frac{\partial \Psi}{\partial r}\frac{\partial y}{\partial \theta}\right] \tag{56}$$

where

$$J = \frac{\partial x}{\partial r}\frac{\partial y}{\partial \theta} - \frac{\partial x}{\partial \theta}\frac{\partial y}{\partial r} \tag{57}$$

is the Jacobian of the transformation. The velocity components referred to the wind axes are then computed using

$$u = V(x)\mathrm{Cos}\alpha + V(y)\mathrm{Sin}\alpha \tag{58}$$

$$v = V(y)\mathrm{Cos}\alpha - V(x)\mathrm{Sin}\alpha \tag{59}$$

CHAPTER III

NUMERICAL PROCEDURE

The vorticity transport equation is solved using finite difference approximations. Some pilot investigations were carried out first for the choice of finite difference scheme and for an implicit procedure for solving the resultant set of algebraic equations. The following differencing schemes were considered for the convective terms of the vorticity transport equation: (1) central differencing, (2) a combination of cetnral and upwind differencing with local cell Reynolds number as the deciding parameter [22] and (3) Arakawa differencing scheme [23]. With the exception of upwind differencing, spurious values of vorticity were found to occur at locations away from the surface when central or Arakawa differencing is used. Such occurrences are attributable to [24, 25] the large grid spacing, and hence the all Reynolds numbers, used in regions of the flow far from the airfoil surface. Since these spurious vorticity values are small and since they do not significantly affect the solution, the low-order accurate upwind differencing was not chosen in preference to the other two differencing schemes. The numerical results obtained through central and Arakawa differencing scheme did not show any significant deviations. Mehta [17] used the Arakawa differencing scheme, which requires more arithmetical operations compared to central differencing, to ensure conservation of total vorticity. In the present study, the method of determining surface vorticity conserves the total vorticity. Hence,

central differencing which requires lesser computational time was preferred over the Arakawa differencing scheme.

For the rest of the terms in the vorticity transport equation (23), a three point backward differening for the time derivative and central differencing for the diffusion terms are used.

The choice of the solution procedure for the fintie difference equation was based on the computer time requirement, for the first six time steps [9]. The procedures tested and their relative computer requirements are as follows. (1) Strongly Implicit Procedure (SIP) with block subdivision-100% (2) SIP method 21 with no block subdivision-220% (3) Alternating Direction Implicit (ADI) method-154% (4) Successive Point Relaxation (used in [17]) - 365% (5) Successive Line Relaxation-254%. It was also found that the ADI method did not yield acceptance solutions for the same time step sizes that were employed with the other methods. The SIP method with block subdivision is selected and the details of this procedure, the numerical methods used for the kinematic calculations and numerical procedure for load calculations are presented in the rest of this chapter.

Numerical Procedure for Vorticity Transport Equation

The grid system in the working plane (κ- plane) is formed by using $\Delta\rho = 1/47$ and $\Delta\theta = \pi/40$ (Fig. 2) and the corresponding grid network in the physical plane is shown in Fig. 1. Subscripts i and j in the following discussion are used to refer to a grid point with $\rho_j = 1.0-(j-1)\Delta\rho$ and $\theta_i = (i-1)\Delta\theta$. Note that $j = 1$ corresponds to $\rho = 1$, the airfoil surface and, $j = 48$ corresponds to $\rho = 0$ which is

roughly a circle of radius 13L in the physical plane.

The vorticity transport equation (23) is approximated using 3-point backward differencing, in general, for the time derivative and central differencing for spatial derivatives. The 3-point differencing for the time derivative is replaced by a two point backward differencing for the first two time steps after the impulsive start. Additionally, the time step, t, used in this study is not constant. Their values are doubled when time rates of change field variables are low and halved when such rates are high. A two-point backward difference for the time derivative is employed again for the first step following a reduction in t. Finite difference expressions for a few typical derivatives are given below.

$$\frac{\partial \omega}{\partial t} = \frac{1}{2\Delta t}\left(3\omega_{ij}^{n+1} - 4\omega_{ij}^{n} + \omega_{ij}^{n-1} \right) \text{, three-point}$$

$$= \frac{1}{\Delta t}\left(\omega_{ij}^{n+1} - \omega_{ij}^{n} \right) \text{, two-point} \tag{60}$$

$$\frac{\partial \omega}{\partial \theta} = \frac{1}{2\Delta\theta}\left(\omega_{i+1,j}^{n+1} - \omega_{i-1,j}^{n+1} \right) \tag{61}$$

$$\frac{\partial \omega}{\partial \rho} = \frac{1}{2\Delta\rho}\left(\omega_{i,j-1}^{n+1} - \omega_{i,j+1}^{n+1} \right) \tag{62}$$

$$\frac{\partial^2 \omega}{\partial \theta^2} = \frac{1}{(\Delta\theta)^2}\left(\omega_{i+1,j}^{n+1} - 2\omega_{ij}^{n+1} + \omega_{i-1,j}^{n+1} \right) \tag{63}$$

The finite difference form of equation (23) is then written for point i,j as

$$B_{ij}\omega^{n+1}_{i,j-1} + D_{ij}\omega^{n+1}_{i-1,j} + E_{ij}\omega^{n+1}_{ij} + F_{ij}\omega^{n+1}_{i+1,j}$$

$$+H_{ij}\omega^{n+1}_{i,j+1} = Q_{ij} \tag{64}$$

where

$$B_{ij} = \frac{L}{Re}\left[\left(\frac{r\rho'}{\Delta\rho}\right)^2 + \frac{r\rho' + r^2\rho''}{2\Delta\rho}\right]_j - \left[\frac{r\rho'}{2\Delta\rho}\right]_j \left(\frac{\partial\psi}{\partial\theta}\right)^n_{i,j-1}$$

$$D_{ij} = \frac{L}{Re}\frac{1}{(\Delta\theta)^2} - \left[\frac{r\rho'}{\Delta\theta}\right]_j \left(\frac{\partial\psi}{\partial\rho}\right)^n_{i-1,j}$$

$$E_{ij} = -2\frac{L}{Re}\left[\left(\frac{r\rho'}{\Delta\rho}\right)^2_j + \frac{1}{(\Delta\theta)^2}\right] - \frac{3}{2\Delta t}\,(r^2H^2)_{ij}$$

$$F_{ij} = \frac{L}{Re}\frac{1}{(\Delta\theta)^2} + \left[\frac{r\rho'}{2\Delta\theta}\right]_{ij}\left(\frac{\partial\psi}{\partial\rho}\right)^n_{i+1,j}$$

$$H_{ij} = \frac{L}{Re}\left[\left(\frac{r\rho'}{\Delta\rho}\right) - \frac{r\rho' + r^2\rho''}{\Delta\rho}\right] + \left(\frac{r\rho'}{2\Delta\rho}\right)_j \left(\frac{\partial\psi}{\partial\theta}\right)^n_{i,j+1}$$

$$Q_{ij} = \frac{1}{2\Delta t}\,(r^2H^2)_{ij}\left[-4\,\omega^n_{ij} + \omega^{n-1}_{ij}\right]$$

The superscript n refers to the time level, and the vorticity values at level (n+1) are unknown. Note that the stream function values are

allowed to lag by one time step. The Strongly Implicit Procedure (21) for solving the set of simultaneous equations given by (65) is outlined below.

Suppose we are interested in solving equations (64) in the range $1 \leq i \leq I$, $1 \leq j \leq J$. The vorticity values on the boundaries of this region, namely $\omega_{o,j}, \omega_{I+1,j}$ for all j, and $\omega_{i,o}, \omega_{i,J+1}$ for all i are known. Equation (65) is written in matrix notation

$$\left[M\right] \{\omega\} = \{Q\} \tag{65}$$

where the superscript, n+1, for has been omitted for convenience. The elements of matrix $[M]$ contain derivatives of stream function which are known as they are written at previous time level, n. The expanded form of the coefficient matrix $[M]$ is shown in Fig. 3a for the case when the equations are ordered such that the index i increases more rapidly than the index j. Note that the notation used in Fig. 3a to identify the elements of matrix $[M]$ does not correspond to the standard matrix notation; the subscript i,j instead refers to the grid point. Matrix $[M]$ is sparse, with only five non-zero diagonals corresponding to the five grid points involved in formulating the finite difference equation for the point i,j. These points are shown using unfilled circles in Fig. 3e.

If Eq. (65) were to be solved by direct elimination procedures, one would first factorize the matrix $[M]$ into the product of a lower triangular and an upper triangular matrix or use a procedure that is essentially equivalent. In such cases the triangular matrices generated will not in general be sparse thus slowing down the elimination process. Instead the matrix $[M]$ could be altered making it amenable to a rapidly converging

iteration process. The altered form of the coefficient matrix will be denoted by $[M] + [N]$. The alteration is done such that when $[M] + [N]$ is factored into a product $[L][U]$, the lower triangular matrix $[L]$ and the upper triangular matrix $[U]$ will also be sparse having only three non-zero elements in each row. The expanded forms of $[L]$ and $[U]$ are shown in Figures 3b, and 3c, and their product, $[L][U] = [M] + [N]$ is shown in Figure 3d. The matrix $[M] + [N]$ now contains seven non-zero elements in each row, as against the five elements in the original matrix $[M]$. The additional two unknowns introduced correspond to the values at the grid points (i-1,j+1) and (i+1,J-1) which are indicated by blackened circles in Fig. 3c. Thus one sees that if the finite difference equations were formulated such that each equation at point (i,j) involved unknowns from all seven grid points shown in Fig. 3c, then the resultant coefficient matrix could easily be factored into sparse upper and sparse lower triangular matrices. To achieve this, the two additional unknowns $\omega^{n+1}_{i-1,j+1}$ and $\omega^{n+1}_{i+1,j-1}$ are introduced into each algebraic equation (64), and their influence is negated by subtracting approximately equal terms which are Taylor series expansions for $\omega^{n+1}_{i-1,j+1}$ and $\omega^{n+1}_{i+1,j-1}$, given by

$$\omega^{n+1}_{i-1,j+1} = -\omega^{n+1}_{ij} + \omega^{n+1}_{i,j+1} + \omega^{n+1}_{i-1,j} \tag{66}$$

$$\omega^{n+1}_{i+1,j-1} = -\omega^{n+1}_{ij} + \omega^{n+1}_{i+1,j} + \omega^{n+1}_{i,j-1} \tag{67}$$

In Eqs. (66) and (67), terms of the order of $(\Delta\rho)^3$, $(\Delta\theta)^3$, $(\Delta\rho\Delta\theta)$ and higher order terms have been neglected. The accuracy of these

approximations would depend upon how closely the grid points are spaced and how smooth are the variations in ω. Since there is no precise control over these factors, the right hand members of (66) and (67) are in addition multiplied by a factor α_p, $0 < \alpha_p < 1$, and a rapidly converging iteration scheme is introduced during which this parameter is cyclically varied.

Introducing this modification into Eq. (64), one obtains

$$B_{ij}\,\omega_{i,j-1} + D_{ij}\,\omega_{i-1,j} + E_{ij}\,\omega_{ij} + F_{ij}\,\omega_{i+1,j} + H_{ij}\,\omega_{i,j+1}$$

$$+ C_{ij}\left[\omega_{i+1,j-1} - \alpha_p\,(-\omega_{ij} + \omega_{i+1,j} + \omega_{i,j-1})\right]$$

$$+ G_{ij}\left[\omega_{i-1,j+1} - \alpha_p\,(-\omega_{ij} + \omega_{i,j+1} + \omega_{i-1,j})\right] = Q_{ij} \qquad (68)$$

where the superscript (n+1) has been omitted for convenience. The coefficient matrix of (68) represents $[M] + [N]$. Upon comparing the elements of this matrix with those of the product $[L]\,[U]$, the following set of equations for the solution of the $[L]$ and $[U]$ matrices are obtained.

$$b_{ij} = B_{ij}/(1 + \alpha_p e_{i,j-1}) \qquad (69)$$

$$c_{ij} = D_{ij}/(1 + \alpha_p f_{i-1,j}) \qquad (70)$$

$$d_{ij} = E_{ij} + \alpha_p (b_{ij}e_{i,j-1} + c_{ij}f_{i-1,j}) - c_{ij}e_{i-1,j} - b_{ij}f_{i,j-1} \quad (71)$$

$$e_{ij} = (F_{ij} - \alpha p\, b_{ij}e_{i,j-1})/d_{ij} \quad (72)$$

$$f_{ij} = (H_{ij} - \alpha p\, c_{ij}f_{i-1,j})/d_{ij} \quad (73)$$

The above set of equations is easily solved by marching in the i-increasing, j-increasing (i j) directions.

Equations (65) is modified by adding $[N]\{\omega\}$ to both sides of the equation and $[M]\{\omega\} - [M]\{\omega\}$ to the right hand side to give:

$$[M+N]\{\omega\} = [M+N]\{\omega\} - [M]\{\omega\} + \{Q\} \quad (74)$$

Since the right hand side of this equation is unknown, an iterative procedure is introduced and the right hand side is computed using known values of previous iteration. Equation (75) is re-written as

$$[M+N]\{\omega\}^{k+1} = [M+N]\{\omega\}^{k} - \beta_1([M]\{\omega\}^{k} - \{Q\}) \quad (75)$$

where k is an iteration counter and β_1 is a relaxation parameter. For computational purposes the above form is further changed using the definitions

$$\{\Delta\omega\}^{k+1} = \{\omega\}^{k+1} - \{\omega\}^{k} \quad (76)$$

$$\{R\}^k = \{Q\} - [M]\{\omega\}^k, \tag{77}$$

to obtain

$$[M+N]\{\omega\}^{k+1} = \beta_1\{R\}^k \tag{78}$$

where $\{R\}$ represents the residue vector the elements of which are computed using Eq. (77), the expanded form of which is obtained from Eq. (64). Replacing $[M+N]$ by the product $[L][U]$,

$$[L][U]\{\Delta\omega\}^{k+1} = \beta_1\{R\}^k \tag{79}$$

Defining an intermediate vector, $\{V\}$, by

$$[L]\{V\} = \beta_1\{R\}^k \tag{80}$$

from Eqs. (79) and (80) one obtains

$$[U]\{\Delta\omega\}^{k+1} = \{V\} \tag{81}$$

The last two equations written out for point (i,j) are

$$b_{ij}V_{i,j-1} + c_{ij}V_{i-1,j} + d_{ij}V_{ij} = \beta_1 R^k_{ij} \tag{82}$$

$$\Delta\omega^{k+1}_{ij} + e_{ij}\Delta\omega^{k+1}_{i+1,j} + f_{ij}\Delta\omega^{k+1}_{i,j+1} = V_{ij} \tag{83}$$

The values of $\Delta\omega$ are computed by marching out Eq. (82) in the $i\uparrow j\uparrow$ direction first and then equation (83) in the $i\downarrow j\downarrow$ direction. The set of equations (69) to (73), Eqs. (82) and (83) along with Eq. (64) for the determination of residues are the necessary equations for the solution.

Stone [21] has given some guide lines for the choice of the numerical values of the cyclic iteration parameter, α_p, and the relaxation parameter β_1. In the model problems tested by Stone [21], he found that β_1 could be set to unity. In the present study however values less than unity were found necessary for satisfactory convergence. The cyclic iteration parameters are generated according to the relation [21].

$$1-\alpha_{pm} = (1-\alpha_{pmax})^{(m-1)/M}, \quad m=1, 2,\ldots M \tag{84}$$

where M is the number of parameters and α_{pmax} is the maximum of these values. In this study the numerical values chosen for these parameters are $M=9$ and $0.75 \leq \alpha_{pmax} \leq 0.95$.

The standard procedure in implementing the SIP method is to apply it in the region bounded by the solid surface ($\rho=1$) and a $\rho=\rho_1$ = constant line which is well removed from the non-negligible vorticity region so that the condition $\omega=0$ could be specified at $\rho=\rho_1$. Since convection is much more rapid than diffusion at moderate and high Reynold's numbers, the vorticity generated at the surface spreads laterally or in the upstream direction only very short distances compared to the general downstream direction. Consequently the value of ρ_1 would be decided by the extent of the wake and thus a large number of data points where vorticity is

negligible enter into the solution procedure, rendering it inefficient. To avoid such an inefficiency the flow field is divided into several blocks and the SIP method is applied individually to each block. Each solution block is bounded by two constant θ-lines, a part of the ρ =1 line, and a $\rho = \rho_B$ line. The value of ρ_B can be different for different blocks. For example, the $\rho = \rho_B$ line can be placed relatively closer to the surface for the block near leading edge compared to the block that encloses the wake of the airfoil (Fig. 2).

In the present study the solution field is divided into four blocks. The locations of constant θ dividing lines are kept flexible and can be changed to suit the shape of the non-negligible vorticity region.

In describing the SIP method, it was stated earlier that the vorticity values on all boundaries are assumed to be known. This implies that ω values at next time level should be known on the surface, on θ = constant lines and on a $\rho = \rho_B$ line for each block. Since these values are not known in advance they are obtained through iterative processes.

On the constant θ boundary lines the vorticity values are determined by Successive Line Relaxation procedure using values of previous iteration for vorticity on adjacent constant θ lines. Equation (64) is rewritten as

$$B_{ij}\omega_{i,j-1}^{n+1,k+1} + E_{ij}\omega_{ij}^{n+1,k+1} + H_{ij}\omega_{i,j+1}^{n+1,k+1}$$

$$= Q_{ij} - D_{ij}\omega_{i-1,j}^{n+1,k} - F_{ij}\omega_{i+1,j}^{n+1,k} \qquad (85)$$

where k is an iteration counter. Since the right hand side of Eq. (85) is known, it gives rise to a tri-diagonal matrix which is readily solved using Thomas algorithm [3]. The vorticity values at these points on the constant θ boundaries are then set to

$$\omega_{ij}^{n+1,k+1} = \omega_{ij}^{n+1,k} + \beta_2 (\Delta\omega)_{ij}^{n+1,k+1} \tag{86}$$

where $(\Delta\omega)_{ij}^{n+1,k+1} = \omega_{ij}^{n+1,k+1} - \omega_{ij}^{n+1,k}$ and β_2 is a relaxation parameter with a value less than unity.

Determination of Surface Vorticity

For the surface vorticity calculations it is assumed that the value of $rH^2\omega$ is uniformly distributed in each cell at the grid point value. Equation (39) is written, for computational purposes, as

$$\zeta_K(\theta_i) = 2\mathrm{Sin}(\alpha+\theta_i) + \sum_{i_o=1}^{IL} \sum_{j_o=2}^{JR_{io}} (\omega r H^2)_{i_o j_o} G_1(r_{j_o}, \theta_{i_o} - \theta_i) \tag{87}$$

where

$$G_3 = \frac{1}{2\pi} \int_{r_1}^{r_2} (r_o^2 - 1) \int_{\beta_1}^{\beta_2} \frac{d\beta}{1+r_o^2 - 2r_o \mathrm{Cos}\beta} \, dr_o$$

$$= \frac{1}{\pi} \int_{r_1}^{r_2} \left[\tan^{-1} \left\{ \frac{1+r_o}{1-r_o} \tan \frac{\beta_1}{2} \right\} - \tan^{-1} \left\{ \frac{1+r_o}{1-r_o} \tan \frac{\beta_2}{2} \right\} \right] dr_o \tag{88}$$

with

$$\beta = \theta_o - \theta; \quad \beta_1 = \theta_{i_o} - \theta_i - \frac{\Delta\theta}{2}; \quad \beta_2 = \theta_{i_o} - \theta_i + \frac{\Delta\theta}{2}$$

$$r_1 = r(\rho_1) = r(\rho_{j_o} - \frac{\Delta\rho}{2}); \quad r_2 = r(\rho_2) = r(\rho_{j_o} + \frac{\Delta\rho}{2})$$

The summations in Eq. (87) is done over the rotational region only. This is indicated by the upper limit, JR, of the inner summation being a function of the outer summation index i_o. The geometric coefficient given by Eq. (88) is precomputed and stored. The integral over r_o in Eq. (88) is numerically evaluated. Having determined the surface vorticity sheet strength, ζ_K, the value of surface vorticity is obtained using

$$\omega_{i,1} = \frac{(\zeta_K)_i}{H^2_{i,1}\Delta r_1} \tag{89}$$

where $\Delta r_1 = r(\rho=1) - r(\rho=1-\frac{\Delta\rho}{2})$, the function $r(\rho)$ being the stretching relation defined through Eq. (18). The surface vorticity determined through Eq. (89), is used during the iteration through a relaxation scheme defined by

$$\omega_{i,1}^{n+1,k+1} = \omega_{i,1}^{n+1,k} + \beta_3 \Delta\omega_{i,1} \tag{90}$$

where

$$\Delta\omega_{i,1} = \omega_{i,1}^{n+1,k+1} - \omega_{i,1}^{n+1,k}$$

Computation of Stream Function Values

The computation of stream function is confined to a region bounded by the surface ($\rho=1$) and a ρ =constant line. The constant ρ line is so chosen that the computation of Ψ is essentially confined to the non-negligible vorticity region. This region is further divided into two or more blocks. Each block is bounded by two constant ρ lines and the θ =0 line (See Fig. 2). On the surface (ρ =1) the value of stream function is specified as zero. On other ρ =constant lines the integral expression (32) is used to obtain Ψ values. On the θ =0 boundary line and for interior points in each block, implicit iterative schemes are used to solve the finite difference form of Eq. (25). Such block division and the combined use of integral representation and finite difference method is found to be faster than using the integral representation alone for the computation of Ψ .

For numerical computations, the integral representation (32) is approximated by

$$\Psi_{i,j} = \sum_{i_o=1}^{IL} \zeta_{K\,i_o} \left[G_2 - G_3(\theta_{i_o} - \theta_i,\ \tilde{r}=1) \right]_{j_o=1}$$

$$+ \sum_{i_o=1}^{IL} \sum_{j_o=2}^{JR_{i_o}} r_{j_o} \cdot (\omega r H^2)_{i_o, j_o} \left[G_2 - G_3(\theta_{i_o} - \theta_i, \tilde{r} \right]_{j_o}$$

$$- \frac{1}{r_j} \mathrm{Sin}(\alpha + \theta_i) \qquad (91)$$

where

$$\tilde{r} = \begin{cases} r_j/r_{j_o}, & \text{if } r_j/r_{j_o} < 1 \\ r_{j_o}/r_j, & \text{if } r_j/r_{j_o} \geq 1 \end{cases} \tag{92}$$

$$G_2 = \frac{\Delta\theta}{2\pi} \left(\ln r_j - \ln r_{j_o}\right) \tag{93}$$

$$G_3 = \frac{1}{4\pi} \int_{\beta_1}^{\beta_2} \left[\ln 1+\tilde{r}^2-2\tilde{r}\cos\beta\right] d\beta \tag{94}$$

with

$$\beta = \theta_o - \theta$$

$$\beta_1 = \theta_{i_o} - \theta_i - \frac{\Delta\theta}{2}$$

$$\beta_2 = \theta_{i_o} - \theta_i + \frac{\Delta\theta}{2}$$

It is assumed that the product $\omega r H^2$ is uniformly distributed in a computational cell along the r = constant line that passes through the grid point of the cell. The integral in Eq. (94) is evaluated numerically. Note that the value of $(\Delta r)_{j_o}$ in Eq. (91) is given, according to the cell definition, by

$$(\Delta r)_j = r\left(\rho_j + \frac{\Delta\rho}{2}\right) - r\left(\rho_j - \frac{\Delta\rho}{2}\right), \quad j \geq 2 \tag{95}$$

where $r(\rho)$ is the stretching relation defined through Eq. (18).

The computation of Ψ for interior points is done by solving the finite difference form of equation (25) which is obtained using central

differences as

$$B_{ij}\Psi_{i,j-1} + D_{ij}\Psi_{i-1,j} + E_{ij}\Psi_{ij} + F_{ij}\Psi_{i+1,j} + H_{ij}\Psi_{i,j+1} = Q_{ij} \tag{96}$$

where

$$B_{ij} = \left(\frac{r}{\Delta\rho}\frac{d\rho}{dr}\right)_j^2 + \frac{1}{2\Delta\rho}\left(r\frac{d\rho}{dr} + r^2\frac{d^2\rho}{dr^2}\right)_j$$

$$D_{ij} = F_{ij} = \frac{1}{(\Delta\theta)^2}$$

$$E_{ij} = -2\left[\left(\frac{r}{\Delta\rho}\frac{d\rho}{dr}\right)_j^2 + \frac{1}{(\Delta\theta)^2}\right]$$

$$H_{ij} = \left(\frac{r}{\Delta\rho}\frac{d\rho}{dr}\right)_j^2 - \frac{1}{2\Delta\rho}\left(r\frac{d\rho}{dr} + r^2\frac{d^2\rho}{dr^2}\right)_j$$

$$Q_{ij} = -r_j^2(H^2\omega)_{i,j}$$

The form of equation (96) is the same as the form of Eq. (64). The Strongly Implicit Procedure described earlier for solving Eq. (64) is used to obtain the solution for the set of simultaneous equations defined by (96). The value of relaxation parameter in Eq. (76) is chosen to be unity for this case.

On the $\theta = 0$ boundary line, the stream function values are determined by employing Successive Line Over-relaxation procedure. For this purpose, Eq. (96) is rewritten as

$$B_{ij}\,\Psi^{k+1}_{i,j-1} + E_{ij}\,\Psi^{k+1}_{ij} + H_{ij}\,\Psi^{k+1}_{i,j+1}$$

$$= Q_{i,j} - D_{ij}\,\Psi^{k}_{i-1,j} - F_{ij}\,\Psi^{k}_{i+1,j} \tag{97}$$

and the resultant tri-diagonal system is solved using Thomas algorithm (3). The values of Ψ are iteratively updated using the relaxation scheme

$$\Psi^{k+1}_{ij} = \Psi^{k}_{kj} + \Delta\omega_{ij}\,\beta_4 \tag{98}$$

where $\Delta\Psi = \Psi^{k+1} - \Psi^{k}$. Through numerical experimentation it was found that an optimum value of β_4 exists and that it is different for different blocks. For the block closest to the sruface labelled as Block 1 in Fig. 2, the optimum value was found to be 1.2. These values were found to be higher for blocks away from surface. For blocks 2 and 3 the values of β_4 used are 1.6 and 1.85 respectively.

Computational Sequence

In summary the following sequence of computations are involved in advancing the solution through one time step:

(1) Initialize $\omega^{n+1,k=1}_{ij} = \omega^{n}_{ij}$ for all grid points, except on the airfoil surface for the first iteration. Make a better guess for surface vorticity values through time wise extrapolation.

(2) Advance iteration counter; scan each block for the extent of non-negligible vorticity region and choose a constant ρ line for each

block for setting $\omega = 0$.

(3) Determine ω values on the side boundaries (i.e., constant lines) of each block the using SLR method (Eq. 85).

(4) Apply the SIP method in each block and determine vorticity values at interior points.

(5) Compute and update surface vorticity values

(6) Test for convergence at all grid points including the surface. If convergence has not been obtained repeat computations from Step 2.

(7) Scan the flow field and decide upon the region where stream function values are to be computed. Subdivide this region into blocks.

(8) Compute stream function on the ρ = constant boundaries of these blocks using integral representation.

(9) Compute Ψ on the $\theta = 0$ line using successive line relaxation.

(10) Using the SIP method, compute Ψ at interior points in each block.

(11) Prepare to advance computation to next time level.

After the values of ω and Ψ have been obtained the computation of loads and velocity components in the physical plane are performed. The velocity in the physical plane is obtained using Equations (56) through (60). The derivatives of stream function are computed using central difference. In computing the pressure coefficients on the surface using Eq. (45), the normal gradient of vorticity on the surface is represented by a one-sided finite difference formula

$$\left.\frac{\partial \omega}{\partial \rho}\right|_{\rho=1} = \frac{\omega_{i,1} - \omega_{i,2}}{\Delta \rho} \tag{99}$$

which has a truncation error $O(\Delta \rho)$.

CHAPTER IV

RESULTS AND DISCUSSION

In order to check the program coding, the study of flow past a circular cylinder at a Reynold's number of 40 (based on cylinder diameter) was undertaken. The computations were done using a coarse grid spacing with $\Delta\theta = \frac{\pi}{18}$ and $\Delta\rho = 1/25$. No stretching relationship was used for this case. The computations were carried out with a starting value of $t = 0.1$ which was subsequently increased to 0.4. The computations were carried out up to a time level of $t = 9.5$. The drag coefficient at this time level is found to be 1.67 which is in reasonable agreement with an experimental [29] value of 1.5. The pressure distribution over the surface is compared with experimental values in Fig. 4. The pressure distribution of the numerical results have been modified by adding a constant so that the C_p values will be the same as that of the experiment at the leading edge. The pressure distribution is found to be in reasonably good agreement.

Impulsively Started Airfoil

The numerical results for the viscous flow past a 9% thick airfoil at a Reynold's number of 1000 (based on airfoil chord length) and at an angle of attack of 15^{o} are discussed in this section. The airfoil geometry is obtained by assigning the following numerical values for the transformation: $\xi_o = -0.05214$, $\eta_o = 0.0$ and $\delta = 0.025$. These constants and hence the airfoil geometry are the same as those of Ref.[17]. The

computations are done using a grid spacing of $\Delta\theta = \frac{\pi}{40}$ and $\Delta\rho = 1.0/47$. With this grid spacing the total number of grid points available becomes 3840, even though with the present formulation all these points are not involved in the computation at all time levels. At very early time levels (up to t = 0.02) the extent of rotational region was about 28% of the total number of grid points. With progress in time the number of non-zero vorticity points in the flow field increases and when the computations were stopped finally at a time level of 28.756, the rotational field involved a total of 3121 grid points. In the present formulation the extent of rotational region evolves naturally during the process of computation, and is not specified a-priori as in the case of the study by Mehta [17]. In Mehta's work a region with 3024 grid points was specified as the rotational region beforehand. The present study indicates this to be excessively large at initial time levels and slightly inadequate at time levels near the end of the computation.

The airfoil geometry and the grid distribution in the physical plane are shown in Fig. 1. The maximum thickness of the airfoil is 8.9998% of chord and is located at 28.89% of chord. It is symmetric and its chord length is 3.7128127 times the radius of the circle. The radii of curvature at the nose and trailing edge are 0.882% and 0.033% of chord respectively. In the physical plane the distance from surface to the first modal point away from surface at typical stations are as follows: at trailing edge (TE) - 5.76×10^{-5}chord; at 0.4706% chordwise location - 1.99×10^{-3}chord; at leading edge 2.50×10^{-4}chord. Fig. 2 shows the discretization of the flow field and the subdivision of the field into four blocks for use with the Strongly Implicit Procedure. Each solution

block is bounded by two constant θ-lines, a part of the $\rho = 1$ line and a $\rho = \rho_j$ line. The value of ρ_j is different in each block. Even though the program has the capability to change the locations of constant dividing lines to accommodate the changes in the shape of the non-negligible vorticity region, during the computational process this was not found necessary. These locations are as defined in Fig. 2 for all time levels, and their corresponding locations in the physical plane are indicated in Fig. 1.

In the numerical results presented, the chordwise distance, denoted by X_C, is measured from the leading edge of the airfoil as shown in Fig. 1 and this distance is normalized with respect to the airfoil chord length. The force and moment coefficients are normalized with respect to the airfoil chord length. The moment is taken about the origin of the coordinate system (which is located at $X_C = 0.502016$) and is positive in the counterclockwise direction. All other quantities shown are normalized with respect to the free stream velocity and the radius of the unit circle. Vorticity and velocity values away from the surface are shown by plotting them along "normal" grid lines (i.e. θ = constant lines). The distance measured along such a grid line from the airfoil surface is denoted by D_N in the figures and this is normalized with respect to the radius of the circle and not the airfoil chord length. The noramlizing reference time is the one obtained by dividing the radius of the circle by the free stream velocity.

Time increments used in the numerical study vary from a value of $t = 0.001$ to 0.512. The solution just after the impulsive start of the airfoil is obtained with $t = 0.001$ and is continued with this value for

six steps. Since the time rate of change of all physical variables is very high after the impulsive start such values of Δt are necessary to obtain proper timewise resolution. As the gradients with respect to time decrease, the Δt values are doubled as often as possible until a maximum of $t = 0.512$ is reached at a time level of $t = 3.668$, and the solution is continued with this value of Δt up to $t = 11.348$. At this stage the flow is fully separated and in order to obtain better resolution, as well as to obtain faster convergence of the iterative procedure for vorticity, the time step values are reduced by one-half. Note that the non-dimensional time increments (as well as time levels) would be divided by a factor of 3.7128127 if the airfoil chord length, instead of the circle radius, were used as characteristic length to normalize time. In such a case the minimum and maximum time steps would have been 0.000269 and 0.1379 respectively. The time increments used at various levels are shown in Table 1. These values are the same as those of Mehta [17] except for minor changes after a time level of $t = 13.14$. In the present study solutions up to a time level of $t = 28.756$ were obtained using 145 time steps whereas in reference [17] a total of 152 steps were used.

The table also shows the residue in the vorticity value that was tolerated during the iterative procedure for vorticity transport equation. The maximum residue of vorticity is invariably found to occur on the airfoil surface either at the trailing edge or at points immediately adjacent to the trailing edge. Recognizing this fact, during the computational process a different tolerance value had been specified for these three points compared to the rest of the grid points. The tolerance level specified for the interior points was 0.5 and the obtained residual

	Time Interval	Δ t	Average values for time interval shown				
			$\lvert\Delta\omega\rvert_{MAX}$	No. of iterations	$\%\lvert\Delta Cp\rvert_{max}$	Total Vorticity Ω	Computer time (sec) per time step*
1	0.0 → 0.006	0.001	2.724	30	1.703	2.16×10^{-4}	35.17
2	0.006 → 0.012	0.002	2.895	19	1.375	6.10×10^{-4}	32.1
3	0.012 → 0.02	0.004	2.910	17	1.978	1.39×10^{-3}	31.0
4	0.02 → 0.036	0.008	2.212	15	1.375	2.13×10^{-4}	31.0
5	0.036 → 0.116	0.016	1.040	22	1.115	6.75×10^{-4}	42.0
6	0.116 → 0.276	0.032	0.927	29	1.078	1.18×10^{-3}	62.0
7	0.276 → 0.596	0.064	0.867	41	4.973	3.58×10^{-3}	70.6
8	0.596 → 1.62	0.128	0.961	32	1.310	1.15×10^{-3}	87.1
9	1.62 → 3.668	0.256	0.678	22	2.144	4.42×10^{-4}	71.4
10	3.668 → 11.348	0.512	0.98	38	5.403	6.78×10^{-4}	118.9
11	11.348 → 14.932	0.256	0.865	31	3.199	2.7×10^{-3}	138.2
12	14.932 → 19.54	0.128	1.05	19	4.24	1.78×10^{-3}	118.7
13	19.54 → 28.756	0.256	1.037	34	5.08	3.39×10^{-3}	171.2
	Average values for 145 Steps		1.133	29	3.765	2.59×10^{-3}	115.36

Table 1. Summary of Time Increments, Residues, Iterations and Computational Time

* CDC-CYBER 70/MODE74-6400CPU

values in general have been much less than this. For the trailing edge and the two neighboring points on the surface the specified tolerance value was 3.0 at initial time levels and was subsequently reduced to 1.5. During the initial time levels the surface vorticity values at the TE are found to be 120 or more and hence the tolerated values are less than or equal to 3% of actual vorticity value. At later time levels the vorticity values at the trailing edge is close to zero and its absolute value does not in general exceed a value of about 20. At these time levels the tolerated residue when expressed as percentage of the actual vorticity value will be high. Continuation of the iteration beyond the numbers indicated in the table has not been found effective in reducing the residue; the residue instead oscillates around a minimum without showing any tendency to reach zero value even though its magnitude does not amplify. The main cause of this convergence problem at the trailing edge is the fact that the scale factor of transformation is very low at the trailing edge. It has a value of 0.00243 at TE and changes by an order of magnitude as one moves to the next grid point on the surface. Since, in the present computational procedure, the computed value of vorticity sheet strength at the surface must be divided by the scale factor to obtain the vorticity value, small errors in the computation of sheet strength get amplified. Nevertheless the coarse tolerances used near the trailing edge do not significantly affect any integrated results (as for example load coefficients) as the elemental length at the trailing edge is extremely small compared to the elemental lengths around other grid points on the surface.

The acceptability of the block subdivisions used for the solution of the vorticity transport equation was checked out by comparing the vorticity values obtained by the following methods: (1) the Successive Line Relaxation procedure with no block subdivision (2) the Strongly Implicit Procedure (SIP) with no block subdivision (3) the SIP method with four blocks and for three different locations of the constant-boundary lines of the block enclosing the trailing edge of the airfoil. This check was carried out for the time period $t = 0.001$ to $t = 0.006$, and the comparison of vorticity values showed no significant deviations, when the values of vorticity are greater than unity.

As pointed out in the last chapter, the vorticity transport equation is rendered linear in this study by letting the values of stream function lag by one time step. The validity of this approximation was checked at time $t = 0.596$, by repeating the computations with the stream function values iteratively updated for the current time level. The maximum relative deviation in the value of vorticity was found to be less than 3%, for values of vorticity greater than unity. The maximum relative error in the values of stream function was found to be about 9%. The time step size for this investigation was 0.064. Even though this check was not repeated at time levels where a maximum step size of $\Delta t = 0.512$ was employed in the computations, the errors at these time levels are not expected to be significant, since the time rates of change of the field variables at these time levels are low.

The effect of step size on the solution was investigated at time $t = 0.724$ by obtaining the solutions at this time level, using the step sizes $\Delta t = 0.063$ and $\Delta t = 0.128$. The previous time level of

computations was $t = 0.596$. Again no significant changes in the values of vorticity were found.

In the numerical integration of surface vorticity gradients for obtaining Cp values a residual error is found to occur. That is, it is found that $Cp(\theta) \neq Cp(\theta+2\pi)$. Such errors, denoted as Cp and expressed as percentages of the maximum absolute value of Cp on the surface, are also indicated in the table giving the summary of residues. The cause of these errors are due to numerical inaccuracies in (1) the determination of vorticity gradients on the surface, (2) the computation of surface vorticity, and (3) the integration procedure for pressure coefficient. Even though Wu [5] has shown that these errors are attributable to the lack of conservation of total vorticity, in the present case this is not expected to be the source of the error since the procedure employed for the determination of surface vorticity automatically conserves vorticity. The total vorticity in the flow field averaged for each time block are also shown in Table 1. These values are only approximate since the integration over the flow field was performed using a simple summation procedure and assuming vorticity to remain constant in each computational cell. Nevertheless these values are found to be small enough to be treated as zero.

The average number of iterations required for the vorticity transport equation and the averaged computer time requirement per time step are also reported in the table for each time interval. The computer time requirement is for both the kinetic and the kinematic calculations. Note that there is no correlation between number of iterations used and the time step, Δt. Also, for the same number of iterations the computer time

requirements at larger time levels will be higher than that for lower time levels. For example, even though the average number of iterations is the same for the time intervals no. 2 and no. 12, the computational time requirements are 32.1 and 118.7 seconds respectively. The reason for this is the fact that at lower time levels the number of non-zero vorticity points that are involved in the computation is significantly less compared to large time levels. A conventional numerical procedure, like that of reference (17) which does not take advantage of this fact would require a computer time of 118.7 seconds for both the time intervals.

The computer time requirement for the stream function calculations is found to be about half of the time taken for the kinetic part during early time levels. At large time levels these two are approximately equal. At points interior to block boundaries, where the finite difference form of Poisson's equation is used to compute Ψ values, the maximum value of the residue, $\Delta\Psi$, has been kept below 10^{-6}. This maximum residue is always found to occur at a point close to the outer boundary of the block. The number of iterations required to achieve this residue varies from about 23 at early time levels to about 60 at large time levels.

The results of the computation are shown in the figures using plots of surface vorticity, surface pressure distribution, vorticity profiles at selected stations on the upper surface, and time history of loads, stagnation points and separation/reattachment points. In the figures where surface vorticity distributions are plotted, the vorticity distributions that correspond to the upper and the lower surfaces are identified as follows: Along the lower surface, vorticity values are positive from

the forward stagnation point to X_c close to the trailing edge. In general the values along lower surface are located in the lower half of the figures. In the plots of surface pressure coeffcient the portion of a curve that corresponds to the upper surface and the portion the corresponds to the lower surface are readily identified by remembering that the lift coefficient always stays positive. The Cp values on the upper surface are ususally lower than the Cp values on lower surface.

The stagnation points, separation and reattachment points at various time levels are defined as those points where the instantaneous value of vorticity on the surface is zero. The locations of these points are determined by linearly interpolating surface vorticity values.

In addition to the quantitative plots, the flow phenomena are also presented using contour plots of streamlines and equi-vorticity lines, and velocity profiles at selected stations on the upper surface. In the contour plots, the plotted values of stream function fall in the range -0.48 to 0.48 in steps of 0.04. For equivorticity contours the selected values are from -9.0 to +9.0 in steps of 2.0. The coordinate values of these contours are obtained by linear interpolation in the working plane first and then they are plotted in the physical plane using the transformation relationships. In the plots of velocity profiles, where the total velocity vectors are plotted along the normal grid line, a length of half an inch represents unit velocity. These profiles are presented for the following chordwise locations: X_{cu} = 0.0349, 0.1353, 0.2890, 0.4760, 0.67, 0.8406 and 0.9581.

Flow Phenomena After Impulsive Start ($t = 0.0$ to 0.596)

At time $t = 0^-$ the airfoil is at rest and at $t = 0^+$ it is impulsively set into motion at free stream velocity. At this instance vorticity exists only on the airfoil surface and the flow away from the surface is a noncirculatory potential flow. When the vorticity exterior to the airfoil surface is set to zero, the equation for the surface vorticity determination automatically yields the appropriate vorticity distribution on the airfoil surface corresponding to such a flow. The plot of the streamline pattern for this flow is shown in Fig. 48. The rear stagnation point (RSP) at this stage is located on the upper surface at a chordwise location of 0.9808. Within a very short time the stagnation point moves to a point close to the trailing edge as shown in Fig. 41. This rapid movement of the rear stagnation point is found to be accompanied by a small separation bubble located between RSP and TE at time levels 0.003 and 0.004. The size of this bubble is too small to be shown in the contour plots as it involves only two very closely spaced grid points near the trailing edge. The rapid movement of the RSP towards the trailing edge is also accompanied by a rapid forward movement of the front stagnation point (FSP). After time $t = 0.012$ the front stagnation point moves backward again. The forward stagnation point is always located on the lower surface while the rear stagnation point is located on the upper surface up to a time level of 0.18 and it mvoes to the lower surface at $t = 0.212$.

In the interpretation of the numerical results the movements of the front stagnation point are often related to the growth or decay of circulation around the airfoil. It is not intended to imply that the

actual circulation around the airfoil excluding the wake region was computed. Since it is difficult to define a precise contour of integration for such purpose, no attempt has been made to determine circulation around the airfoil or in the wake region. The identification of the rearward movement of front stagnation point with intensification of circulation around the airfoil and the forward movement of the FSP with decay of circulation is heuristic. Thus the rearward movement of FSP after time $t = 0.012$ is interpreted to indicate the growth of circulation around the airfoil.

After the impulsive start, the values of vorticty as well as the vorticity gradients are very large (Fig. 25, 32, 40). Consequently the load coefficients are also very high. At time $t = 0.001$ the actual values of these coefficients are $C_L = 738$, $C_D = 297$ and $C_M = 1.55$. As the vorticity is diffused outward from the surface the high velocity region near surface (See Fig. 74) at early time levels produces a strong convective transport of vorticity in the downstream direction. Effectively, then values of both vorticity and vorticity gradients fall off rapidly thus reducing the values of force and moment coefficients. From the very high initial velues mentioned above the lift and drag coefficients attain values close to 1.0 at a time level of $t = 0.1$.

The surface vorticity distributions after impulsive start are shown in Figures 6 and 7. At these time levels the vorticity values at the leading edge are negative and at the trailing edge they are positive. The first appearance of a local minimum for the upper surface vorticity near the leading edge is observed at $t = 0.068$ as shown in Fig. 7. The onset of adverse pressure gradient around this location is clearly shown

in the plot of surface pressure distribution (Fig. 17). The region of adverse pressure gradient increases with time as could be seen from Figs. 17 and 18. As time progresses this would induce a flow separation.

An increase in the boundary layer thickness both on the upper surface and the lower surface with increase in time level is seen from Figures 48 51 by observing the displacement of $\Psi = \pm 0.04$ streamlines farther away from the surface. The velocity profiles shown on the upper surface in Figs. 74 and 75 indicate this even more clearly.

From the plot of equi-vorticity lines in Figures 48 → 51 curling up of the vorticity field near the TE is observed. In Fig. 51 the vorticity values inside the curled up region are positive. The innermost contour, which is a closed loop has a value of $\omega = 9.0 = \text{constant}$. The highest value at a grid point inside this loop is 11.3. Such a strong curling up of the positive vorticity field near the trailing edge closely resembles the classical concepts of vortex roll up and starting vortex.

The location of the "starting vortex" as a function of time is shown in Fig. 5. This location is an approximate estimate obtained by considering the position of maximum value of vorticity inside the "starting vortex" region. The straight line distance of this point, normalized with respect to the airfoil chord length, from the leading edge of the airfoil is denoted as S_ℓ in Fig. 5. Except for time levels immediately after the impulsive start, the starting vortex moves downstream at constant velocity, which is roughly two thirds of the freestream velocity. For comparison, the path of a particle moving at free stream speed is also plotted in Fig. 5. This "starting vortex" does not continue to exist for long periods and the vorticity in this region diffuses

rapidly. The rapid decay of the peak value of vorticity is also shown in Fig. 5.

Development of Separation Bubble (Time $t = 0.596 \rightarrow 6.74$)

The onset of the first separation bubble is noticed in the contour plots at time $t = 2.132$ (Fig. 53). At one time step earlier than this level, i.e. at $t = 1.876$, no separation bubble is identifiable either from the values of vorticity or stream function. But from Figure 53 as well as Figure 43 it is seen that the bubble starts with a fairly finite length at time $t = 2.132$. By interpolation from Fig. 43 it would seem appropriate to decide that the separation bubble started off at a time level of about 1.92. Interpolating again from Fig. 43 the chordwise station where the bubble first occurred is obtained as $X_C = 2.3$. From the surface vorticity profile shown in Fig. 9, it is observed that the location of the local minimum of vorticity on the upper surface coincides with this region. The size of the bubble increases with time until it almost extends over the entire upper surface, as the separation point moves forward towards the leading edge and as the reattachment point moves rearward towards the trailing edge. (Figs. 43 and 54). At time $t = 6.228$ the separation and reattachment points are about 95% chord length apart. The height of the bubble at $X_C = 0.476$ measured along the normal grid line is $D_N = 0.176$ as determined from the zero streamline position. This bubble bursts at the next time level of $t = 6.74$. As the bubble size grew during the time interval 2.132 to 6.228 the strength of the bubble also increased even though in the contour plots no further streamlines appeared inside the bubble. This increase in strength may be inferred from the

increased magnitudes of reversal flow velocities as shown in Figures 76 to 78.

During this time interval of 0.596 to 6.228 the value of C_L increases with time (Fig. 46). Up to the time level of 2.132 the reason for this increase can be visualized as due to an effective increase in circulation around the airfoil. This is borne out by the equivorticity contours shown in Figures 51 and 52. Afterwards the increase in lift is due to the presence of the bubble which causes increased negative pressures on the upper surface. This is seen from Figure 18 by considering the pressure distribution for t = 1.62 and t = 6.228. While the lower surface pressure distribution almost remains the same for these two time levelss the Cp values on the upper surface have substantially decreased. The total drag coefficient during the presence of the bubble more or less remains constant (Fig. 46).

Separated Flow (t = 6.74→ 12.116)

The reattachment point of bubble A lifts off the surface of the airfoil at time t = 6.74 causing separated flow over almost the entire upper surface (Fig. 55) The separation point continues to move forward towards the LE, though at a much slower rate (Fig. 43). At the very next time level a small separation bubble with counterclockwise flow in it appears at the trailing edge (Fig. 43). The rear stagnation point of the airfoil becomes the separation point of this bubble which is labelled as C in the figures. The bubble size is very small until a time level of t = 11.860 and its presence is not very clearly seen in the stream line plots of Figs. 55 through 57. The strength of recirculation in the burst

bubble increases with time as evidenced by the increased number of streamlines in this region (Figures 56 → 58). The increased magnitudes of velocity in the reversed flow region can also be visualized from the velocity vector plots shown in Figures 78 and 79.

The extent of positive surface vorticity on the upper surface increases with time as shown by the plots for $t = 6.228$ and $t = 8.788$ in Figures 9 and 10. As time progresses a local minimum of surface vorticity occurs on the upper surface. At a time period of $t = 11.86$ this minimum appears at $X_C = 0.57$ as shown in Fig. 10. This again indicates the onset of adverse pressure gradient around this location for the reversed flow. Referring to the surface pressure distribution shown in Fig. 19, at $t = 10.836$ a weak adverse pressure gradient is first seen to extend from $X_C = 0.64$ to $X_C = 0.46$. This adverse pressure gradient is more pronounced at $t = 11.86$, and it will lead to flow separation and appearance of a bubble as will be discussed in the next section.

The rate of increase of lift coefficient diminishes during this time interval, even though its value increases to a maximum of 1.52 at time $t = 9.0$ (Fig. 47). The increase in the effective circulation around the airfoil up to a time level of $t = 8.2$ is also indicated by the rearward movement of the forward stagnation point (Fig. 41). After this time level the FSP moves forward again indicating the decrease of net circulation and hence the lift coefficient. The time level at which maximum rearward displacement of FSP is attained does not coincide with the time level for maximum lift coefficient. The total drag coefficient starts increasing at a time level of about 5.5 (Fig. 47). It continues to increase beyond the time level at which C_L reaches a maximum. The major

contributing part to total drag coefficient is the drag due to pressure. Since the effective bluff body area, as judged by the zero stream line contours, increases rapidly with time (Fig. 54 58) the pressure drag coefficient also increases.

The vorticity profiles at leading edge (Fig. 27) shows that the absolute value of vorticity decreases during the time period 8.788 through 13.652. This is constant with the forward movement of the FSP (Fig. 41). Profiles of vorticity at chordwise station $X_C = 0.476$ (Fig. 34) show that the vorticity gradient changes its sign during this time interval. This is the resultant of reversed flow and hence upstream convection.

Formation of bubble B and its lift off ($t = 12.166 \rightarrow 18.26$)

From the contour plots shown in Figs. 59 through 64 the following events are observed for this time period. Within the separated region on the upper surface a counterclockwise bubble appears at time $t = 12.372$. Its separation and reattachment points at this time level are located at $X_C = 0.645$ and 0.545 respectively (Fig. 43). By interpolation from Fig. 43 this bubble could be estimated to have been started at t= 12.15. (The previous time level of computation was 12.116). This bubble is labeled as bubble B in figures. The size of this bubble increases rapidly up to a time level of about 15.06, by way of its separation point moving back towards the trailing edge and its reattachment point moving forwards (Fig. 43 and 44). At time $t = 15.06$ the RP of this bubble reverses its direction of movement and moves towards the trailing edge. While this bubble is growing in size, the trailing edge bubble, C

decreases in its size, (Figs. 43 and 44) and it appears only as a dot in Fig. 60. Bubble C is also a counterclockwise bubble. At time t = 15.06 the size of bubble C starts increasing again. From Fig. 43 it is seen that from t = 15.06 onwards bubble B moves towards to trailing edge until it merges with the growing bubble C at time t = 16.34.

As the height of bubble B increases the recirculating region A is roughly divided into two regions which are labeled as A' and D (Fig. 61). At time t = 17.748 the merged bubbles (B+C) lift off from the surface. The zero stream line around region D reattaches to the surface at the location which was the RP of (B+C) earlier (Fig. 63). Also the separation point of (B+C) now becomes the rear stagnation point of the airfoil and a stagnation stream line starting from this point encircles the region A'. It is also seen that the bubble A' becomes weaker and is washed off down stream.

The equi-vorticity contours in Figs. 59 68 show a significant increase in the extent of rotational region in the lateral direction, particularly over the upper surface of the airfoil. Close to the surface inside bubbles B and C the vorticity is negative. Also on the upper half of the flow region away from the surface there is a very large region of negative vorticity. The closed loops of equi-vorticity lines in the outer negative vorticity region (Fig. 61) signifies the presence of the bubble A'. The closed loops of equivorticity lines move downstream with a certain amount of lateral shift as time progresses (Fig. 61 65).

The formation of the anticlockwise bubble B is also visualized from the velocity vector plots of Fig. 80. The velocity vectors close to the surface have reversed their flow directions at location X_C = 0.67 at time

level t = 15.316 compared to earlier time levels. It is also seen that ahead of the bubble B the magnitudes of reversed flow velocities have significantly reduced. A comparison of the vector plots between t = 15.316 and t = 16.212 in Fig. 80 also shows that the counterclockwise bubble C from the trailing edge has extended to the chordwise location $X_C = 0.9581$.

As the bubble B is being formed, the surface vorticity values upstream of the bubble decrease (Fig. 10) indicating a reduction in the values of velocity gradients in the reversed flow region of the upper surface. The vorticity values at the surface inside the bubble B are negative and their magnitudes increase with time. The rate at which these values increase is high initially when the bubble is growing which is consistent with the rate at which the bubble size itself increases as indicated in Figs. 43 and 44. Between the separation point of bubble B and the reattachment point of bubble C the surface vorticity values are positive. As bubble B grows in size the area of recirculation region between bubbles B and C decreases and the maximum positive surface vorticity value in this region increases with time up to a time level of t = 14.42 (Fig. 10 and 11). When the rate of growth of bubble B decreases at t = 15.06 (Fig. 44) and when it starts moving towards the trailing edge, the local maximum of vorticity in this region decreases. Finally when bubbles B and C have merged the surface vorticity inside the combined bubbles becomes entirely negative at t = 16.468 (Fig. 12). These variations in the surface vorticity values imply the following conclusions with respect to the skin friction coefficient on the upper surface of the airfoil. Ahead of the bubble B, the positive values of

surface vorticity tend to reduce the friction drag. Because of decreasing positive vorticity values with time, such negative contribution to drag diminish with time. Similarly between bubble B and C a negative contribution to skin friction drag prevails. This negative contribution rapidly increases with time up to $t = 15.06$ and the rapidly decreases again (Fig. 10 and 11). Inside bubbles B and C where vorticity is negative the contribution to skin friction drag is positive. The trailing edge vorticity which is not shown in the figures is positive at these time levels.

Figures 10, 11 and 12 also indicate that the surface vorticity values on the lower surface increase with time in contrast to the behavior exhibited at time levels earlier than $t = 8.788$. This is consistent with the continuing forward movement of the FSP as shown in Fig. 42. Until bubble B starts moving towards the trailing edge at $t = 15.06$, the rate at which the FSP moves forward is relatively slow. After this time level the rate of forward movement of FSP sharply increases and stays at this rate until time $t \approx 18.0$. The above discussion suggests the rates at which the overall circulation is changing with time. The circulation decays at a slow rate up to time $t \approx 15.06$ causing a gradual or slow fall of the lift coefficient (Fig. 47). The value of lift coefficient falls much more rapidly after this time level.

The plots of surface pressure coefficient given in Figs. 20 and 21 indicate the following. Upstream of the bubble, from $X_c \approx 0.1$ to $X_c \approx 0.5$, the Cp values remain approximately constant on the upper surface. This is essentailly due to decreasing vorticity gradients at these locations for these time levels. The effective area under the

pressure curves decrease only slowly for the time periods indicated in Fig. 20 thus indicating a slow drop in the C_L values up to $t = 15.06$. Figure 20 also shows that the leading edge suction relative to the trailing edge pressure falls at a slower rate during this time period compared to the earlier time levels. After time $t = 15.06$, this leading edge suction decays at a very high rate as seen from Fig. 18. In other words, the C_p value at the trailing edge relative to the forward stagnation point increases very rapidly. Fig. 21 also indicates a rapid decay of the contribution to lift due to pressure distribution in the region X_c 0.5, where bubbles B and C are located.

The merged bubble B+C lifts off from the surface at a time level of 17.748. The effect of the lift off on the surface pressure distribution is shown in Fig. 21, through the plots for the time levels $t = 16.468$ and $t = 18.772$. At time level $t = 16.468$ the reattachment point of bubble (B+C) is located at $X_{cu} = 0.51$. The flow ahead of this point is directed upstream near the surface and the flow aft of this point is directed downstream (Fig. 81). Fig. 21 shows a nearly zero pressure gradient for flow ahead of $X_C = 0.51$ and a very strong favorable pressure gradient for the flow aft of this point at time $t = 16.468$. Subsequent to the bubble lift off, at time $t = 18.772$, the location $X_C = 0.601$ becomes the reattachment point of bubble D (Fig. 44). The flow ahead of this point is directed upstream near the surface. For this flow the pressure plot at $t = 18.772$ shows (Fig. 21) an existence of adverse pressure gradient from $X_C \approx 0.44$ to $X_C \simeq 0.32$. This would cause the appearance of another bubble E which is discussed in the next section.

The lift off of bubble (B+C) also causes the rear stagnation streamline to appear again as seen from Fig. 62. Since the bursting of the first bubble A at time t = 6.74, the trailing edge has been the separation point of a trailing edge bubble, and the rear stagnation streamline did not exist for the time period t = 6.74 to t = 17.620.

Appearance and Growth of Bubble E (t = 18.26→ 28.756)

During the time interval t = 18.26 to 28.756, for which the typical flow patterns are shown in Figs. 64 to 72, the following events are observed. At time level t = 18.26 a counterclockwise bubble, labeled E in the figures, appears on the upper surface. The separation and reattachment points of this bubble are located at X_C = 0.363 and X_C = 0.357 respectively. This bubble is located inside the clockwise bubble D and thus it occurs in the reversed flow region. At this time level of t = 18.26 the bubble is characterized by negative vorticity at one nodal point on the surface in an otherwise positive vorticity region. Consequently the bubble size is too small to be shown in Fig. 64. As time progresses the size of bubble E grows (Figs. 44, 65, 66) with both width and height increasing. At time t = 19.284, the growth of this bubble causes bubble D to be partitioned into two separate bubbles which are labeled as D and D' in Fig. 67. Bubble E itself is opened to outer flow. The partitioned bubbles D and D' are both clockwise bubbles. With progress in time, bubble D' moves towards the trailing edge at almost a constant rate (Fig. 44). During this process the strength of the bubble D' decreases as evidenced by the decreasing number of streamlines inside the bubble (Figs. 67→70). Bubble D initially decreases in size

until time $t = 21.2$ when its length reaches a minimum (Fig. 44). At this time level the reattachment point of bubble D' has almost reached the trailing edge. Subsequent to time $t = 21.2$ the size of bubble D increases first at a slower rate and then at a much higher rate starting with time $t \approx 22.1$. The rapid increase in the growth rate of bubble D is followed by the bursting of bubble D' (Fig. 71). At time level 25.772 bubble D extends from $X_C = 0.05$ to $X_C = 0.98$. Subsequent to this time level there is no significant increase in the size of this bubble even though the strength of this bubble increases. The bursting of bubble D' is immediately followed by the occurence of a trailing edge bubble, labeled F in the figures. The trailing edge bubble F is counterclockwise in sense and is analogous to the bubble C discussed earlier. At time $t = 25.172$ this bubble is dissolved. In addition to the formation of these new bubbles during this time interval, it is also observed that the bubble (B+C) grows weaker and is washed off downstream.

An examination of the surface vorticity distribution for the time level of $t = 17.492$ in Fig. 12 reveals the appearance of a local minimum of vorticity at $X_C = 0.33$. This location of minimum shifts downstream with increasing time. The appearance of bubble E coincides with this location. Up to a time level of about $t = 24.404$ the wavy nature of the upper surface vorticity, with surface vorticity values changing between positive and negative values (Figs. 13, 14), is attributable to the presence of one or more of the bubbles D, E, D' and F. After this time level when only bubble D is present, the upper surface vorticity values inside this bubble still possess the wavy nature of distribution (Fig. 15). During the time interval 20.82 to 28.756 the lower surface

vorticity values decrease with time indicating the rearward movement of the forward stagnation point. This is seen to be true from Fig. 42. Consequently there is an overall increase in circulation and lift coefficient (Fig. 47). The drag coefficient during this period shows an oscillatory variation the likeness of which is different from that of the lift coefficient.

The surface pressure coefficients shown in Figs. 22 through 24 show a rapid increase in the included area up to a time level of about $t = 22.868$ which is consistent with the rapid increase of C_L during this period. The small drop in the value of C_L at $t \simeq 22.0$ is associated with the bursting of the bubble D' at this time level. The plots of pressure distribution also indicate the following. The leading edge suction relative to the trailing edge pressure increases rapidly up to a time level of 22.668. The rate of increase decreases subsequent to this time level. Also, after time $t = 25$, when only bubble D is present, there is virtually no adverse pressure gradient for the reversed flow on the upper surface (Fig. 24).

General Comments on the Flow Phenomena

Finally the following observations on the flow phenomena are made with respect to the entire time levels studied from $t = 0.0$ to $t = 28.756$.

The rear stagnation point, when it exists, is mostly found on the upper surface except for the time period $t = 0.212 \rightarrow 0.98$ when it is located on the lower surface. There is no RSP on the airfoil surface for the time periods $6.74 \rightarrow 17.620$ and $22.1 \rightarrow 24.916$. During these time

periods the RSP becomes the separation point of a trailing edge bubble.

The forward most location of FSP is $X_C = 0.014738$ and it occurs at time $t = 0.012$. The rearmost location of FSP is found to be $X_C = 0.028$ at $t = 8.276$. Excluding the initial time levels after impulsive start, the maximum value of C_L initially is 1.525 and it occurs at time $t = 9.0$ This does not coincide with the time level for rearmost location of FSP. When computations are terminated at time $t = 28.756$, its value again is 1.525. The lowest value of C_L is 0.625 occuring at $t \approx 19.25$. Time levels for maximum/minimum C_D in general do not coincide with time levels for maximum or minimum of C_L. Excluding again the time levels after impulsive start the maximum value of C_D is 0.44. During the time period 14.0 to 24.0 it oscillates about a mean value of 0.4.

Judging from the contour plots of streamlines it is estimated that one cycle of vorticity shedding is completed during the time period $t = 6.228$ to $t = 25.428$. With the airfoil chord as the cahracteristic length the Strouhal number, defined by L/TV_∞ where T is the period of a cycle, is then found to be 0.196.

Comparative Evaluation of Present Results

Several new concepts in the computational procedure for the study of viscous flow past two dimensional bodies have been introduced in this work. The integral representation for the kinematic aspect of the problem even though is not an entirely new concept (6), its reformulation in terms of stream function and its application to a fairly complex flow problem were undertaken for the first time in the present study. An

explicit and accurate method of determining surface vorticity, subdivision of the flow field into smaller blocks for the kinetics of the problem are the additional new features introduced in this study. These new aspects in the computational procedure have been introduced with two main objectives: (1) To obtain accurate values of flow variables on the boundaries (vorticity on the surface and stream function at the far boundary) and (2) to reduce the computer time requirements of the prevailing numerical procedures for viscous flow problems. A meaningful test of these new concepts is possible only when these are applied to study a case for which acceptably accurate results are available. Additionally, to achieve this purpose, it is desirable to keep flow parameters, geometry, and grid spacings the same as the study against which present results are to be compared. With this criteria in mind the geometry of the airfoil and the grid system have been kept the same as those of Mehta [17]. The results of present study are now compared with those of Mehta [17] in the following discussion.

The following computational procedures of Mehta [17] are significantly different from the present study and it is important to bear these in mind while comparing the results of these two studies. (1) The surface vorticity in Reference [17] is computed using a conventional approach. Essentially, the vorticity value on the surface is determined using the velocity gradient at the surface which is obtained by numerical differentiation. (2) At an arbitrarily chosen outer boundary the stream function value is determined by assuming diffusion and pressure gradient to be negligible. (3) Finite difference equation of the vorticity transport equation is formed using Arakawa differencing scheme and the resultant

equations are solved using successive under relaxaion. (4) Poisson's equation for the stream function is solved in the entire domain using finite differences. Additionally the stream function values are iteratively updated to obtain their values at the same time level as that of vorticity. It is to be noted that the finite difference equation used for the determination of surface vorticity necessitates this iteration. (5) A region of flow field is specified as irrotational a priori.

Between the two studies the general sequence of time dependent events and the topological character of streamline patterns are in very good agreement. But the details differ with respect to the formation, growth and separation of bubbles after the bursting of the first bubble at time $t = 6.74$. Up to this time level the typical comparisons of the values of vorticity and surface pressures shown in various figures are in good agreement. The trailing edge vorticity values, however, significantly differ between the two studies. Note that both in the present study and in that of Mehta higher values of residues are tolerated at the trailing edge compared to interior points to obtain convergence.

Referring to Fig. 41, after the impulsive start, the time variation of the location of FSP shows a much smoother variation compared to that of Mehta (17). In the present study the rear stagnation point after a time level of $t = 0.08$ stays always at locations $X_C \approx 0.999$. In Ref. 17 this is found to fluctuate to a lower value of 0.9982.

The surface vorticity distributions shown in Figs. 6 through 10 show good agreement between the two studies, except for the following difference. The time level of occurance and extent of local minimum/maximum of vorticity, which indicates the birth of a bubble, do not match

between the two studies. Other key differences between the present study and that of Mehta [17] can be summarized by comparing the bubble formation and bursting at different time levels, as discussed below.

(1) The birth of bubble A in the present study occurs at time t = 1.9 and it bursts at a time level of 6.74. The corresponding time levels in Ref. 17 are 1.62 and 8.82 respectively.

(2) Immediately following this burst of bubble A, a trailing edge bubble C appears in the present study and the bubble B occurs at a later time level of t = 12.132. In Mehta's study bubble B occurs at a time level of about t = 11 and bubble C appears at a later time level. In the present study whenever there is no rear stagnation point at the trailing edge, a small counterclockwise trailing edge bubble is present. This is not found true in Mehta's Study and there are time levels found with neither a stagnation point nor a trailing edge bubble.

(3) After bubbles B and C merge they stay merged and lift off in the present case. In Ref. 17 sometime after their merger they separate again and only bubble C lifts off. Bubble B stays on the surface to play the roll of bubble E of the present case.

(4) At a time level of 27.0 another separation bubble is observed in Mehta's Study, which is absent in the present case.

Finally with regard to the computer time requirement the present study required a total of about four hours and thirty minutes on CYBER 70/MODEL 74 CPU 6400. The average per time step turns out to be 110 seconds. Mehta [17] required a total of 24 hours on UNIVAC 1108 which gives an average of about 9.5 minutes per time step. (The Computational Speed of CYBER 70-CPU6400 was determined to be about 1.1 times faster than UNIVAC 1108 by running the same program in both the machines).

CHAPTER V

CONCLUDING REMARKS

In this study, methods that yield fast and accurate solutions to Navier-Stokes equation for two-dimensional incompressible external flow past finite bodies have been developed and presented. In particular, for two-dimensional bodies that could be conformally mapped on to a unit circle a versatile computer program is made available that could generate numerical solution using less computer time compared to prevailing methods. The major conclusions of this study with respect to the methodology that has been developed and with respect to the numerical results that were obtained for viscous flow past a 9% thick airfoil at an angle of attack of 15^{o} and a Reynolds number of 1000 are summarized in this section. A few suggestions outlining the scope for further work are also presented.

The following new approaches have been introduced in the present study for the numerical solution of the Navier-Stokes equations for incompressible flows. (1) A generalized integral representation that is different from Green's function technique for the stream function is presented. (2) A new approach for the determination of surface vorticity is developed and presented. (3) A Block Sub-Division technique for the solution of the vorticity transport equation and of Poisson's equation for stream function is introduced.

The integro-differential formulation that has been developed and presented in this study is valid when the dependent variables in the Navier-Stokes equations are vorticity and stream function. Compared to the existing integral formulation (6) in terms of velocity this approach offers reduction in both computer time and data storage requirement since only one dependent variable is involved in computations. The integral representation for stream function retains all the following advantages of the velocity formulation.

(1) The solution field can be confined to the non-negligible vorticity region alone thus offering significant reduction in computational time and storage requirement for external flow problems.

(2) For external flow problems, the difficulty of satisfying the free stream velocity boundary conditions infinitely far away from solid surface is eliminated. There is no need to choose a large distance to specify the boundary condition or to develop some other approximate boundary condition at a boundary only a finite distance away. The correct boundary condition is satisfied truly at infinity.

(3) The flow field can be divided into several smaller compartments and the computation of the field variable inside each compartment can be accomplished independently of the other compartments. A flexibility associated with this is that either the integral representation or any other finite difference method can be employed to compute the values inside these compartments.

With the integral representation for the kinematics, the vorticity boundary condition on the solid surface is established correctly through kinematic considerations alone. The explicit procedure presented in this

study for surface vorticity calculation is advantageous in terms of solution accuracy and computational speed compared to implicit procedures of previous [5] integral methods. Even though this procedure is developed on the basis of the integral representation, it is in general applicable in conjunction with finite difference or finite element methods. Since the surface vorticity calculation procedure automatically conserves vorticity there is no need to employ special differencing schemes in the finite difference equation for vorticity transport to ensure conservation of total vorticity. The computation of surface vorticity is done independent of the values of stream function (or velocity) near the surface. Consequently it becomes possible to let stream function values lag by one time step without having to let surface vorticity lag by one time step.

In the numerical procedure used for the vorticity transport equation, the Strongly Implicit Procedure is shown to be superior to Successive Point Relaxation and Successive Line Relaxation procedures. In addition it is shown that subdivision of the flow field into several blocks further reduces the computer time.

On the numerical study of flow past an impulsively started airfoil at an angle of attack of 15^{o}, the following conclusions on the overall characteristics of the flow are found to be similar to those of Mehta [17].

(1) Immediately after the impulsive start the rear stagnation point moves very rapidly to the trailing edge.

(2) Subsequently a starting vortex is visualized through concentric equivorticity lines.

(3) The flow separation always takes place at a location where the

rate of change of vorticity along the surface is zero, and the formation of a bubble is preceded by an adverse pressure gradient.

(4) Clockwise bubbles when extended downstream towards the trailing edge burst and streamlines from below the surface become part of this bubble.

(5) Anti-clockwise bubbles either lift off the surface or open up to streamlines from above the surface.

(6) The lift increases with an increase in the size of attached clockwise bubbles and decreases when attached anti-clockwise bubbles grow.

A feature that was not observed in Mehta's [17] Study is that when the flow is separated and when there is no rear stagnation streamline, a small trailing edge separation bubble is always present.

With regard to the computer time requirement for the airfoil problem, the present study is found to be about five times faster than the methods employed by Mehta [17]. The major factors contributing to the time reduction are:

(1) The solution field is confined essentailly to non-negligible vorticity region.

(2) Block subdivisions are used which offer a reduction in the number of algebraic equations involved in each block. Additionally, the sizes of these blocks can be appropriately chosen to suit the shape of the non-negligible vorticity region.

(3) Since the numerical evaluation of surface vorticity is done independent of the computation of stream function, it has been possible to allow stream function to lag by one time step.

If the stream function values were updated to current time level through iteration, the present procedure would yield solutions using about 50% of the computer time required by Mehta [17]. This is a significant reduction in computer time requirements since the computational procedures of Mehta are already efficient for the following two major reasons. (1) The transformation of fluid domain to the interior of unit circle and the stretching relationship of Mehta [17] already offers a great flexibility in the design of grid system. (2) Additionally, in Reference 17 a portion of the flow field where vorticity is expected to be negligible has been excluded from the solution procedure. A careful revision of the program coding and the introduction of some of the refinements recommended below are expected to improve further the efficiency of present method.

Based on the experience of the present computational study the following recommendations are considered appropriate to increase the accuracy of numerical results with further reduced computer time requirements. More accurate methods for evaluating the integrals involved in the computation of stream function and surface vorticity are needed. Instead of assuming vorticity to be uniformly distributed in each computational cell, usage of linear variations or variations represented by Fourier Sine series would yield more accurate results. Accurate evaluation techniques of the integrals for the velocity-vorticity formulation are already available [27] and similar developments are necessary for the stream function - vorticity formulation. With such accurate formulations the number of nodal points necessary for adequate description of the flow behavior can be significantly reduced. Additionally the application of

the flow field segmentation method, which is available for the velocity-vorticity formulation (7), must be explored for the stream function formulation. A more accurate method of computing the surface pressure coefficient must be established. The possible use of higher order polynomials for computing the normal gradient of vorticity on the surface is to be explored.

APPENDIX

DERIVATIONS OF MAJOR EQUATIONS REQUIRED IN COMPUTATION

The derivations of major equations namely (1) the governing differential equations in the transformed plane, (2) expression for the scale factor of transformation, (3) integral representation for stream function and (4) explicit relation for the determination of surface vorticity, are presented in this appendix. These derivations follow closely those of Wu [26].

Governing Differential Equations in Transformed Plane

For two-dimensional incompressible viscous flow of a Newtonian fluid, the governing differential equations, formulated in terms of vorticity ω and stream function Ψ , in Cartesian coordinates are

$$\frac{\partial \omega}{\partial t} = - \frac{\partial \Psi}{\partial y}\frac{\partial \omega}{\partial x} + \frac{\partial \Psi}{\partial x}\frac{\partial \omega}{\partial y} + \nu\left(\frac{\partial^2 \omega}{\partial x^2} + \frac{\partial^2 \omega}{\partial y^2}\right) \qquad (A.1)$$

$$\frac{\partial^2 \Psi}{\partial x^2} + \frac{\partial^2 \Psi}{\partial y^2} = -\omega \qquad (A.2)$$

Now consider a conformal transformation defined by

$$\kappa = f(z) \qquad (A.3)$$

where

$$\kappa = \xi + i\eta$$

$$z = x + iy$$

The function $f(z)$ is considered analytic and hence its derivative exists. Its derivative can then be expressed [28] as

$$\frac{d\kappa}{dz} = \frac{\partial \xi}{\partial x} + i \frac{\partial \eta}{\partial x} = \frac{\partial \eta}{\partial y} - i \frac{\partial \xi}{\partial y} \tag{A.4}$$

It follows then

$$\frac{\partial \xi}{\partial x} = \frac{\partial \eta}{\partial y} \quad \text{and} \quad \frac{\partial \xi}{\partial y} = - \frac{\partial \eta}{\partial x} \tag{A.5}$$

and

$$\frac{\partial^2 \xi}{\partial x^2} + \frac{\partial^2 \xi}{\partial y^2} = \frac{\partial^2 \eta}{\partial y \partial x} - \frac{\partial^2 \eta}{\partial x \partial y} = 0 \tag{A.6}$$

$$\frac{\partial^2 \eta}{\partial x^2} + \frac{\partial^2 \eta}{\partial y^2} = - \frac{\partial^2 \xi}{\partial y \partial x} + \frac{\partial^2 \xi}{\partial x \partial y} = 0 \tag{A.7}$$

Now consider a scalar function $\omega(x,y)$. Its partial derivatives can be written as

$$\frac{\partial \omega}{\partial x} = \frac{\partial \omega}{\partial \xi}\frac{\partial \xi}{\partial x} + \frac{\partial \omega}{\partial \eta}\frac{\partial \eta}{\partial x}$$

$$\frac{\partial \omega}{\partial y} = \frac{\partial \omega}{\partial \xi}\frac{\partial \xi}{\partial y} + \frac{\partial \omega}{\partial \eta}\frac{\partial \eta}{\partial y}$$

$$\frac{\partial^2 \omega}{\partial x^2} = \frac{\partial^2 \omega}{\partial \xi^2}\left(\frac{\partial \xi}{\partial x}\right)^2 + \frac{\partial \omega}{\partial \xi}\frac{\partial^2 \xi}{\partial x^2} + \frac{\partial^2 \omega}{\partial \eta^2}\left(\frac{\partial \eta}{\partial x}\right)^2 + \frac{\partial \omega}{\partial \eta}\frac{\partial^2 \eta}{\partial x^2}$$

$$\frac{\partial^2 \omega}{\partial y^2} = \frac{\partial^2 \omega}{\partial \xi^2}\left(\frac{\partial \xi}{\partial y}\right)^2 + \frac{\partial \omega}{\partial \xi}\frac{\partial^2 \xi}{\partial y^2} + \frac{\partial^2 \omega}{\partial \eta^2}\left(\frac{\partial \eta}{\partial y}\right)^2 + \frac{\partial \omega}{\partial \eta}\frac{\partial^2 \eta}{\partial y^2}$$

Adding the last two expressions and using Eqs. A.4 through A.7,

$$\frac{\partial^2 \omega}{\partial x^2} + \frac{\partial^2 \omega}{\partial y^2} = \left[\frac{\partial^2 \omega}{\partial \xi^2} + \frac{\partial^2 \omega}{\partial \eta^2}\right]\left(\frac{d\kappa}{dz}\right)^2 \qquad \text{(A.8)}$$

Similarly, if Ψ is another scalar function,

$$-\frac{\partial \omega}{\partial x}\frac{\partial \Psi}{\partial y} + \frac{\partial \omega}{\partial y}\frac{\partial \Psi}{\partial x}$$

$$= -\left[\frac{\partial \omega}{\partial \xi}\frac{\partial \xi}{\partial x} + \frac{\partial \omega}{\partial \eta}\frac{\partial \eta}{\partial x}\right]\left[\frac{\partial \Psi}{\partial \xi}\frac{\partial \xi}{\partial y} + \frac{\partial \Psi}{\partial \eta}\frac{\partial \eta}{\partial y}\right]$$

$$+ \left[\frac{\partial \omega}{\partial \xi}\frac{\partial \xi}{\partial y} + \frac{\partial \omega}{\partial \eta}\frac{\partial \eta}{\partial y}\right]\left[\frac{\partial \Psi}{\partial \xi}\frac{\partial \xi}{\partial x} + \frac{\partial \omega}{\partial \eta}\frac{\partial \eta}{\partial x}\right]$$

$$= \left[- \frac{\partial \omega}{\partial \xi} \frac{\partial \Psi}{\partial \eta} + \frac{\partial \omega}{\partial \eta} \frac{\partial \Psi}{\partial \xi} \right] \left(\frac{d\kappa}{dz} \right)^2 \qquad (A.9)$$

If one represents the coordinates of κ-plane in polar coordinates, then

$$\kappa = \xi + i\eta = re^{i\theta} = r(\cos\theta + i\sin\theta)$$

and

$$\frac{\partial^2 \omega}{\partial \xi^2} + \frac{\partial^2 \omega}{\partial \eta^2} = \frac{\partial^2 \omega}{\partial r^2} + \frac{1}{r} \frac{\partial \omega}{\partial r} + \frac{1}{r^2} \frac{\partial^2 \omega}{\partial \theta^2}$$

$$\frac{\partial \Psi}{\partial \xi} \frac{\partial \omega}{\partial \eta} - \frac{\partial \Psi}{\partial \eta} \frac{\partial \omega}{\partial \xi} = \frac{1}{r} \left[\frac{\partial \Psi}{\partial r} \frac{\partial \omega}{\partial \theta} - \frac{\partial \Psi}{\partial \theta} \frac{\partial \omega}{\partial r} \right]$$

Using these in Eqs. A.8 and A.9, one obtains

$$\frac{\partial^2 \omega}{\partial x^2} + \frac{\partial^2 \omega}{\partial y^2} = \left[\frac{\partial^2 \omega}{\partial r^2} + \frac{1}{r} \frac{\partial \omega}{\partial r} + \frac{1}{r^2} \frac{\partial^2 \omega}{\partial \theta^2} \right] \left(\frac{d\kappa}{dz} \right)^2 \qquad (A.10)$$

$$- \frac{\partial \Psi}{\partial y} \frac{\partial \omega}{\partial x} + \frac{\partial \Psi}{\partial x} \frac{\partial \omega}{\partial y} = \frac{1}{r} \left[\frac{\partial \Psi}{\partial r} \frac{\partial \omega}{\partial \theta} - \frac{\partial \Psi}{\partial \theta} \frac{\partial \omega}{\partial r} \right] \left(\frac{d\kappa}{dz} \right)^2 \qquad (A.11)$$

Defining the scale factor of transformation as

$$H = \left| \frac{dz}{d\kappa} \right|$$

and using Eqs. A10 and A11, the transformation of the governing equations A1 and A2 in the working plane (κ-plane) is established as

$$r^2 H^2 \frac{\partial \omega}{\partial t} = r\left[\frac{\partial \Psi}{\partial r}\frac{\partial \omega}{\partial \theta} - \frac{\partial \Psi}{\partial \theta}\frac{\partial \omega}{\partial r}\right] + \nu\left[r^2\frac{\partial^2 \omega}{\partial r^2} + r\frac{\partial \omega}{\partial r} + \frac{\partial^2 \omega}{\partial \theta^2}\right] \qquad (A.12)$$

and

$$\frac{\partial^2 \Psi}{\partial r^2} + \frac{1}{r}\frac{\partial \Psi}{\partial r} + \frac{1}{r^2}\frac{\partial^2 \Psi}{\partial \theta^2} = -\omega H^2 \qquad (A.13)$$

Furthermore, if the radial coordinate is stretched using a relation of the form $r = r(\rho)$, typical derivatives with respect to r would be rewritten as

$$\frac{\partial \Psi}{\partial r} = \frac{\partial \Psi}{\partial \rho}\frac{d\rho}{dr}$$

$$\frac{\partial^2 \Psi}{\partial r^2} = \frac{\partial^2 \Psi}{\partial \rho^2}\left(\frac{d\rho}{dr}\right)^2 + \frac{\partial \Psi}{\partial \rho}\frac{d^2\rho}{dr^2}$$

Then Eqs. A12 and A13 become

$$r^2 H^2 \frac{\partial \omega}{\partial t} = r\frac{d\rho}{dr}\left[\frac{\partial \Psi}{\partial \rho}\frac{\partial \omega}{\partial \theta} - \frac{\partial \Psi}{\partial \theta}\frac{\partial \omega}{\partial \rho}\right]$$
$$+ \nu\left[\left(r\frac{d\rho}{dr}\right)^2\frac{\partial^2 \omega}{\partial \rho^2} + r\left(\frac{d\rho}{dr} + r\frac{d^2\rho}{dr^2}\right)\frac{\partial \omega}{\partial \rho} + \frac{\partial^2 \omega}{\partial \theta^2}\right] \qquad (A.14)$$

and

$$\left(\frac{d\rho}{dr}\right)^2 \frac{\partial^2\Psi}{\partial\rho^2} + \left(\frac{1}{r}\frac{d\rho}{dr} + \frac{d^2\rho}{dr^2}\right)\frac{\partial\Psi}{\partial\rho} + \frac{1}{r^2}\frac{\partial^2\Psi}{\partial\theta^2} = -\omega H^2 \tag{A.15}$$

Scale Factor of Transformation

Consider the conformal transformation

$$z = \frac{1}{\kappa} + \gamma + \frac{\kappa c^2}{1+\gamma\kappa} \tag{A.16}$$

Which transforms a circle in κ-plane to a flat plate or an ellipse or an airfoil into the z-plane, depending on the values assigned for the constants γ and C^2. The scale factor of the transformation is defined by

$$H = \left|\frac{dz}{d\kappa}\right|$$

Consider the case when γ is real and for notational convenience define $\gamma \equiv a$ and $c^2 \equiv b$. Then

$$\frac{dz}{d\kappa} = -\frac{1}{\kappa^2} + \frac{b}{(1+a\kappa)^2}$$

Let

$$\kappa = re^{i\theta} = r\cos\theta + ir\sin\theta$$

$$(1+a\kappa) = \rho\, e^{i\phi} = \rho\cos\phi + i\rho\sin\phi$$

$$r\cos\theta = \xi$$

$$r\sin\theta = \eta$$

Then

$$1 + a\xi + ia\eta = \rho(\cos\phi + i\sin\phi)$$

The derivative $\frac{dz}{d\kappa}$ is written out as

$$\frac{dz}{d\kappa} = -\frac{1}{r^2 e^{i2\theta}} + \frac{b}{\rho^2\, e^{i2\phi}}$$

$$= -\frac{1}{r^2}\cos 2\theta + \frac{b}{\rho^2}\cos 2\phi + i\left[\frac{1}{r^2}\sin 2\theta - \frac{b}{\rho^2}\sin 2\phi\right]$$

And

$$\left|\frac{dz}{d\kappa}\right|^2 = \frac{1}{r^4} + \frac{b^2}{\rho^4} - \frac{2b}{r^2\rho^2}\left[\cos 2\theta\cos 2\phi + \sin 2\theta\sin 2\phi\right] \qquad (A.17)$$

Now $\cos\phi = \frac{1+ar\cos\theta}{\rho}$; $\sin\phi = \frac{ar\sin\theta}{\rho}$

Therefore

$$\text{Cos}2\phi = 2\text{Cos}^2\phi - 1 = \frac{2}{\rho^2}(1 + a^2r^2\,\text{Cos}^2\theta + 2ar\text{Cos}\theta) - 1$$

$$= \frac{1}{\rho^2}\,(1 + 2ar\text{Cos}\theta + 2a^2r^2\text{Cos}2\theta - a^2r^2) \qquad \text{(A.18)}$$

$$\text{Sin}2\phi = 2\text{Sin}\phi\,\text{Cos}\phi = \frac{1}{\rho^2}\,(2ar\text{Sin}\theta + 2a^2r^2\text{Cos}\theta\,\text{Sin}\theta) \qquad \text{(A.19)}$$

Also

$$\text{Cos}2\theta\text{Cos}2\phi = (2\text{Cos}^2\theta - 1)\,\text{Cos}2\phi$$

$$\text{Sin}2\theta\text{Sin}2\phi = (2\text{Sin}\theta\text{Cos}\theta)\text{Sin}2\phi$$

Using equations A.18 and A.19 in the above expressions and adding them

$$\text{Cos}2\theta\text{Cos}2\phi + \text{Sin}2\theta\text{Sin}2\phi = \frac{1}{\rho^2}\left[-1 + a^2r^2 + 2ar\text{Cos}\theta + 2\text{Cos}^2\theta\right]$$

Using this in Eq. A.17,

$$\left|\frac{dZ}{dK}\right|^2 = \frac{1}{r^4} + \frac{b^2}{\rho^4} - \frac{2b}{r^2\rho^2}\left[\frac{1 + a^2r^2 + 2ar\text{Cos}\theta}{\rho^2} + \frac{2\text{Cos}^2\theta - 2}{\rho^2}\right]$$

or

$$H^2 = \left|\frac{dz}{dK}\right|^2 = \left(\frac{1}{r^2} - \frac{b}{\rho^2}\right)^2 + \frac{4b}{r^2\rho^4}\,\text{Sin}^2\theta \qquad \text{(A.20)}$$

where

$$\rho^2 = 1 + a^2r^2 + 2ar\text{Cos}\theta$$

$b = c^2$, the constant in Eq. A16

Eq. A.20 is valid when the real part of γ in A.16 is equal to 'a' and when its imaginary part is zero. In such a case, when Eq. A16 is used to obtain airfoil geometries it would yield symmetrical airfoil.

Integral Representation for Stream Function

The kinematics of viscous flow is described, along with appropriate boundary conditions, by the Poisson's equation

$$\nabla^2\Psi = -\omega$$

in the domain R bounded by the boundary B. For external flow problems the boundary B is considered in two parts. Let S be the part formed by the body and C be the farstream boundary that encloses the body. On S no-slip conditions prevail and on C it is required

$$\frac{\partial\Psi}{\partial y} = u_\infty$$

$$\frac{\partial\Psi}{\partial x} = -v_\infty$$

where x and y represent Cartesian coordinates and u and v are respectively velocities along these axes.

Let P and Q be single valued functions in the domain of

integration with continuous second derivatives. By Green's theorem,

$$\iint_{R^-} (P\nabla^2 Q - Q\nabla^2 P)dR = \int_{B'} (P\vec{\nabla}Q - Q\vec{\nabla}P)\cdot\vec{n}dB$$

Let P and Q be defined by

$$P = \Psi$$

$$Q = \ln \frac{1}{|\vec{r}_o - \vec{r}|} = \ln \frac{1}{r'}$$

The function Q is not continuous at $\vec{r} = \vec{r}_o$. In order to be able to use Green's theorem this region is excluded, and Green's theorem is applied in region R^- which is region R minus the area enclosed by a small circle of radius ϵ centered at $\vec{r} = \vec{r}_o$. The circumferential boundary of this excluded region is denoted by E, and the boundary B' represents B plus E.

From the definitions of P and Q it follows

$$\vec{\nabla}Q = \frac{\vec{r}'}{r'^2} \quad \text{where} \quad \vec{r}' = \vec{r}_o - \vec{r} \quad \text{and} \quad r' = |\vec{r}_o - \vec{r}|$$

$$\nabla^2 Q = \nabla\cdot(\nabla Q) = 0, \quad \text{if } r' \neq 0$$

$$\nabla^2 P = \nabla^2 \Psi = -\omega$$

Using these in Green's theorem,

$$\iint_R \omega \ln\frac{1}{r'} dR_o = -\int_B \left\{ \Psi \frac{\vec{r}'\cdot\vec{n}_o}{r'^2} + \ln\frac{1}{r'} (\vec{\nabla}\Psi)\cdot\vec{n}_o \right\} dB_o$$

$$-\int_E \left\{ \Psi \frac{\vec{r}'\cdot\vec{n}_o}{r'^2} + \ln\frac{1}{r'} (\vec{\nabla}\Psi)\cdot\vec{n}_o \right\} dB_o$$

Now consider this equation as $\varepsilon \to 0$. On the left hand side the region of integration becomes R and the first integral on the right hand side is not affected. The second integral can be rewritten as

$$I = -\int_o^{2\pi} \Psi \frac{(\vec{r}_o - \vec{r})\cdot\vec{n}_o}{\varepsilon^2} \varepsilon d\theta - \int_o^{2\pi} \ln\frac{1}{\varepsilon} (\vec{\nabla}\Psi\cdot\vec{n}_o)\varepsilon d\theta$$

$$= -\int_o^{2\pi} \Psi \frac{(-\varepsilon)}{\varepsilon^2} \varepsilon\, d\theta - \int_o^{2\pi} \varepsilon \ln\frac{1}{\varepsilon} (\vec{\nabla}\Psi\cdot\vec{n}_o) d\theta$$

and in the limit $\varepsilon \to 0$,

$$I = \int_o^{2\pi} \Psi\, d\theta = 2\pi\Psi$$

Thus one has

$$\Psi(\vec{r}) = \frac{1}{2\pi} \iint_R \omega(\vec{r}_o) \ln\frac{1}{\vec{r}_o - \vec{r}} dR_o$$

$$+ \frac{1}{2\pi} \int_B \Psi(\vec{r}_o) \frac{(\vec{r}_o - \vec{r})\cdot\vec{n}_o}{|\vec{r}_o - \vec{r}|^2} dB_o$$

$$+ \frac{1}{2\pi} \int_B \vec{\nabla}\Psi(\vec{r}_o)\cdot\vec{n}_o \ln\frac{1}{\vec{r}_o - \vec{r}} dB_o \qquad (A.21)$$

We note that $\ln \frac{1}{|\vec{r}_o - \vec{r}|} \to -\infty$ as $|\vec{r}_o - \vec{r}| \to \infty$. This could be avoided and the convergence of the integral over region R can be assured by adding to Eq. A21 the quantity

$$\frac{1}{2\pi} \iint_R \omega(\vec{r}_o) \ln|\vec{r}| \, dR_o$$

This quantity is zero since

$$\frac{1}{2\pi} \ln|\vec{r}| \iint_R \omega(\vec{r}_o) dR_o = 0$$

by the principle of conservation of total vorticity. Thus Eq. A21 is more conveniently written as

$$\Psi(\vec{r}) = \frac{1}{2\pi} \iint_R \omega(\vec{r}_o) \ln \frac{|\vec{r}|}{|\vec{r}_o - \vec{r}|} \, dR_o$$

$$+ \frac{1}{2\pi} \int_B \Psi(\vec{r}_o) \frac{(\vec{r}_o - \vec{r}) \cdot \vec{n}_o}{|\vec{r}_o - \vec{r}|^2} \, dB_o$$

$$+ \frac{1}{2\pi} \int_B \left\{ \vec{\nabla}\Psi(\vec{r}_o) \cdot \vec{n}_o \right\} \ln \frac{1}{|\vec{r}_o - \vec{r}|} \, dB_o \quad \text{(A.22)}$$

The integrals over the boundary B are evaluated by using known boundary conditions. Let the boundary B consist of S, the solid surface and C, a circle of radius $\rho \to \infty$. Then

$$\Psi = 0, \frac{\partial \Psi}{\partial n} = 0 \quad \text{on} \quad S \tag{A.23}$$

$$\Psi = u_\infty \rho \sin\theta - v_\infty \rho \cos\theta, \quad \frac{\partial \Psi}{\partial n} = u_\infty \sin\theta - v_\infty \cos\theta \quad \text{on C.} \tag{A.24}$$

With these conditions the integrals over the boundary S vanish in Eq. A.22, and only the integrals over boundary C need be considered.

$$I_1 = \int_{B=C} \Psi(\vec{r}_o) \frac{(\vec{r}_o - \vec{r}) \cdot \vec{n}_o}{|\vec{r}_o - \vec{r}|^2} \, dB_o$$

$$= \int_o^{2\pi} (u_\infty \rho \sin\theta_o - V_\infty \rho \cos\theta_o) \frac{\rho - r\cos(\theta_o - \theta)}{\rho^2 + r^2 - 2\rho r \cos(\theta_o - \theta)} \rho d\theta_o$$

Letting $\beta = \theta_o - \theta$, and omitting odd integrals,

$$I_1 = \int_o^{2\pi} \frac{(u_\infty \cos\beta \sin\theta - v_\infty \cos\beta \cos\theta)(\rho - r\cos\beta)}{\rho^2 + r^2 - 2\rho r \cos\beta} \rho^2 d\theta_o$$

$$= (u_\infty \sin\theta - v_\infty \cos\theta) \int_o^{\pi} \frac{2\rho\cos\beta - r(1+\cos 2\beta)}{1 + \left\{\frac{r}{\rho}\right\}^2 - 2\frac{r}{\rho}\cos\beta} \, d\beta$$

$$= \pi r (u_\infty \sin\theta - v_\infty \cos\theta)$$

$$I_2 = -\frac{1}{2} \int_{B=C} \frac{\partial \Psi}{\partial n} \ln |\vec{r}_o - \vec{r}|^2 \, dB_o$$

$$= -\frac{1}{2} \int_o^{2\pi} (u_\infty \sin\theta_o - v_\infty \cos\theta_o) \ln \left\{ r^2 + \rho^2 - 2\rho r \cos(\theta_o - \theta) \right\} \rho d\theta_o$$

Integrating by parts

$$I_2 = -r \int_0^{2\pi} \mathrm{Sin}(\theta_o - \theta) \frac{u_\infty \mathrm{Cos}\,\theta_o + v_\infty \mathrm{Sin}\,\theta_o}{r^2+\rho^2-2\rho r \mathrm{Cos}(\theta_o-\theta)} \rho^2 d\theta_o$$

Again letting $\beta = \theta_o - \theta$ and omitting odd integrals,

$$I_2 = -r \int_0^{2\pi} \mathrm{Sin}\,\beta \; -u_\infty \mathrm{Sin}\beta\, \mathrm{Sin}\theta + v_\infty \mathrm{Cos}\theta\, \mathrm{Sin}\beta \frac{d\theta_o}{1+\frac{r^2}{\rho^2}-2\frac{r}{\rho}\mathrm{Cos}\beta}$$

$$= (u_\infty \mathrm{Sin}\theta - v_\infty \mathrm{Cos}\theta) r \int_0^{\pi} \frac{1-\mathrm{Cos}2\beta}{1+\frac{r^2}{\rho^2}-2\frac{r}{\rho}\mathrm{Cos}\beta} d\beta$$

$$= \pi r (u_\infty \mathrm{Sin}\theta - v_\infty \mathrm{Cos}\theta)$$

Using these in A.22 one obtains,

$$\Psi(\vec{r}) = \frac{1}{2\pi} \iint_R \omega(\vec{r}_o) \ln \frac{|\vec{r}|}{|\vec{r}_o - \vec{r}|} dR_o + r(u_\infty \mathrm{Sin}\theta - v_\infty \mathrm{Cos}\theta) \qquad (A.25)$$

Integral Representation for Ψ in the transformed plane

Consider now the transformation to κ-plane with H being the scale factor of transformation. The governing equation, A13, is still a Poisson's equation, and the source term becomes $-\omega H^2$ instead of $-\omega$. We let

$$\omega_\kappa = \omega H^2$$

and in formal analogy with Eq. A.22 write

$$\Psi\ (\vec{r}_K) = \frac{1}{2\pi} \iint_R \omega_K(\vec{r}_{K_o}) \ln \frac{\vec{r}_K}{|\vec{r}_{K_o} - \vec{r}_K|}\, dR_{K_o}$$

$$+ \frac{1}{2\pi} \int_B \Psi\ (\vec{r}_{K_o}) \frac{(\vec{r}_{K_o} - \vec{r}_K)\cdot\vec{n}_{K_o}}{|\vec{r}_{K_o} - \vec{r}_K|^2}\, dB_{K_o}$$

$$+ \frac{1}{2\pi} \int_{B_K} \left[\vec{\nabla}_K \Psi\ (\vec{r}_{K_o})\cdot\vec{n}_{K_o}\right] \ln \frac{1}{|\vec{r}_{K_o} - \vec{r}_K|}\, dB_{K_o} \qquad (A.26)$$

In the transformed plane, the region R_K is bounded by B_K which consists of the body S_K and the farstream boundary C_K. In S_K, $\Psi = 0$ and $\frac{\partial \Psi}{\partial n} = 0$ so the contribution of S_K to the line integrals in Eq. A26 is zero. The transformation under consideration transforms the region exterior to the body in the physical plane to the interior of a unit circle in the transformed plane. Therefore a circle of radius $\rho \to \infty$ in the physical plane would transform to a circle of radius $\varepsilon = \frac{1}{\rho} \to 0$ in the working plane. Since Ψ is invariant in the transformation, the stream function value which prevails on the circle of radius $\varepsilon \to 0$ is

$$\Psi = -\frac{1}{\varepsilon}\,(u_\infty \mathrm{Sin}\theta_K + u_\infty \mathrm{Cos}\theta_K), \text{ on } C_K$$

as $r_K = \frac{1}{r}$ and $\theta_K = -\theta$.

Also

$$\left.\frac{\partial \Psi}{\partial n}\right|_{r_K = \varepsilon} = -\left.\frac{\partial \Psi}{\partial r_K}\right|_{r_K = \varepsilon} = -\frac{1}{\varepsilon^2}\,(u_\infty \mathrm{Sin}\theta_K + v_\infty \mathrm{Cos}\theta_K)$$

Therefore

$$I_1 = \int_{B_K=C_K} \psi(\vec{r}_{K_o}) \frac{(\vec{r}_{K_o}-\vec{r}_K)\cdot\vec{n}_{K_o}}{|\vec{r}_{K_o}-\vec{r}_K|^2} dB_{K_o}$$

$$= \int_0^{2\pi} \frac{(u_\infty \sin\theta_{K_o} + v_\infty \cos\theta_{K_o})\{\varepsilon - r\cos(\theta_{K_o}-\theta_K)\}}{\varepsilon\{r_K^2 + \varepsilon^2 - 2r_K\varepsilon\cos(\theta_{K_o}-\theta_K)\}} \varepsilon\, d\theta_{K_o}$$

Letting $\beta = \theta_{K_o} - \theta$, and omitting odd integrals,

$$I_1 = \int_0^{2\pi} \frac{(u_\infty \sin\theta_K \cos\beta + v_\infty \cos\theta_K \cos\beta)(\varepsilon - r_K\cos\beta)}{r_K^2\left[1 + \frac{\varepsilon}{r_K} - 2\frac{\varepsilon}{r_K}\cos\beta\right]} d\beta$$

$$= \frac{(u_\infty \sin\theta_K + v_\infty \cos\theta_K)}{r_K} \int_0^{\pi} \frac{\frac{2\varepsilon}{r_K}\cos\beta - 1 - \cos 2\beta}{1 + \frac{\varepsilon^2}{r_K^2} - \frac{2\varepsilon}{r_K}\cos\beta} d\beta$$

$$= -\frac{\pi}{r_K}(u_\infty \sin\theta_K + v_\infty \cos\theta_K)$$

$$I_2 = \int_{B_K=C_K} -\frac{1}{2}\left[\vec{\nabla}_K \psi(\vec{r}_{K_o})\cdot\vec{n}_{K_o}\right] \ln|\vec{r}_{K_o}-\vec{r}_K|^2 dB_{K_o}$$

$$= \int_0^{2\pi} \frac{1}{2}\frac{(u_\infty \sin\theta_K + v_\infty \cos\theta_K)}{\varepsilon^2} \cdot \ln\left[r_K^2 + \varepsilon^2 - 2r_K\varepsilon\cos(\theta_{K_o}-\theta_K)\right]\varepsilon\, d\theta_{K_o}$$

Integrating this by part, letting $\beta = \theta_{K_o} - \theta_K$, and dropping odd integrals one obtains

$$I_2 = \int_0^{2\pi} -\frac{(u_\infty \sin\theta_K + v_\infty \cos\theta_K)\sin^2\beta}{r_K\left[1 + \frac{\varepsilon^2}{r_K^2} - 2\frac{\varepsilon}{r}\cos\beta\right]} d\beta$$

$$= -\frac{\pi}{r_K}(u_\infty \sin\theta_K + v_\infty \cos\theta_K)$$

Thus Eq. A26 reduces to

$$\Psi(\vec{r}_K) = \frac{1}{2\pi}\iint_{R_K} \omega_K(\vec{r}_{K_o}) \ln \frac{|\vec{r}_K|}{|\vec{r}_{K_o}-\vec{r}_K|} dR_{K_o}$$

$$- \frac{1}{r_K}(u_\infty \sin\theta_K + v_\infty \cos\theta_K) \qquad (A.27)$$

4. Equation for Surface Vorticity Calculation

In the equation for the stream function (Eq. A27) separating the vorticity on the solid surface, S_K, from the region R_K one may write

$$\Psi(\vec{r}) = \frac{1}{2\pi}\iint_{R_K - S_K} \omega_{Ko} \ln \frac{r}{|\vec{r}_o - \vec{r}|} dR_o$$

$$+ \frac{1}{2\pi}\int_{S_K} \zeta_K \ln \frac{r}{|\vec{r}_o - \vec{r}|} dS_o - \frac{1}{r}(u_\infty \sin\theta + v_\infty \cos\theta) \qquad (A.28)$$

In the above equation and in what follows the notation $\vec{r}$ implies the position vector $\vec{r} = \vec{r}_K(r_K, \theta_K)$ in the working plane. The subscript K is dropped for convenience. The surface distribution of voriticty is denoted by ζ_K in Eq. A28. The distribution of ζ_K on the surface must be determined so as to satisfy the condition $\Psi = 0$ inside the solid surface which corresponds to the region $r \geq 1$ in the working plane.

Since the differential equations describing the kinematic relation between vorticity and stream function are linear, the method of superposition is valid. Consider ζ_K in two parts

$$\zeta_K = \zeta_{K1} + \zeta_{K2} \tag{A.29}$$

and let ζ_{K1} be the contribution of free stream condition to the surface vorticity and let ζ_{K2} be the contribution of vorticity away from surface.

The distribution ζ_{K1} is readily determined by considering the surface vorticity distribution corresponding to a potential flow past a circular cylinder which is available in standard texts. When the exterior of the circle is conformally mapped into the interior of a unit circle, this becomes

$$\zeta_{K1} = 2(u_\infty \sin\theta + v_\infty \cos\theta) \tag{A.30}$$

It shall now be verified that the stream function associated with ζ_{K1}, as given above, is indeed zero for the region $r \geq 1$. Consider

$$I = \frac{1}{2\pi} \int_{S_K} \zeta_K \ln \frac{r}{|\vec{r}_o - \vec{r}|} \, dS_{K_o}$$

$$= \frac{1}{2\pi} \int_0^{2\pi} 2V_\infty \sin(\alpha + \theta_o) (\ln r) \, r_o d\theta$$

$$- \frac{1}{2\pi} \int_0^{2\pi} 2V_\infty \sin(\alpha + \theta_o) \frac{1}{2} \ln \left[r_o^2 + r^2 - 2rr_o \cos(\theta_o - \theta) \right] r_o d\theta_o$$

where $V_\infty = (u_\infty^2 + v_\infty^2)^{\frac{1}{2}}$ and $\alpha = \tan^{-1} \frac{v_\infty}{u_\infty}$. The first integral in the above expression vanishes. Since the distribution of vorticity is on the

surface, one sets $r_o = 1$. Integrating by parts,

$$I = -\frac{V_\infty}{2\pi} \int_0^{2\pi} \mathrm{Sin}(\alpha + \theta_o) \frac{2r\mathrm{Sin}(\theta_o - \theta)}{1+r^2-2r\mathrm{Cos}(\theta_o - \theta)} \, d\theta_o$$

Letting $\beta = \theta_o - \theta$ and hence $\alpha + \theta_o = (\theta+\alpha)+\beta$,

$$I = \frac{V_\infty r}{\pi} \int_\theta^{2\pi-\theta} \frac{[\mathrm{Cos}\beta\mathrm{Cos}(\theta+\alpha) - \mathrm{Sin}\beta\mathrm{Sin}(\theta+\alpha)]\mathrm{Sin}\beta}{1+r^2-2r\mathrm{Cos}\beta} \, d\beta$$

Deleting odd integral that vanishes, and noting that even integral is periodic in β with a period of 2π, one has

$$I = \frac{V_\infty R\mathrm{Sin}(\theta+\alpha)}{\pi} \int_o^{\pi} \frac{2\mathrm{Sin}^2\beta}{1+r^2-2r\mathrm{Cos}\beta} \, d\beta$$

or

$$I = \frac{V_\infty r\mathrm{Sin}(\theta+\alpha)}{\pi} \frac{\pi}{r^2}, \quad \text{For} \quad r > 1$$

$$= \frac{V_\infty}{r} \mathrm{Sin}(\theta+\alpha)$$

$$= \frac{1}{r} (u_\infty \mathrm{Sin}\,\theta + V_\infty \mathrm{Cos}\,\theta)$$

Using this in Eq. A28

$$\Psi = I - \frac{1}{r}(u_\infty \mathrm{Sin}\theta + V_\infty \mathrm{Cos}\theta) = 0,$$

and thus the contribution of $\zeta_{K\,1}$ to stream function in the solid region is zero.

To determine the contribution to surface vorticity due to vorticity away from surface, consider an elemental vorticity $\omega_{K_o} dR_{K_o}$ located at $\vec{r}_o$. Let its contribution to surface vorticity be the elemental distribution $d\zeta_{K2}$. The distribution $d\zeta_{K2}$ will be equal to the tangential velocity at the surface, $r = a$, corresponding to a flow field which induces zero normal velocity at $r = a$. Such a flow field can be constructed by the method of images. Denote $\omega_K \; dR_K = \Omega$ and let it be located at the point (r_o, θ_o). Its image point is then $\left(\frac{a^2}{r_o^2},\ \theta\right)$ and the vorticity value at the image point is $-\Omega$.

The interior of the circle with radius 'a' constitutes the fluid domain; the outward normal is in the positive r-direction and the unit tangent vector is directed in negative θ-direction. The tangential velcoity at the surface is then defined by

$$V_t\Big|_{r=a} = -V_\theta\Big|_{r=a} = \frac{\partial \Psi}{\partial r}\Big|_{r=a},$$

which is obtained by differentiating Eq. A27 with respect to r.

Now

$$\frac{\partial \Psi}{\partial r} = \frac{1}{2\pi} \iint_{R_K} \omega_{K_o} \frac{r_o^2 - r r_o \mathrm{Cos}(\theta_o - \theta)}{r(r^2 + r_o^2 - 2 r r_o \mathrm{Cos}(\theta_o - \theta))} dR_{K_o} - \frac{1}{r^2}\mathrm{Sin}(\alpha+\theta)$$

Ignoring the free stream contribution and applying this to compute the tangential velocity at $r = a$ due to vorticity Ω at (r_o, θ_o) and $-\Omega$ at

$$\left(\frac{a^2}{r_o},\ \theta_o\right),$$

$$d\zeta_{K_2} = \frac{\Omega}{2\pi a}\left[\frac{r_o^2 - a r_o \cos\beta}{a^2 + r_o^2 - 2a r_o \cos\beta} - \frac{\frac{a^4}{r_o^2} + a\frac{a^2}{r_o}\cos\beta}{a^2 + \frac{a^4}{r_o^2} - 2a\frac{a^2}{r_o}\cos\beta}\right]$$

where $\beta = \theta_o - \theta$

or

$$d\zeta_{K_2} = \frac{\Omega}{2\pi a}\left[\frac{r_o^2 - a^2}{a^2 + r_o^2 - 2a r_o \cos\beta}\right] \tag{A.31}$$

When the coordinates are normalized with respect to the radius of the circle

$$d\zeta_{K_2} = \frac{1}{2\pi}\left[\frac{r_o^2 - 1}{1 + r_o^2 - 2r_o\cos(\theta_o - \theta)}\right]\omega_{K_o} dR_{K_o}$$

We now show that the contribution to stream function in the solid region due to vorticity $\omega_{K_o} dR_{K_o}$ together with the contribution due to the surface vorticity distribution given by Eq. A31 is zero.

Ignoring the free stream contribution to stream function in Eq. A28, the contribution to stream function due to elemental vorticity $\Omega = \omega_{K_o} dR_{K_o}$ and due to $d\zeta_{K_2}$ given by Eq. A31 can be written as

$$\Psi(r, \theta) = -\frac{\Omega}{4\pi}\ln\left[\frac{r_o^2 + r^2 - 2r r_o\cos(\theta_o - \theta)}{r^2}\right]$$
$$-\frac{\Omega}{8\pi^2}(r_o^2 - 1)\int_o^{2\pi}\frac{1}{1 + r_o^2 - 2r_o\cos(\theta_o - \alpha)}\ln\left[\frac{1 + r^2 - 2r\cos(\alpha - \theta)}{r^2}\right]d\alpha$$

The elemental vorticity in the field is located at point (r_o, θ_o) with $r_o < 1$; the stream function is computed at point (r, θ) with $r > 1$, i.e. in the solid region; the surface distribution of vorticity given by Eq. A31 is placed around the unit circle. The integral

$$I = \int_0^{2\pi} \frac{1}{(1+r_o^2-2r_o\mathrm{Cos}(\theta_o-\alpha))} \ln\left[\frac{1+r^2-2r\mathrm{Cos}(\alpha-\theta)}{r^2}\right] d\alpha$$

is evaluated now using method of residues.

Let $z = re^{i\theta}$; $z_1 = 1.e^{i\alpha}$; $z_o = r_o e^{i\theta_o}$. Note that $|z_o| < 1$, and $|z| > 1$ since stream function is computed in the solid region. With these definitions,

$$1 + r^2 - 2r\mathrm{Cos}(\alpha-\theta) = |z_1 - z|^2 = (z_1 - z)(\bar{z}_1 - \bar{z})$$

$$1 + r_o^2 - 2r_o\mathrm{Cos}(\theta_o - \alpha) = |z_o - z_1|^2 = (z_o - z_1)(\bar{z}_o - \bar{z}_1)$$

$$r^2 = z\bar{z} \quad \text{and} \quad d\alpha = \frac{dz_1}{iz_1}$$

Then

$$I = \frac{1}{i} \int \frac{\ln\left[(z_1 - z)(\bar{z}_1 - \bar{z})/z\bar{z}\right]}{(z_1 - z_o)(\bar{z}_1 - \bar{z}_o)} \frac{dz_1}{z_1}$$

$$= \frac{1}{i} \int \frac{\ln\left[(z_1 - z)(\bar{z}_1 - \bar{z})/z\bar{z}\right]}{(z_1 - z_o)(1 - z_1\bar{z}_o)} dz_1$$

$$= -\frac{1}{i}\int \frac{\ln\left[(z_1-z)(\bar{z}_1-\bar{z})/z\bar{z}\right]}{(z_1-z_o)\left(z_1-\frac{1}{\bar{z}_o}\right)\bar{z}_o}\,dz_1$$

The contour of integral is chosen as the unit circle defined by $|z_1| = 1$. Then, the branch points due to the logarithmic function in the above integral lie outside the unit circle as $|z|>1$. Thus the function is analytic on and inside the chosen contour of integration with a simple pole at $z_1 = z_o$.

Then

$$I = -2\pi i\,\frac{1}{i}\left[\frac{\ln\left[(z_o-z)(\bar{z}_o-\bar{z})/z\bar{z}\right]}{(z_o\bar{z}_o-1)}\right]$$

$$= -\frac{2}{(r_o^2-1)}\ln\left[\frac{|z_o-z|^2}{r^2}\right]$$

$$= -\frac{2\pi}{(r_o^2-1)}\ln\left[\frac{r_o^2+r^2-2rr_o\cos(\theta_o-\theta)}{r^2}\right]$$

Thus it is verified that

$$\Psi\ (r_1,\theta) = -\frac{\Omega}{4\pi}\ln\left[\frac{r_o^2+r^2-2rr_o\cos(\theta_o-\theta)}{r^2}\right]+\frac{\Omega}{4\pi}\ln\left[\frac{r_o^2+r^2-2rr_o\cos(\theta_o-\theta)}{r^2}\right]$$

$$= 0 \quad \text{for} \quad r>1$$

Since the governing equations for kinematics are linear, the surface vorticity due to vorticity in the entire flow field away from surface can be written as

$$\zeta_{K2} = \iint_{R_K-S_K}\frac{1}{2\pi}\,\frac{(r_o^2-1)\omega_{K_o}dR_{K_o}}{1+r_o^2-2r_o\cos(\theta_o-\theta)}$$

Using this along with equations A29 and A30, one finally obtains

$$\zeta_K = \frac{1}{2\pi} \iint_{R_K - S_K} \frac{(r_o^2-1)\omega_{K_o} dR_{K_o}}{1+r_o^2-2r_o\text{Cos}(\theta_o-\theta)} + 2V_\infty \text{Sin}(\alpha + \theta)$$

where V_∞ is magnitude of free stream velocity and α is angle of attack.

Conservation of Total Vorticity

The contribution of free stream condition to the surface vorticity is defined by Eq. A.30. The contribution of this surface vorticity distribution to the total vorticity in the flow field is zero since

$$\int_o^{2\pi} \zeta_{K_1} d\theta = \int_o^{\pi} 2(u_\infty \text{Sin}\theta + V_\infty \text{Cos}\,\theta)\, d\theta = 0 \qquad (A.32)$$

The elemental surface vorticity distribution, $d\zeta_{K_2}$, due to elemental vorticity $\Omega = \omega_K\, dR_K$, is defined by Eq. A31. Then

$$\Omega + \int_o^{2\pi} (d\zeta_{K_2}) d\theta = \Omega + \frac{(r_o^2-1)\Omega}{2\pi} \int_o^{2\pi} \frac{d\theta}{1+r_o^2-2r_o\text{Cos}(\theta_o-\theta)}$$

$$= \Omega + \frac{(r_o^2-1)\Omega}{2\pi} \frac{2\pi}{(1-r_o^2)}$$

$$= 0$$

Since this is true for each elemental vorticity located in the flow field it is true that

$$\iint_{R_K - S_K} \omega_{K_o} \, dR_{K_o} + \int_o^{2\pi} \zeta_{K2} \, d\theta = 0 \qquad (A.33)$$

Since the surface vorticity $\zeta_K = \zeta_{K1} + \zeta_{K2}$, Eq. A32 and A33 together imply that the total vorticity in the flow field is always zero.

LIST OF REFERENCES

1. Chapman, D. R., Mark, H. and Pritle, M. W., "Computers vs. Wind Tunnels for Aerodynamic Flow Simulations," Astronautics and Aeronautics, April 1975, pp. 22-10.

2. Crocco, L., "A Suggestion for the Numerical Solution of the Steady Navier-Stokes Equations," AIAA Journal, Vol. 3, No. 10, Oct., 1965, pp. 1824-1832.

3. Roache, P. J., Computational Fluid Dynamics, Hermosa Publishers, Albuquerque, New Mexico, 1972.

4. Frenkiel, F. N., and Stewartson, K., editors, "High Speed Computing in Fluid Dynamics," The Physics of Fluids, Vol. 12, No. 12, Supplement II, 1969.

5. Wu, J. C., "Numerical Boundary Conditions for Viscous Flow Problems," AIAA Journal, Vol. 14, No. 8, August 1976, pp. 1042-1049.

6. Wu, J. C., and Thompson, J. F., "Numerical Solutions of Time-dependent Incompressible Navier-Stokes Equations Using an Integro-differential Formulation," Computers and Fluids, Vol. I, pp. 197-215, 1973.

7. Wu, J. C., Spring, A. H., and Sankar, N. L., "A Flow Field Segmentation Method for the Numerical Solution of Viscous Flow Problems," Proc. of the IV International Conference on Numerical Methods in Fluid Dynamics, pp. 452-457, Springer-Verlag, 1975.

8. Thompson, J. F., Shanks, S. P., and Wu, J. C. "Numerical Solution of Three-dimensional Navier-Stokes Equations Showing Trailing Tip Vortices," AIAA Journal, Vol. 12, pp. 787-794, 1974.

9. Wu, J. C., and Sampath, S., "A Numerical Study of Viscous Flow Around an Airfoil," AIAA Paper 76-337 , 12 pages, 1976.

10. Jain P. C., and Rao, K. S., "Numerical Solution of Unsteady Viscous Incompressible Fluid Flow Past a Circular Cylinder," The Physics of Fluids, Vol. 12, No. 12, Supplement II, pp. 57-64, 1969.

11. Dennis, S. C. R., and Chang, G., "Numerical Integration of the Navier-Stokes Equations for Steady Two-Dimensional Flow," The Physics of Fluids, Vol. 12, No. 12, Supplement II, pp. 88-93, 1969.

12. Rimon, Y., "Numerical Solution of the Incompressible Time-Dependent Viscous Flow Past a Thin Oblate Spheroid," The Physics of Fluids, Vol. 12, No. 12, Supplement II, pp. 65-75, 1969.

13. Thames, F. C., "Numerical Solution of the Incompressible Navier-Stokes Equations About Arbitrary Two-Dimensional Bodies," PH.D. Thesis, Mississippi State University, Mississippi, 1975.

14. Thoman, D. C., and Szewczyk, A. A., "Time-Dependent Viscous Flow Over a Circular Cylinder," The Physics of Fluids, Vol. 12, No. 12, Supplement II, pp. 76-87, 1969.

15. Takami, H., and Keller, H. B., "Steady Two-Dimensional Viscous Flow of an Incompressible Fluid past a Circular Cylinder," The Physics of Fluids, Vol. 12, No. 12, Supplement II, pp. 51-56, 1969.

16. Y. Takaisi, "Numerical Studies of a Viscous Liquid past a Circular Cylinder," The Physics of Fluids, Vol. 12, No. 12, Supplement II, pp. 86-87, 1969.

17. Mehta, U. B., "Starting Vortex, Separation Bubbles and Stall--A Numerical Study of Laminar Unsteady Flow Around an Airfoil," Ph.D. Thesis, Illinois Institute of Technology, Chicago, Illinois, 1972.

18. Leal, L. G., and Acrivos, A., "Structure of Steady Closed Streamline Flows Within a Boundary Layer," The Physics of Fluids, Vol. 12, No. 12, Supplement II, pp. 105-113, 1969.

19. Cheng, S. I., "Numerical Integration of Navier-Stokes Equations," AIAA Paper No. 70-2, 1970.

20. Dorr, F. W., "The Direct Solution of the Discrete Poisson Equation on a Rectangle," SIAM Review, Vol. 12, No. 2, April 1970, pp. 248-263.

21. Stone, H. L., "Iterative Solution of Implicit Approximations of Multidimensional Partial Differential Equations," SIAM Journal of Numerical Analysis, Vol. 5, No. 3, pp. 530-558, 1969.

22. Runchall, A. K., "Convergence and Accuracy of Three Finite Difference Schemes for a Two-Dimensional Conduction and Convection Problem," International J. for Numerical Methods in Engg, Vol. 24, pp. 541-550, 1972.

23. Arakawa, A., "Numerical Simulation of Large Scale Atmospheric Motions," SIAM-AMS Proceedings, Vol. N, numerical Solution of Field Problems in Continuum Physics, American Mathematical Society, 1970.

24. Lugt, H. J., and Hausling, H. J., "Laminar Flow Past an Abruptly Accelerated Elliptic Cylinder at 45^{0}-degree Inclination," J. of Fluid Mechanics, Vol. 65, Oct. 2, 1974, pp. 711-734.

25. Lin, C. L. and Lee S. C., "Transient State Analysis of Separated Flow Around a Sphere," Computers and Fluids, Vol. I, pp. 235-250, 1973.

26. Wu, J. C., "Integro-differential Method for Stream Function--Vorticity Formulation of Navier-Stokes Equations," Unpublished Notes, Georgia Institute of Technology, Georgia, 1975.

27. Wahbah, M. M. "Evaluation of Shape Functions Associated with the Finite Element Solution of the Integral Representation for Two-dimensional Flows," Unpublished Notes, Georgia Institute of Technology, Atlanta, Georgia, 1976.

28. Churchill, R. V., Introduction to Complex Variables and Applications, McGraw Hill Book Co., N. Y., 1948.

29. Grove, A. S., Shair, F. H., Peterson, E. E., and Acrivos, A., "An Experimental Investigation of Steady Separated Flow Past a Circular Cylinder," J. of Fluid Mechanics, Vol. 33, Part 1, 1964, pp. 60-80.

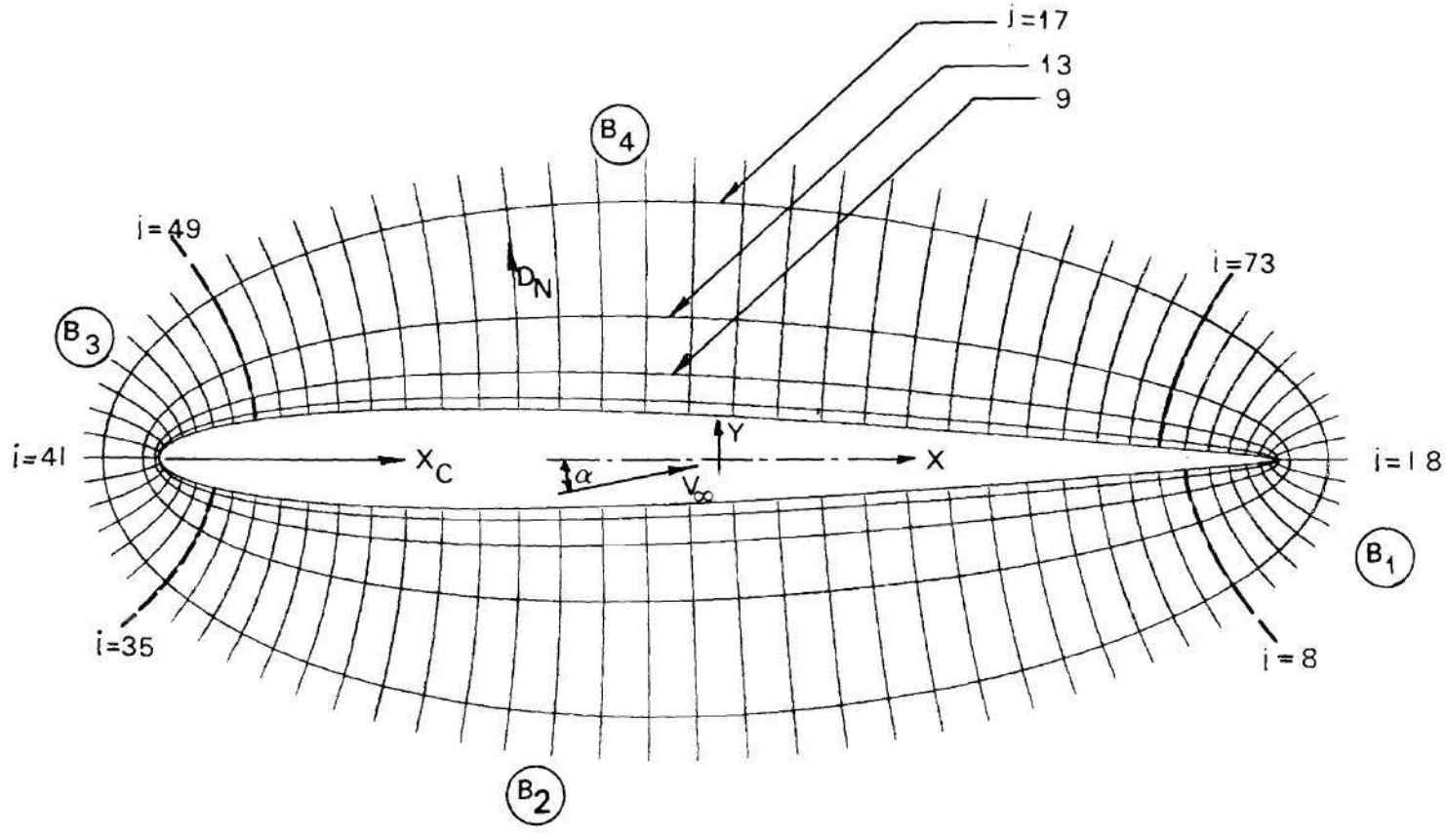

Figure 1. Grid Distribution and Notations in Physical Plane

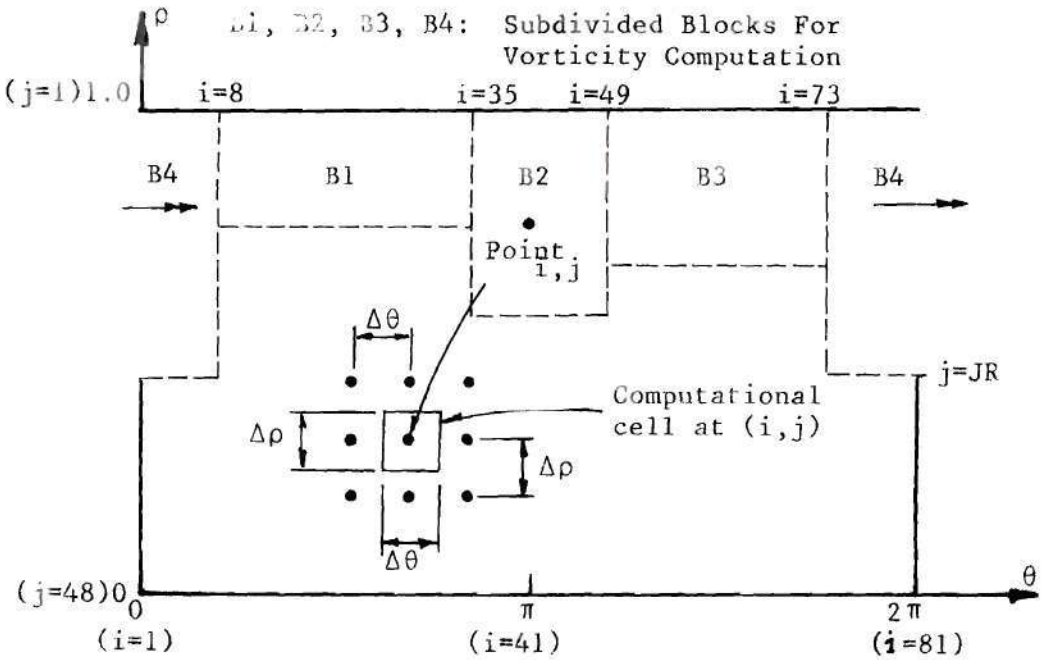

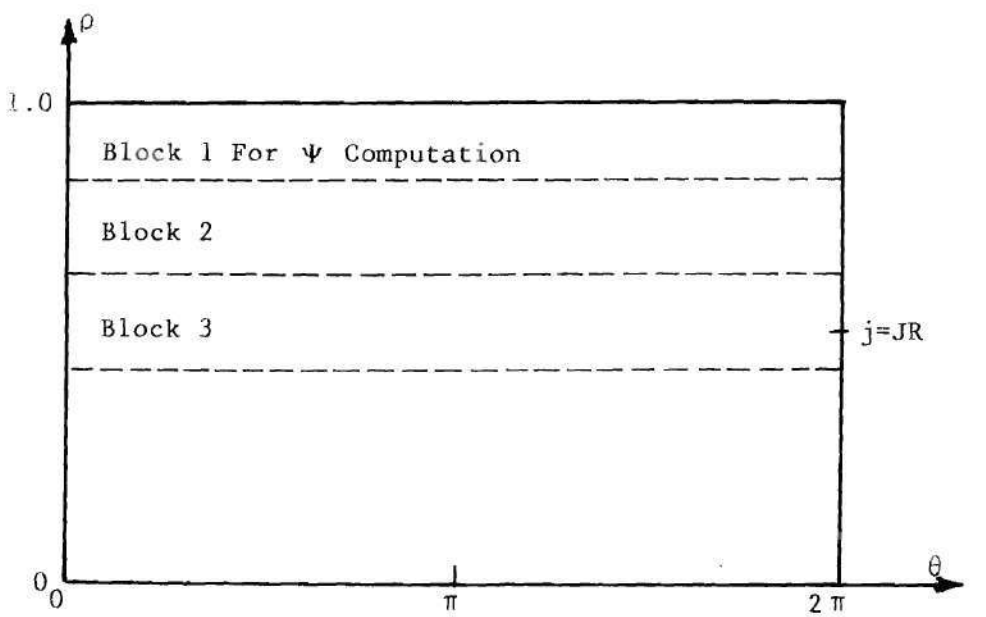

Figure 2. Grid Definition And Block Subdivisions in Working Plane

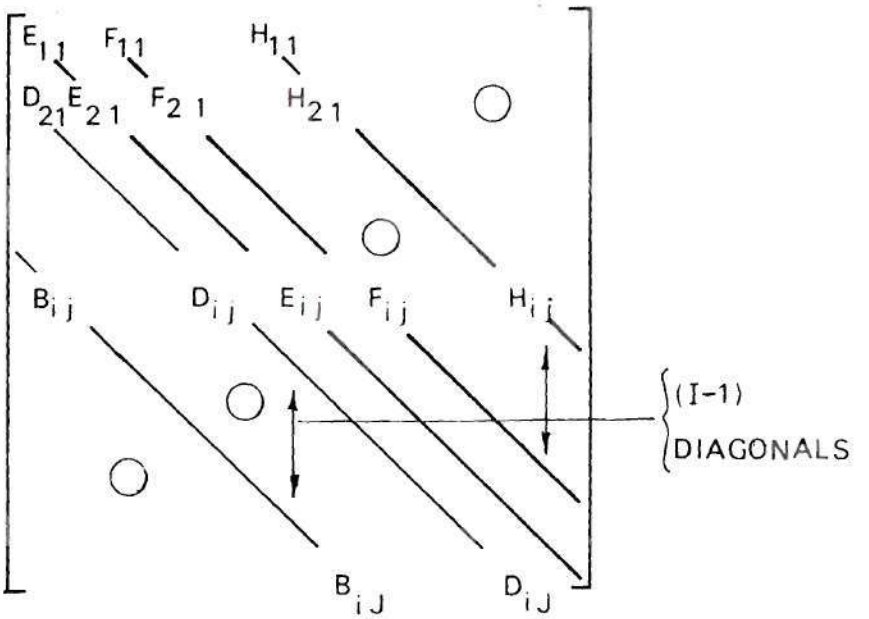

Figure 3a. Elements of Matrix [M]

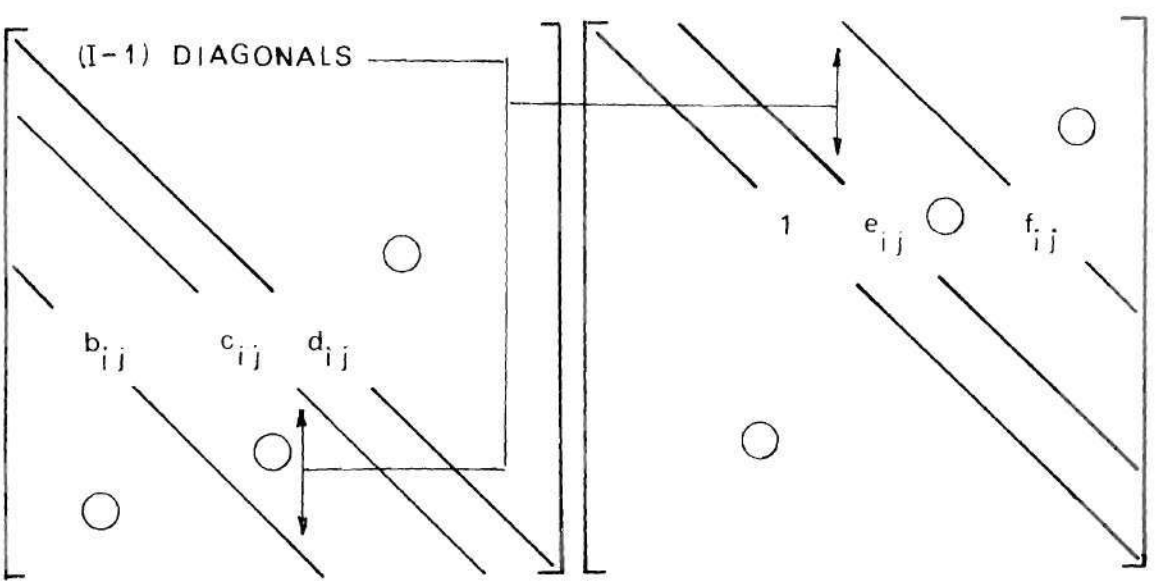

Figures 3b and 3c. Matrix [L] and Matrix [U]

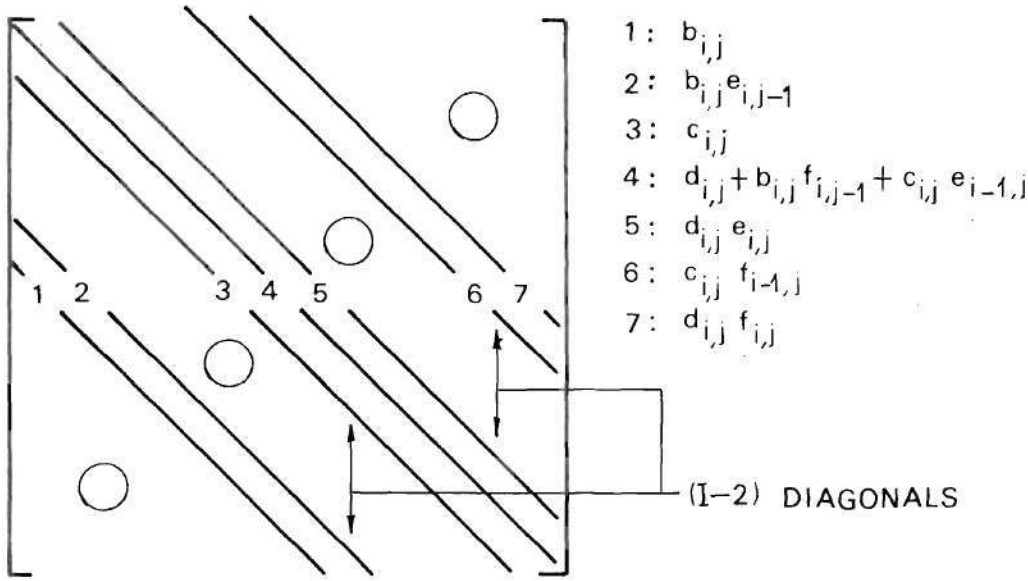

Figure 3d. Product Matrix [L] [U]

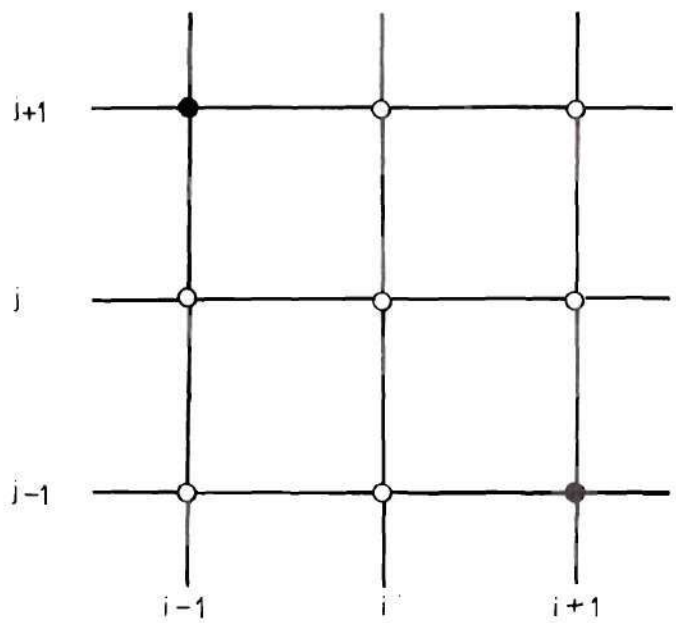

Figure 3e. Grid Points Involved in the Equation for point (i,j)

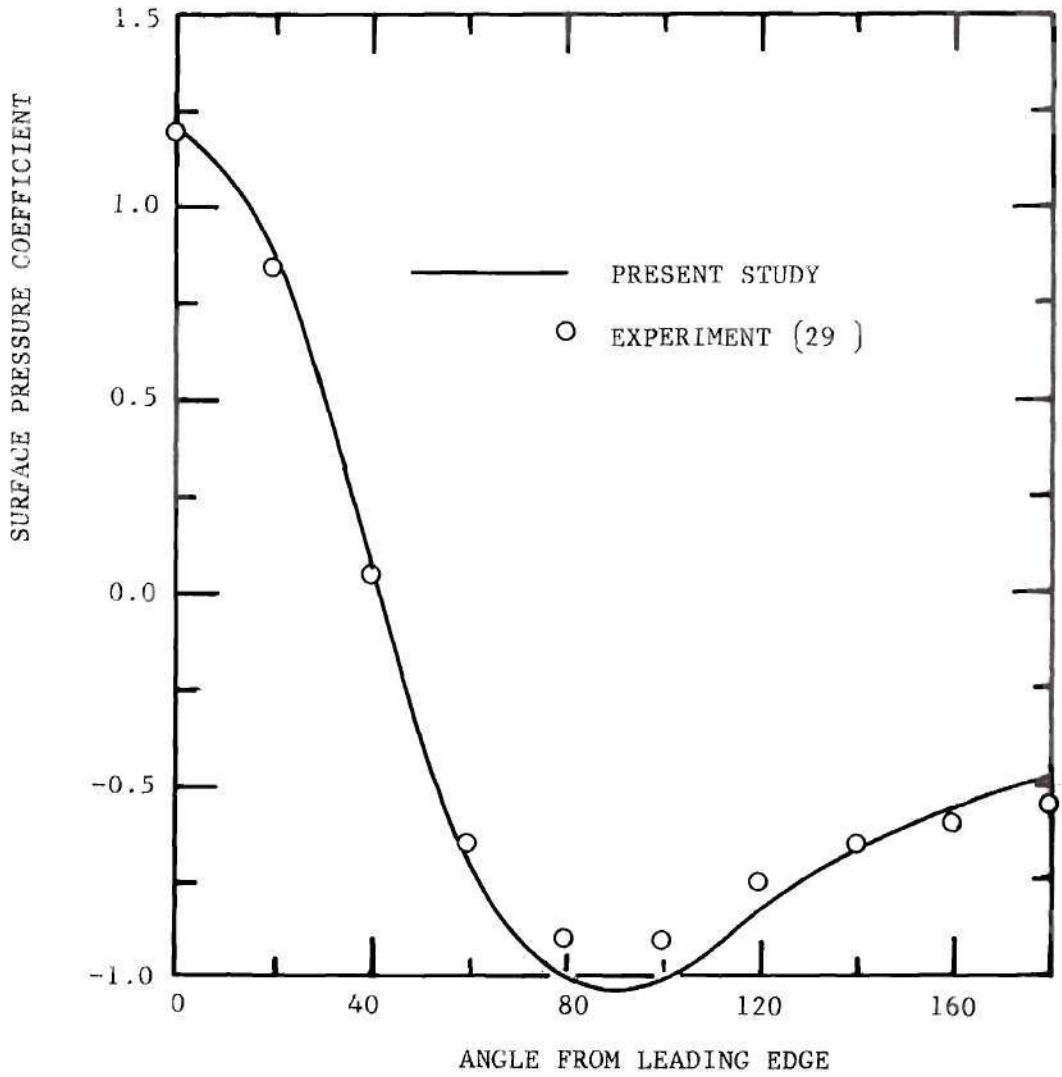

Figure 4. Surface Pressure Distribution over Circular Cylinder at Re = 40

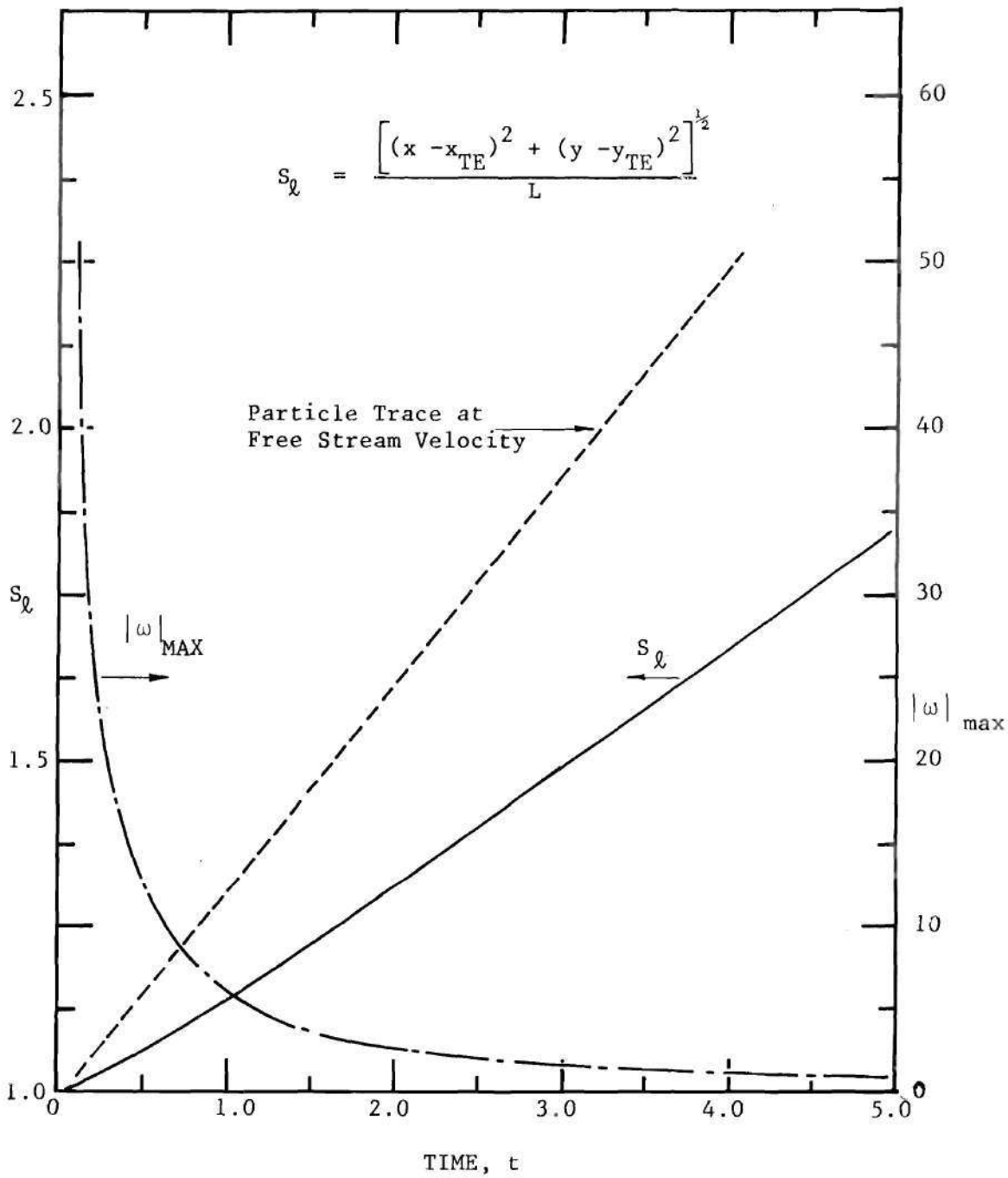

Figure 5. Variation in the Location of Starting Vortex and the Maximum Vorticity Value Inside Starting Vortex

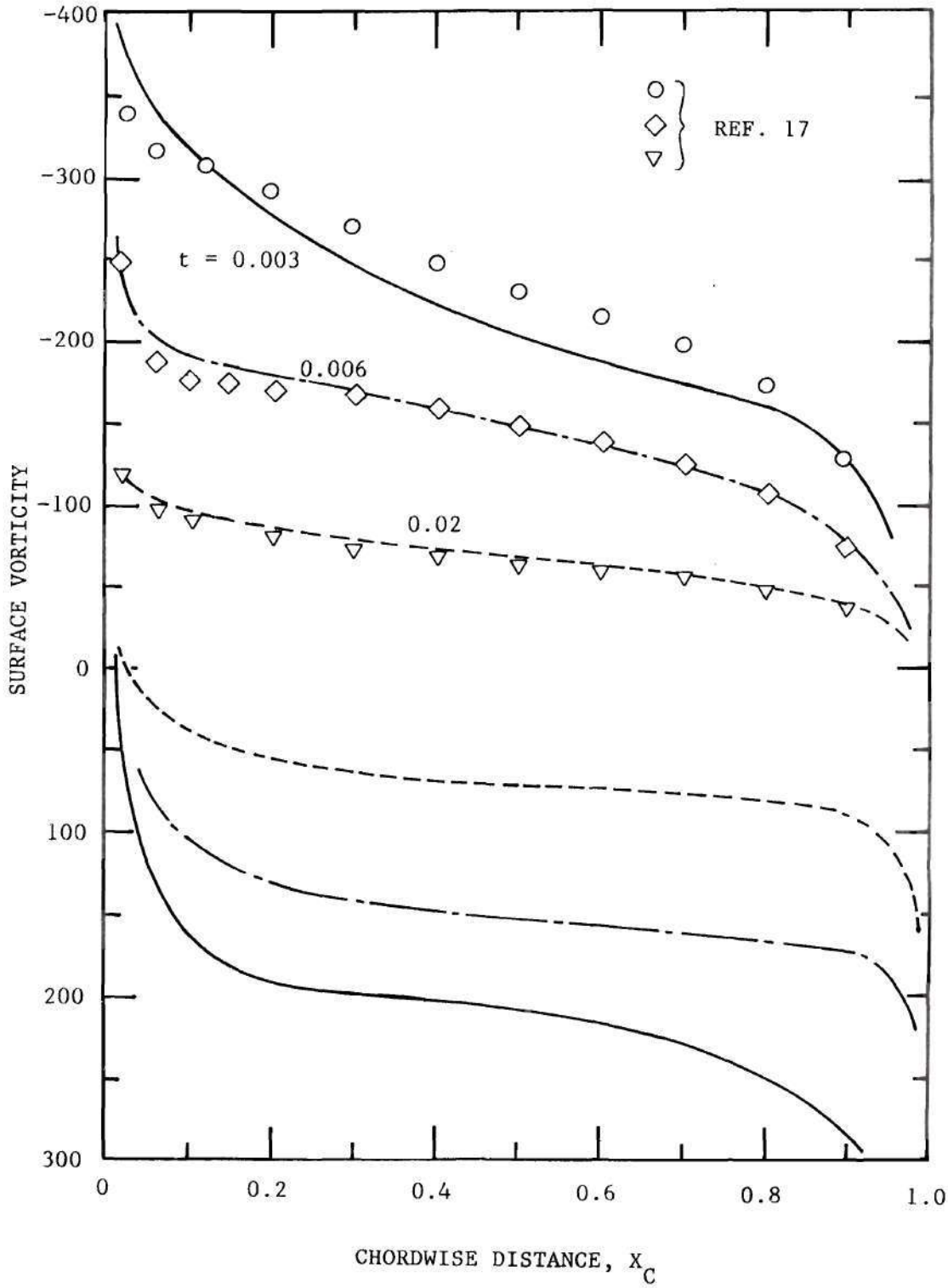

Figure 6. Surface Vorticity Distributions for t = 0.003 to t = 0.02

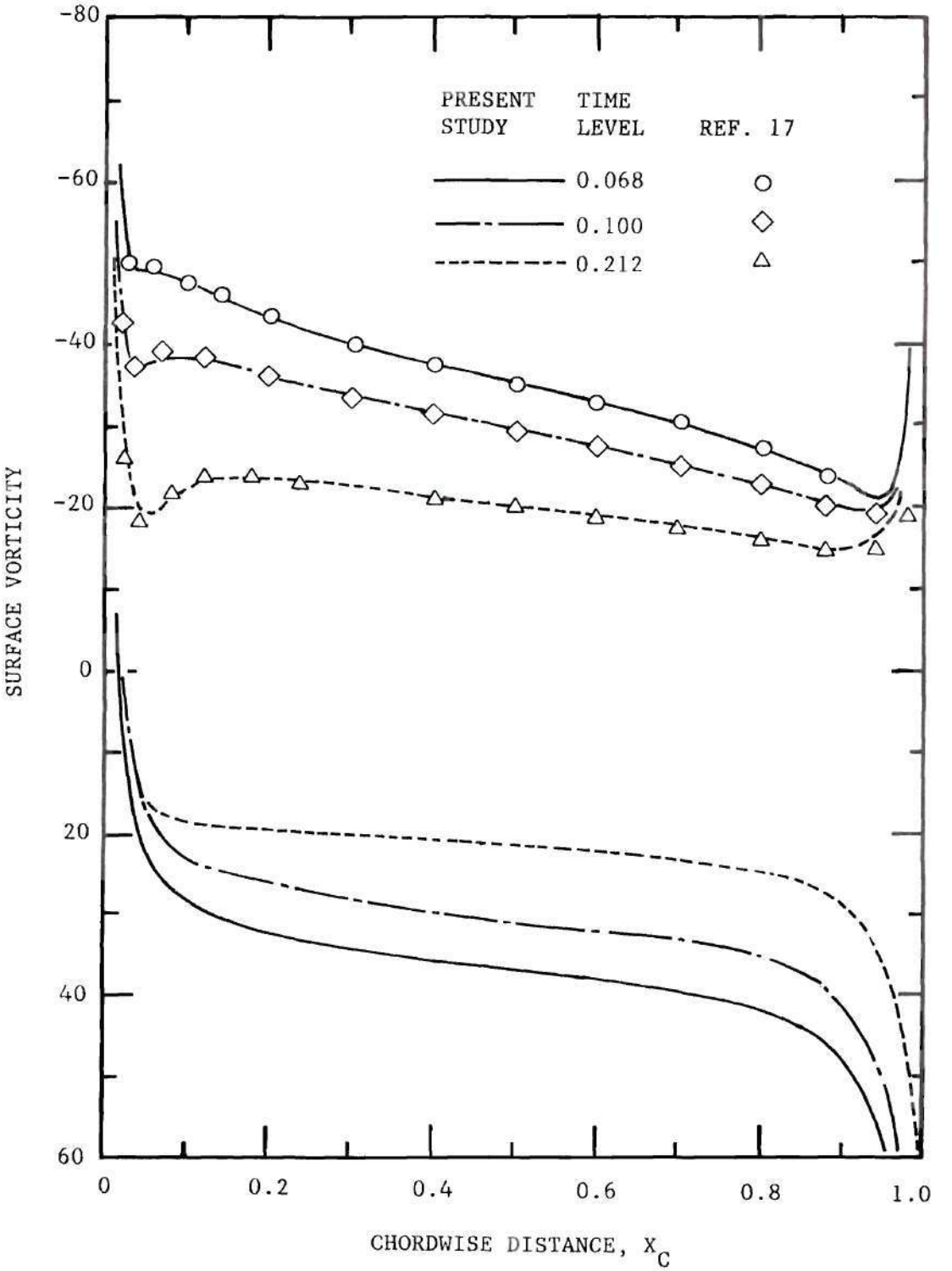

Figure 7. Surface Vorticity Distributions for t = 0.068 to t = 0.212

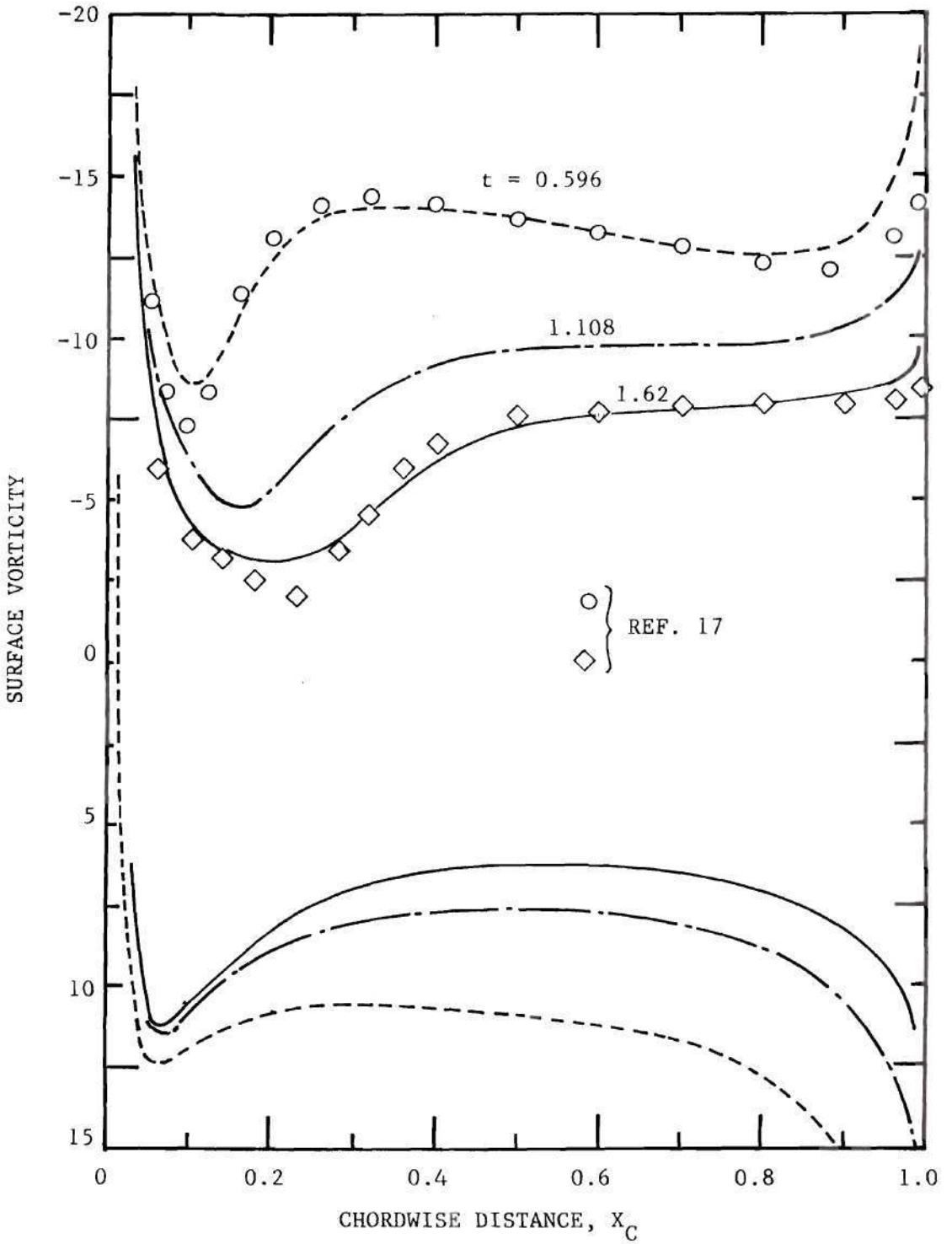

Figure 8. Surface Vorticity Distributions for t = 0.596 to t = 1.62

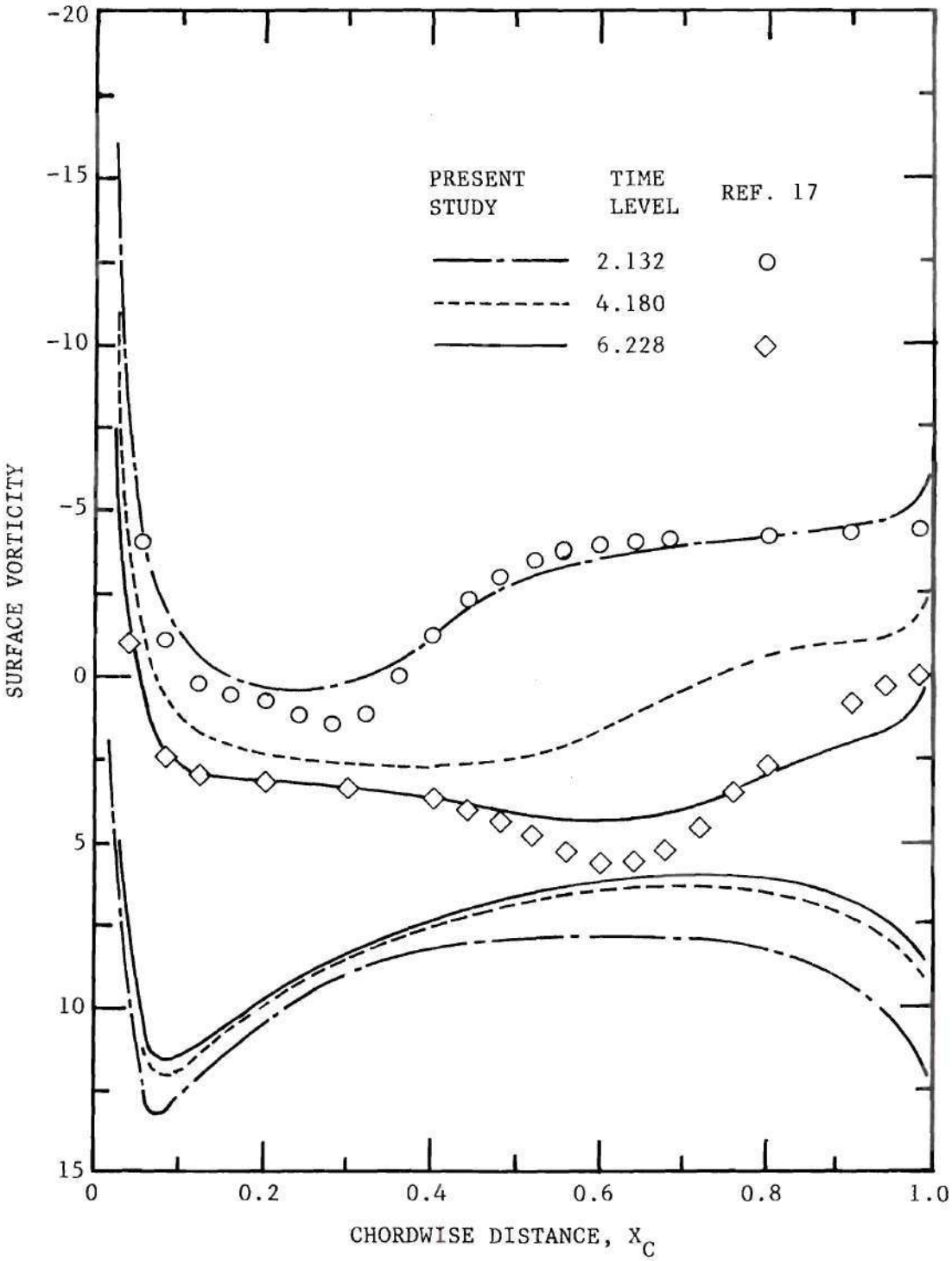

Figure 9. Surface Vorticity Distributions for t = 2.132 to t = 6.228

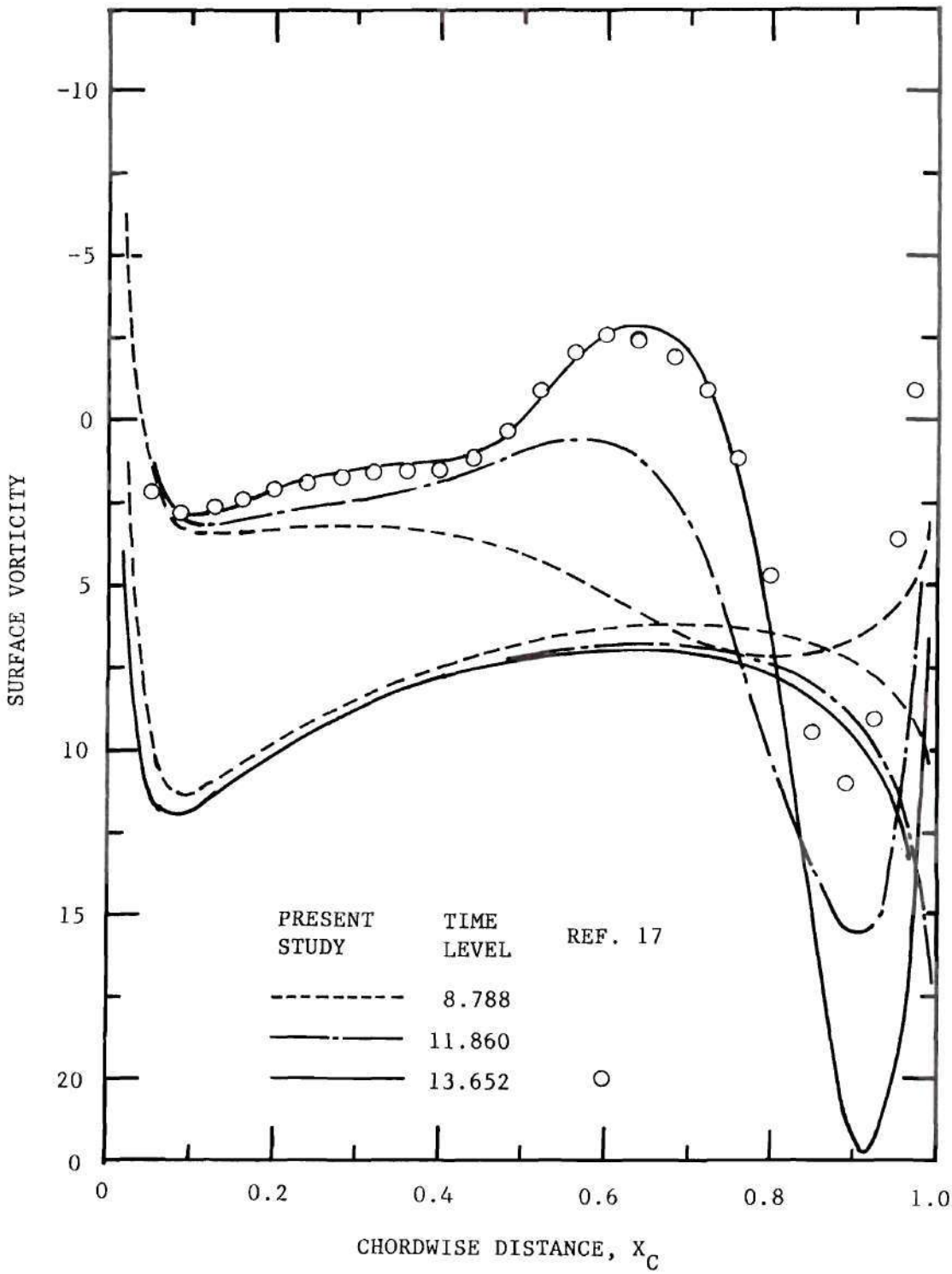

Figure 10. Surface Vorticity Distributions for t = 8.788 to t = 13.652

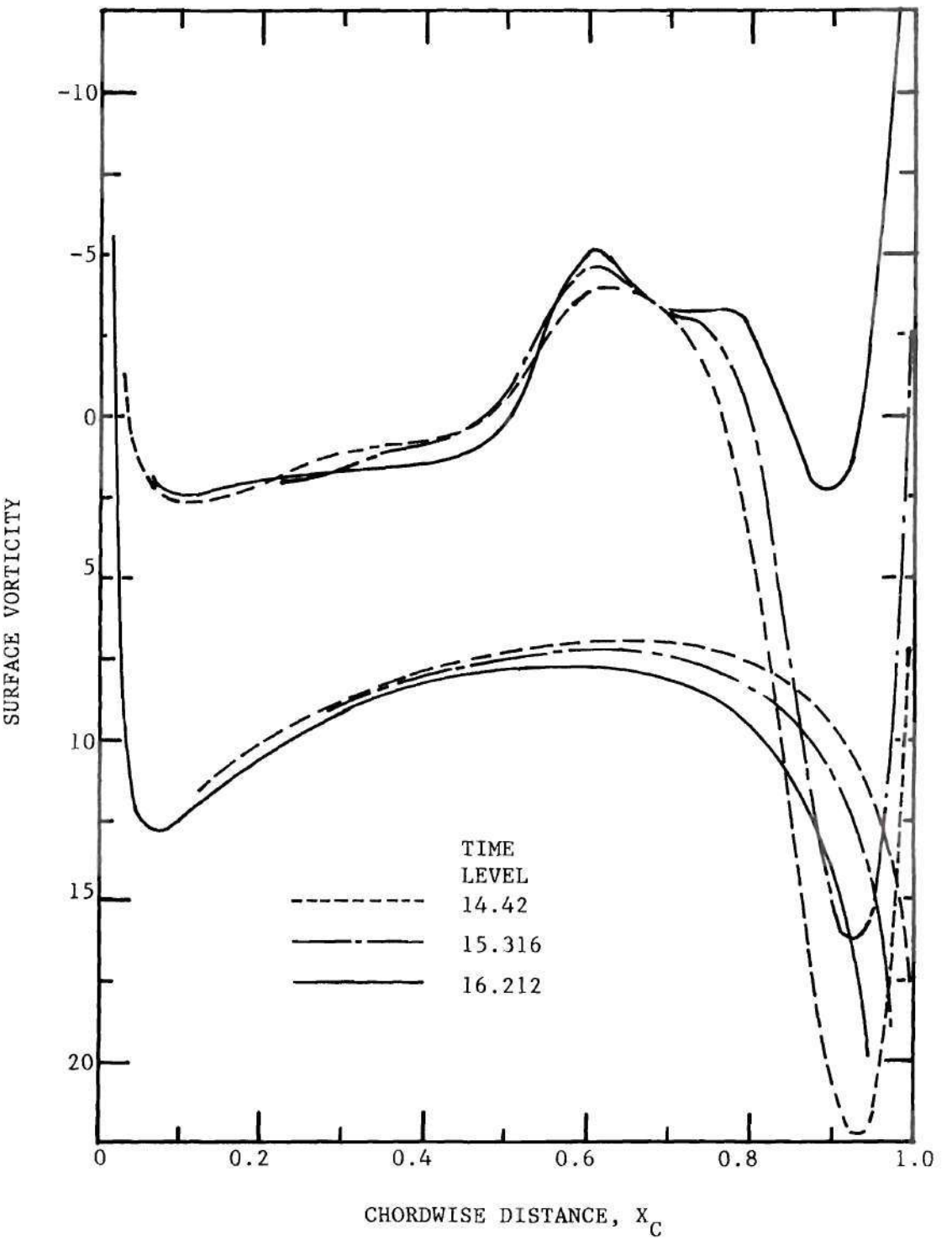

Figure 11. Surface Vorticity Distributions for $t = 14.42$ to $t = 16.212$

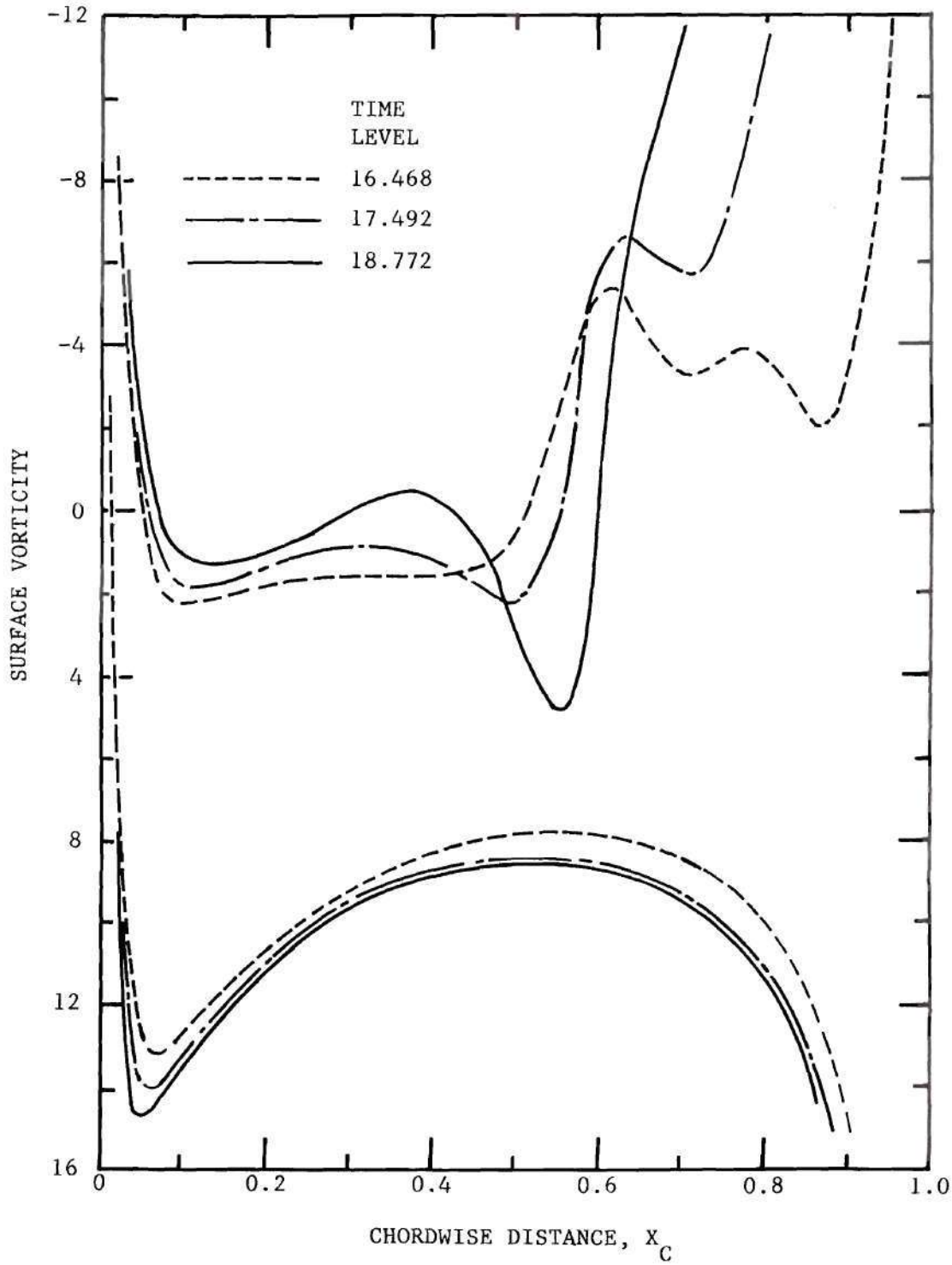

Figure 12. Surface Vorticity Distributions for t = 16.468 to 18.772

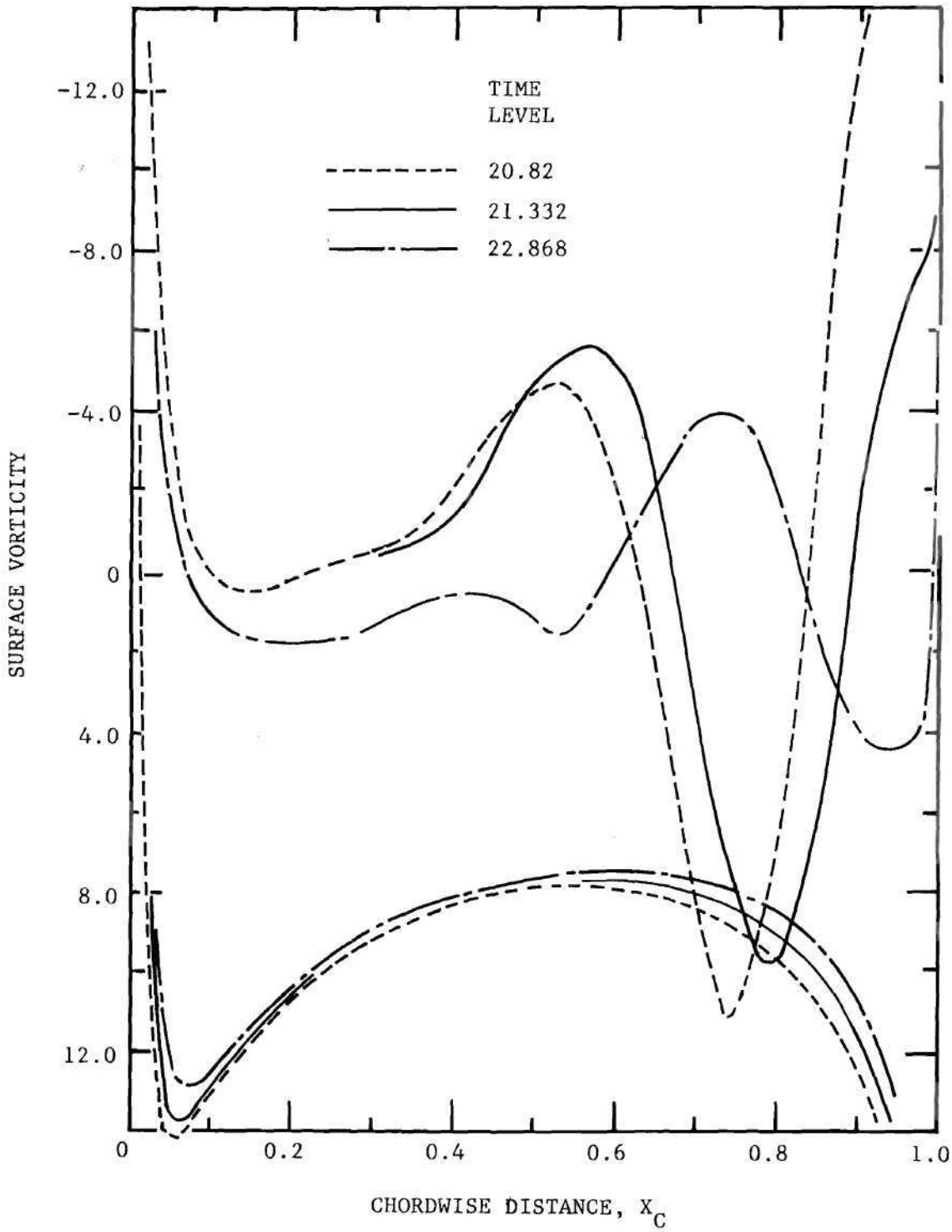

Figure 13. Surface Vorticity Distributions for t = 20.82 to t = 22.868

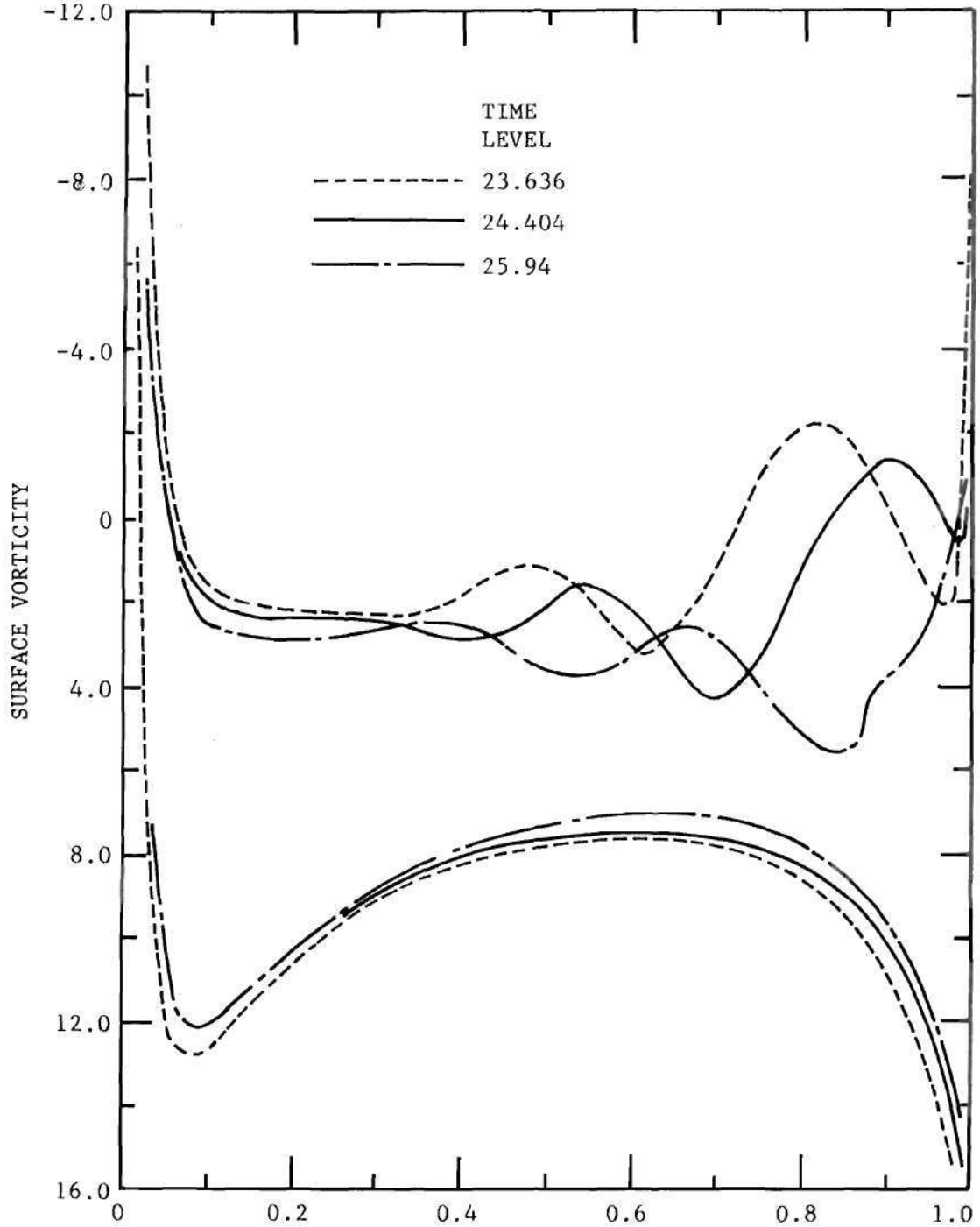

Figure 14. Surface Vorticity Distributions for
t = 23.636 to t = 25.94

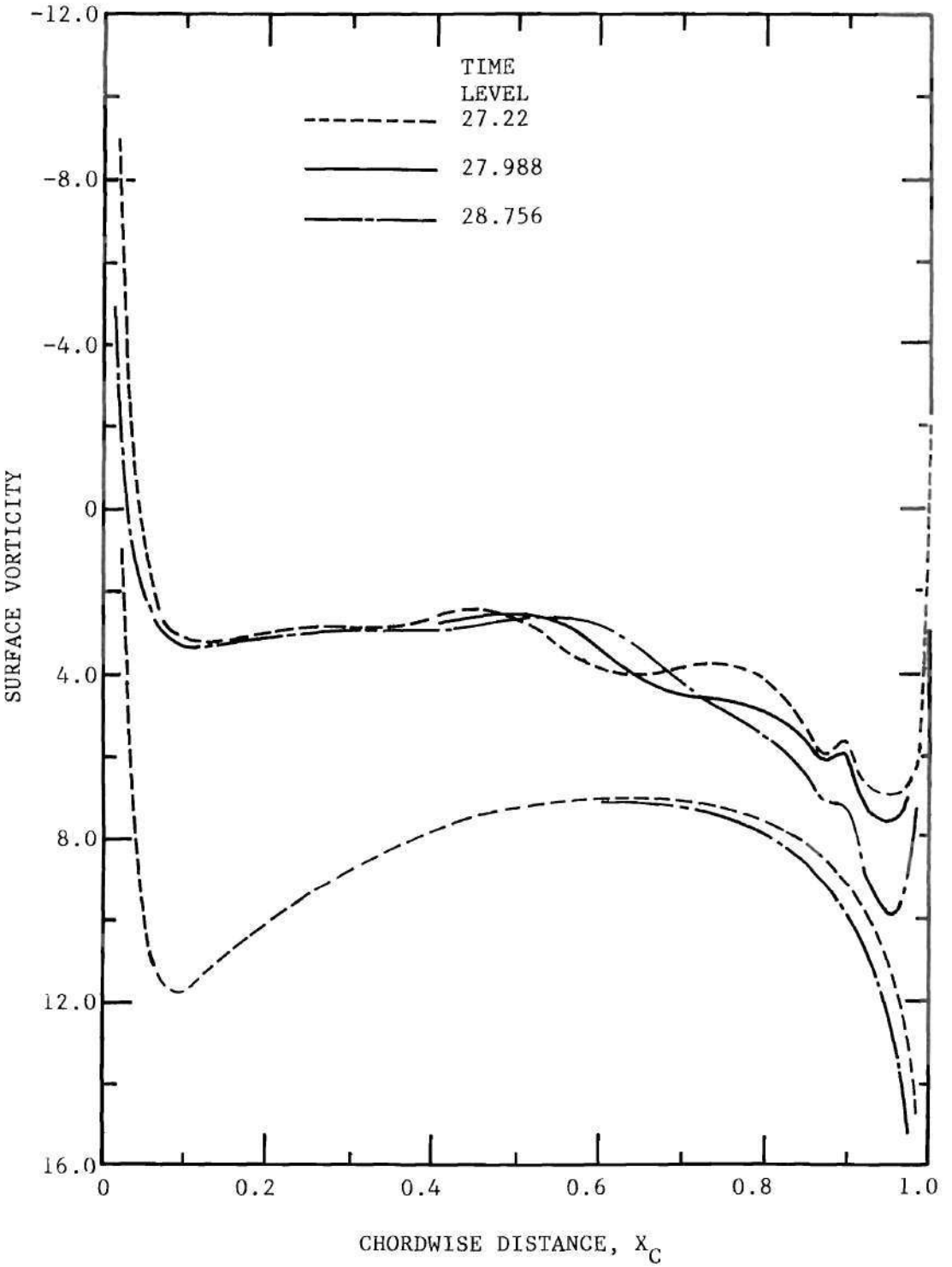

Figure 15, Surface Vorticity Distributions for
t = 27.22 to t = 28.756

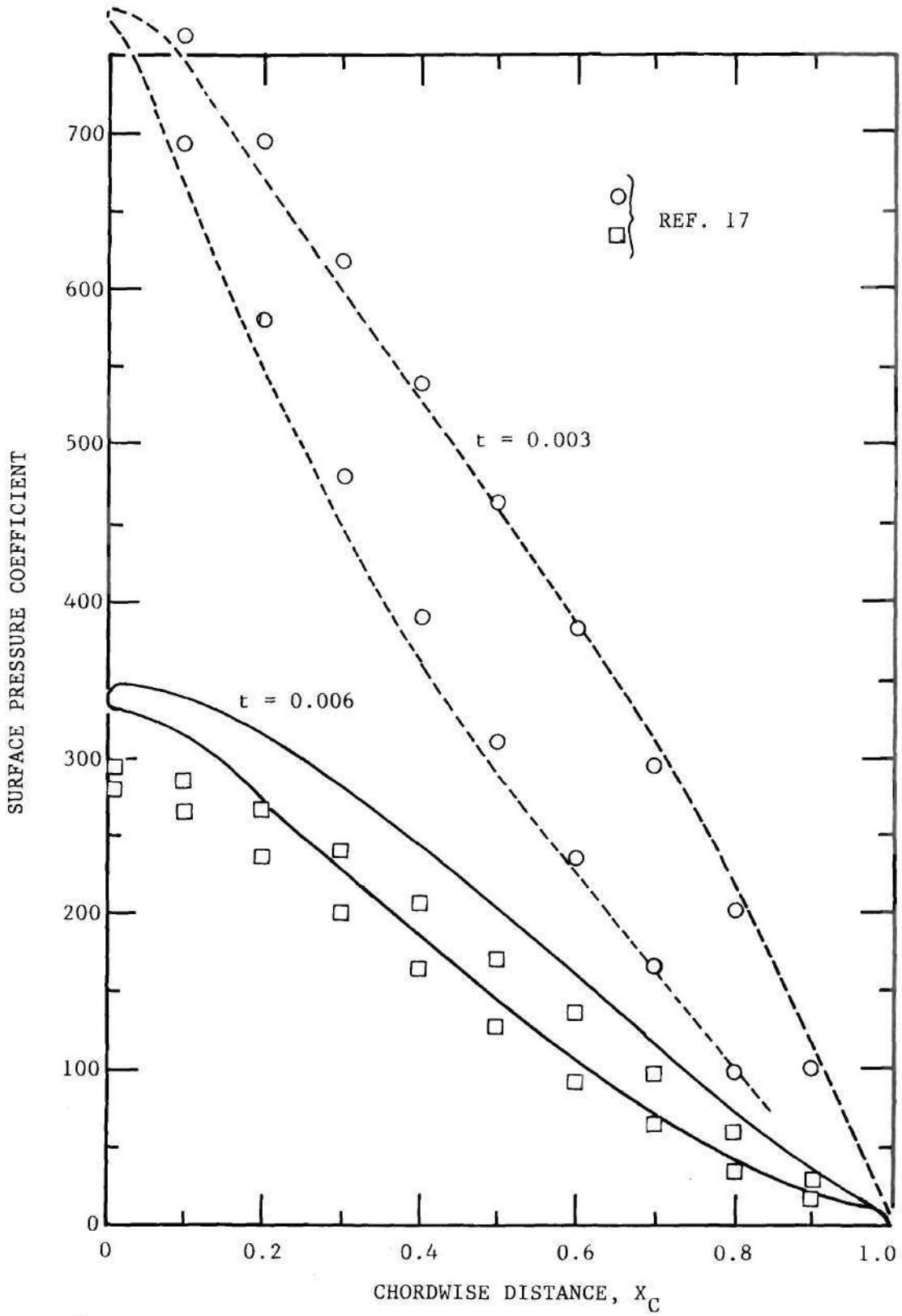

Figure 16. Surface Pressure Distributions for t = 0.003 and t = 0.006

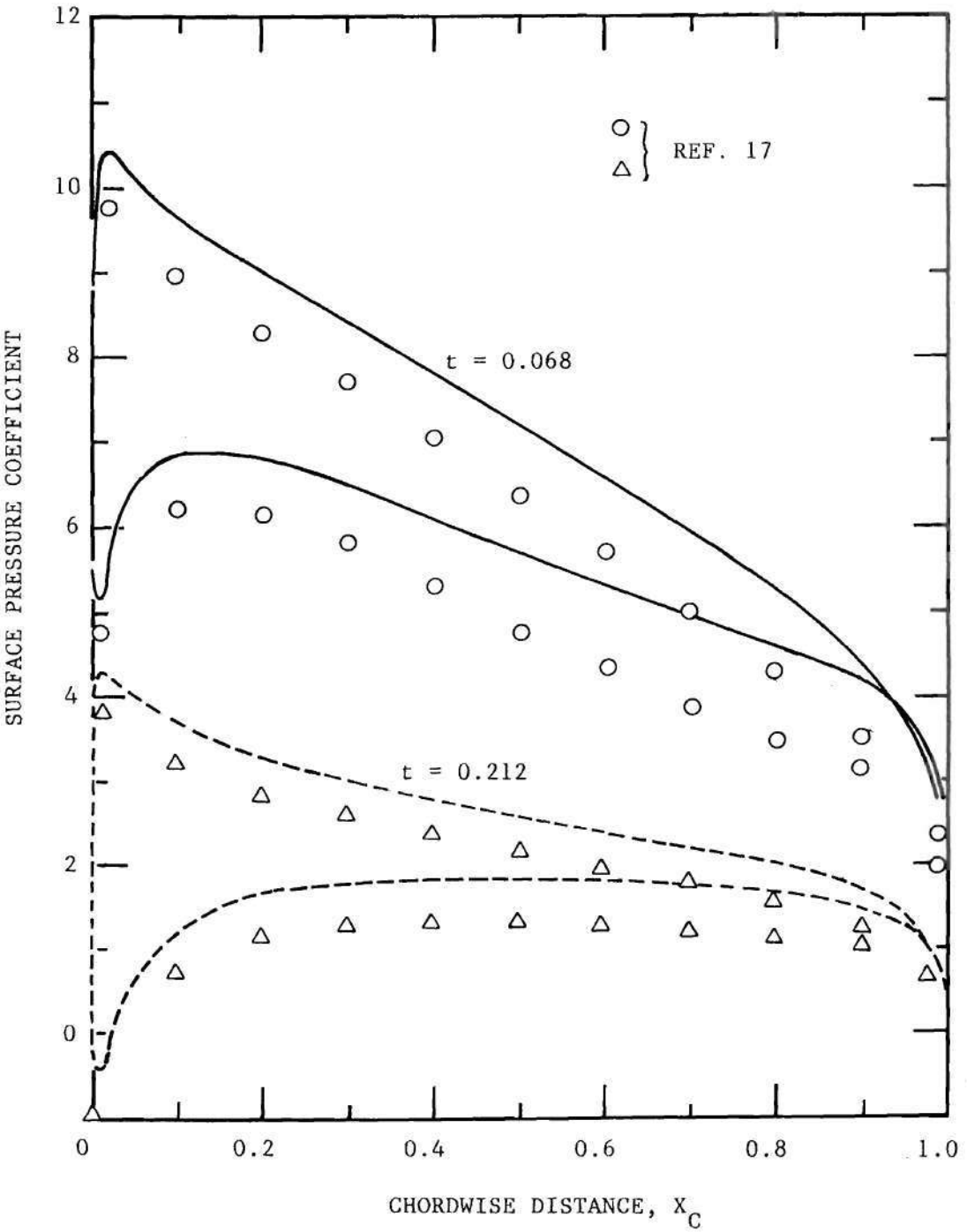

Figure 17. Surface Pressure Distributions for t = 0.068 and t = 0.212

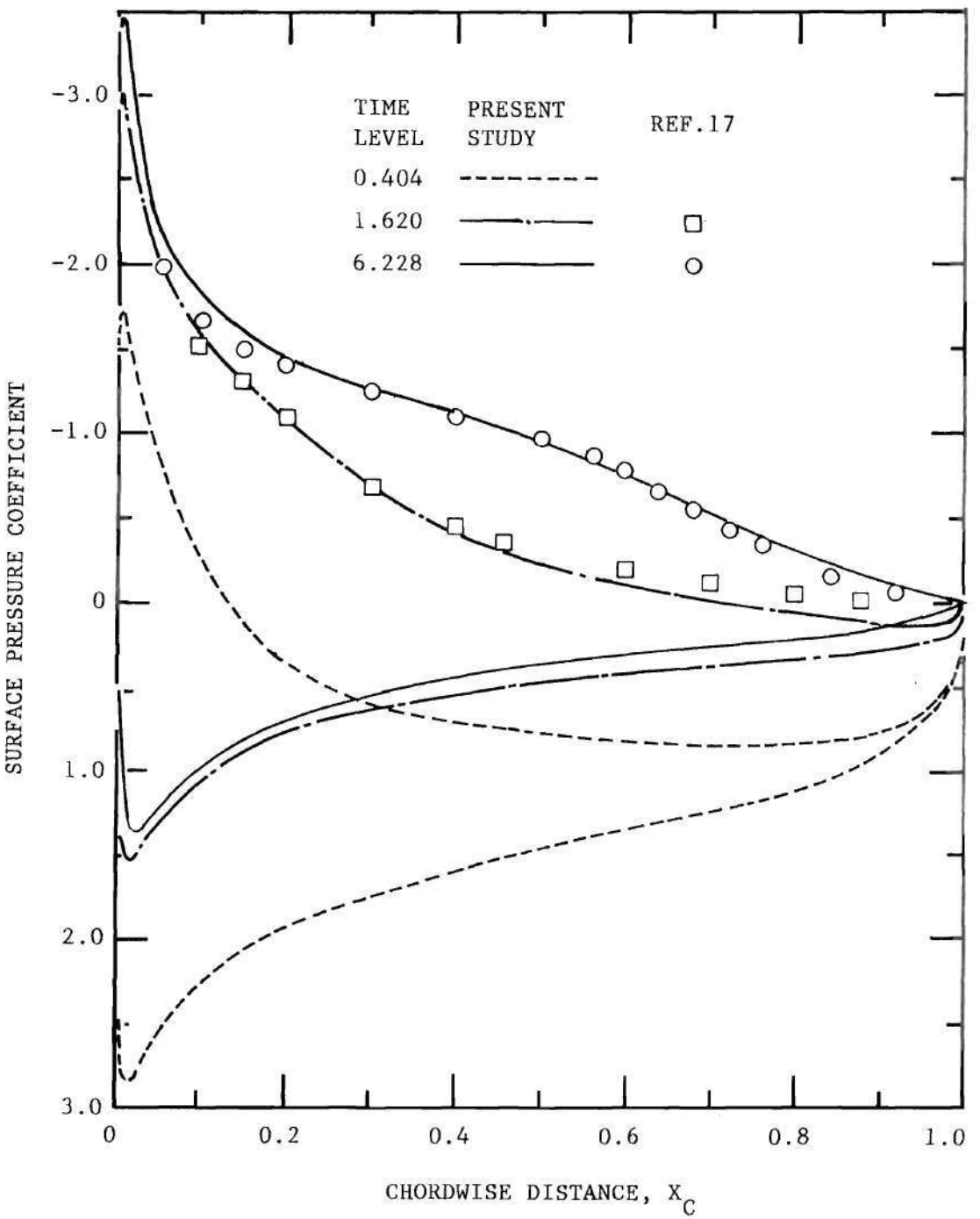

Figure 18. Surface Pressure Distributions for t = 0.404 to t = 6.228

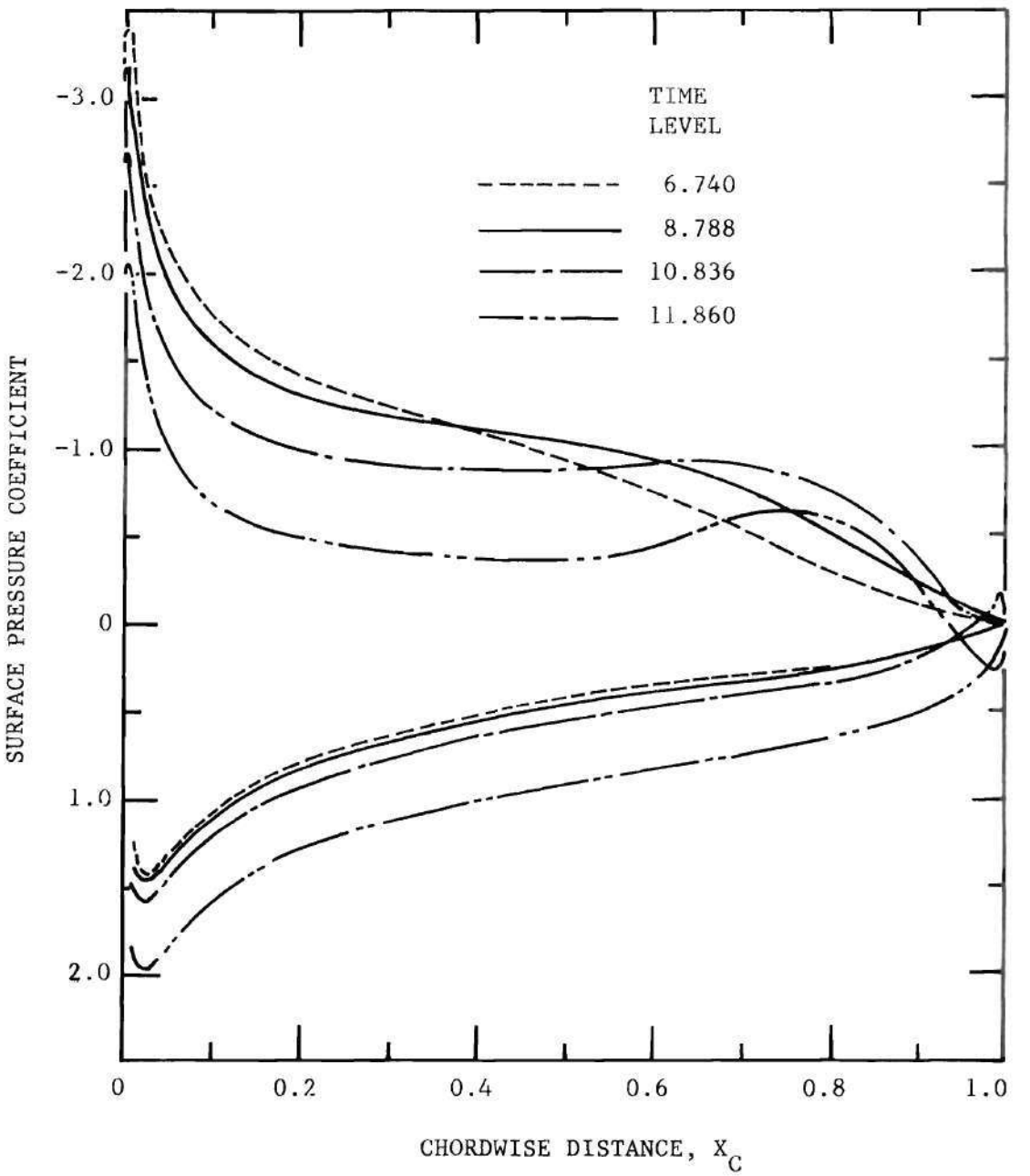

Figure 19. Surface Pressure Distributions for t = 6.74 to t = 11.86

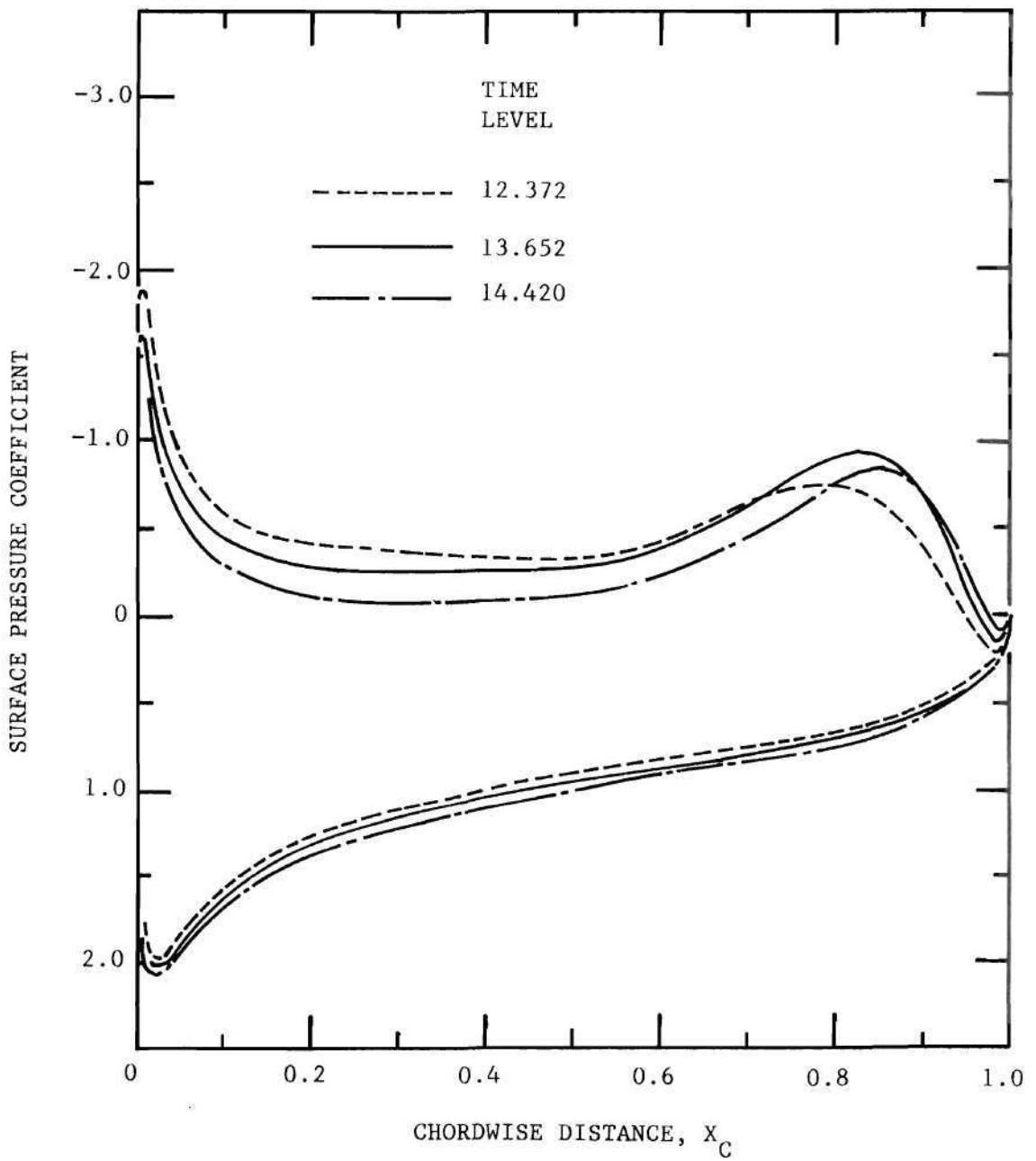

Figure 20. Surface Pressure Distributions for t = 12.372 to t = 14.42

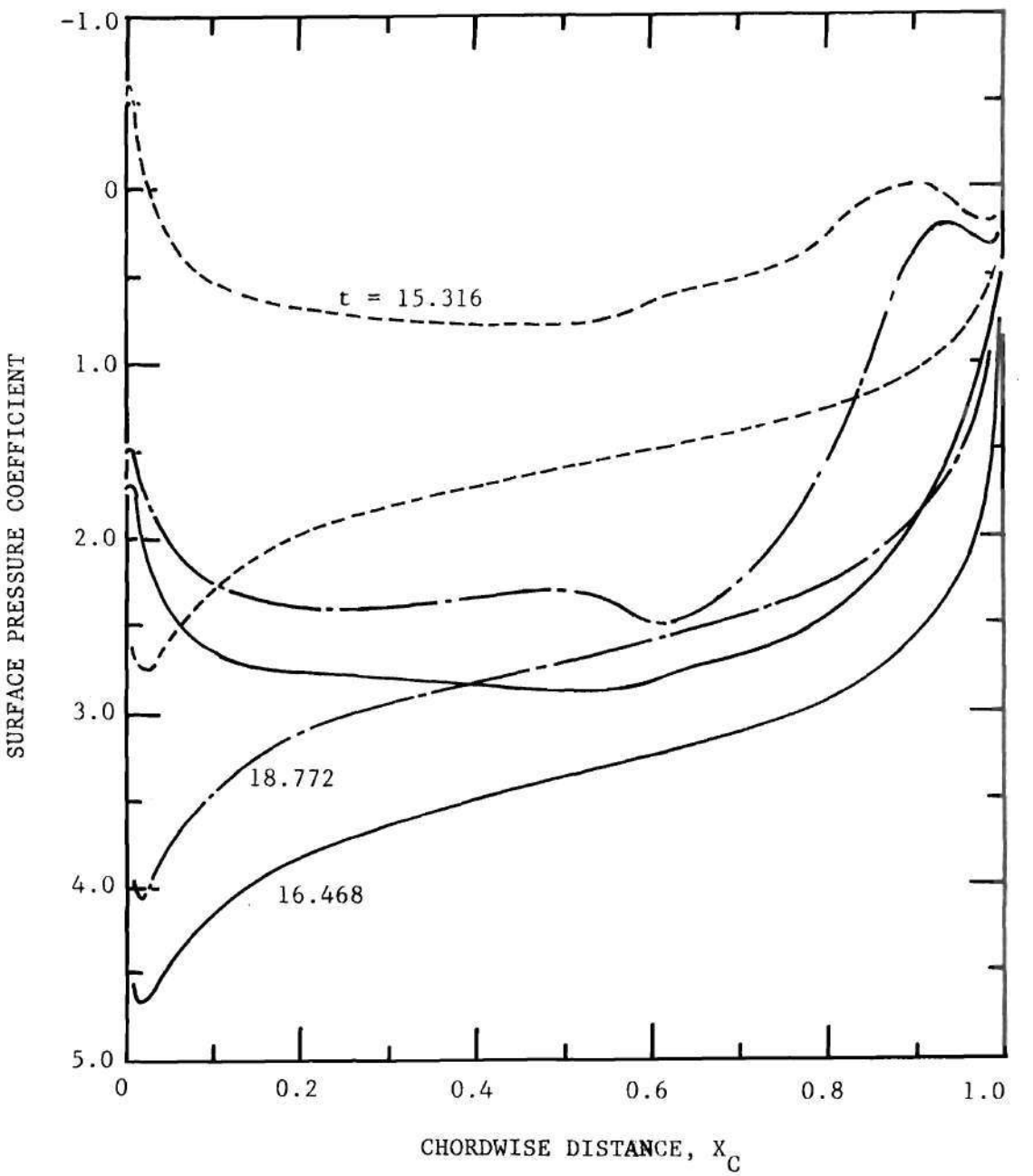

Figure 21. Surface Pressure Distributions for t = 15.316 to t = 18.772

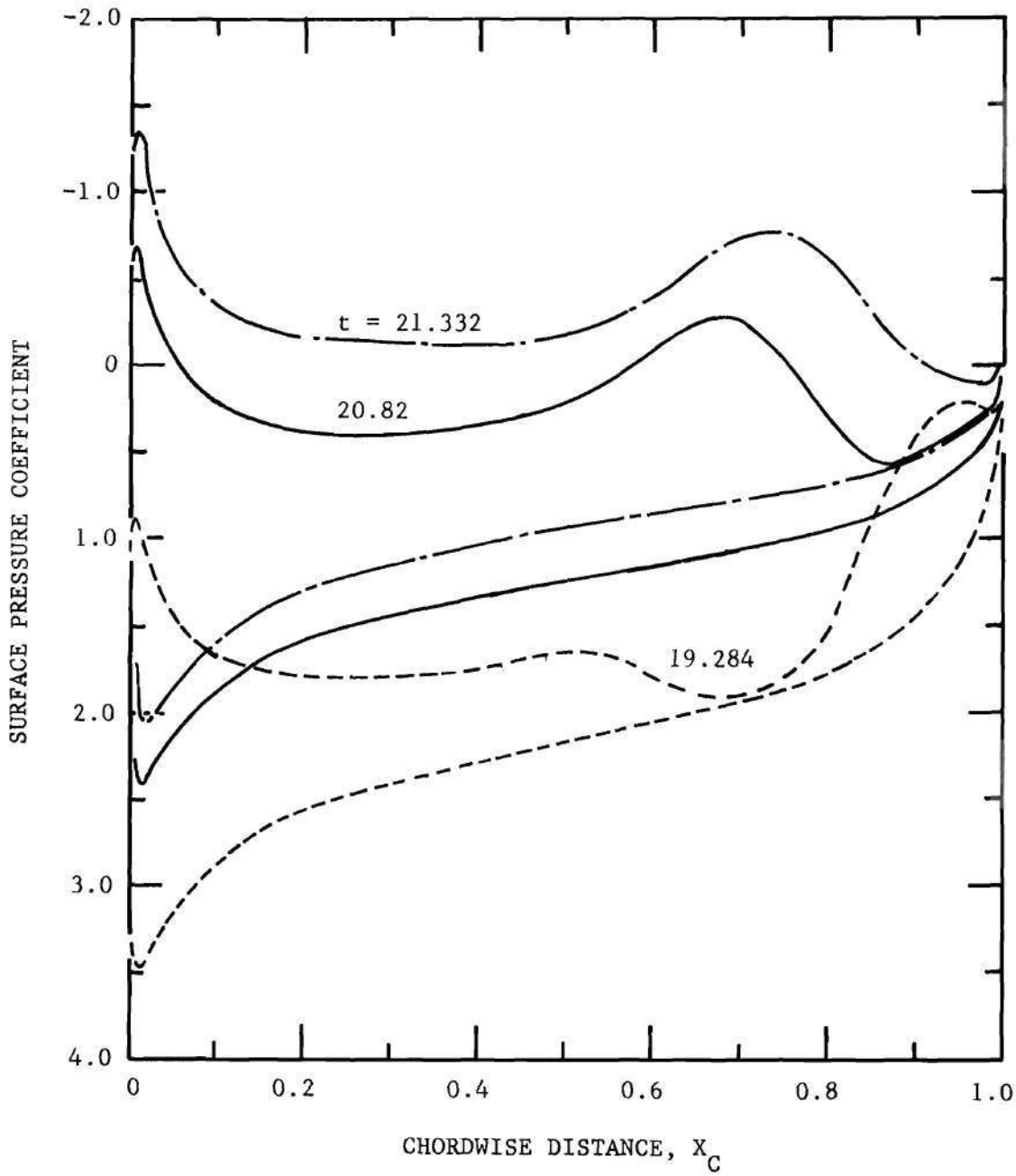

Figure 22. Surface Pressure Distributions for t = 19.284 to t = 21.332

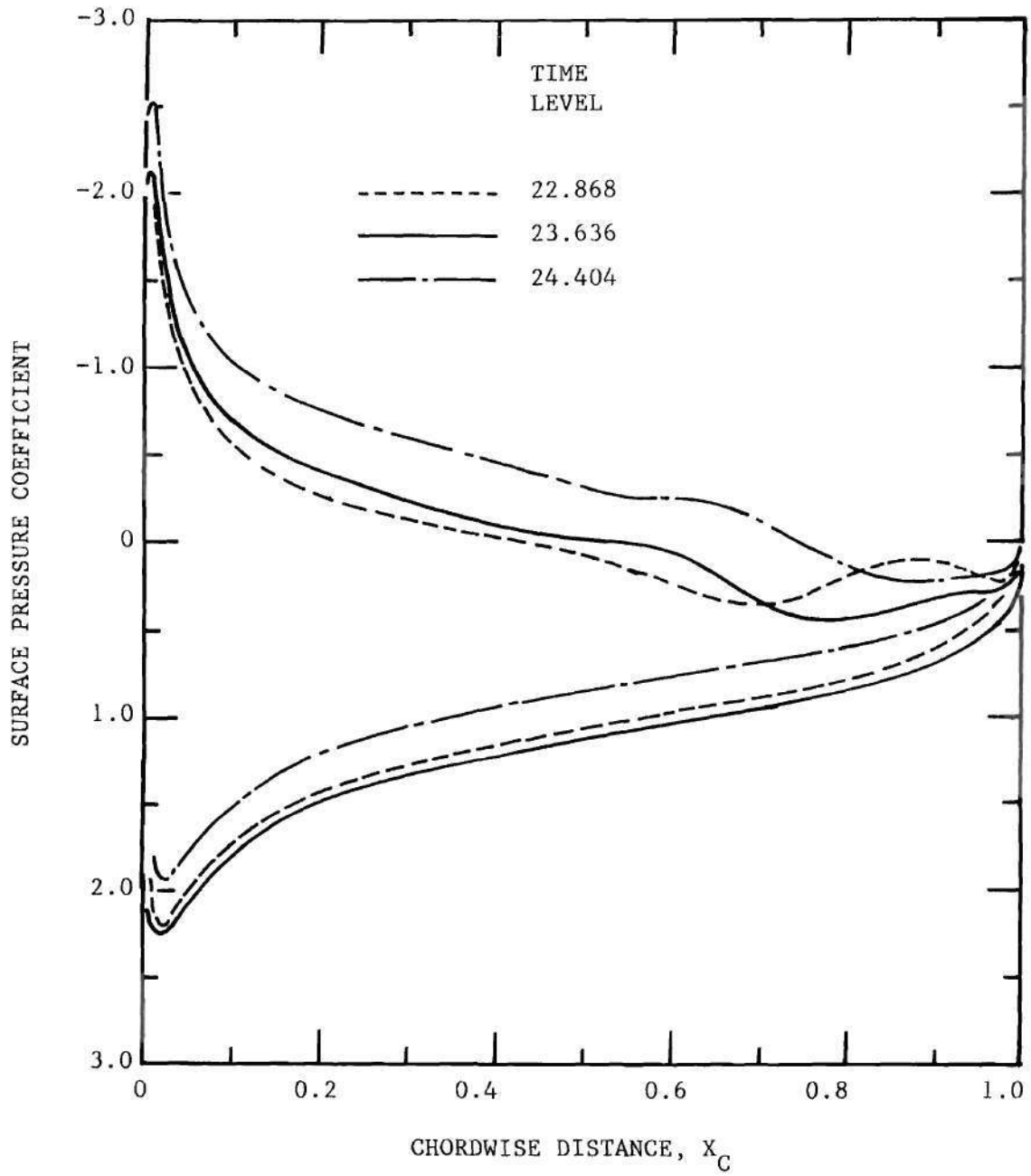

Figure 23. Surface Pressure Distributions for t = 22.868 to t = 24.404

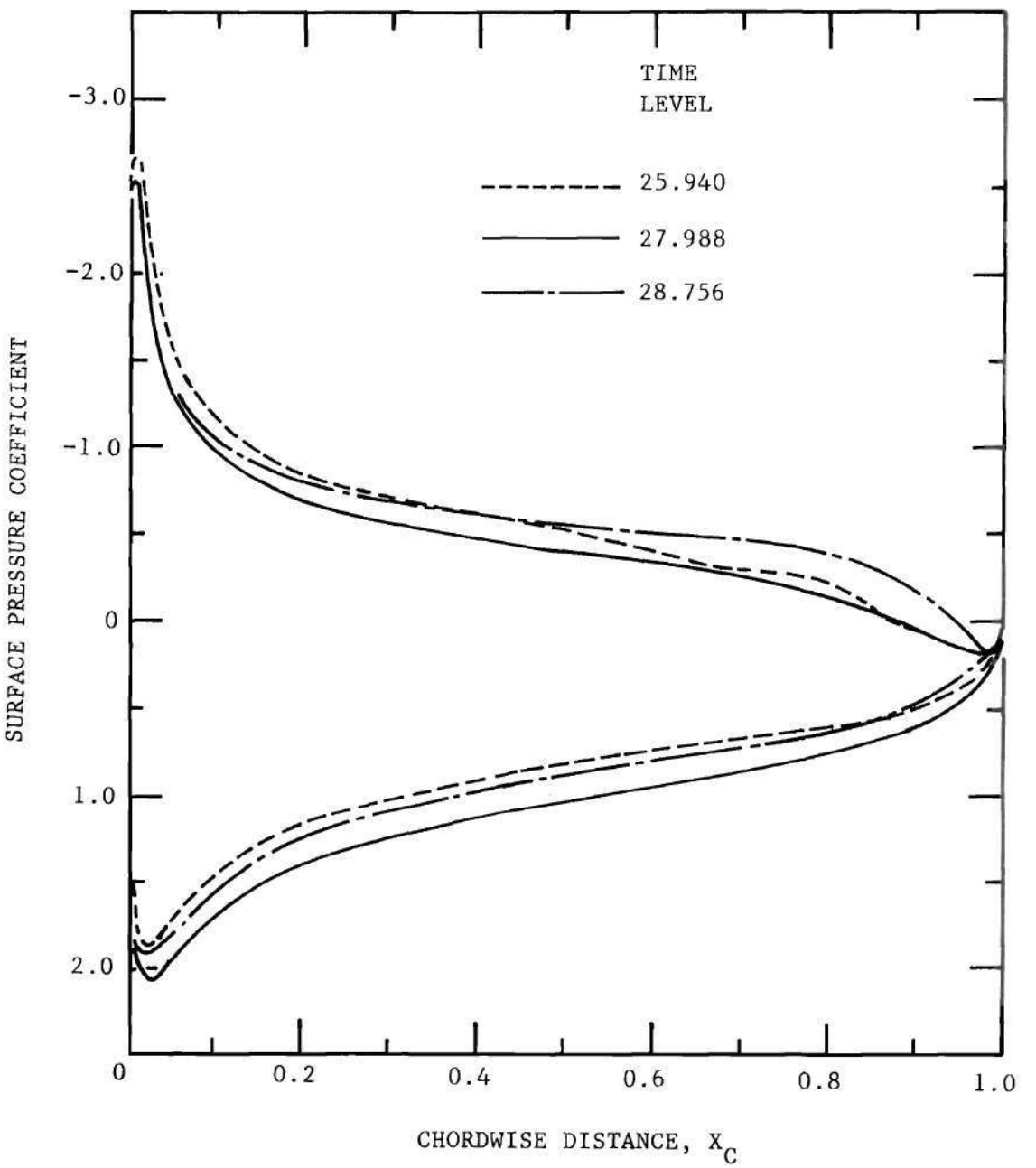

Figure 24. Surface Pressure Distributions for t = 25.940 to t = 28.756

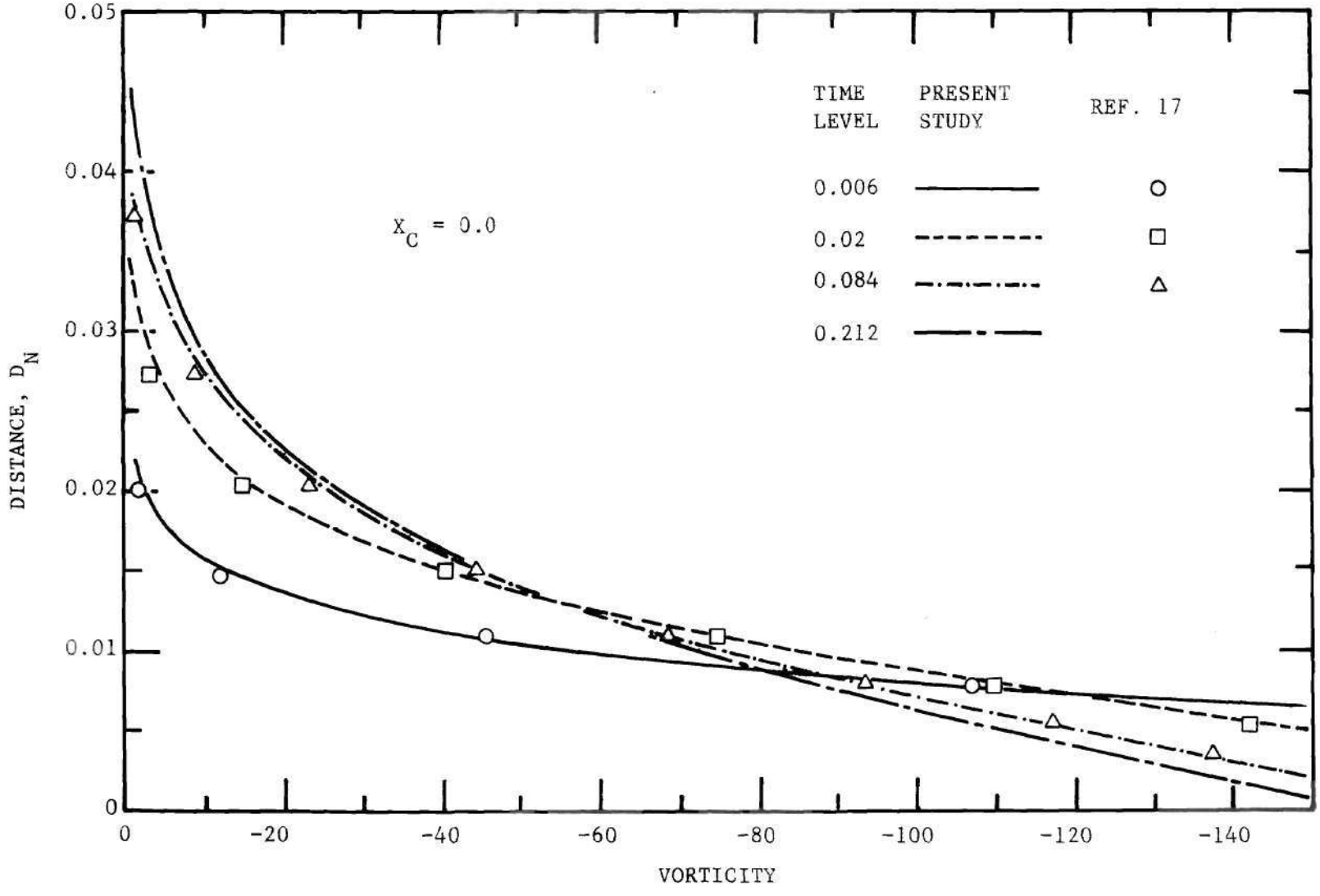

Figure 25. Vorticity Profiles at X_C = 0.0 for t = 0.006 to t = 0.212

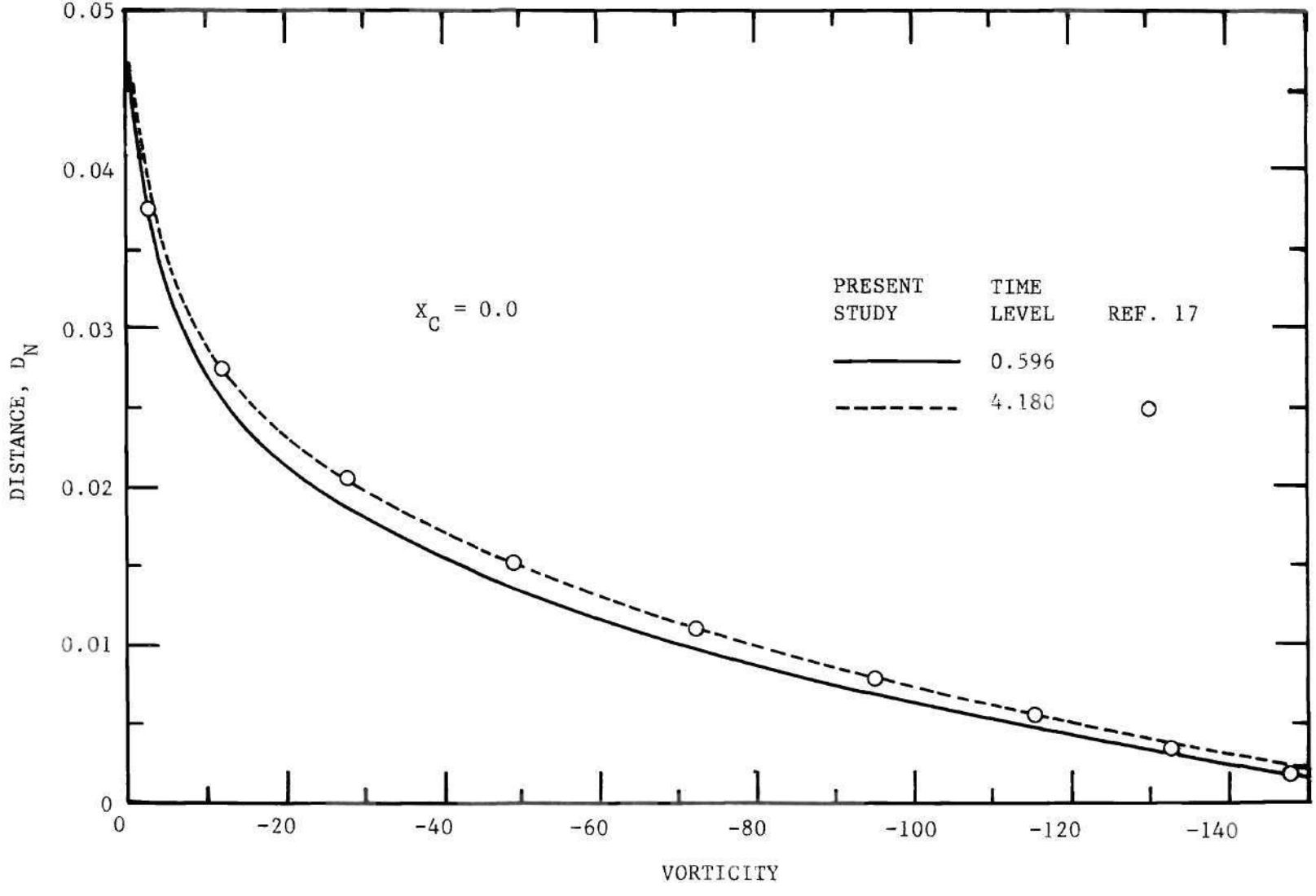

Figure 26. Vorticity Profiles at X_C = 0.0 for t = 0.596 and t = 4.180

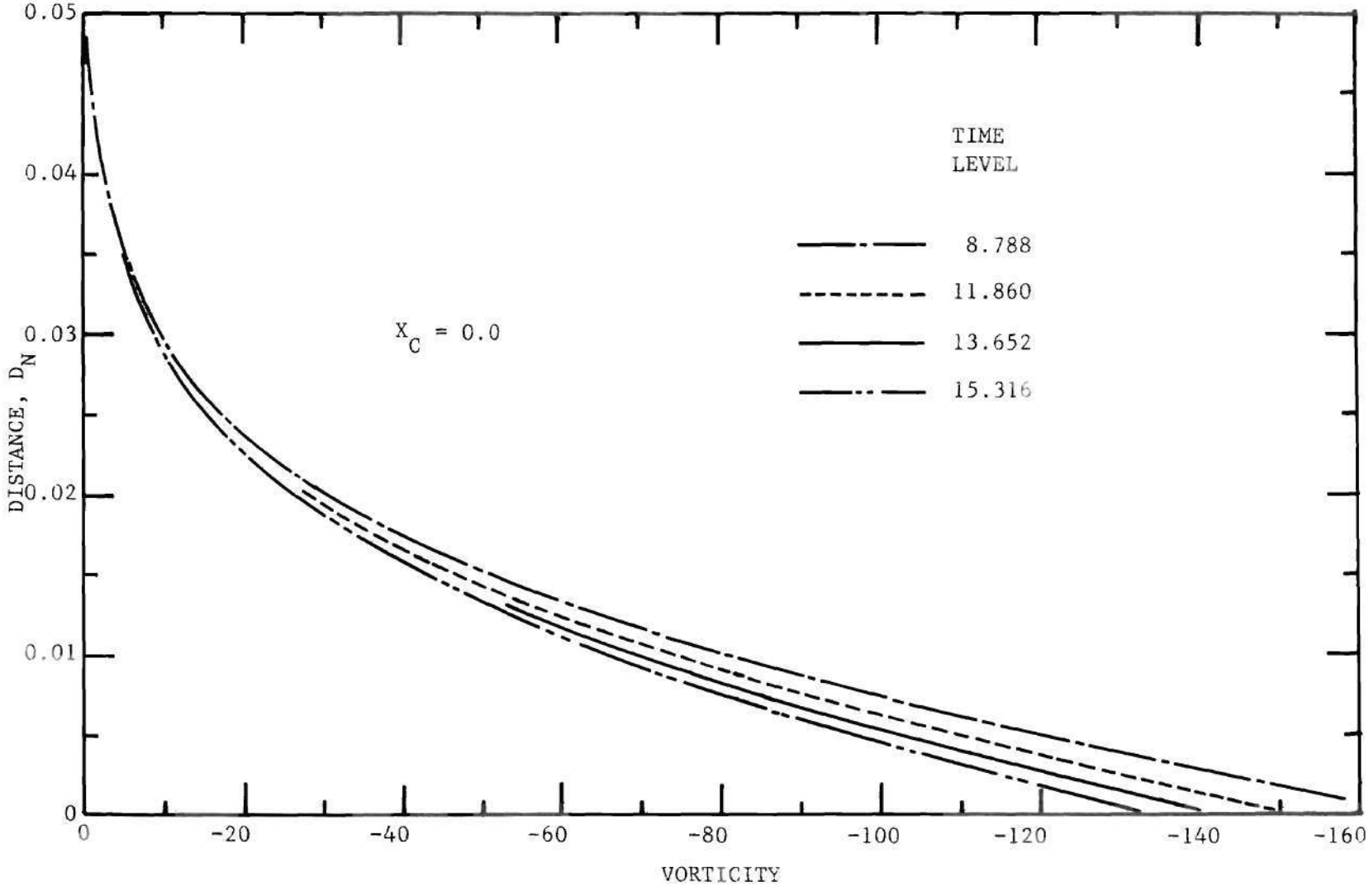

Figure 27. Vorticity Profiles at X_C = 0.0 for t = 8.788 to t = 15.316

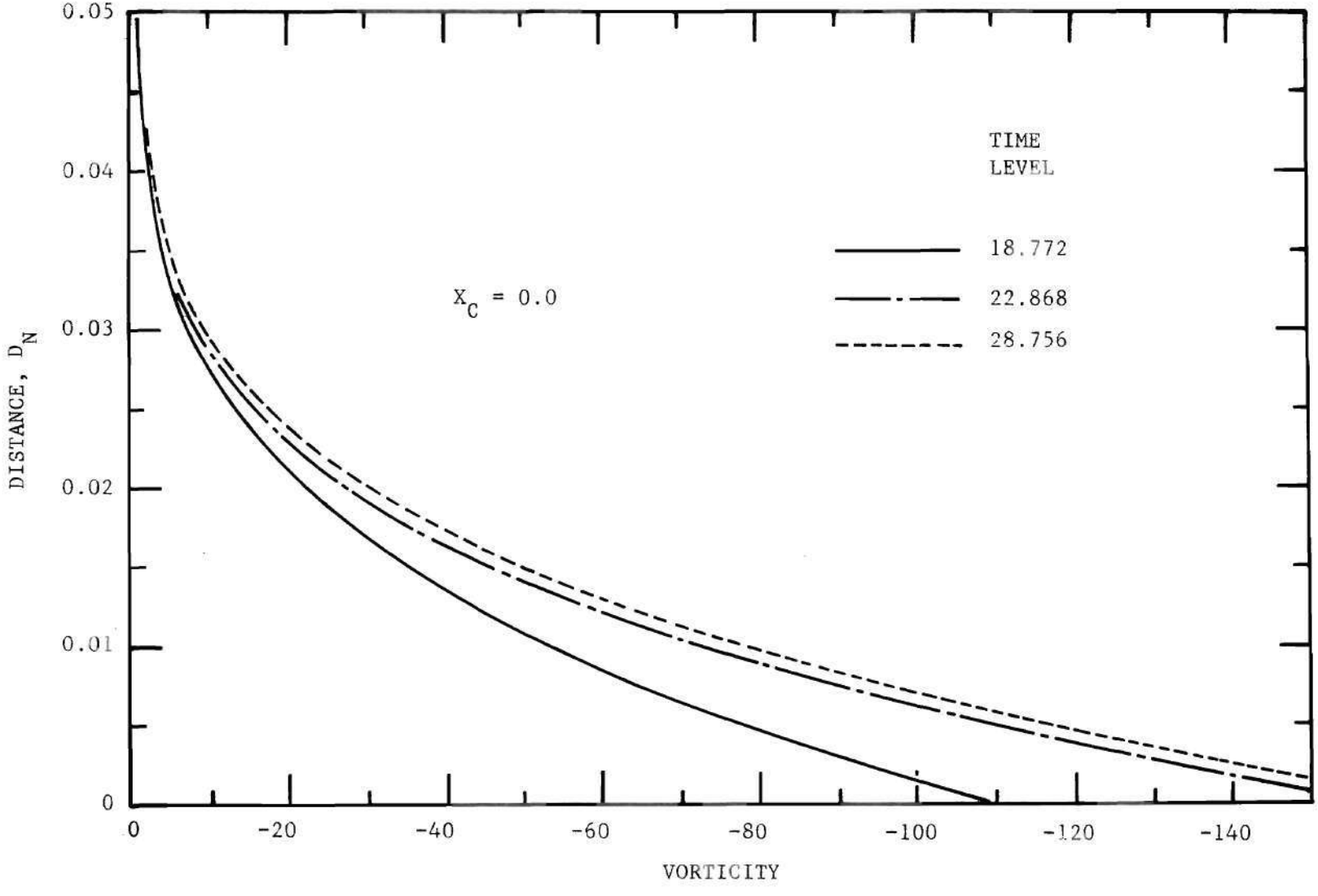

Figure 28. Vorticity Profiles at X_C = 0.0 for t = 18.772 to t = 28.756

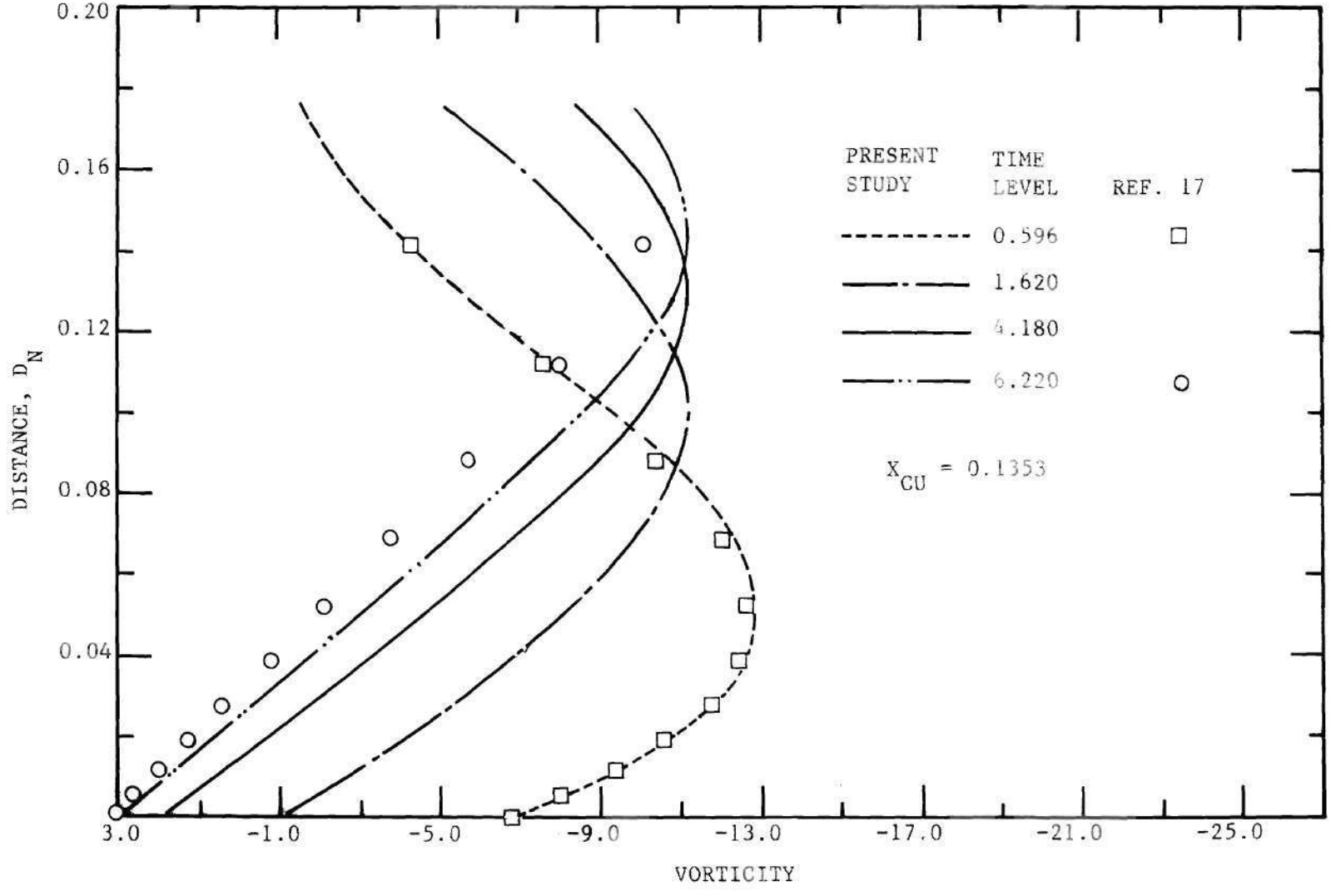

Figure 29. Vorticity Profiles at X_{CU} = 0.1353 for t = 0.596 to t = 6.220

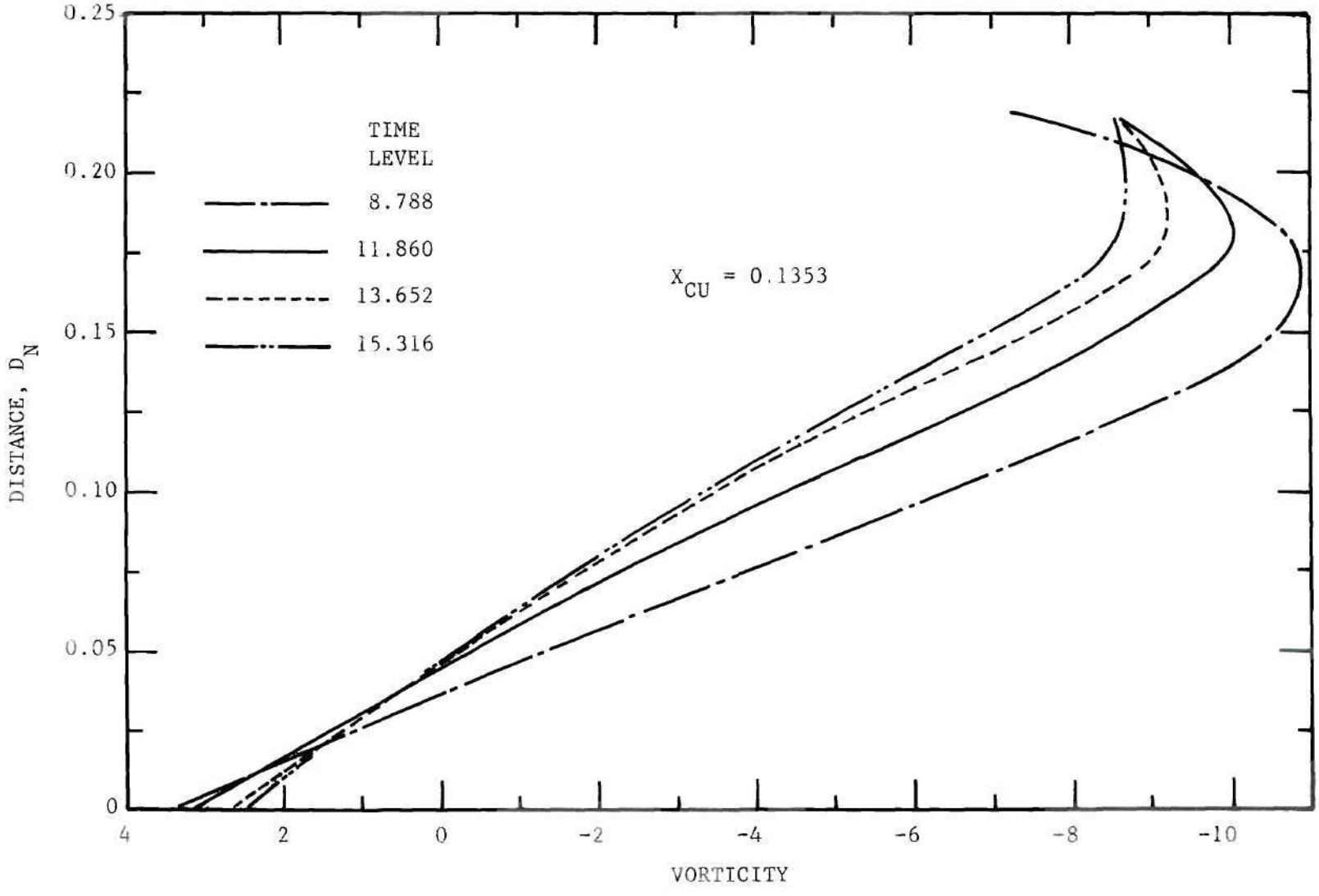

Figure 30. Vorticity Profiles at X_{CU} = 0.1353 for t = 8.788 to t = 15.316

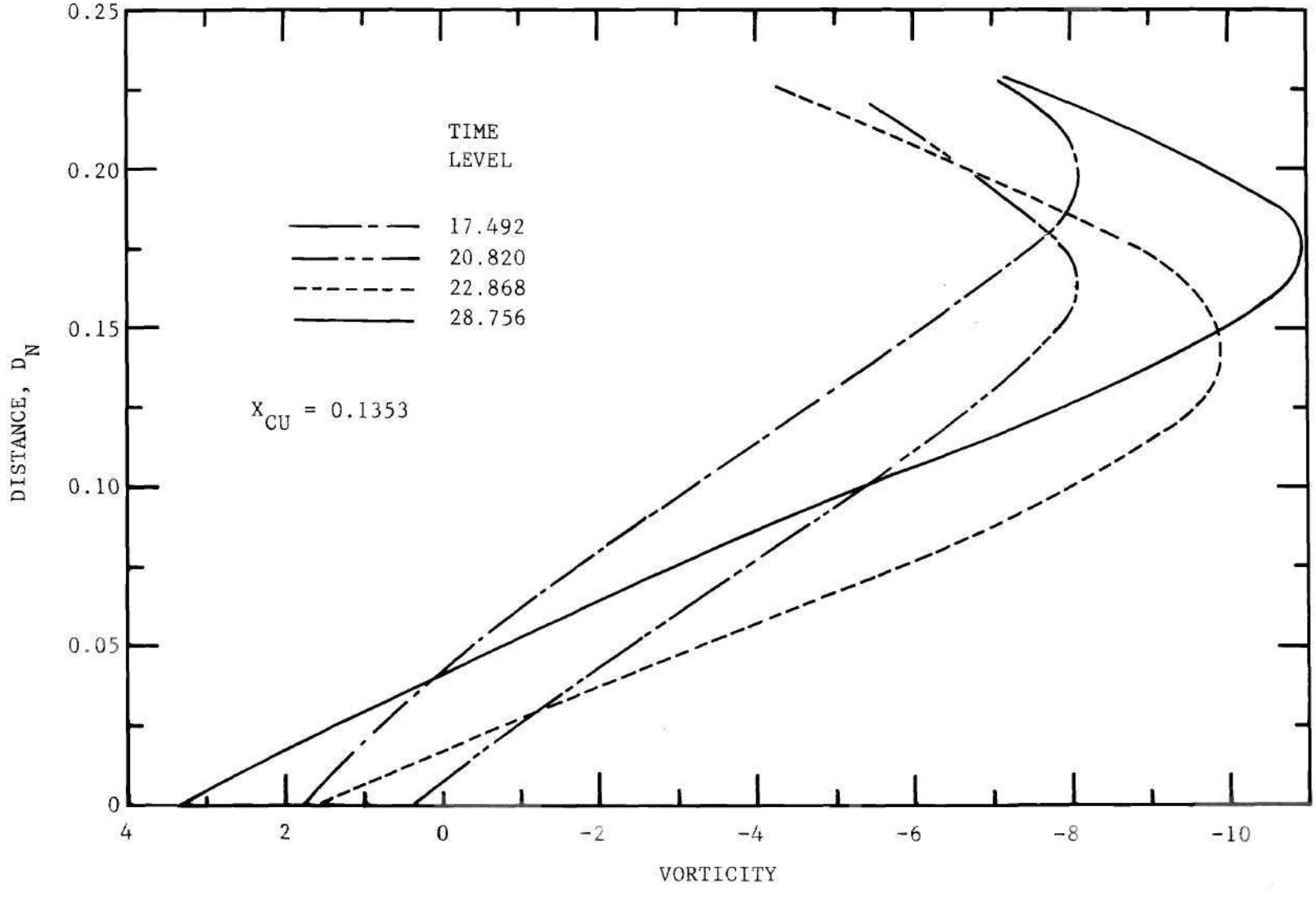

Figure 31. Vorticity Profiles at X_{CU} = 0.1353 for t = 17.492 to t = 28.756

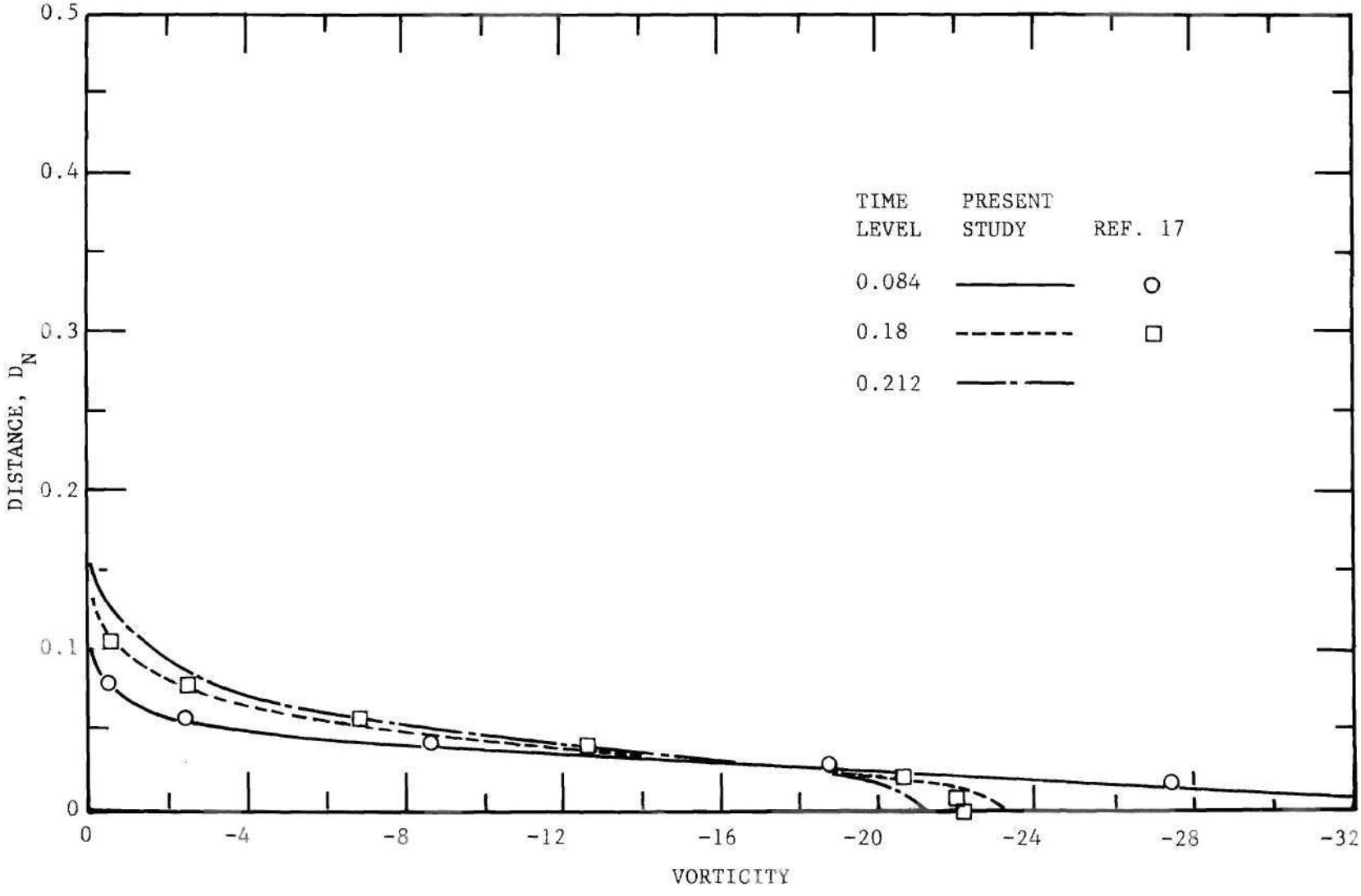

Figure 32. Vorticity Profiles at X_{CU} = 0.476 for t = 0.084 to t = 0.212

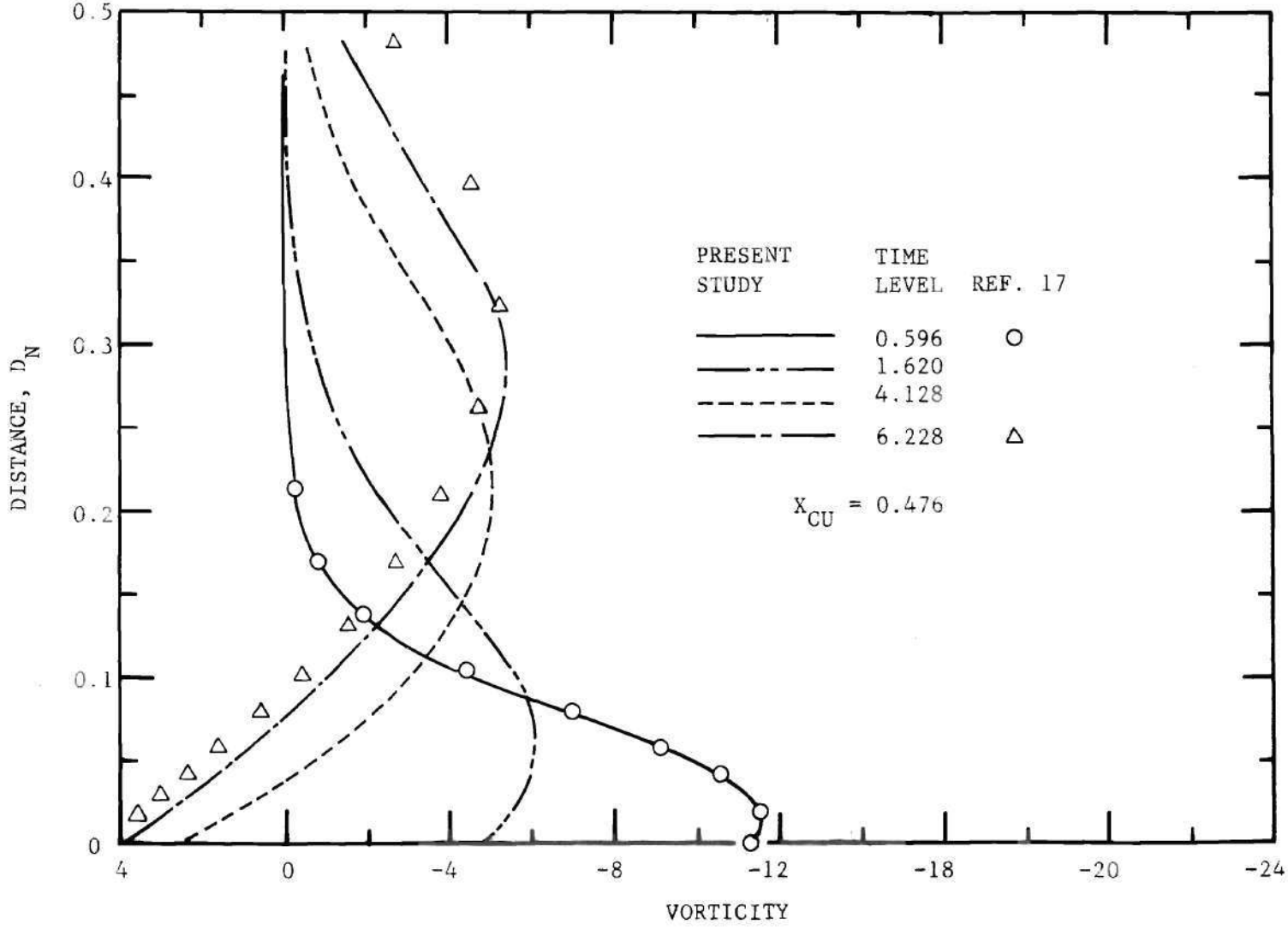

Figure 33. Vorticity Profiles at X_{CU} = 0.476 for t = 0.596 to t = 6.228

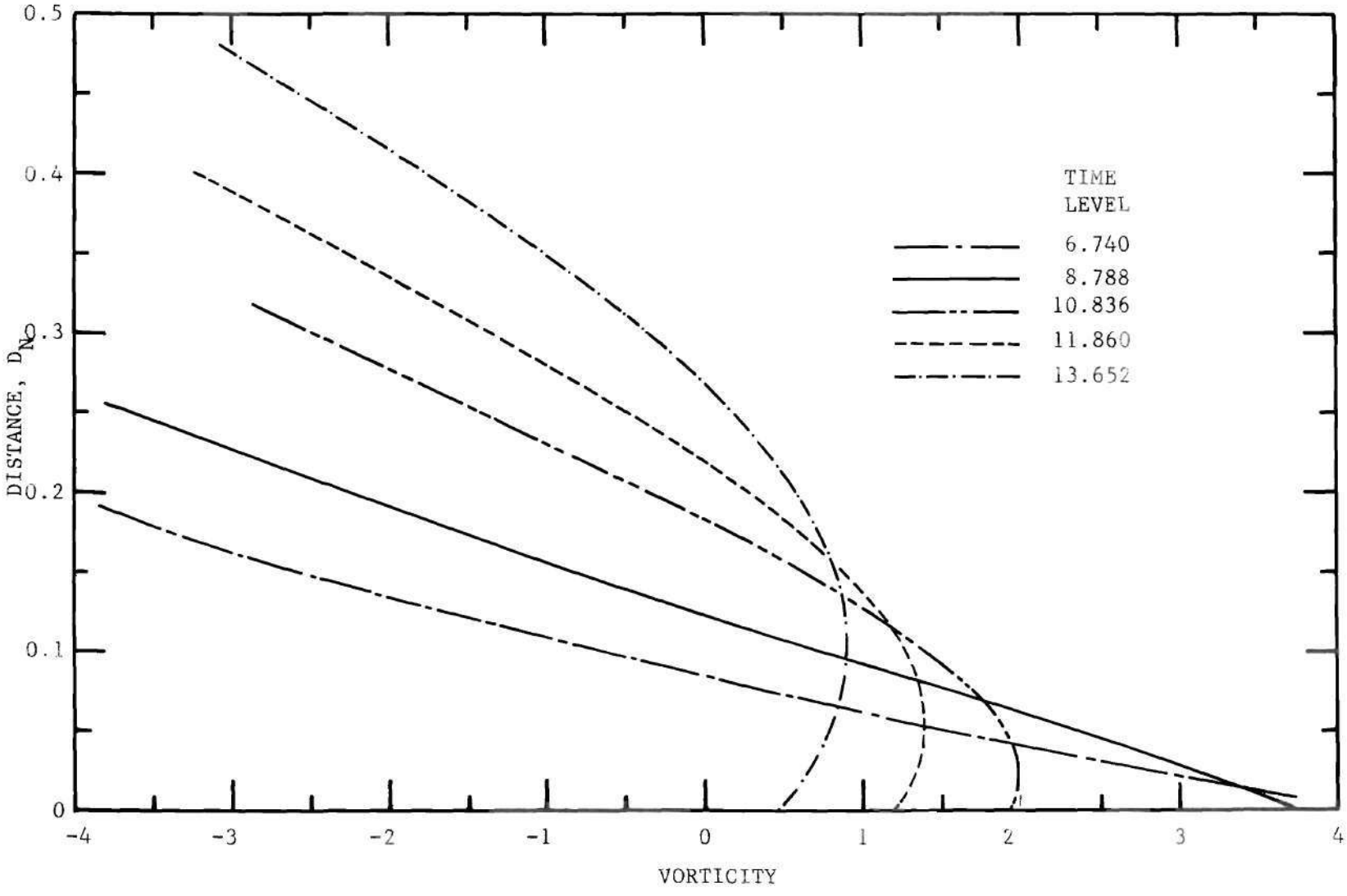

Figure 34. Vorticity Profiles at X_{CU} = 0.476 for t = 6.74 to t = 13.652

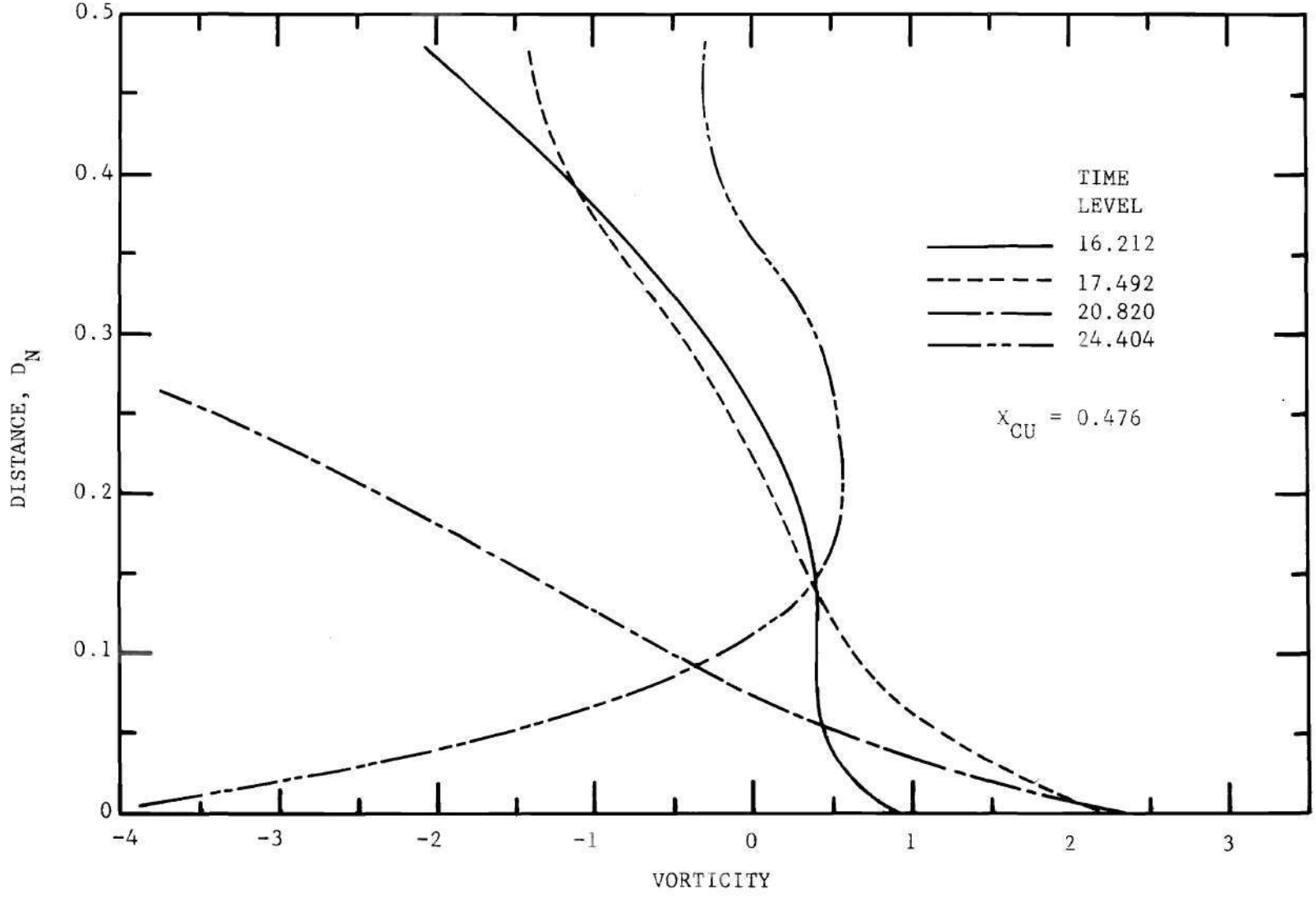

Figure 35. Vorticity Profiles at X_{CU} = 0.476 for t = 16.212 to t = 24.404

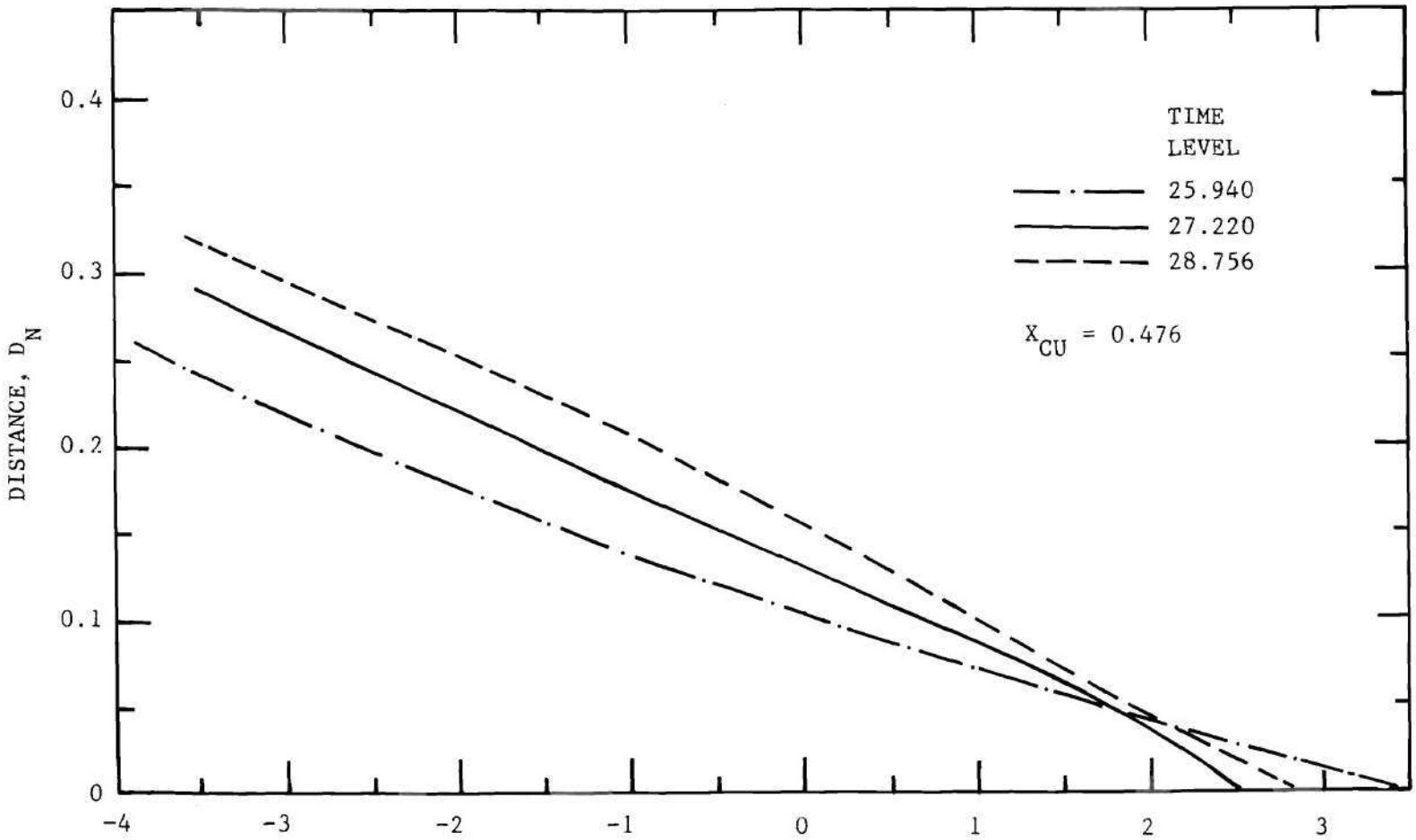

Figure 36. Vorticity Profiles at X_{CU} = 0.476 for t = 25.940 to t = 28.756

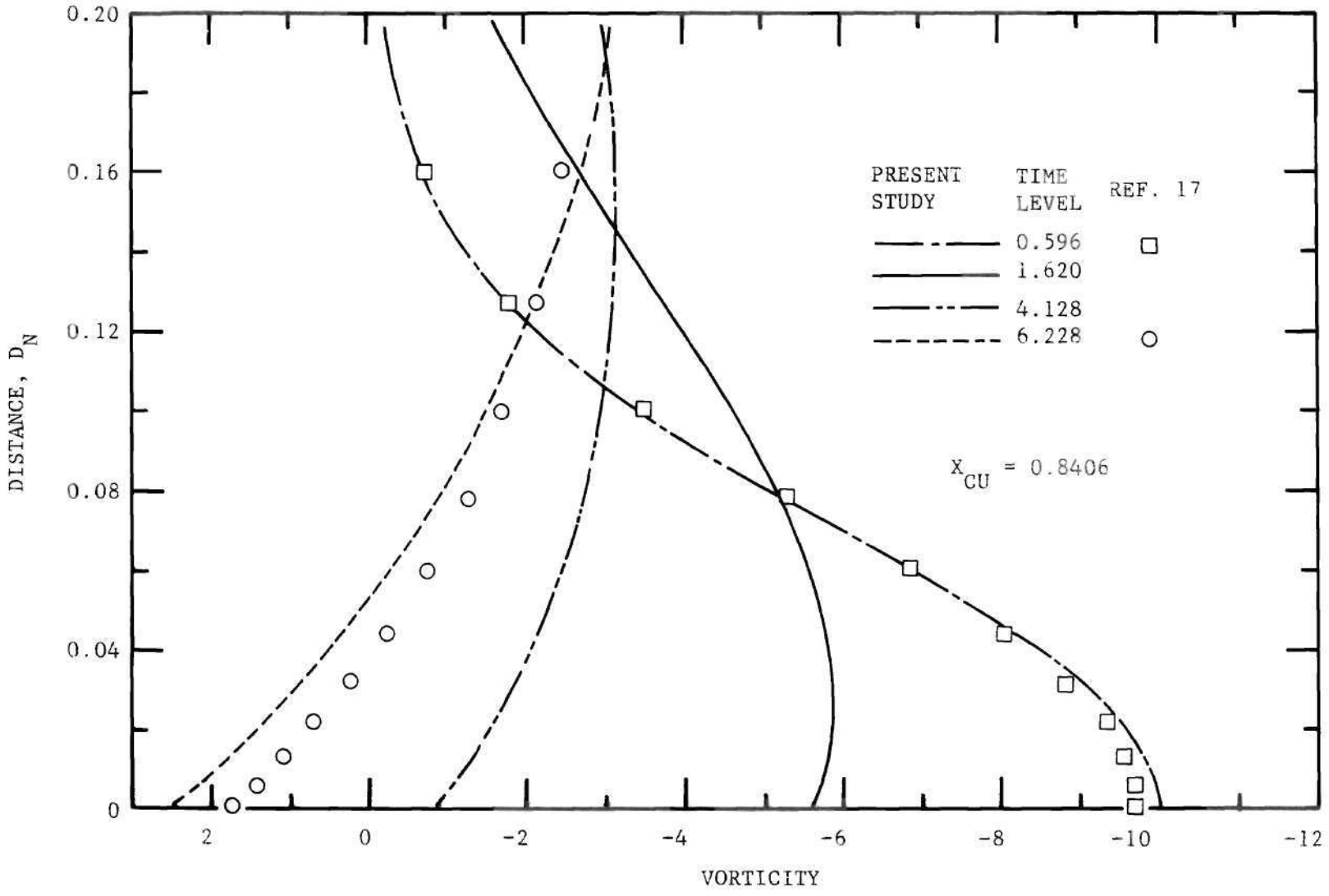

Figure 37. Vorticity Profiles at X_{CU} = 0.8406 for t = 0.596 to t = 6.228

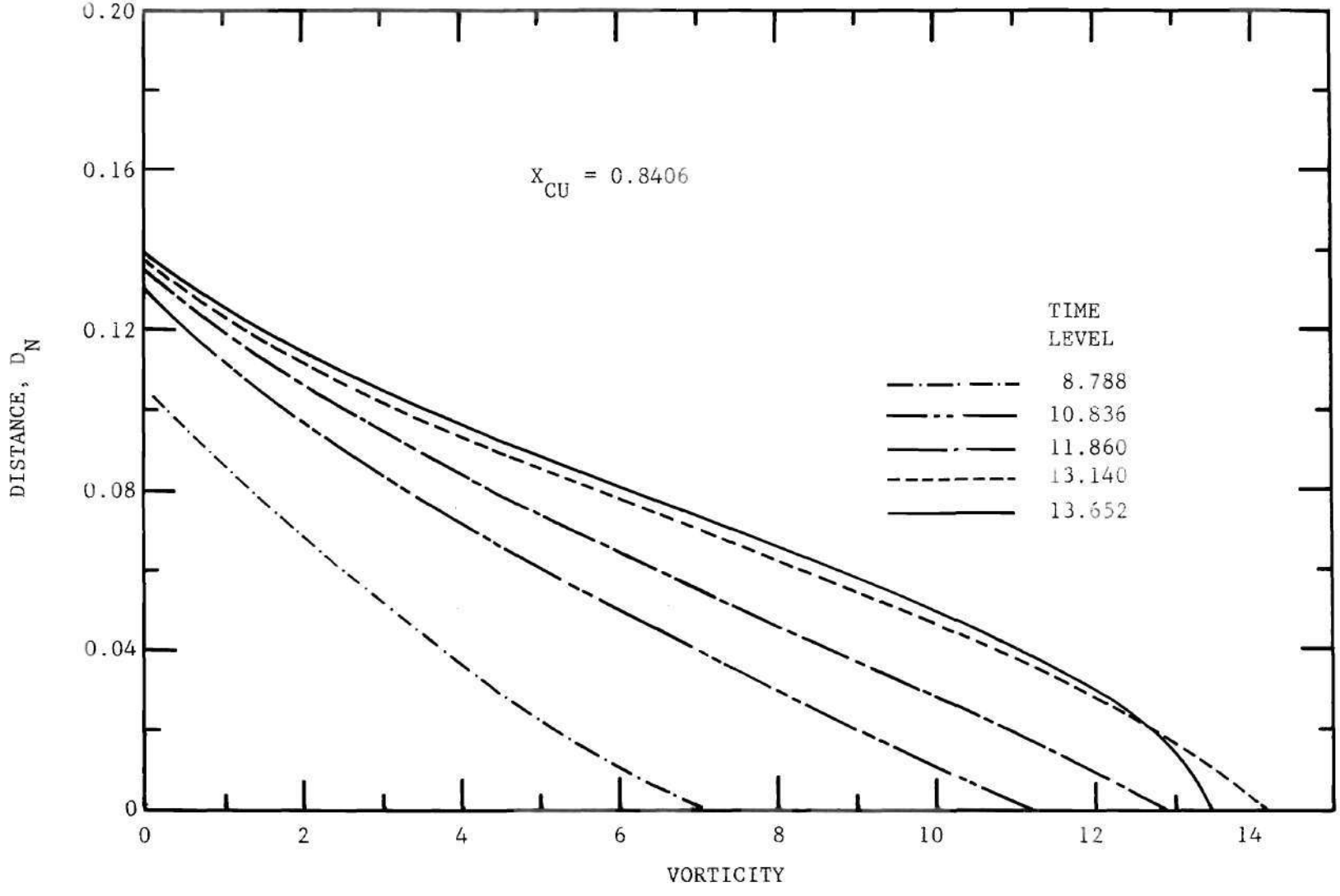

Figure 38. Vorticity Profiles at X_{CU} = 0.8406 for t = 8.788 to t = 13.652

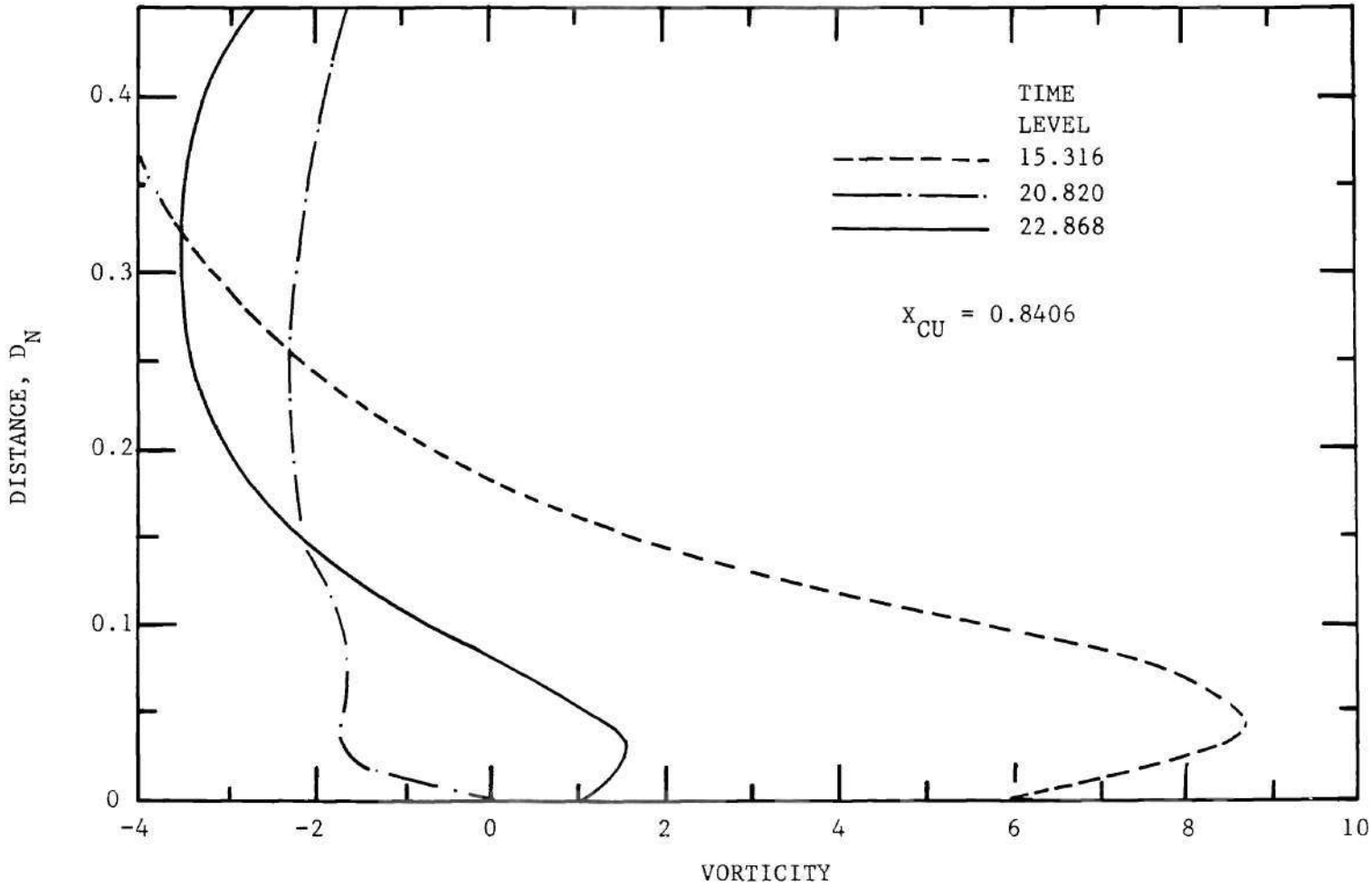

Figure 39. Vorticity Profiles at X_{CU} = 0.8406 for t = 15.316 to t = 22.868

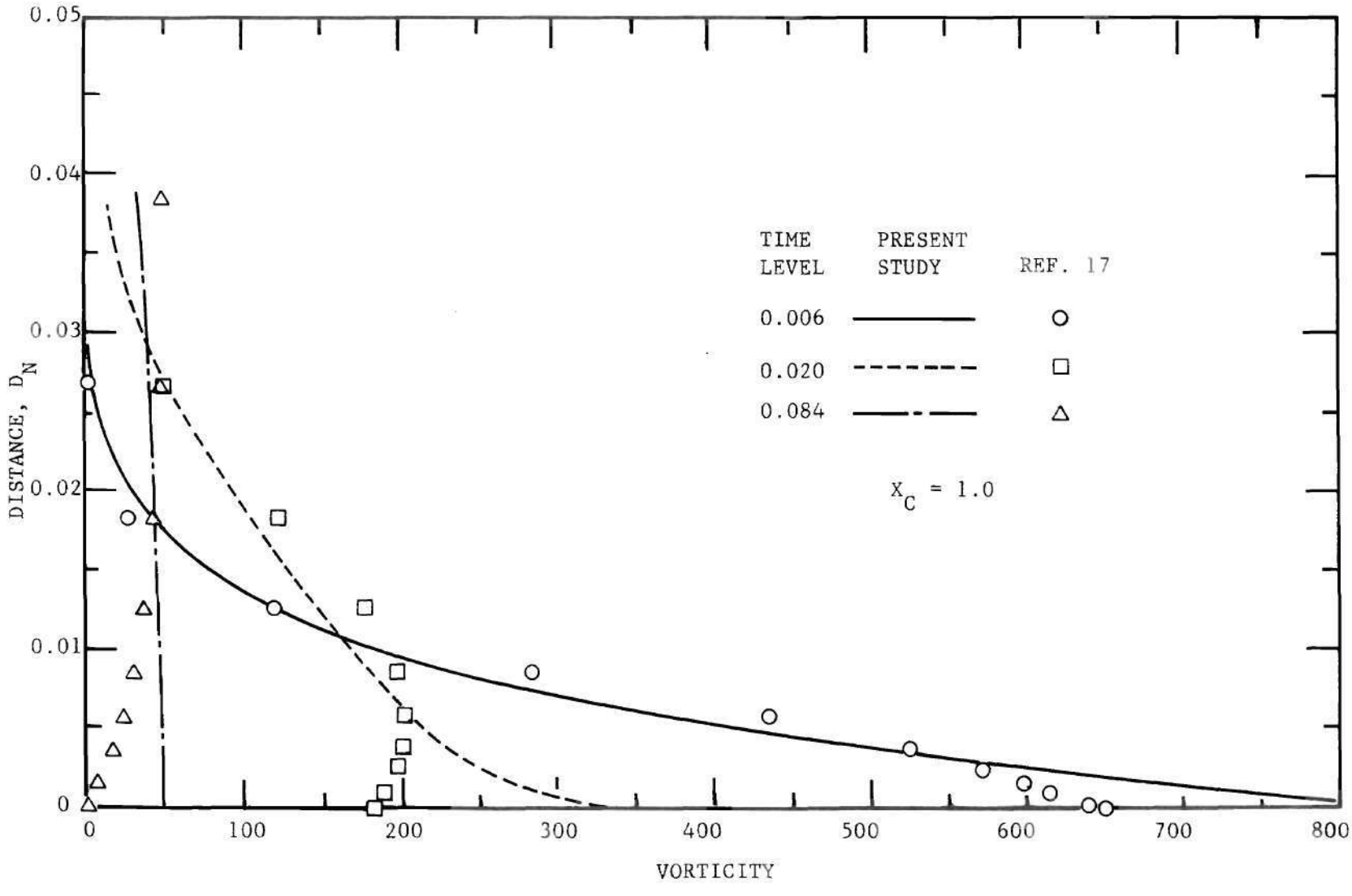

Figure 40. Vorticity Profiles at X_C = 1.0 for t = 0.006 to t = 0.084

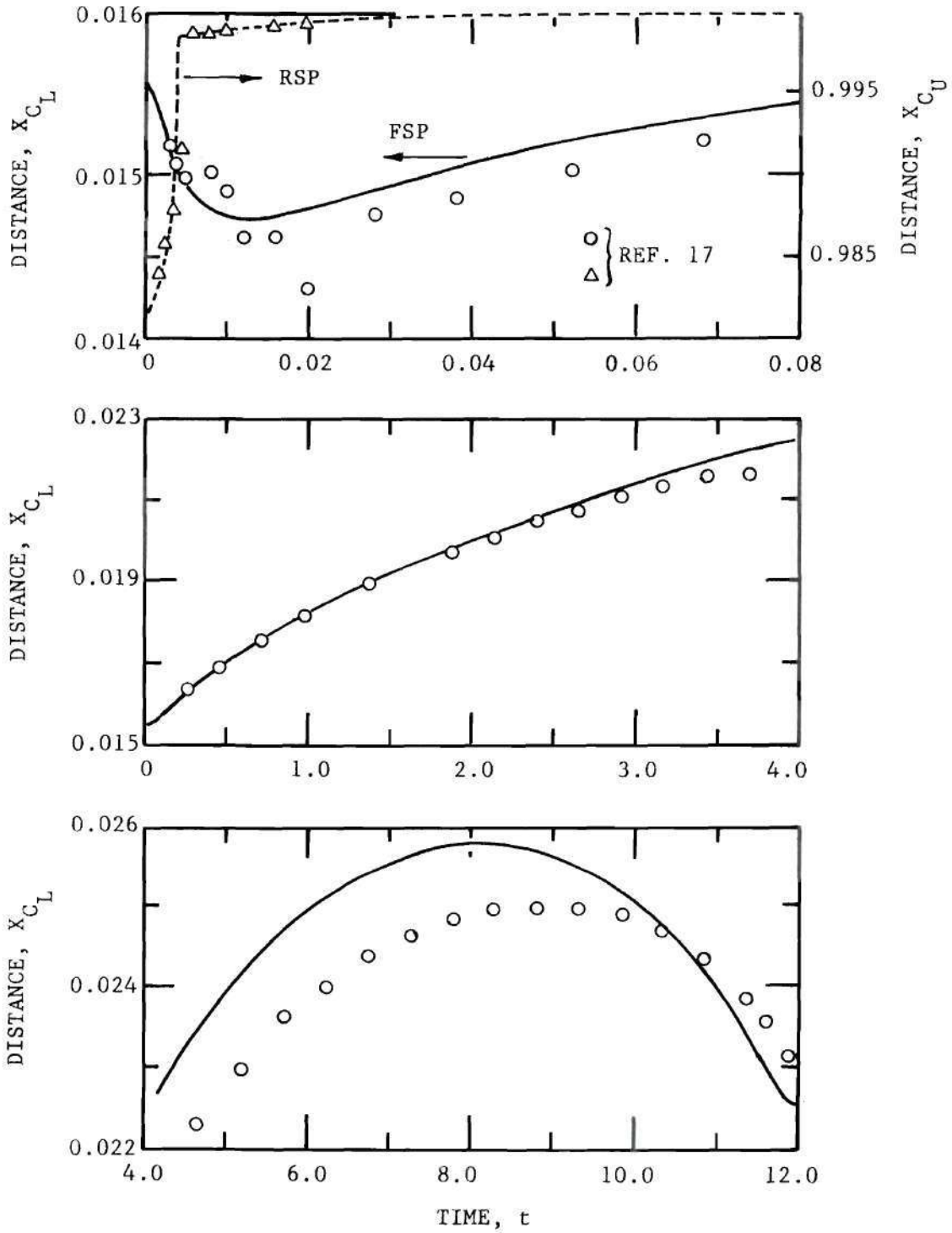

Figure 41. Locations of Front and Rear Stagnation Points, t = 0 to t = 12.0

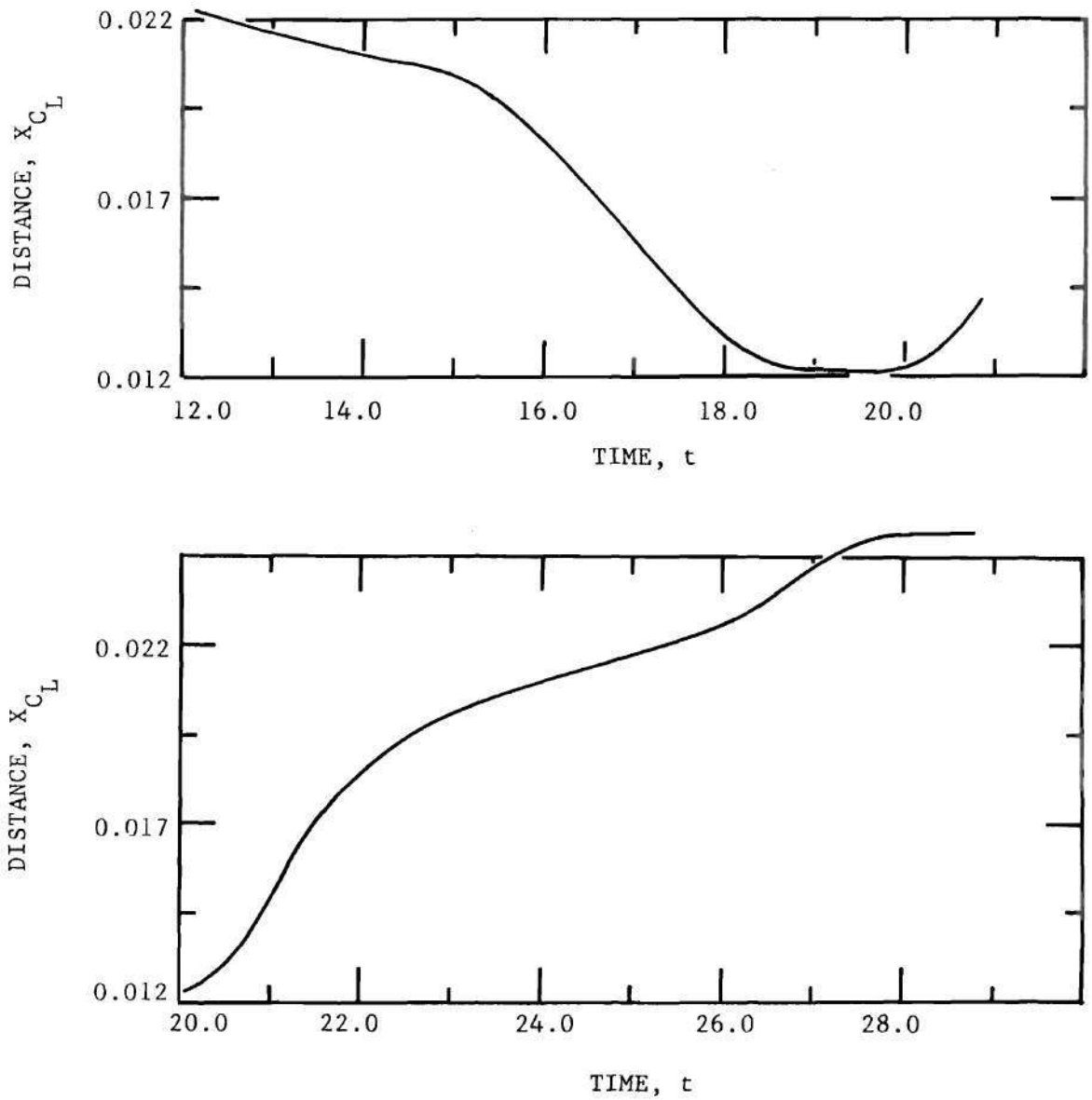

Figure 42. Location of Front Stagnation Point
t = 12.0 to 1 = 28.756

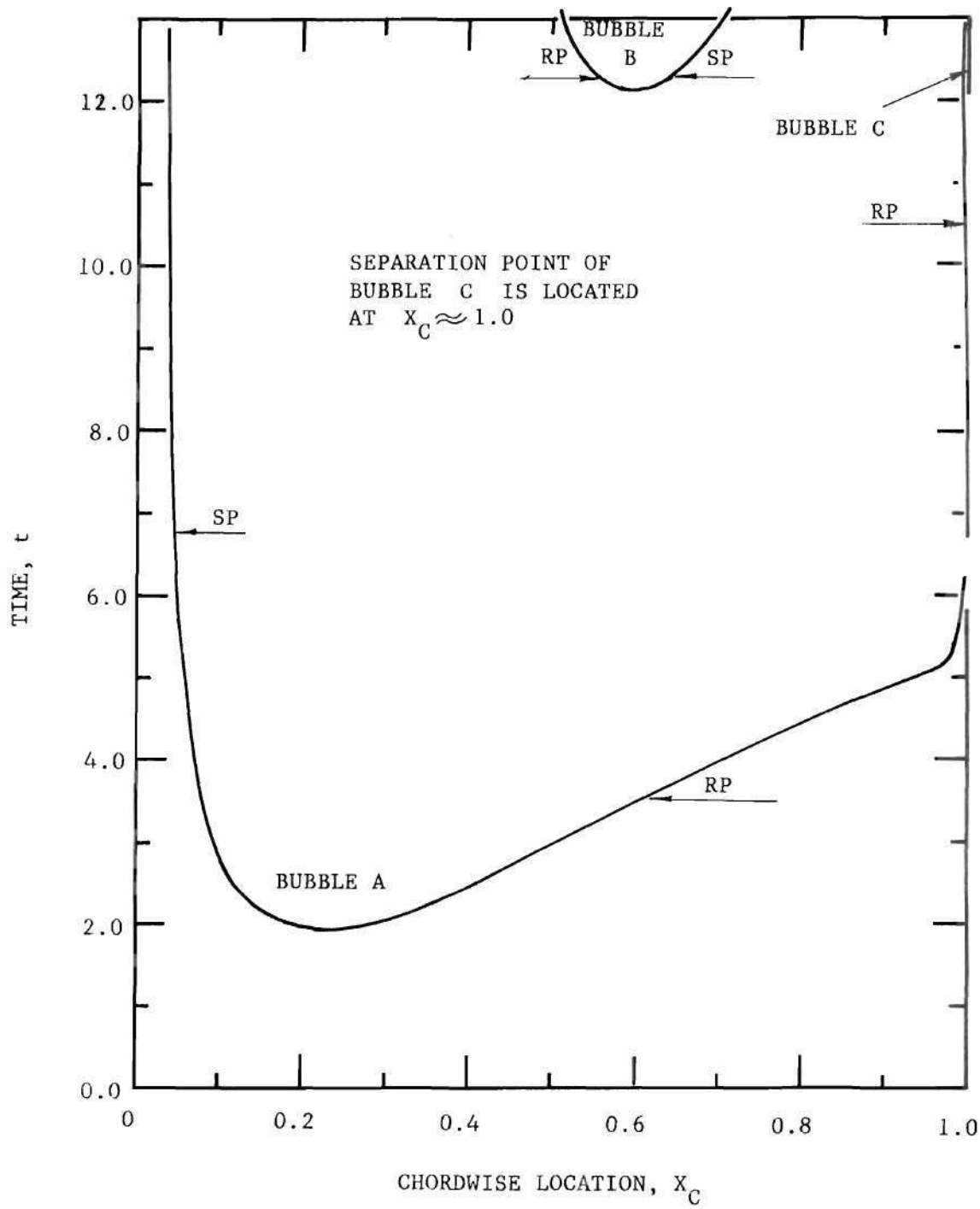

Figure 43. Locations of Separation and Reattachment Points, t = 0.0 to t = 13.0

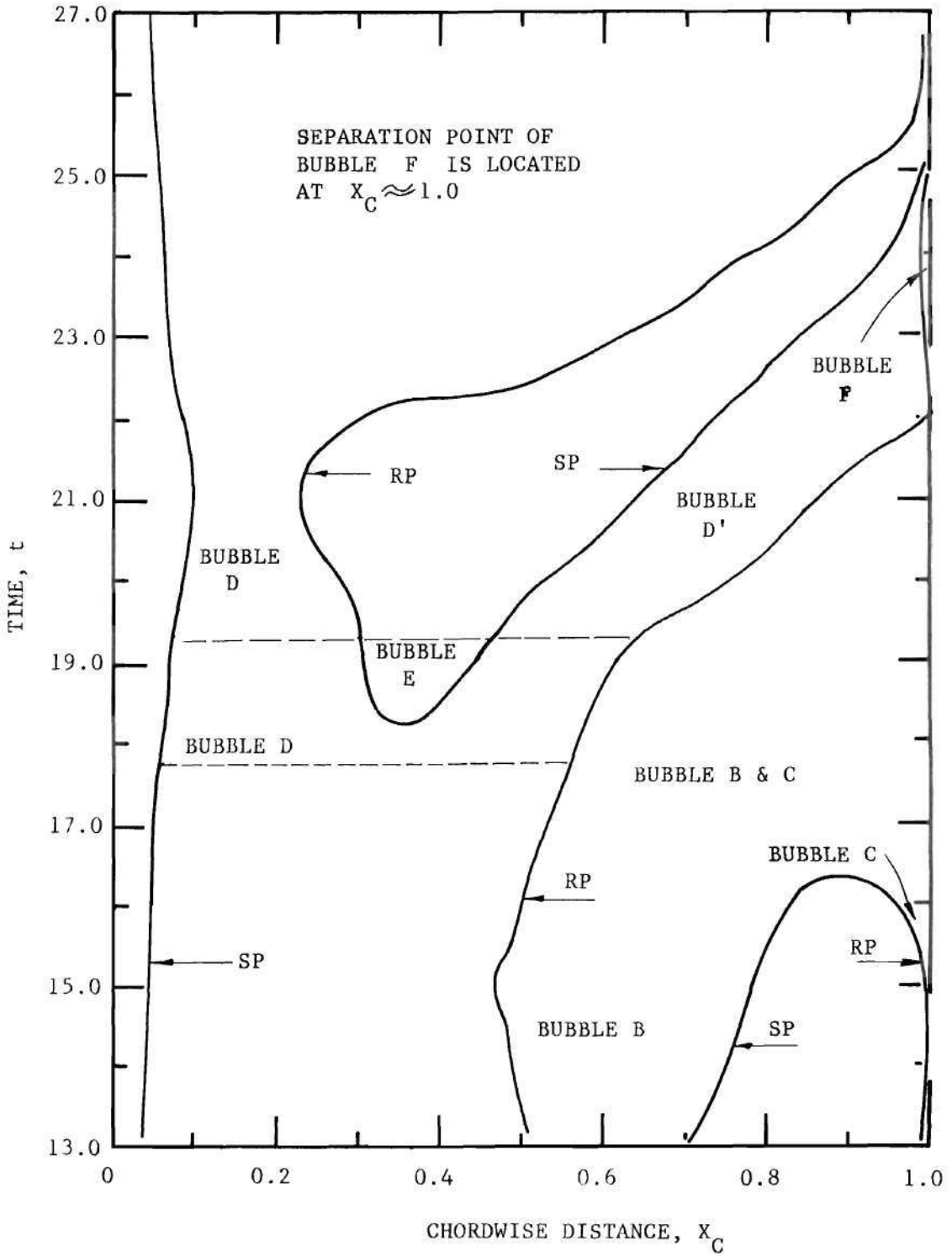

Figure 44. Locations of Separation and Reattachment Points (t = 13.0→27.0)

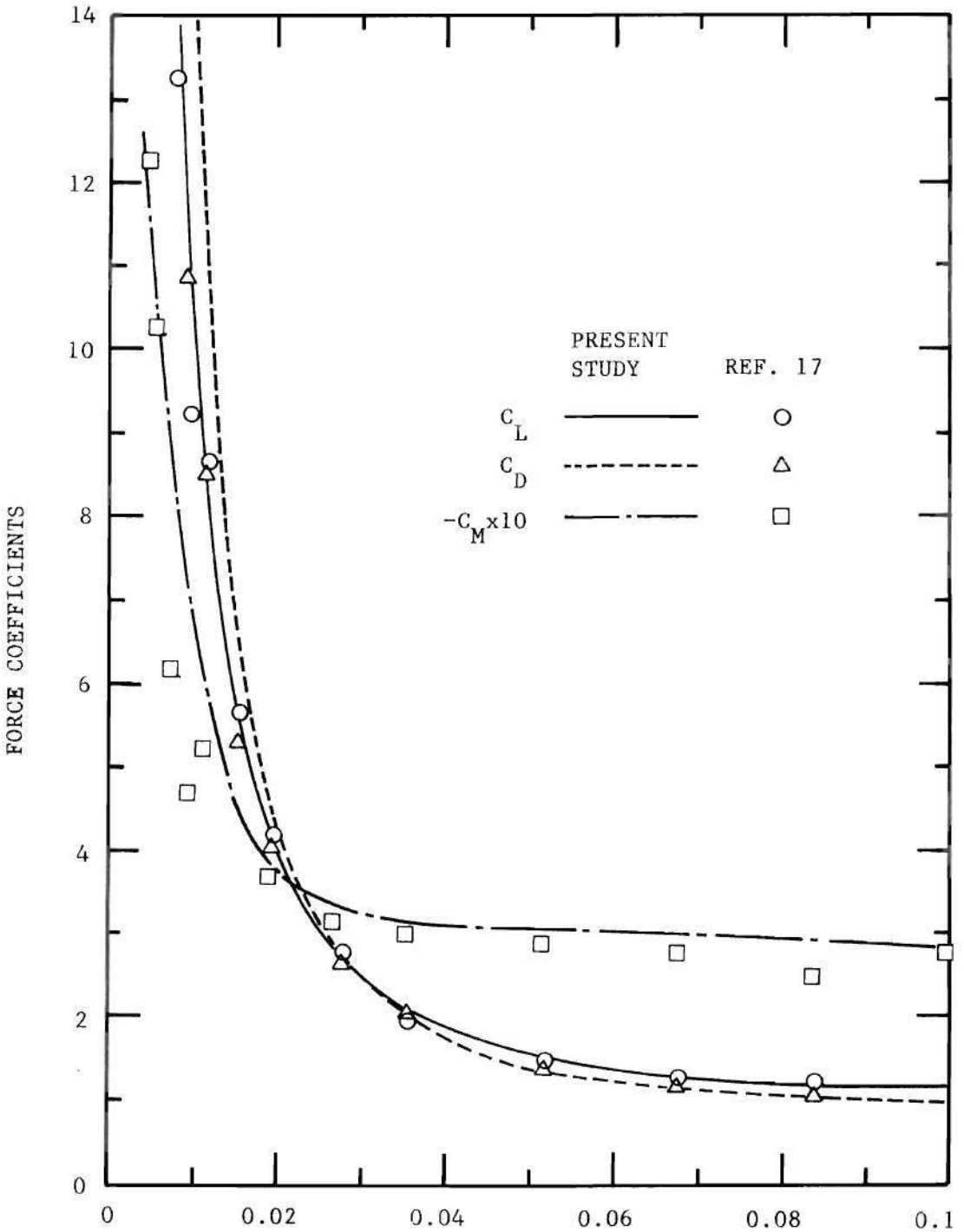

Figure 45. Time Histories of Loads, t = 0.0 to t = 0.1

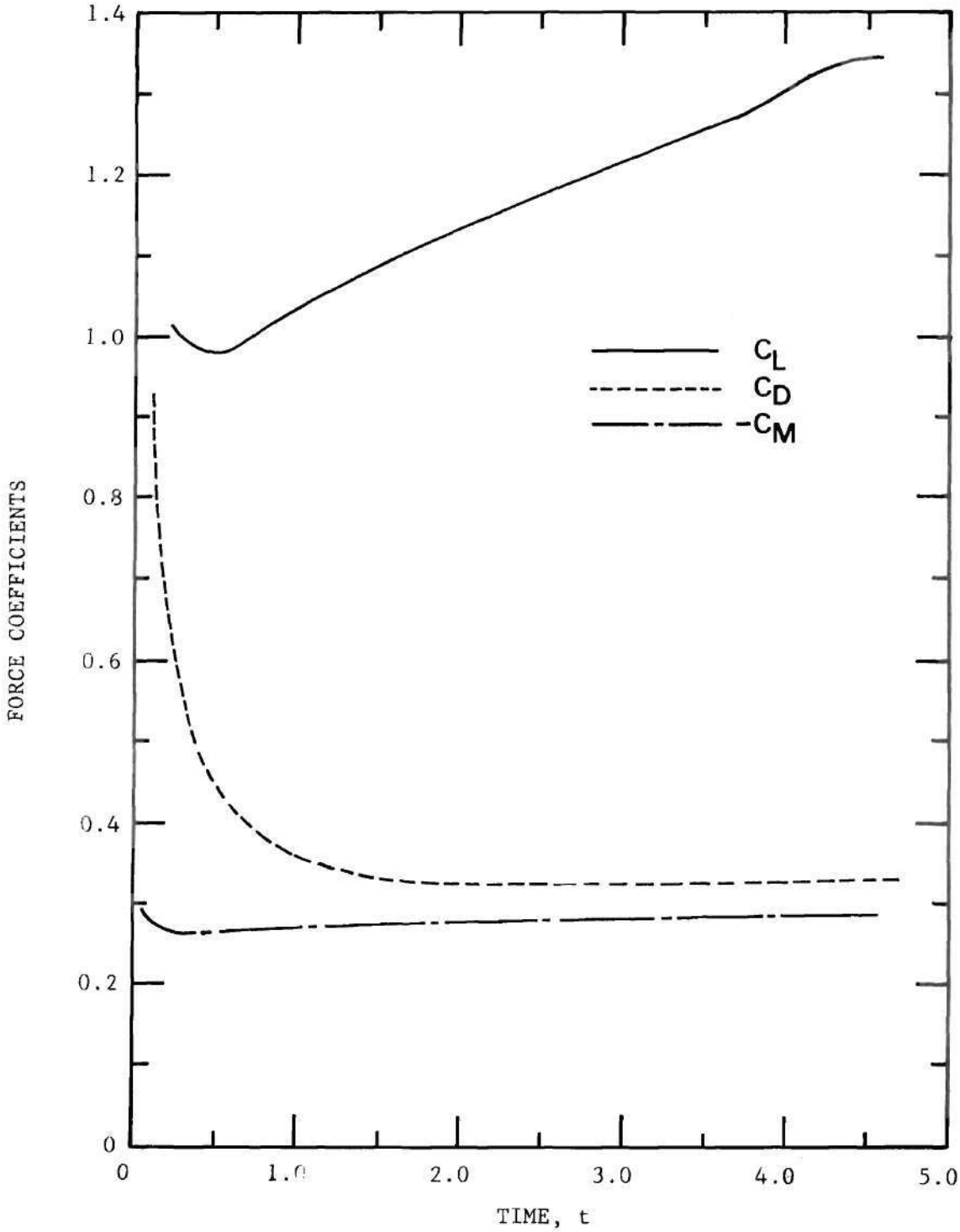

Figure 46. Time Histories of Loads, t = 0.1 to t = 4.692

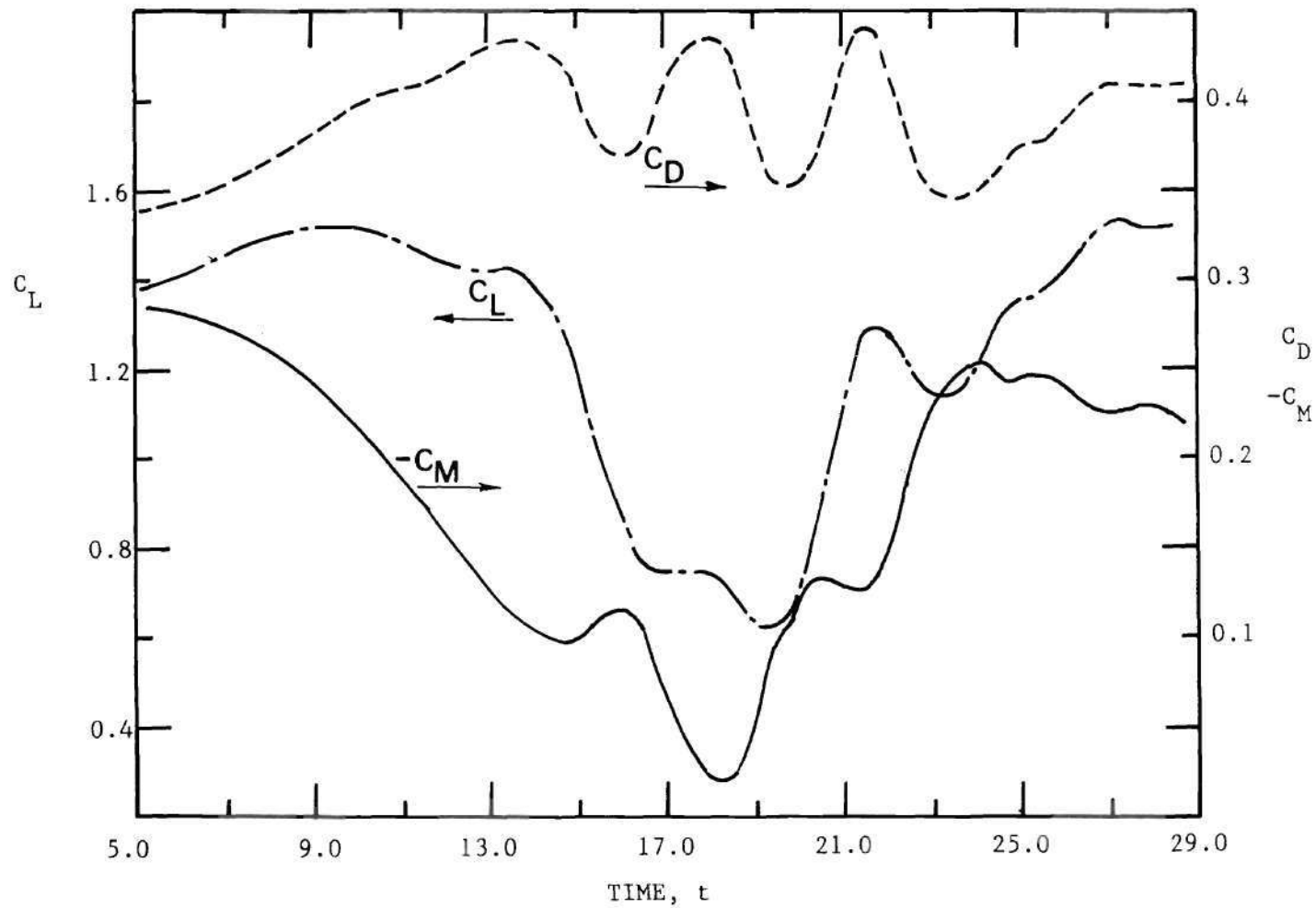

Figure 47. Time Histories of Loads, t = 5.0 to t = 28.756

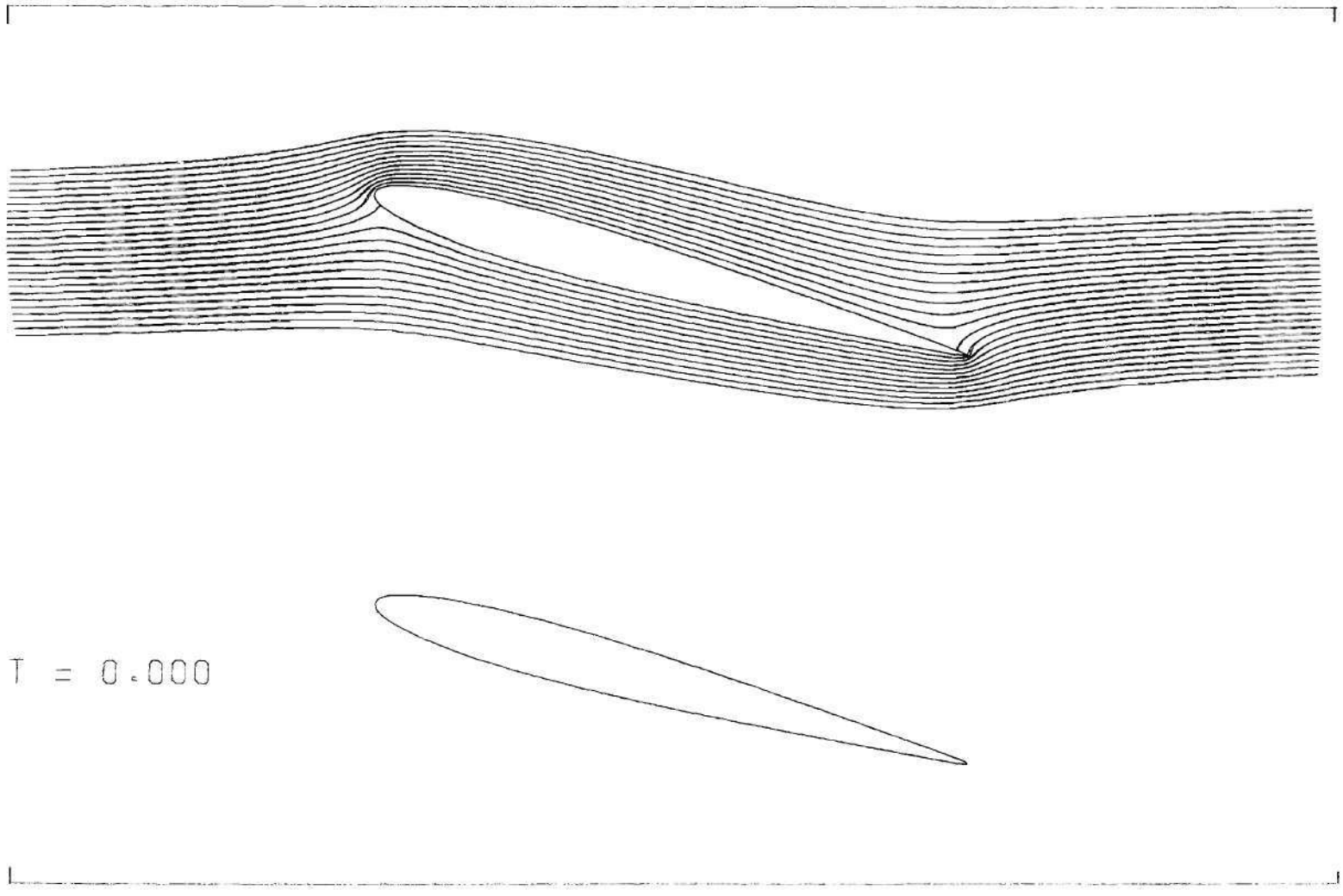

Figure 48. Streamlines and Equi-vorticity Contours at t = 0.000

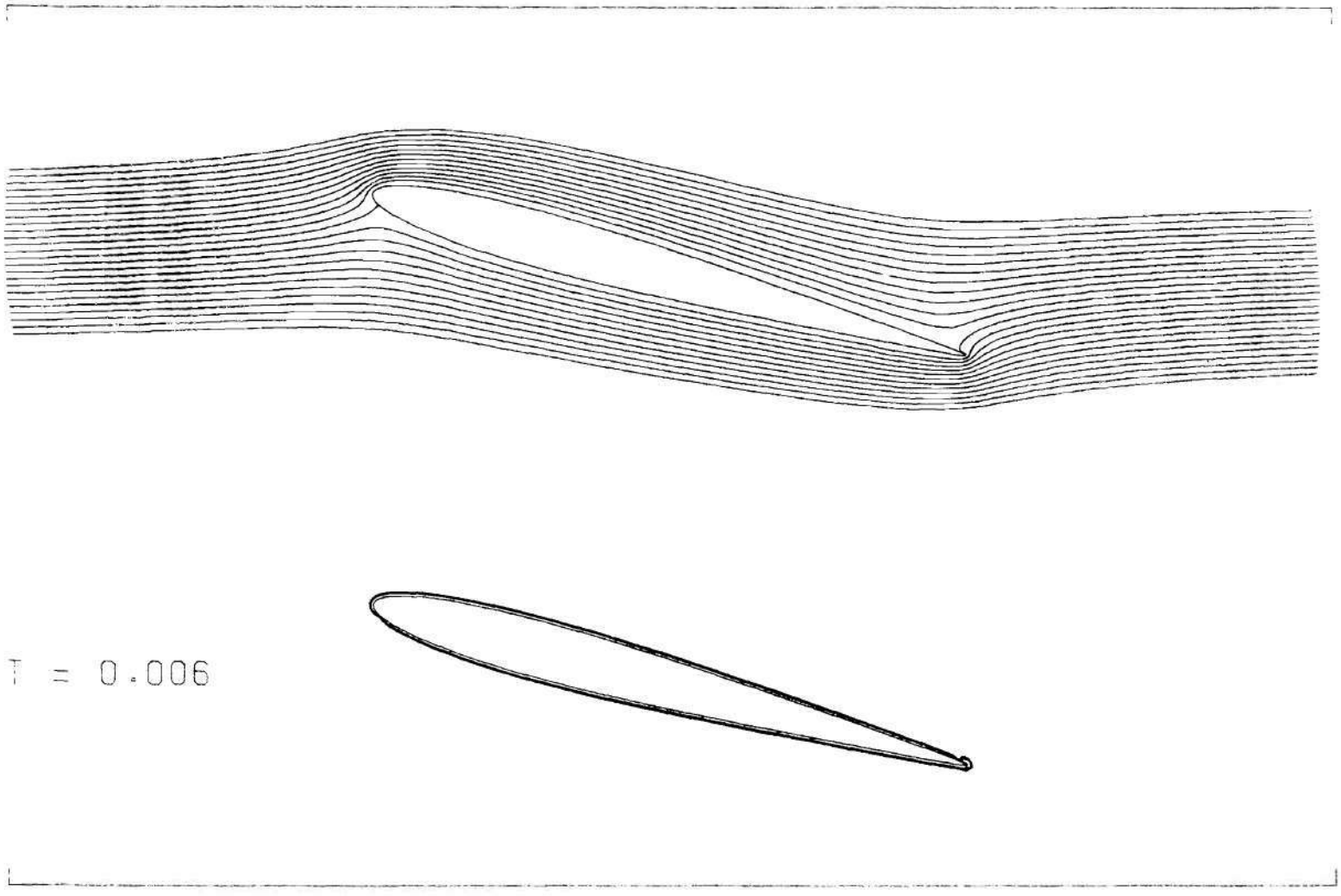

Figure 49. Streamlines and Equi-vorticity Contours at t = 0.006

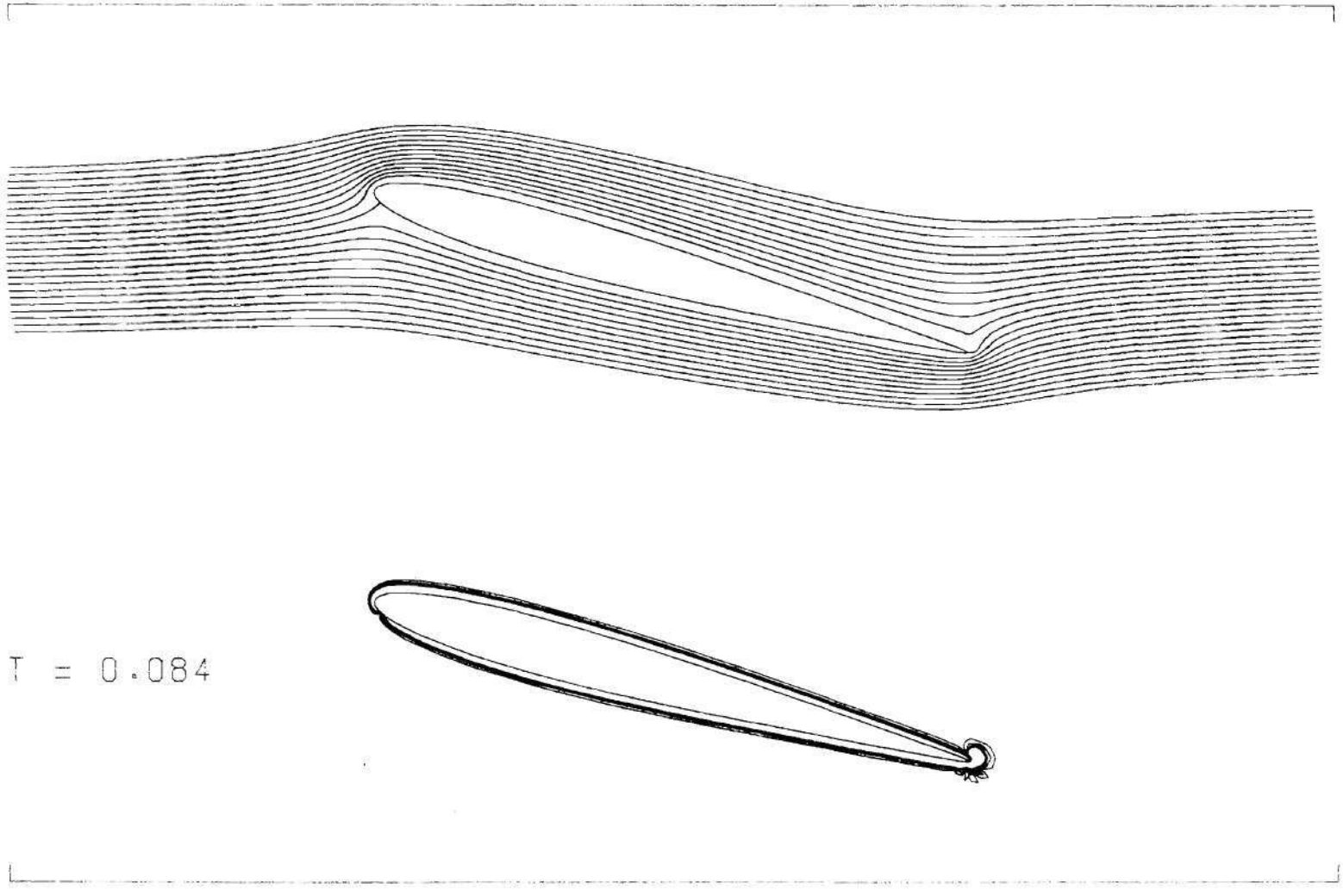

Figure 50. Streamlines and Equi-vorticity Contours at t = 0.084

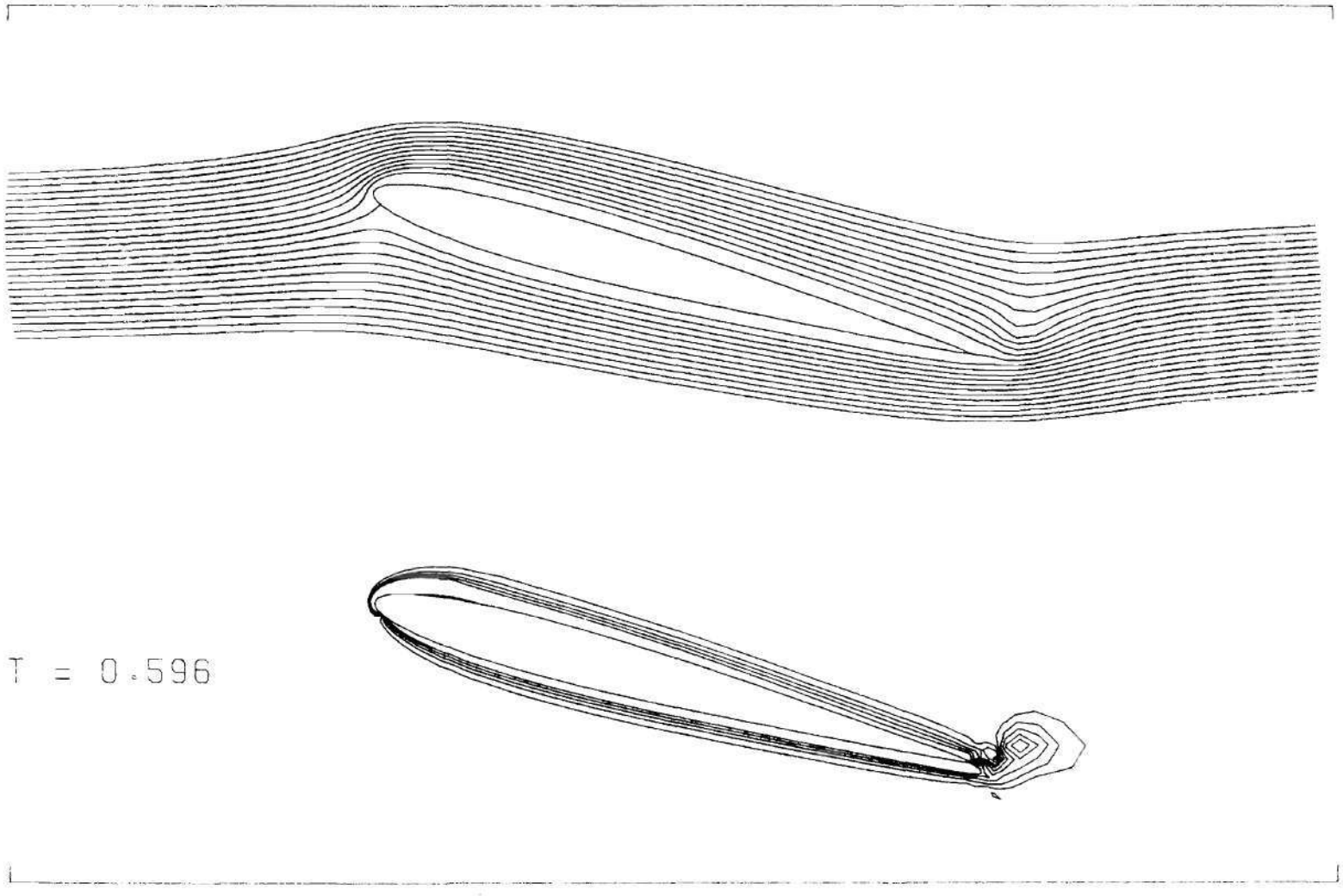

Figure 51. Streamlines and Equi-vorticity Contours at t = 0.596

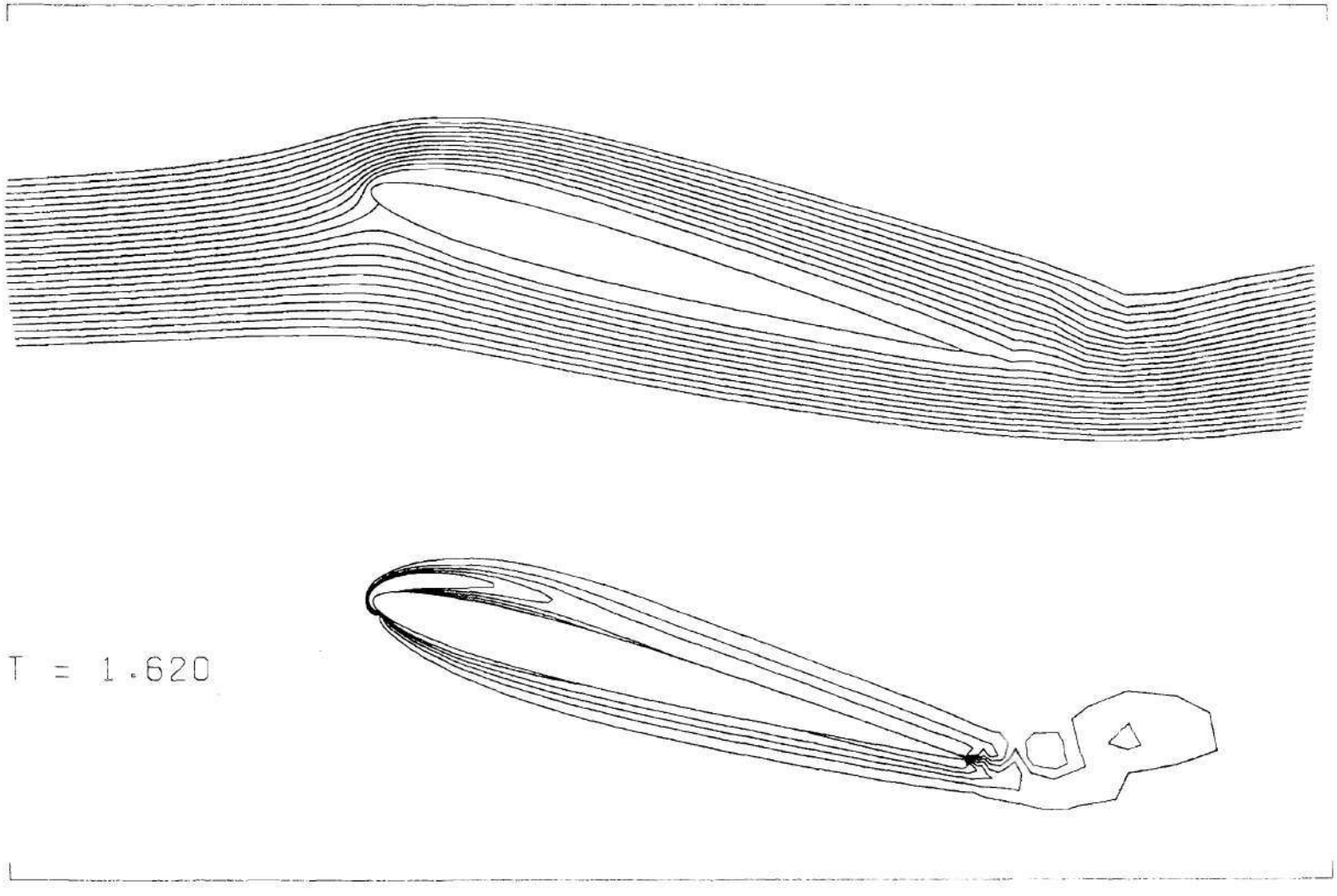

Figure 52. Streamlines and Equi-vorticity Contours at t = 1.620

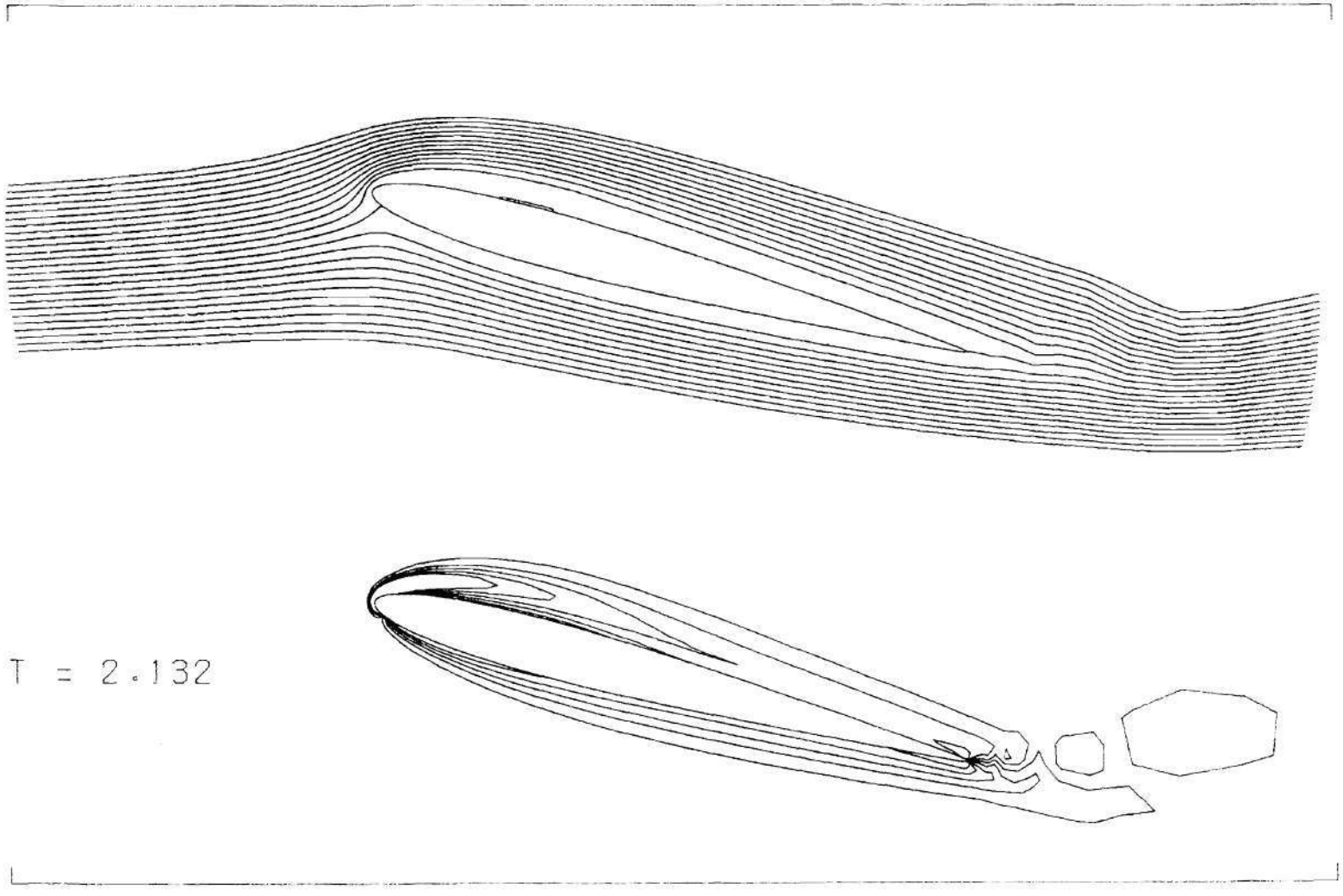

Figure 53. Streamlines and Equi-vorticity Contours at t = 2.132

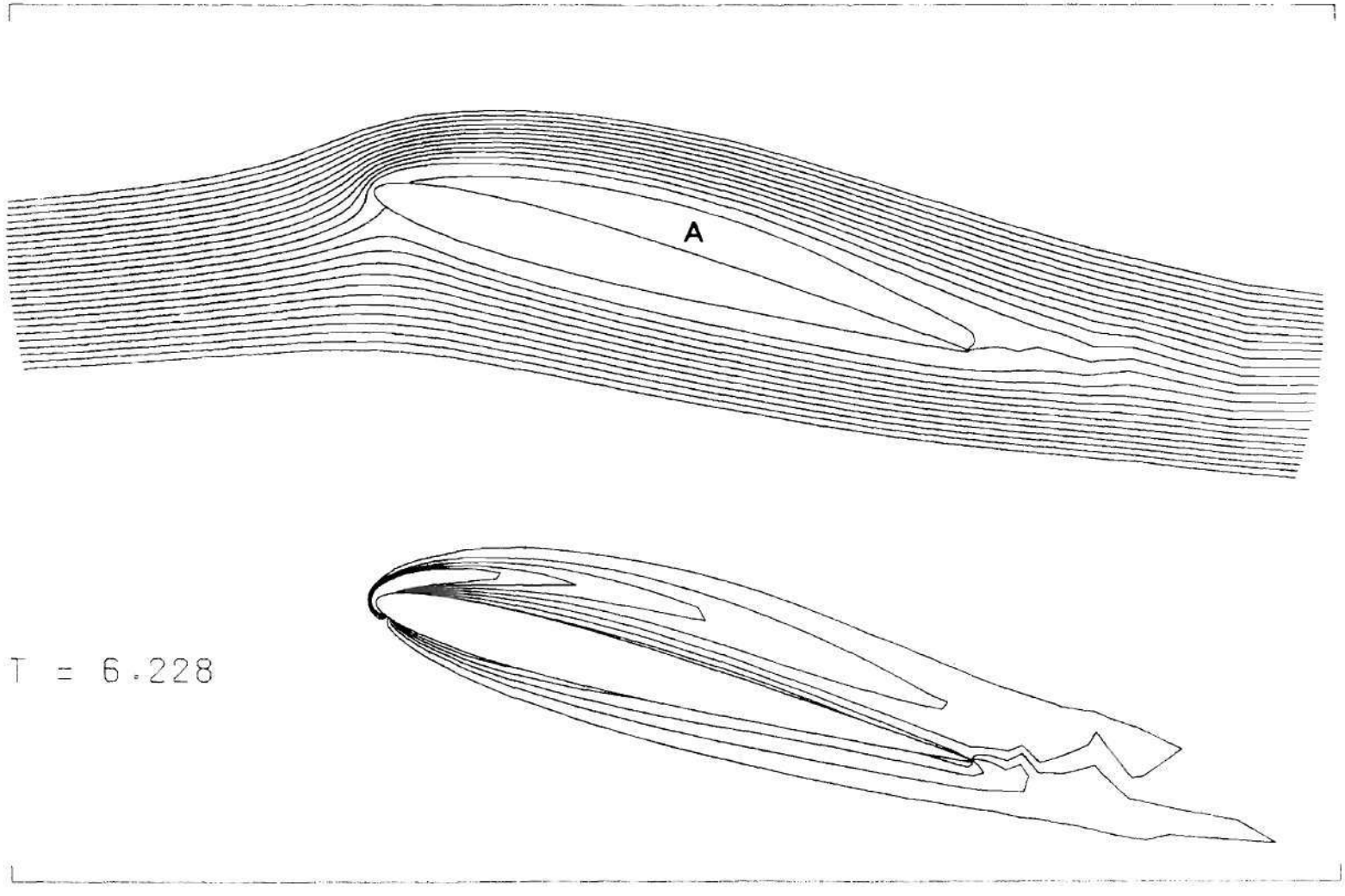

Figure 54. Streamlines and Equi-vorticity Contours at t = 6.228

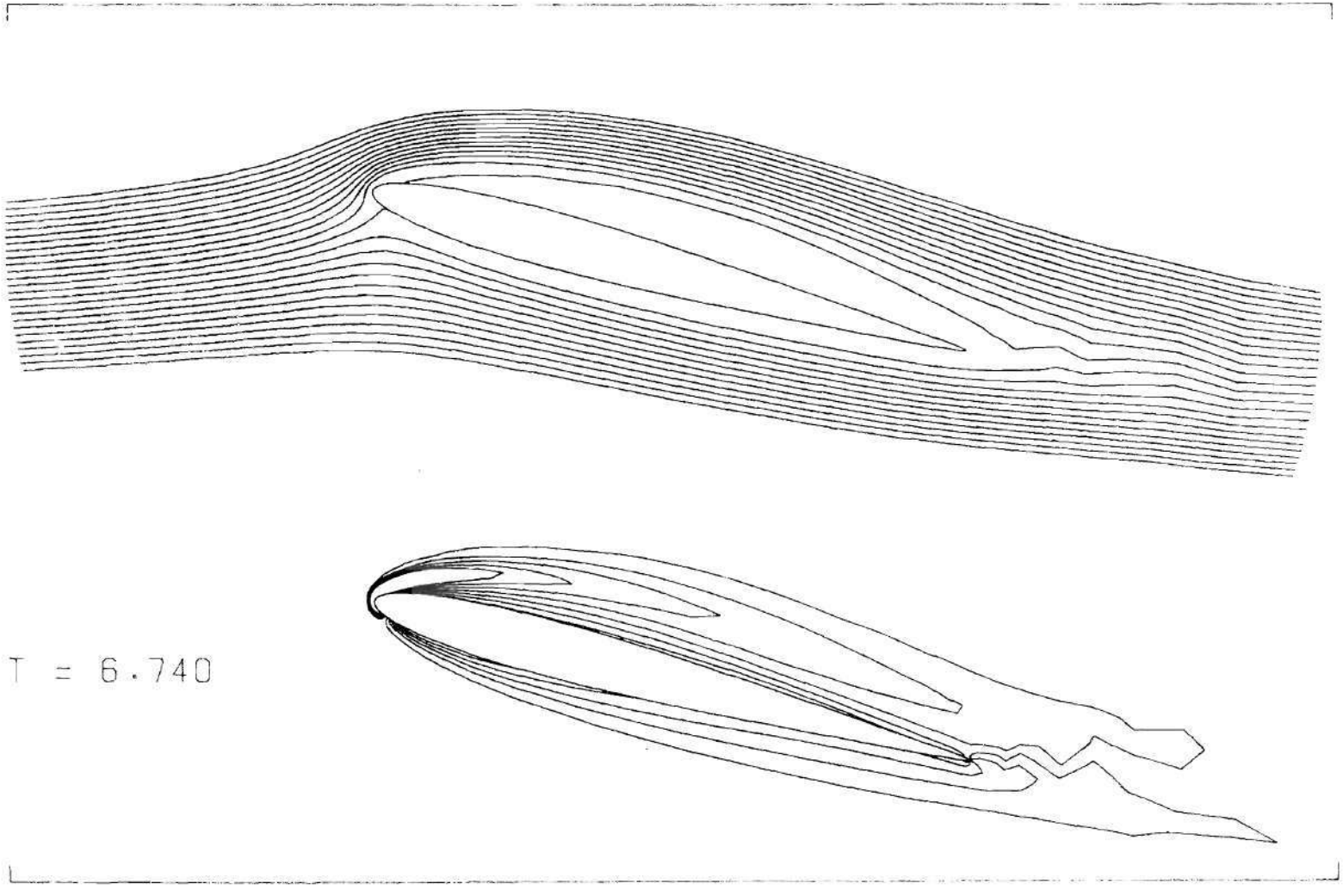

Figure 55. Streamlines and Equi-vorticity Contours at t = 6.740

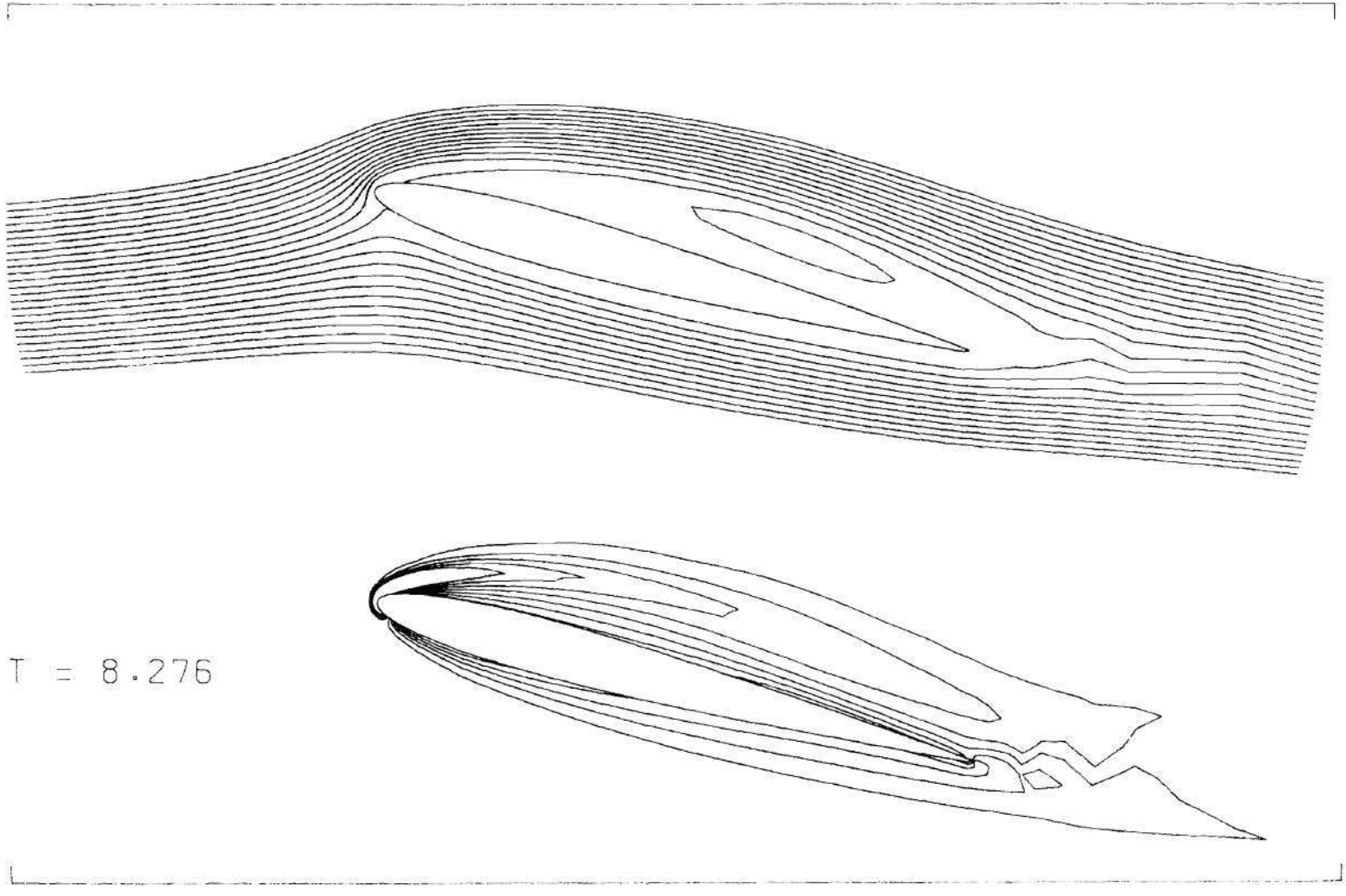

Figure 56. Streamlines and Equi-vorticity Contours at t = 8.276

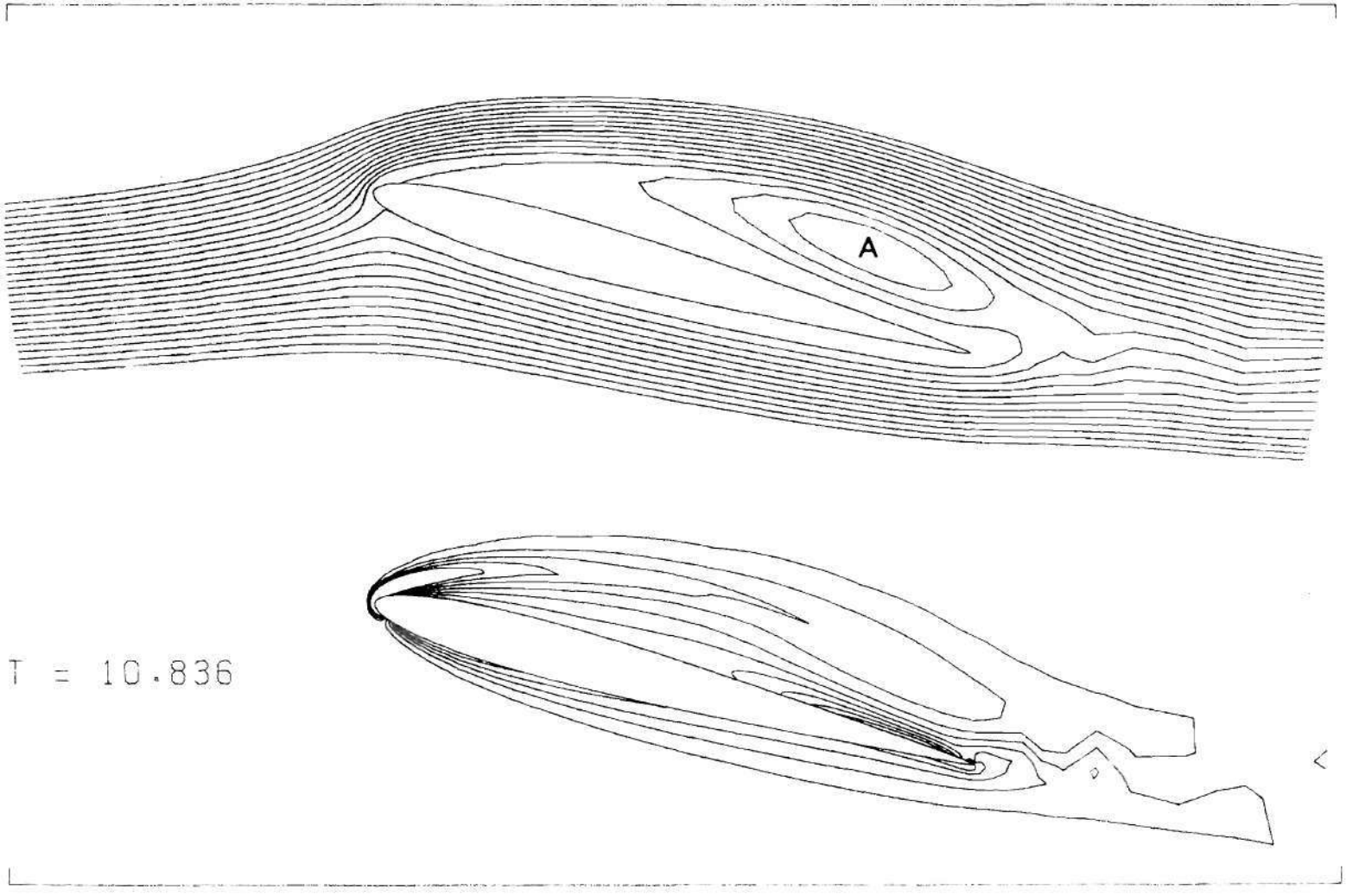

Figure 57. Streamlines and Equi-vorticity Contours at t = 10.836

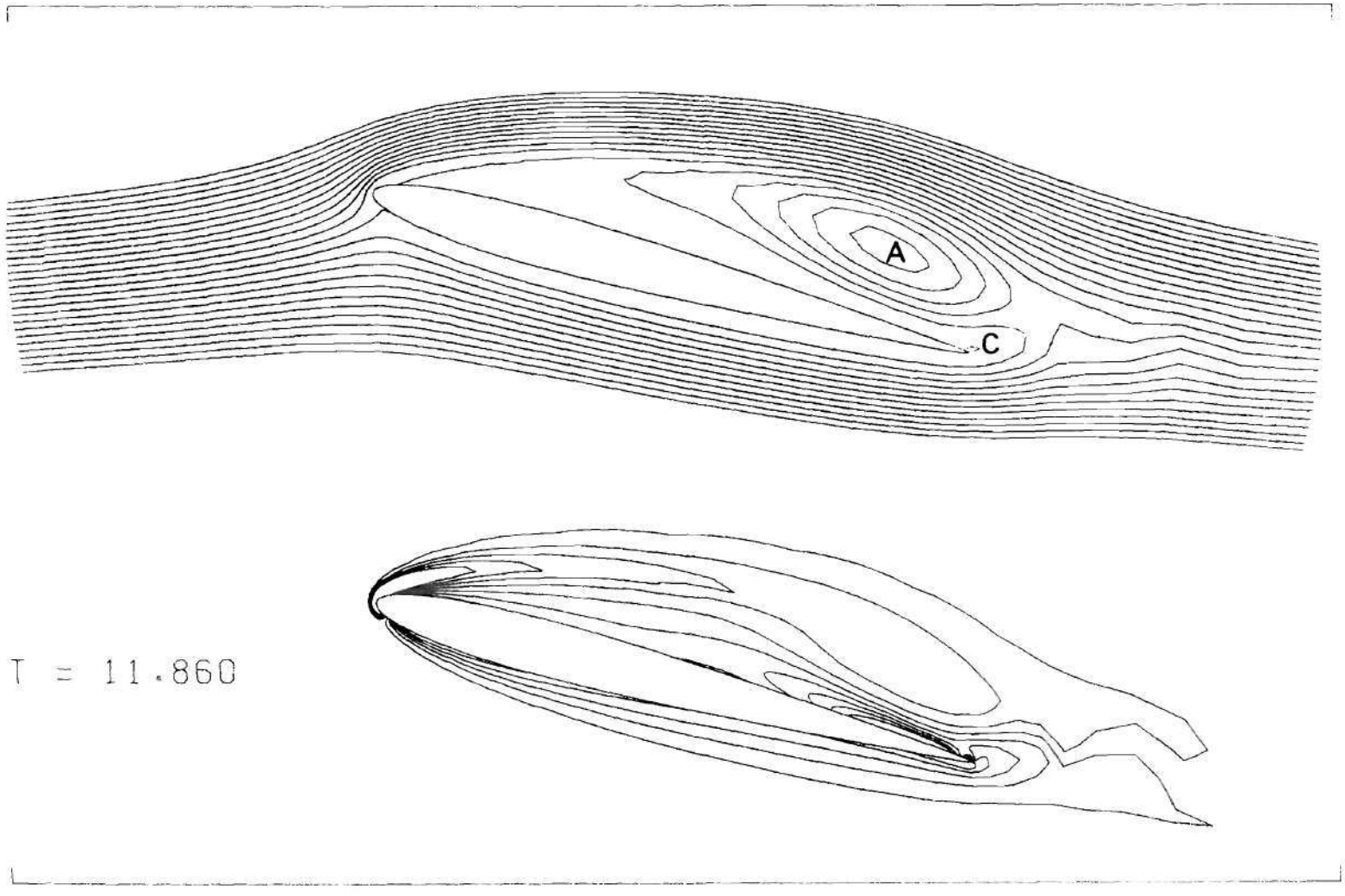

Figure 58. Streamlines and Equi-vorticity Contours at t = 11.860

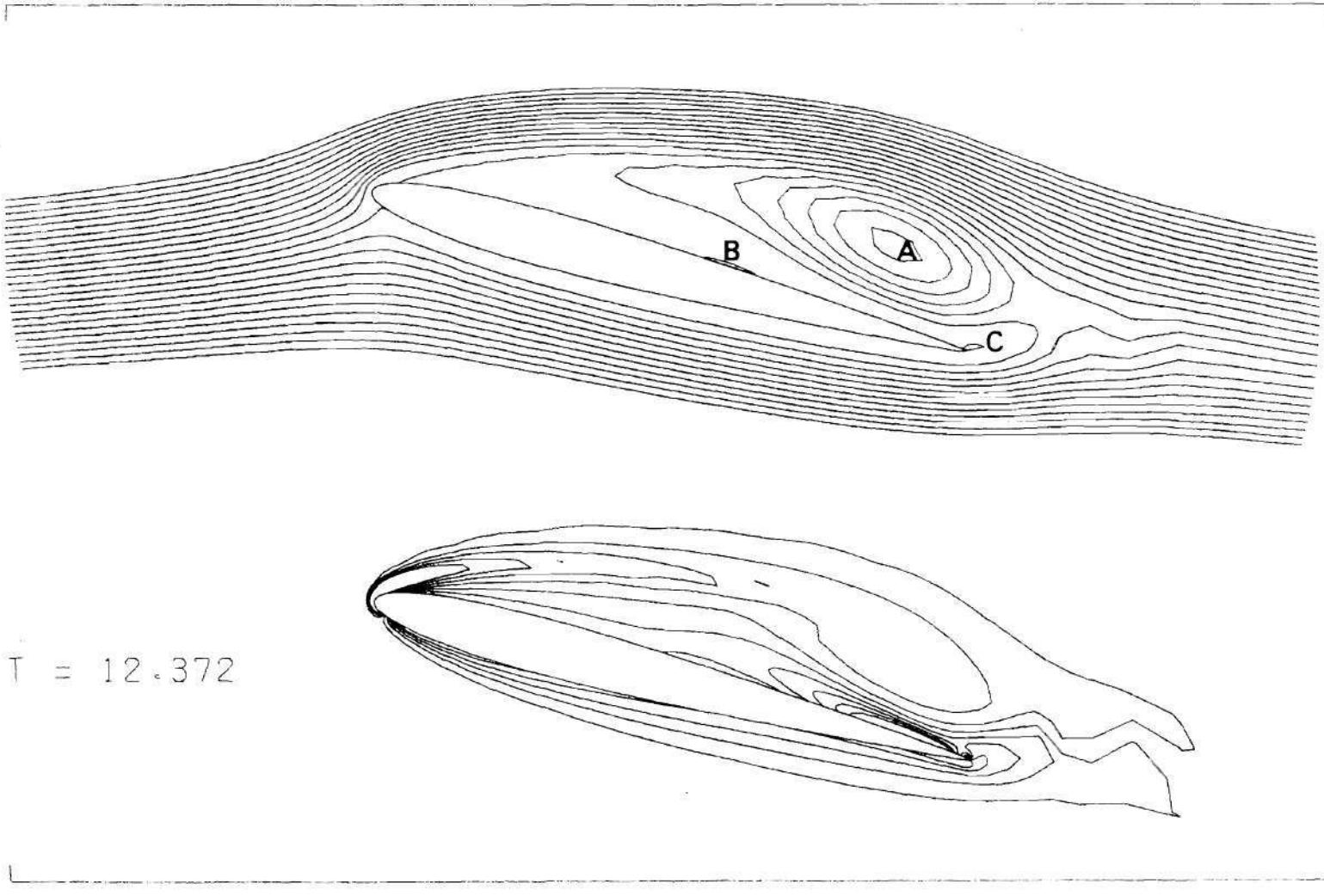

Figure 59. Streamlines and Equi-vorticity Contours at t = 12.372

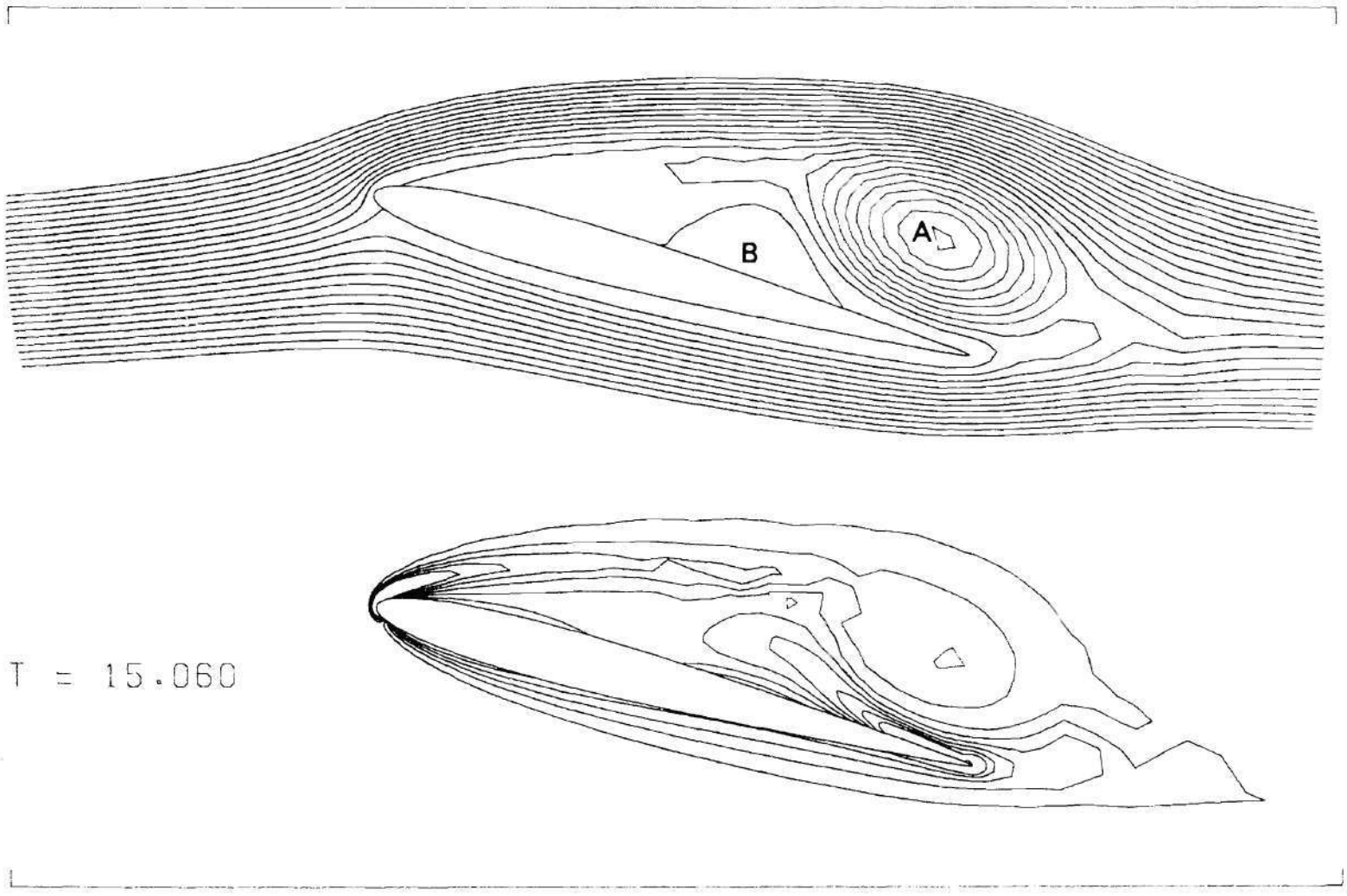

Figure 60. Streamlines and Equi-vorticity Contours at t = 15.060

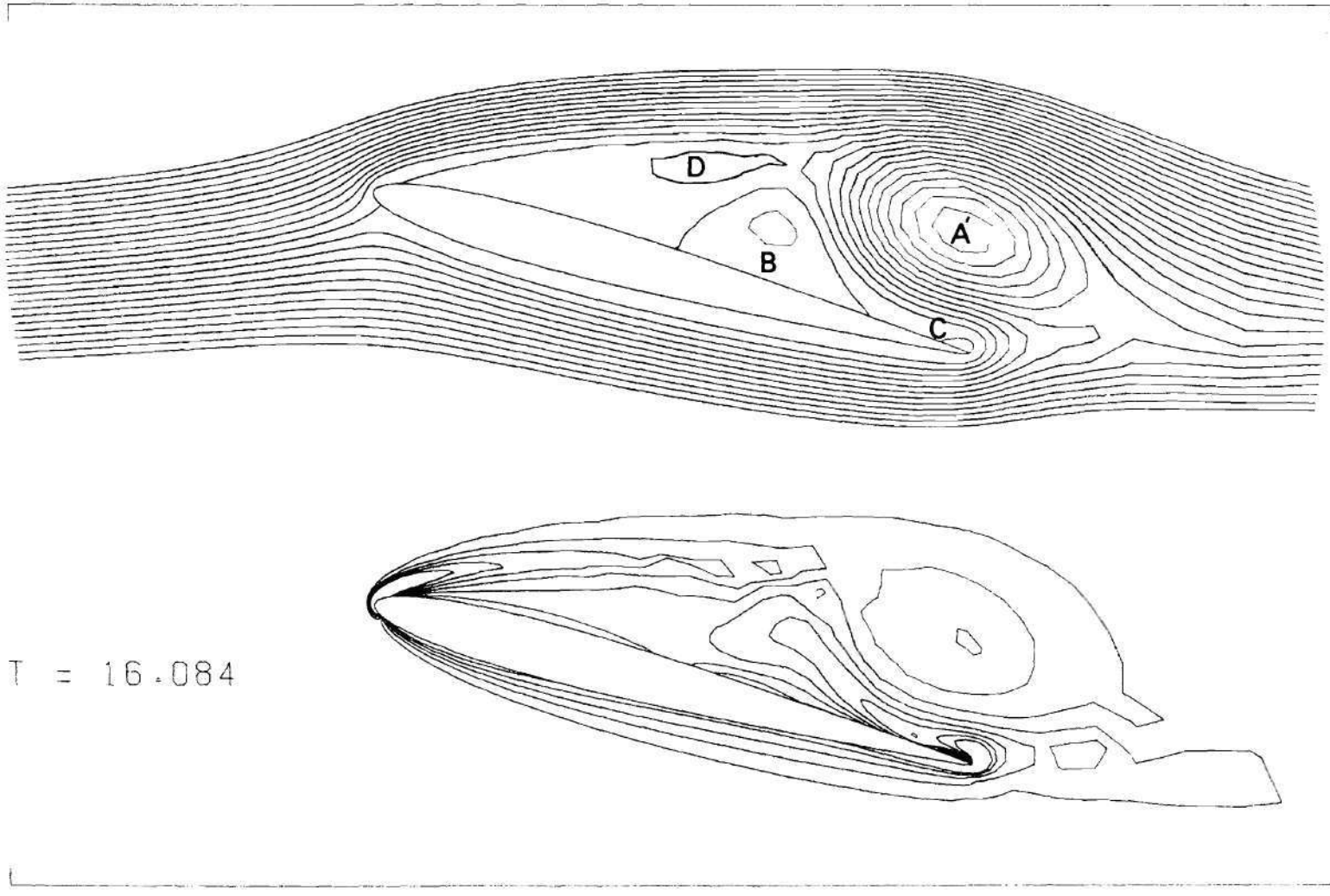

Figure 61. Streamlines and Equi-vorticity Contours at t = 16.084

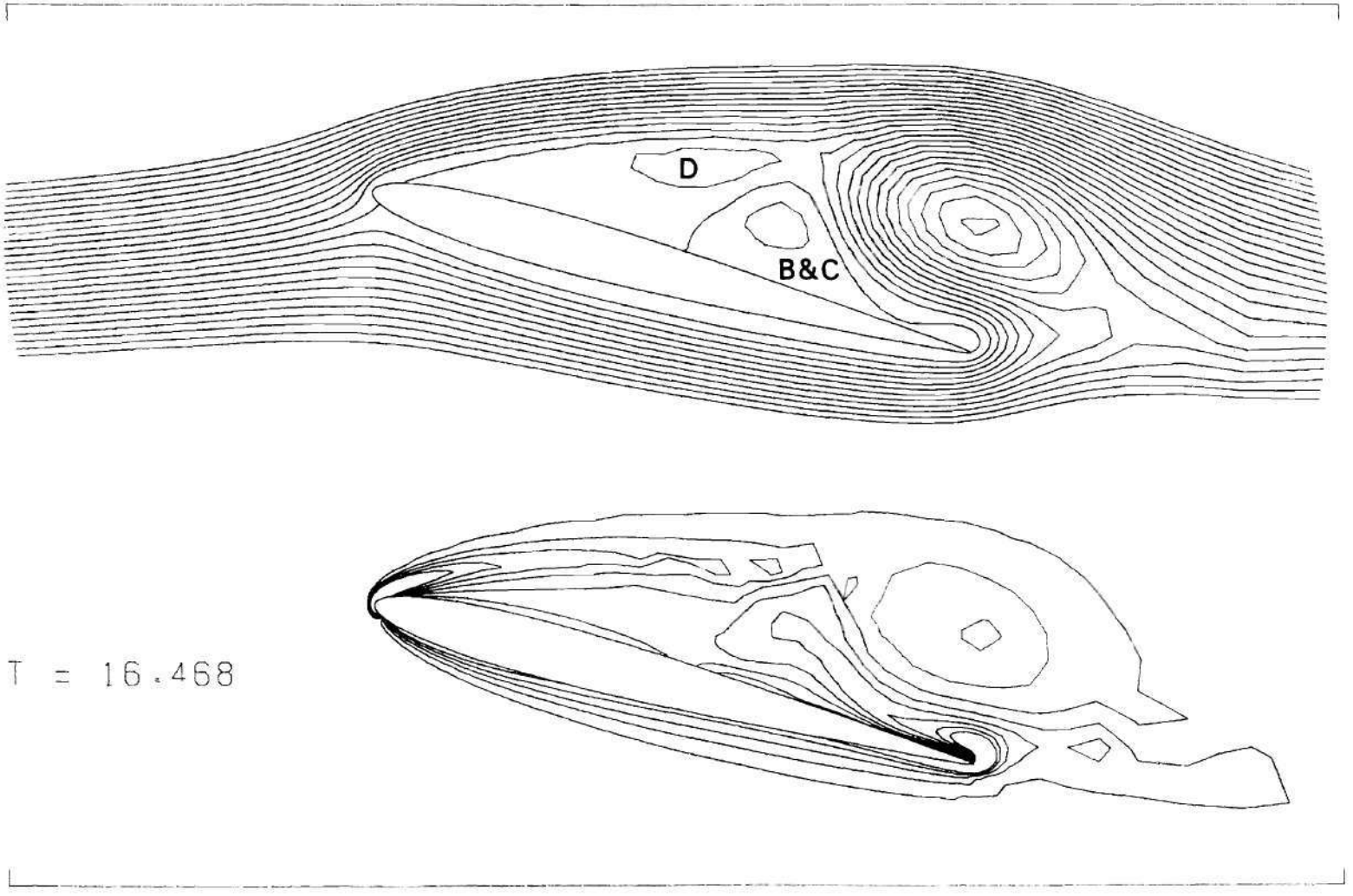

Figure 62. Streamlines and Equi-vorticity Contours at t = 16.468

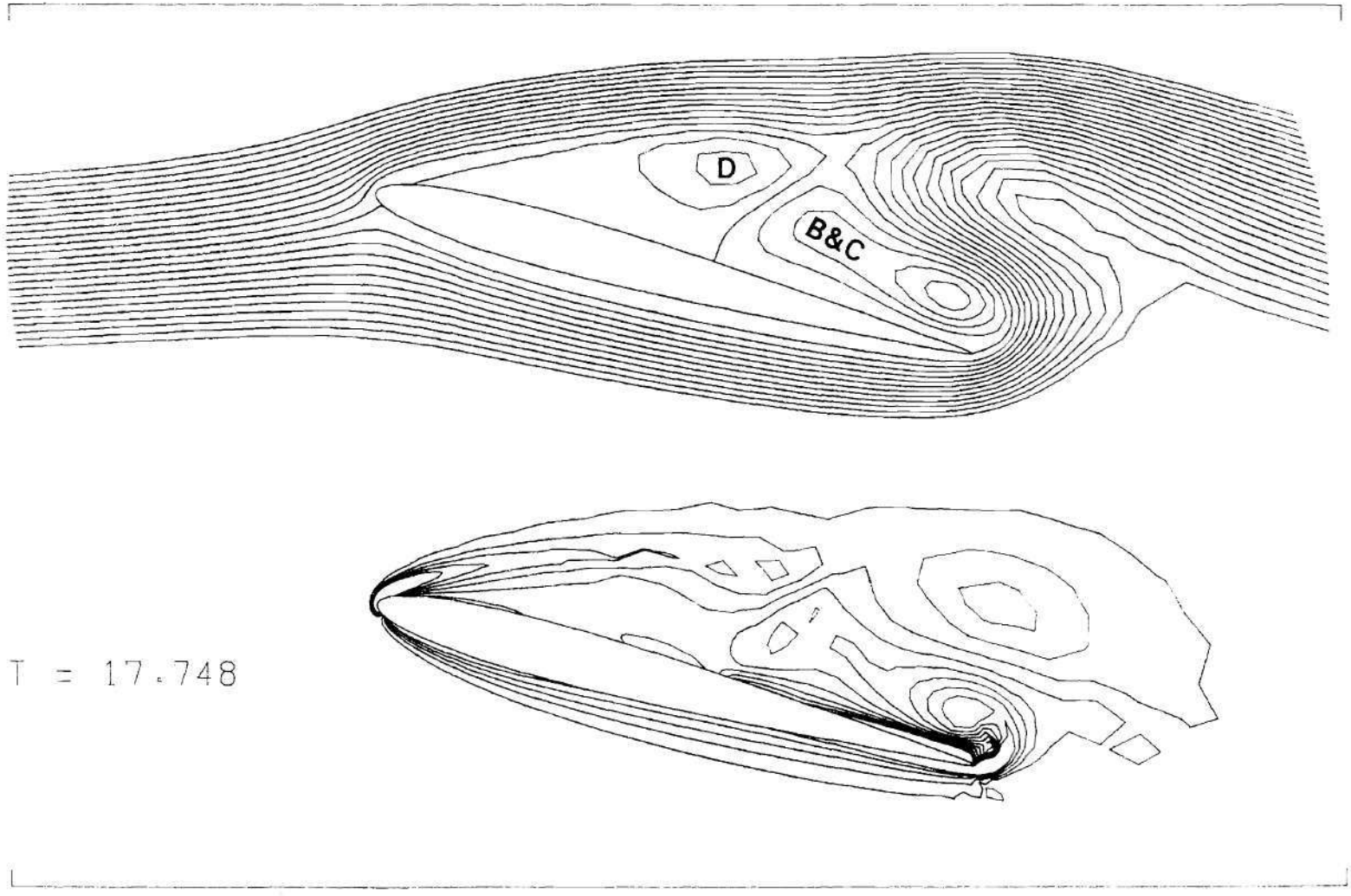

Figure 63. Streamlines and Equi-vorticity Contours at t = 17.748

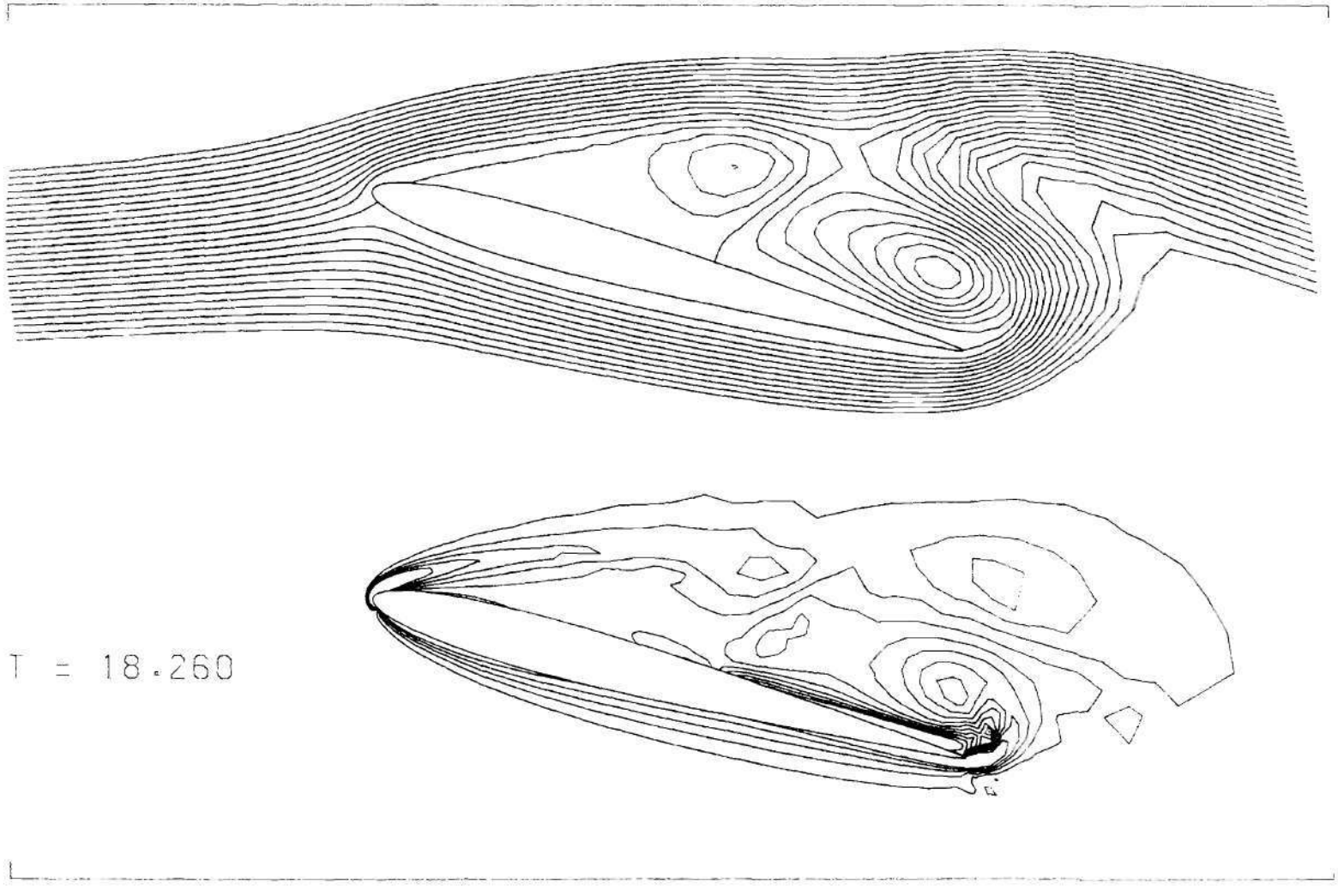

Figure 64. Streamlines and Equi-vorticity Contours at t = 18.260

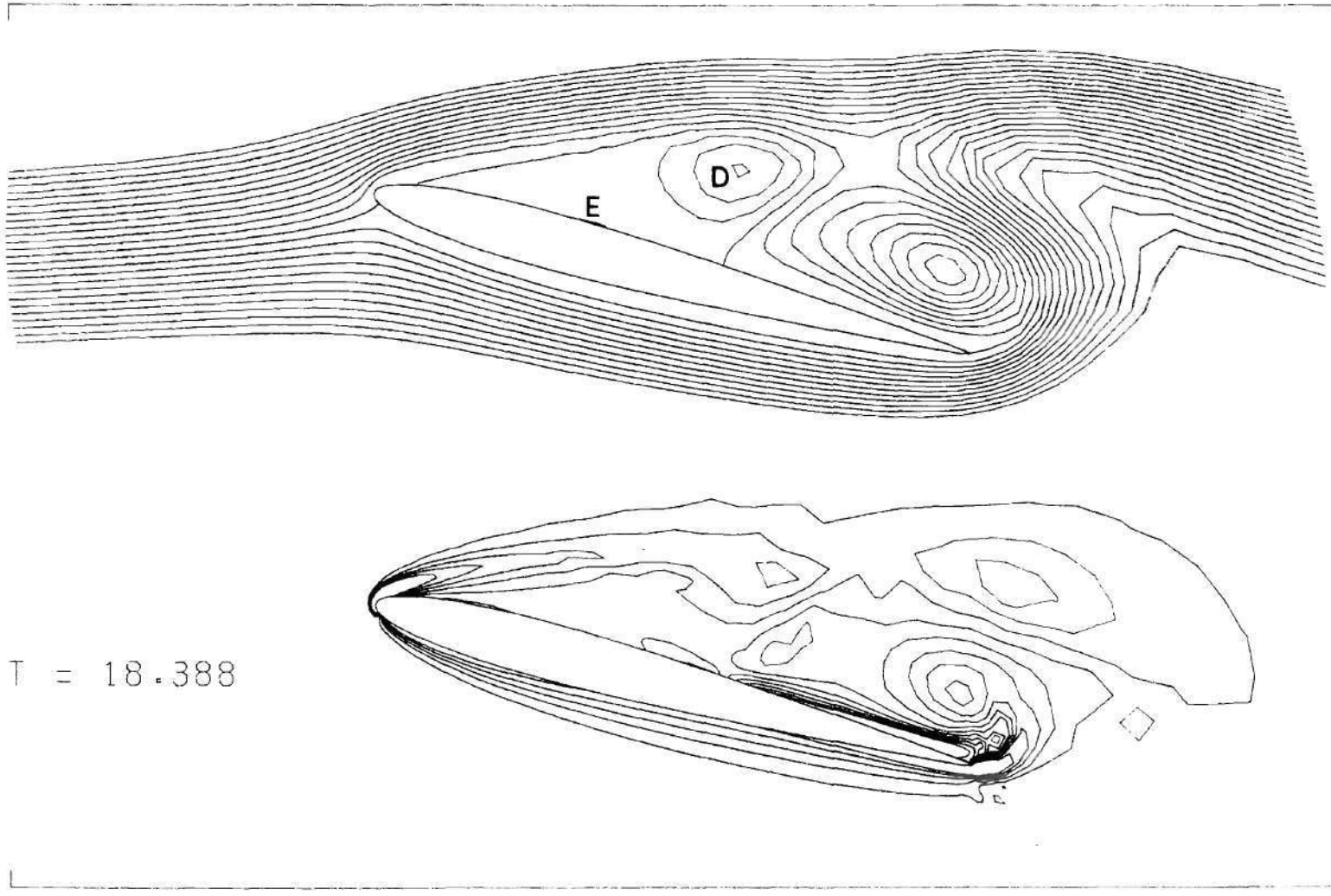

Figure 65. Streamlines and Equi-vorticity Contours at t = 18.388

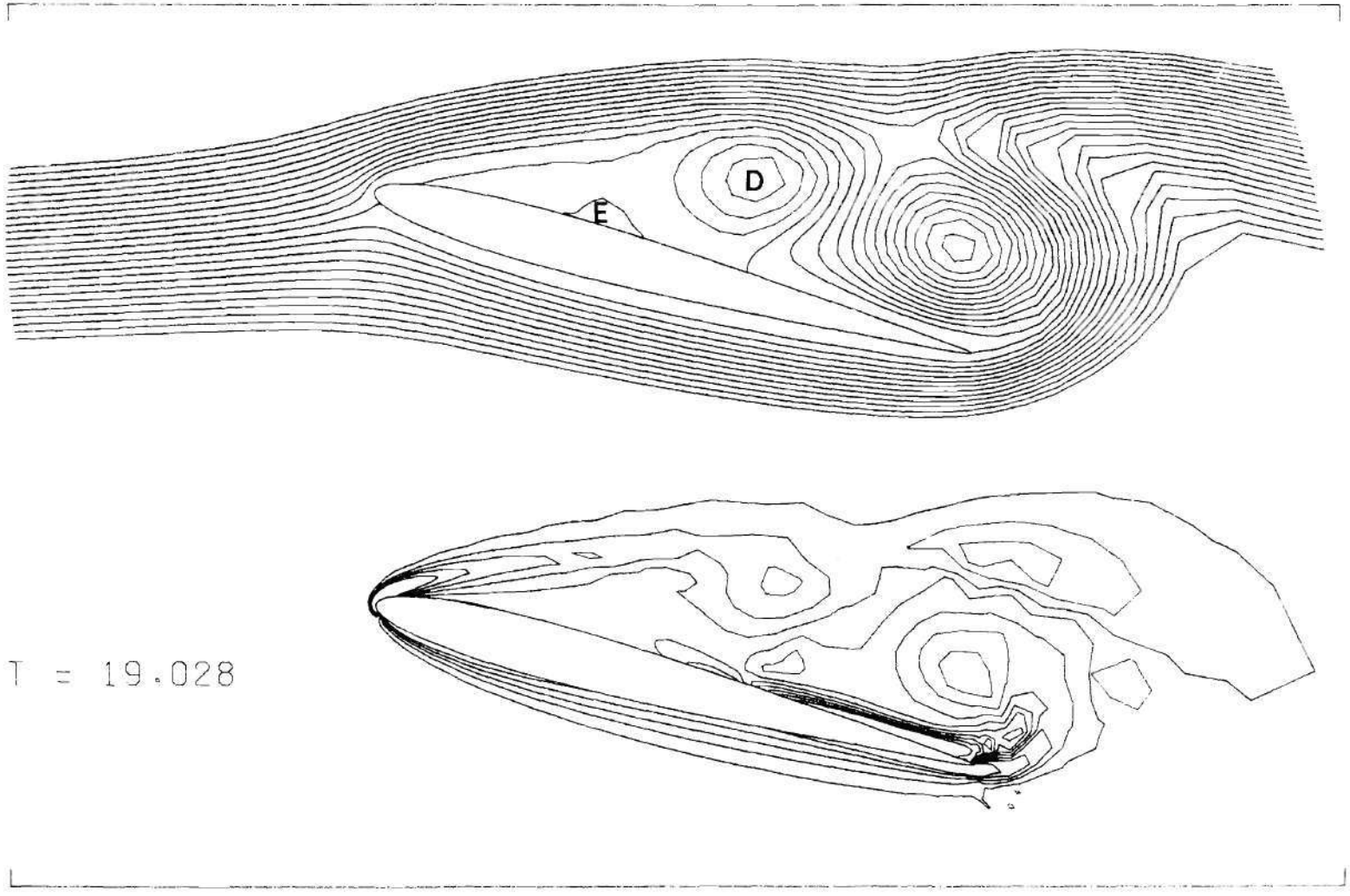

Figure 66. Streamlines and Equi-vorticity Contours at t = 19.028

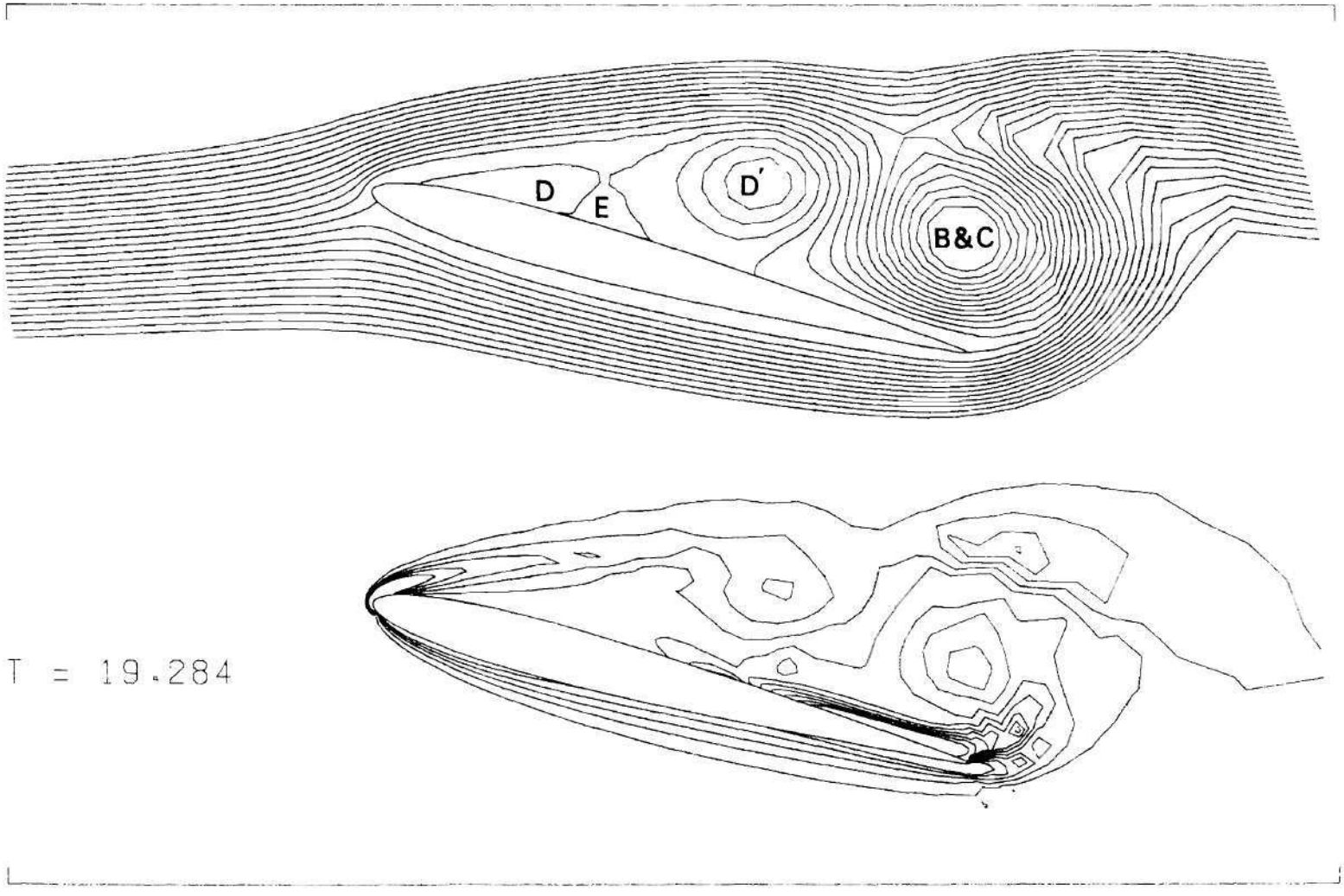

Figure 67. Streamlines and Equi-vorticity Contours at t = 19.284

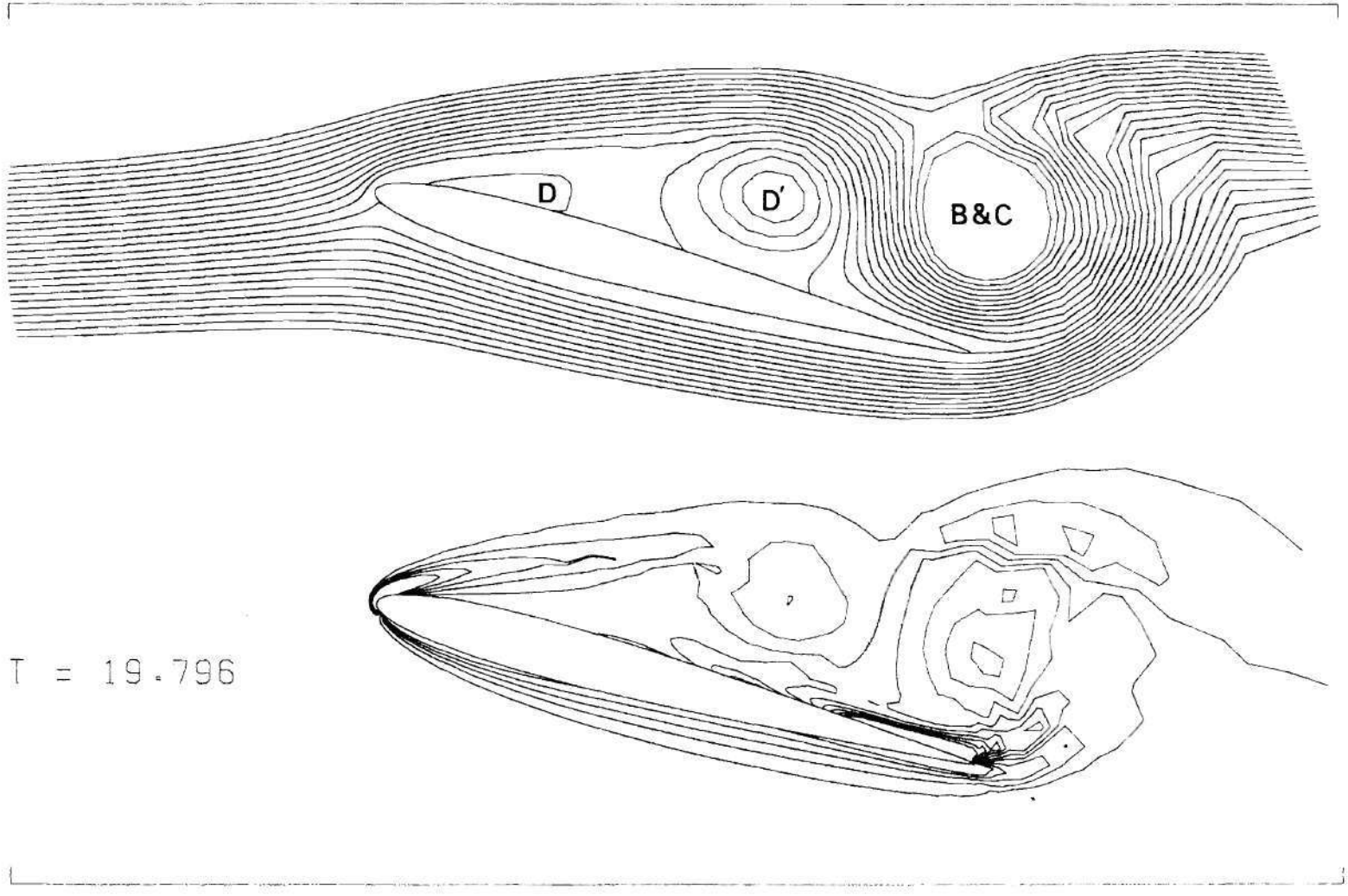

Figure 68. Streamlines and Equi-vorticity Contours at t = 19.796

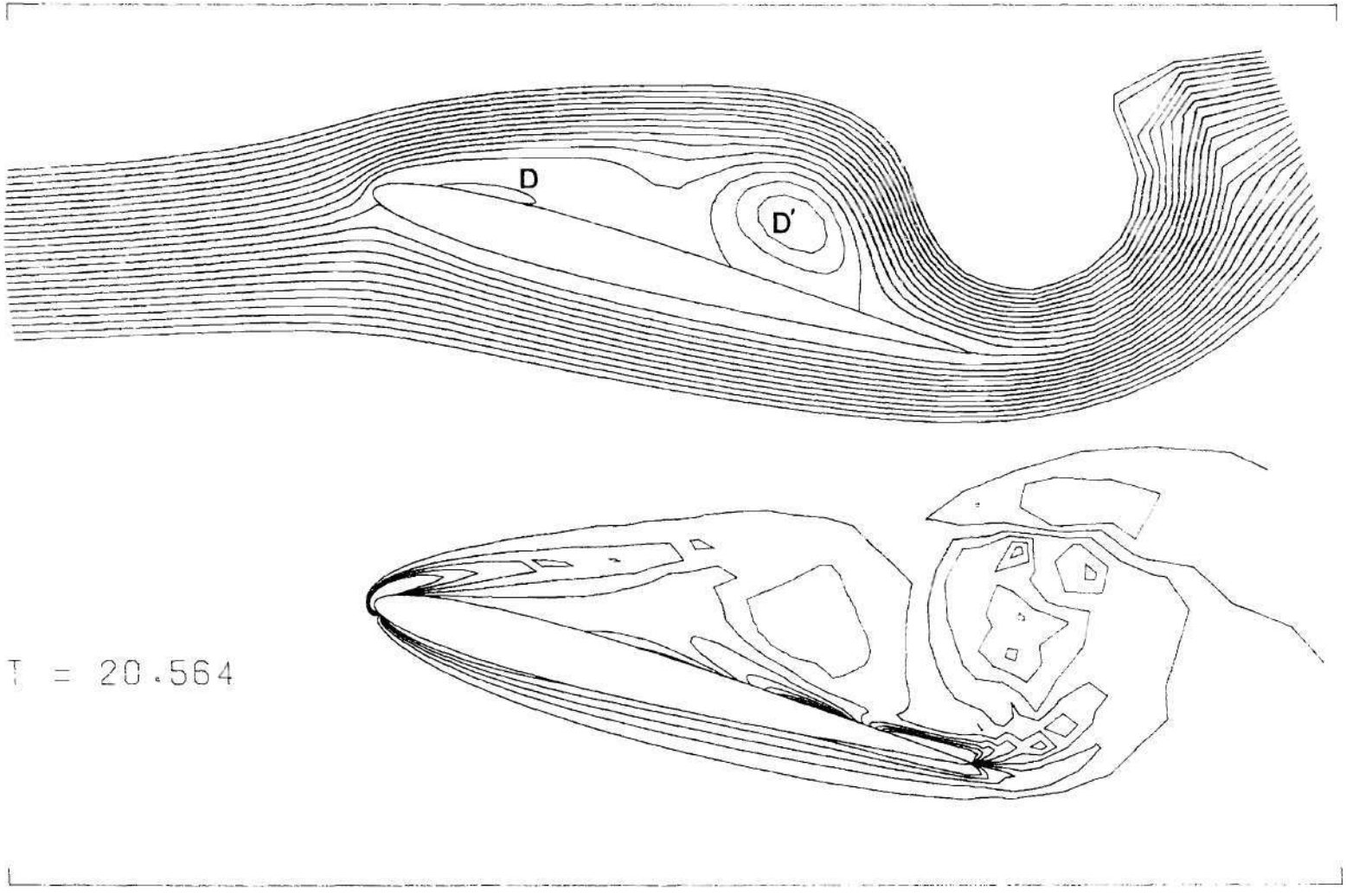

Figure 69. Streamlines and Equi-vorticity Contours at t = 20.564

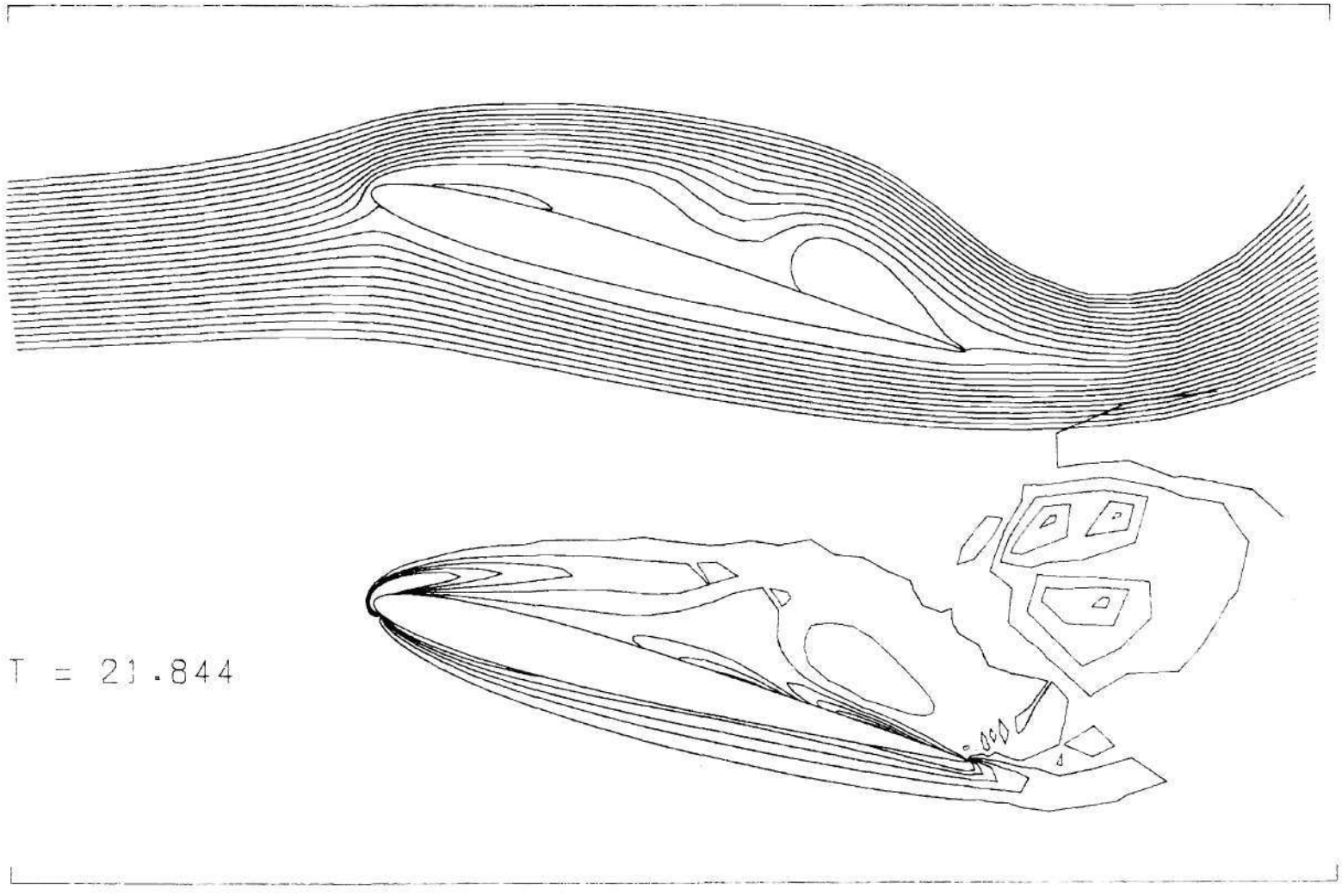

Figure 70. Streamlines and Equi-vorticity Contours at t = 21.844

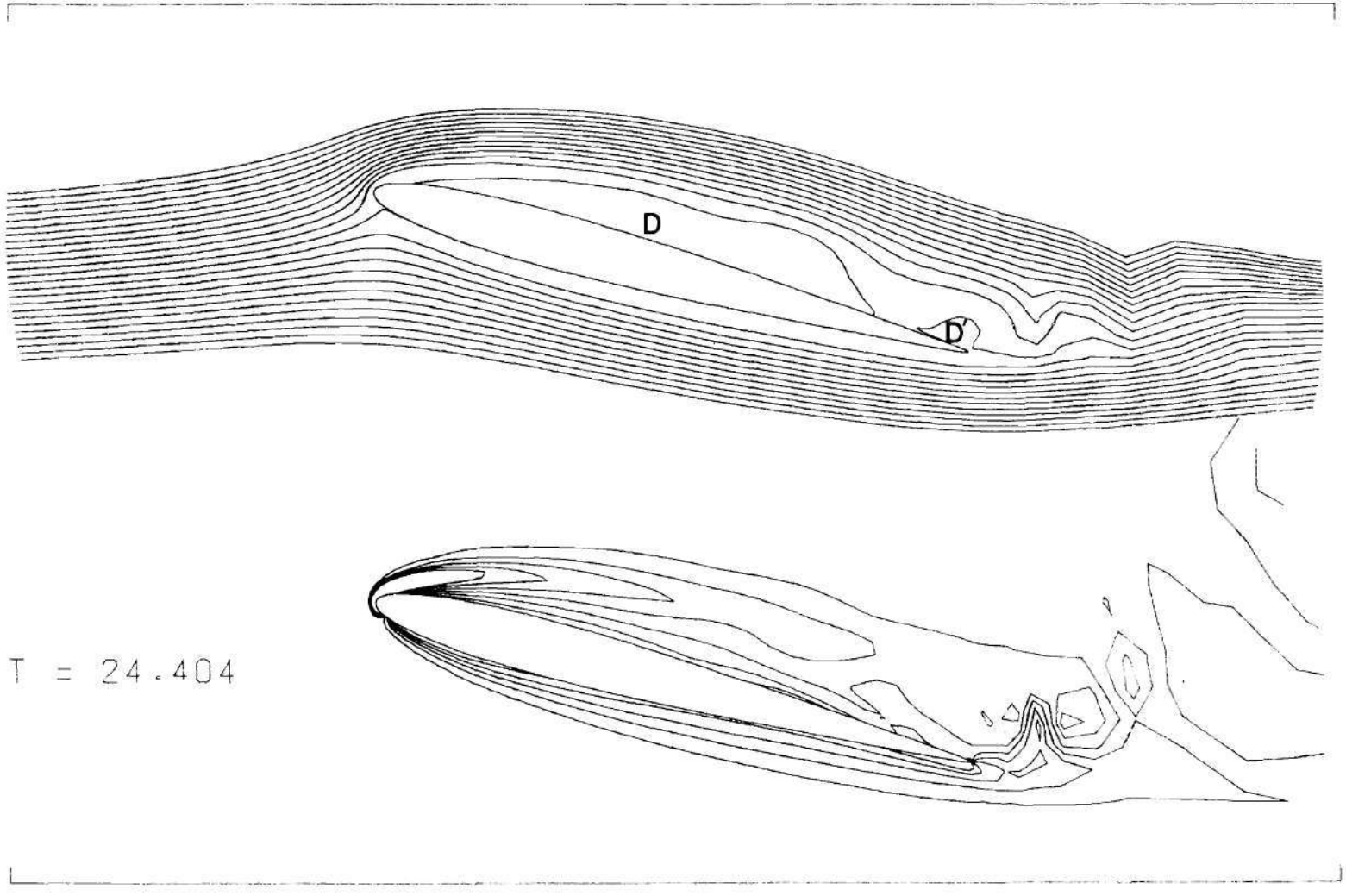

Figure 71. Streamlines and Equi-vorticity Contours at t = 24.404

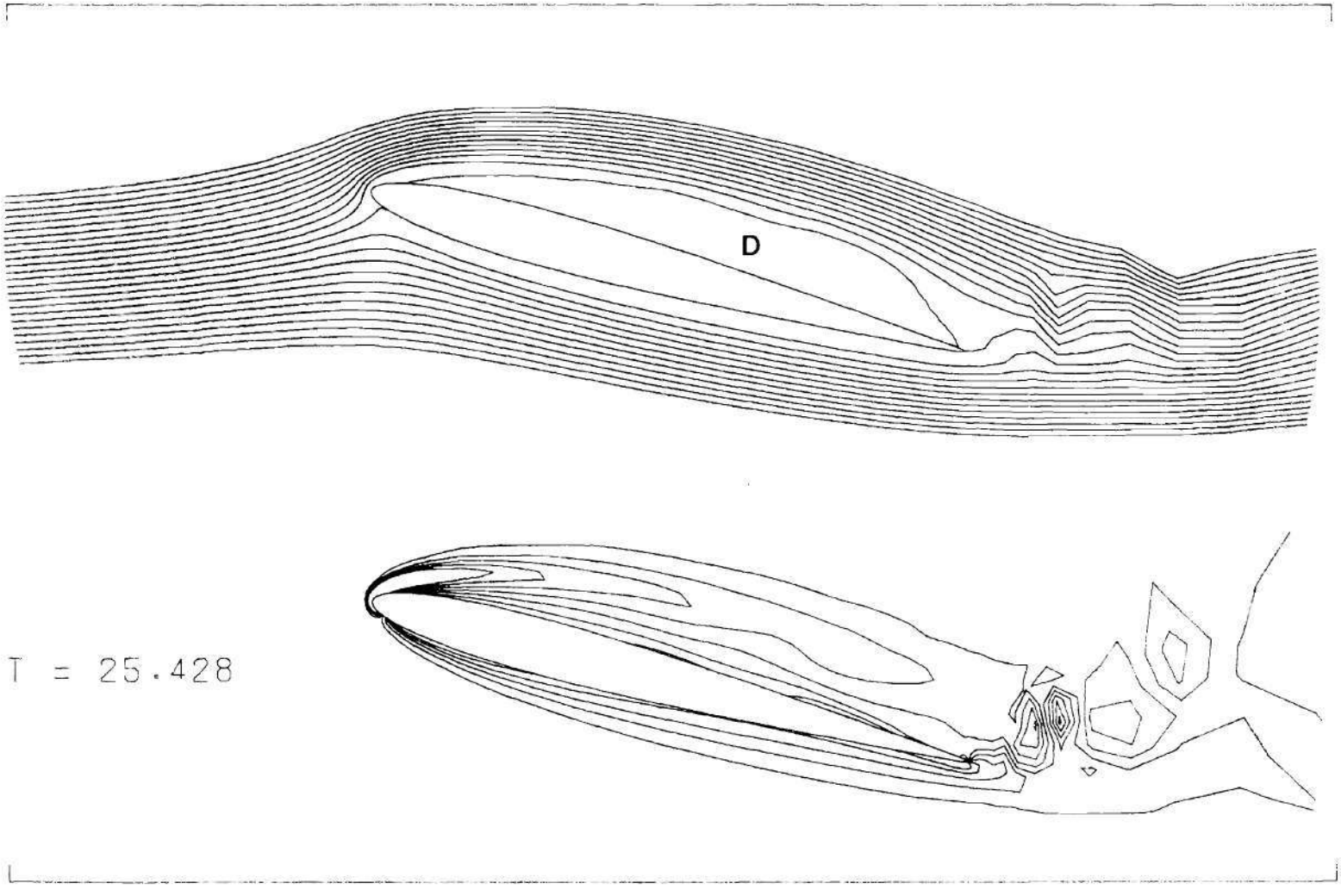

Figure 72. Streamlines and Equi-vorticity Contours at t = 25.428

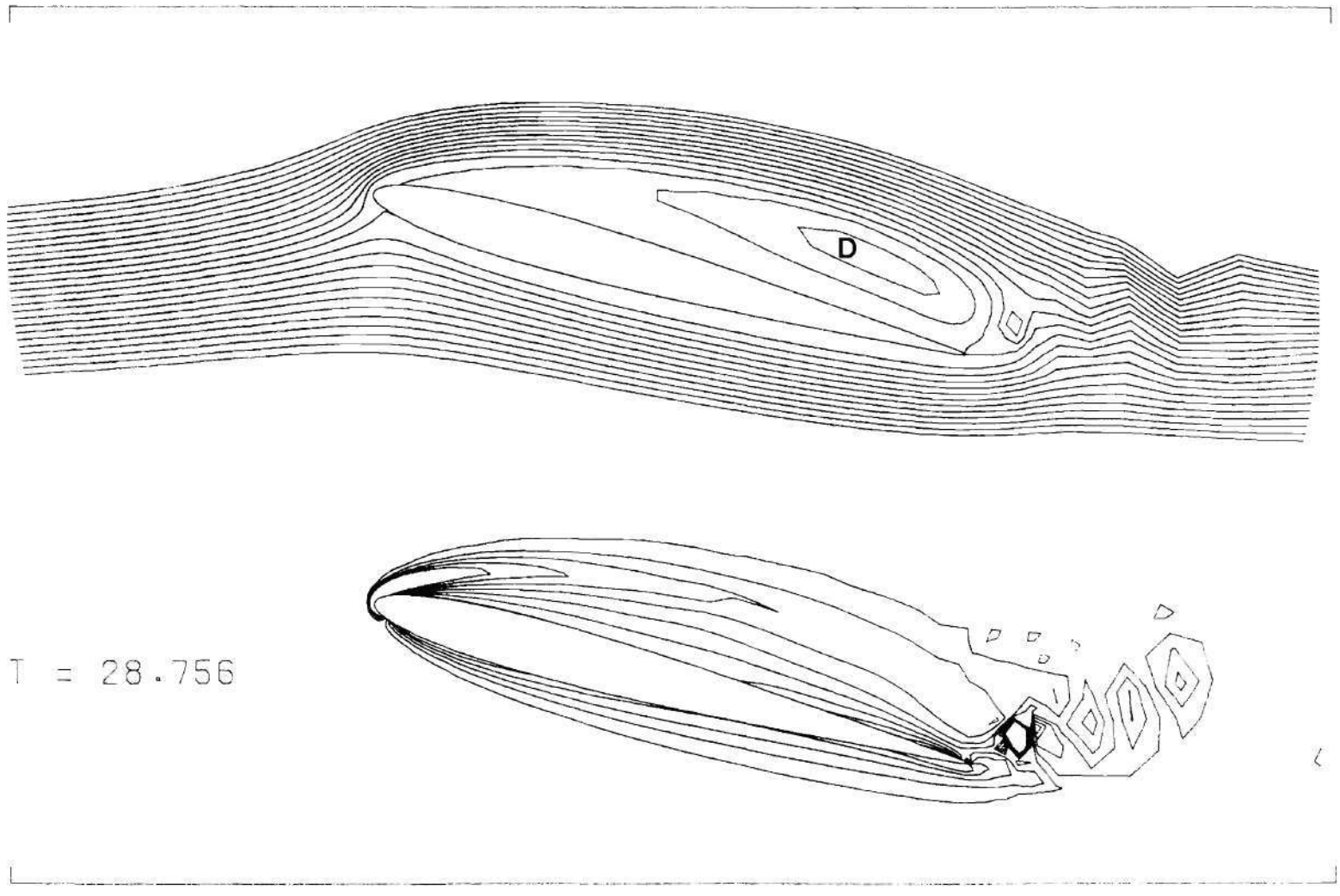

Figure 73. Streamlines and Equi-vorticity Contours at t = 28.756

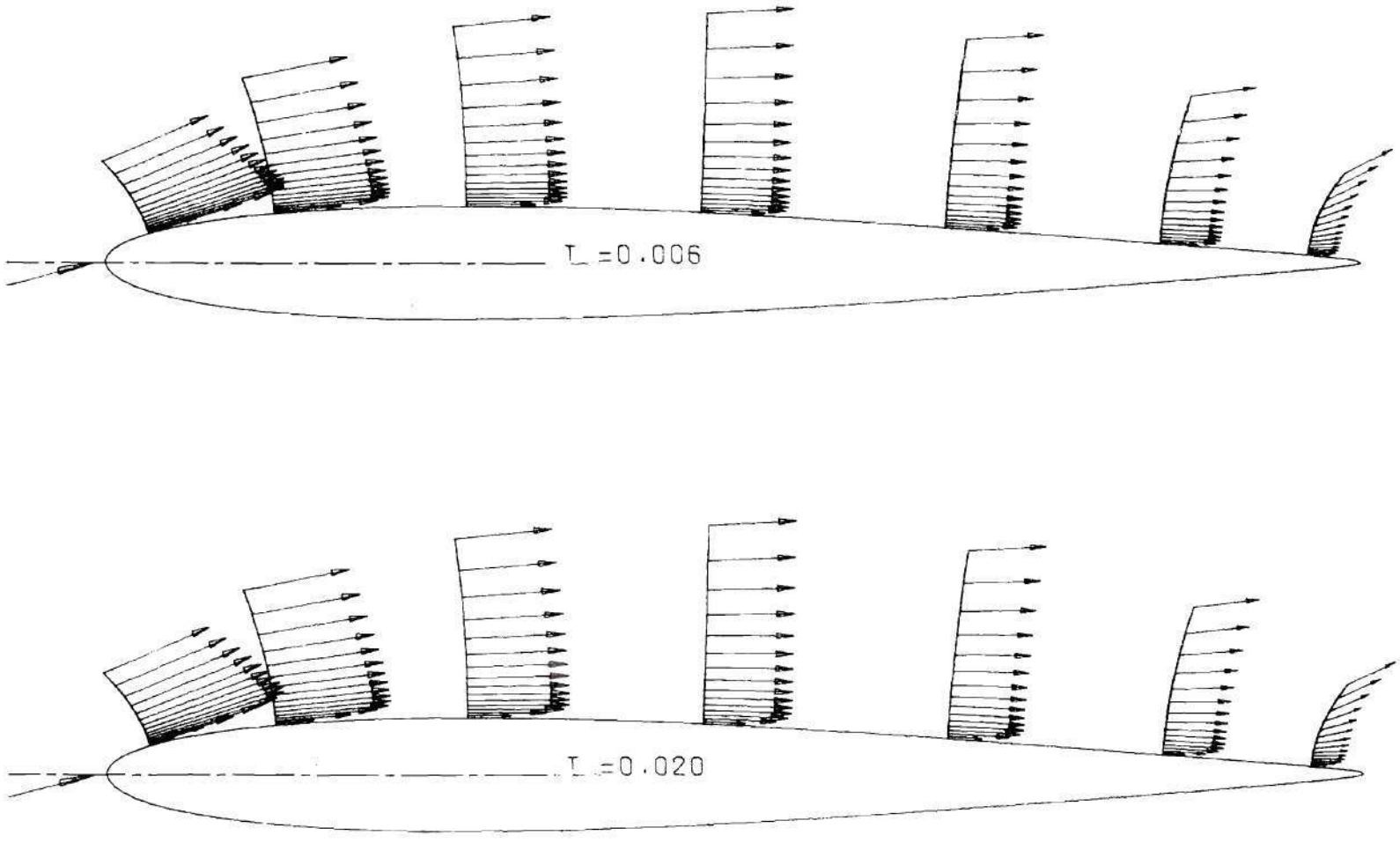

Figure 74. Velocity Profiles at t = 0.006 and t = 0.020

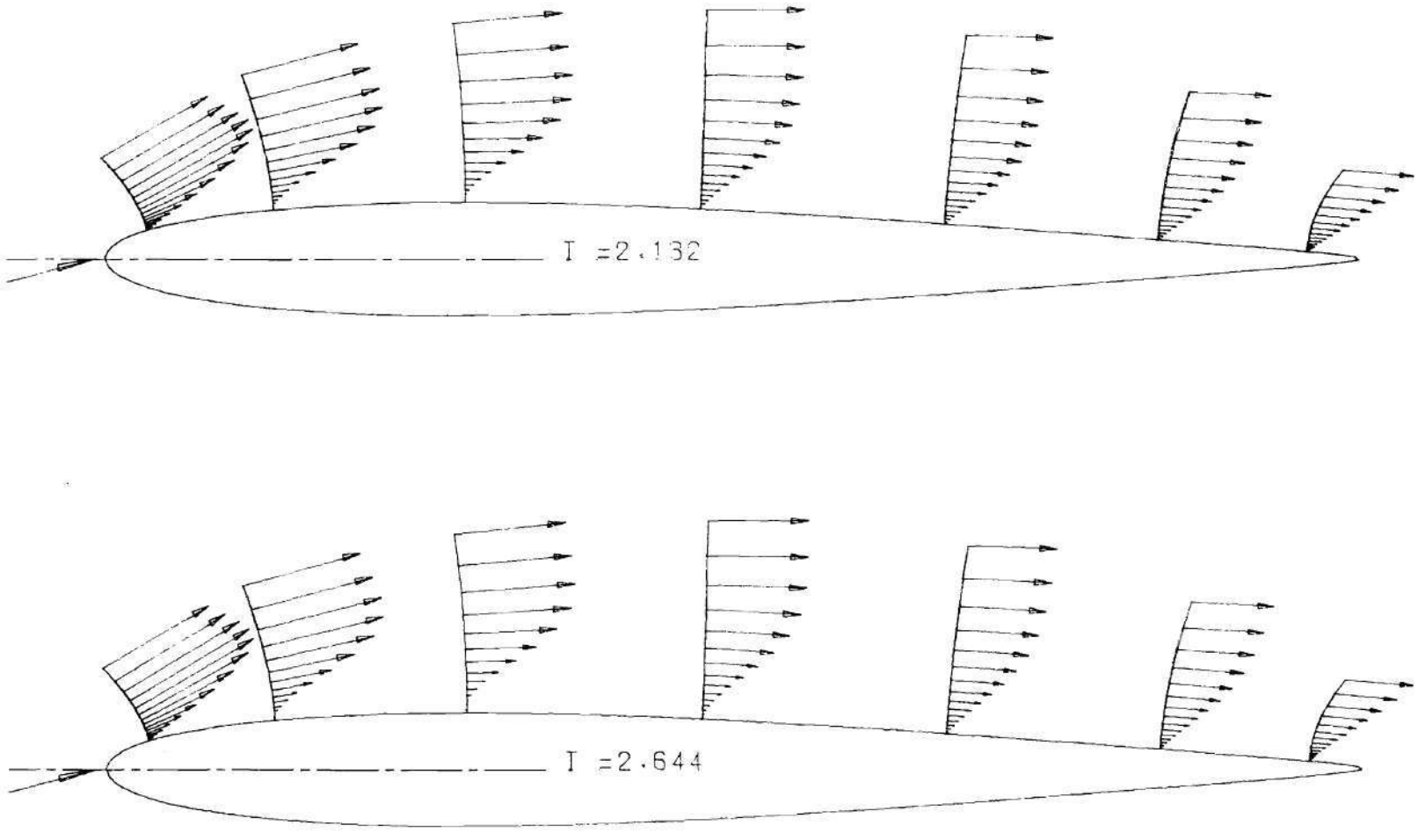

Figure 76. Velocity Profiles at t = 2.132 and t = 2.644

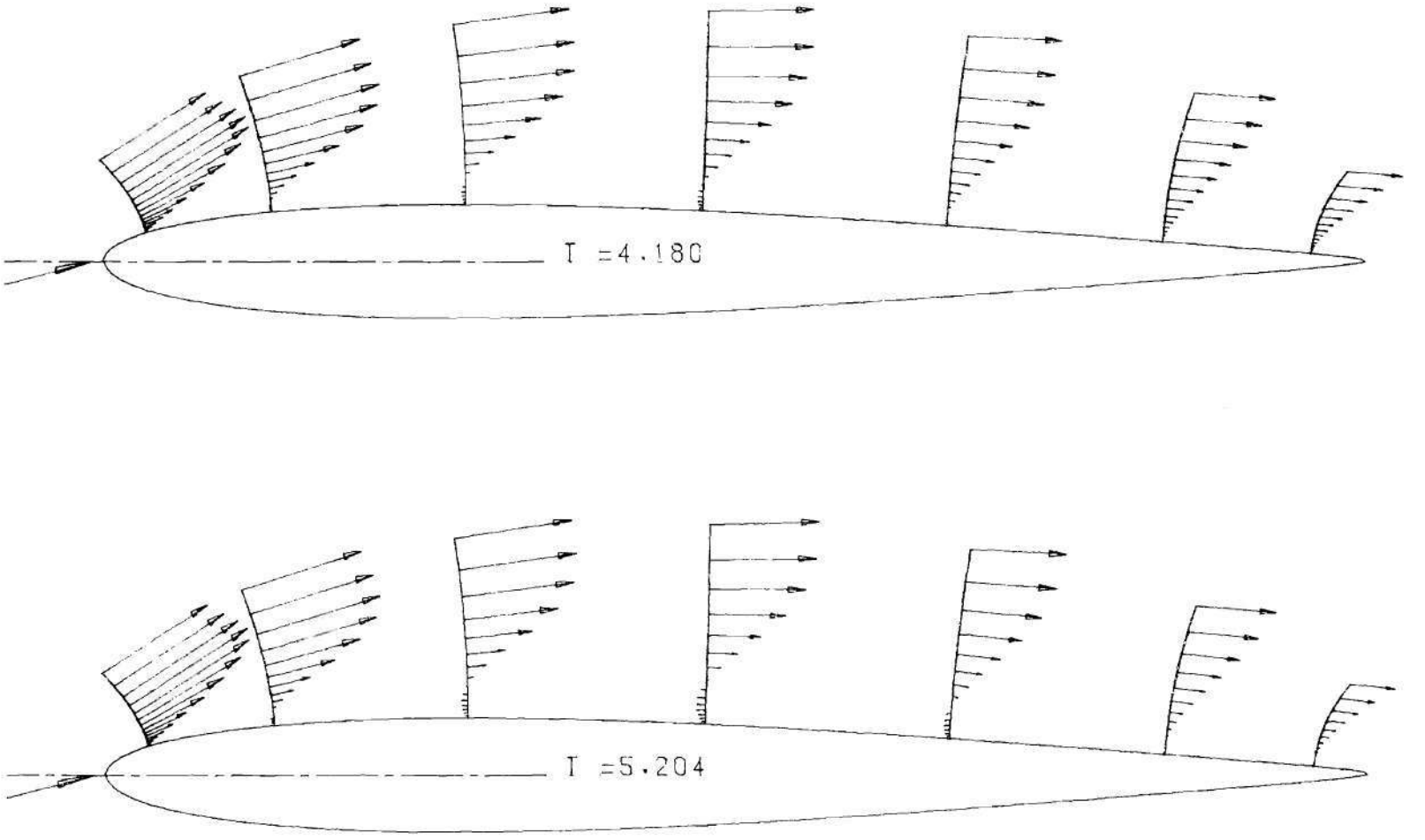

Figure 77. Velocity Profiles at t = 4.180 and t = 5.204

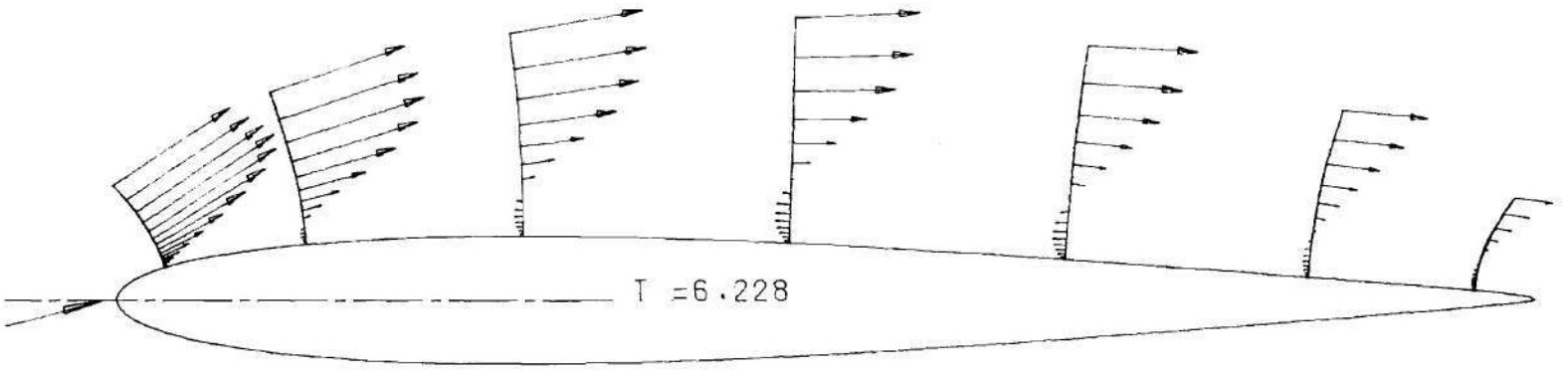

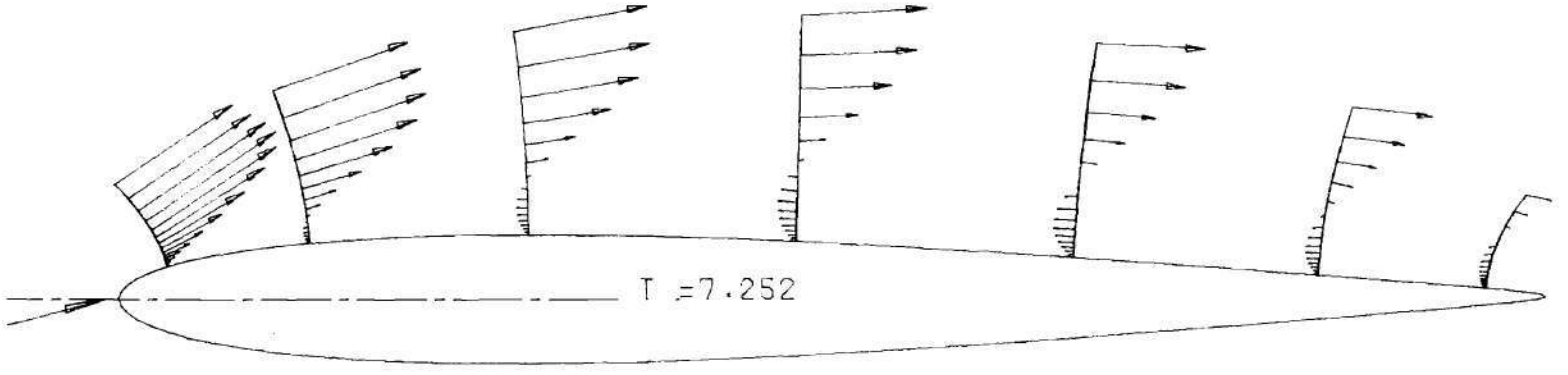

Figure 78. Velocity Profiles at t = 6.228 and t = 7.252

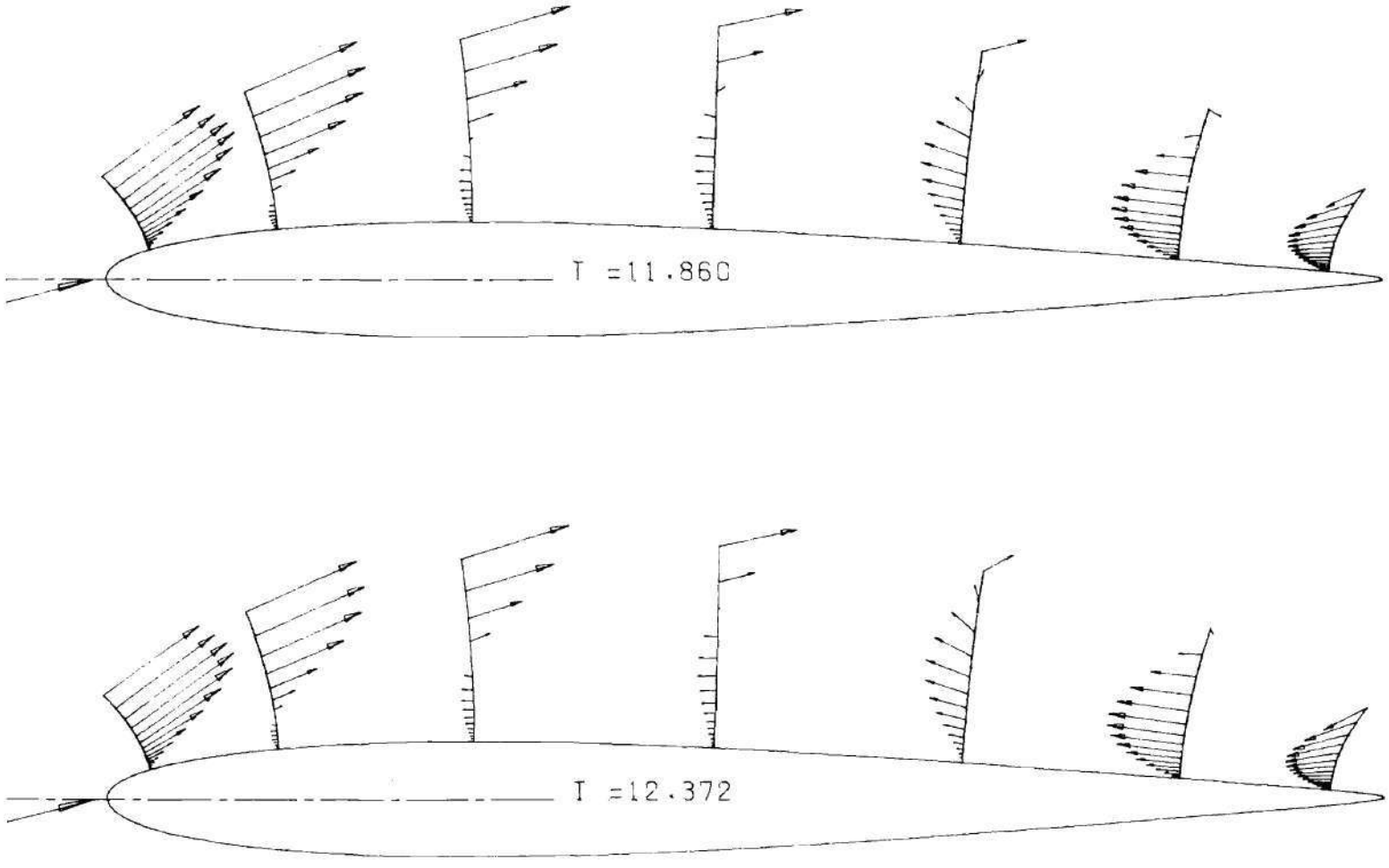

Figure 79. Velocity Profiles at t = 11.860 and t = 12.372

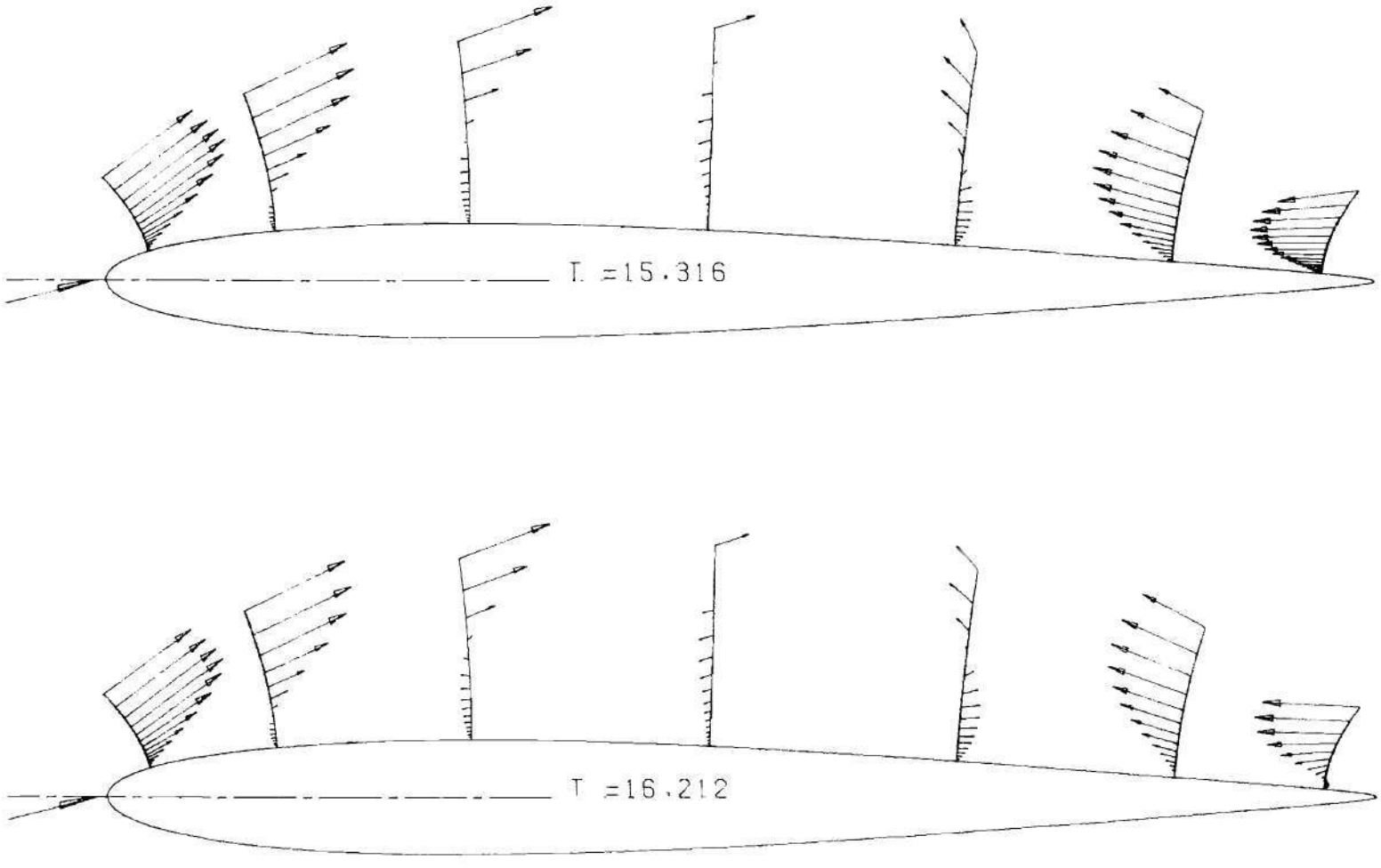

Figure 80. Velocity Profiles at t = 15.316 and t = 16.212

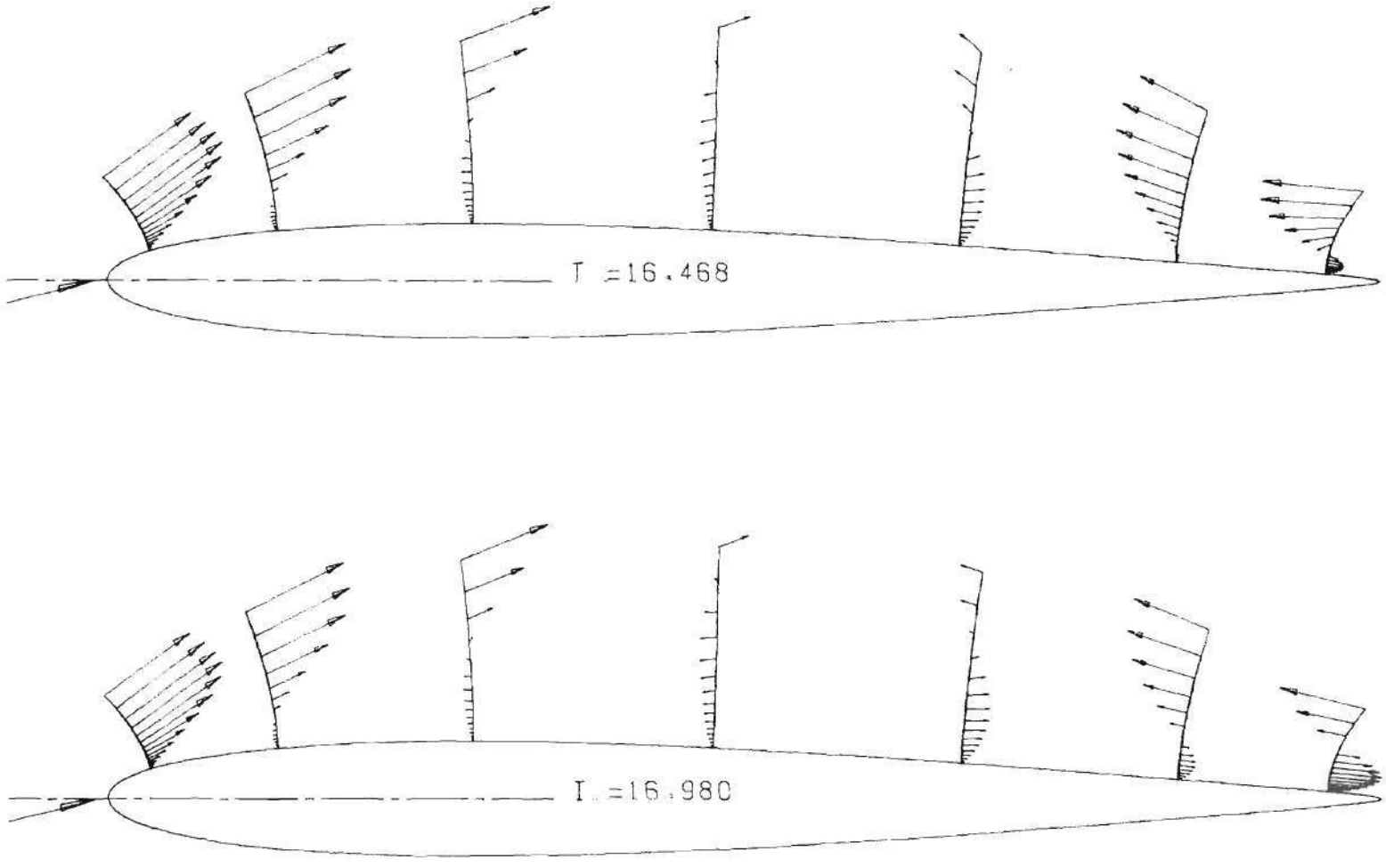

Figure 81. Velocity Profiles at t = 16.468 and t = 16.980

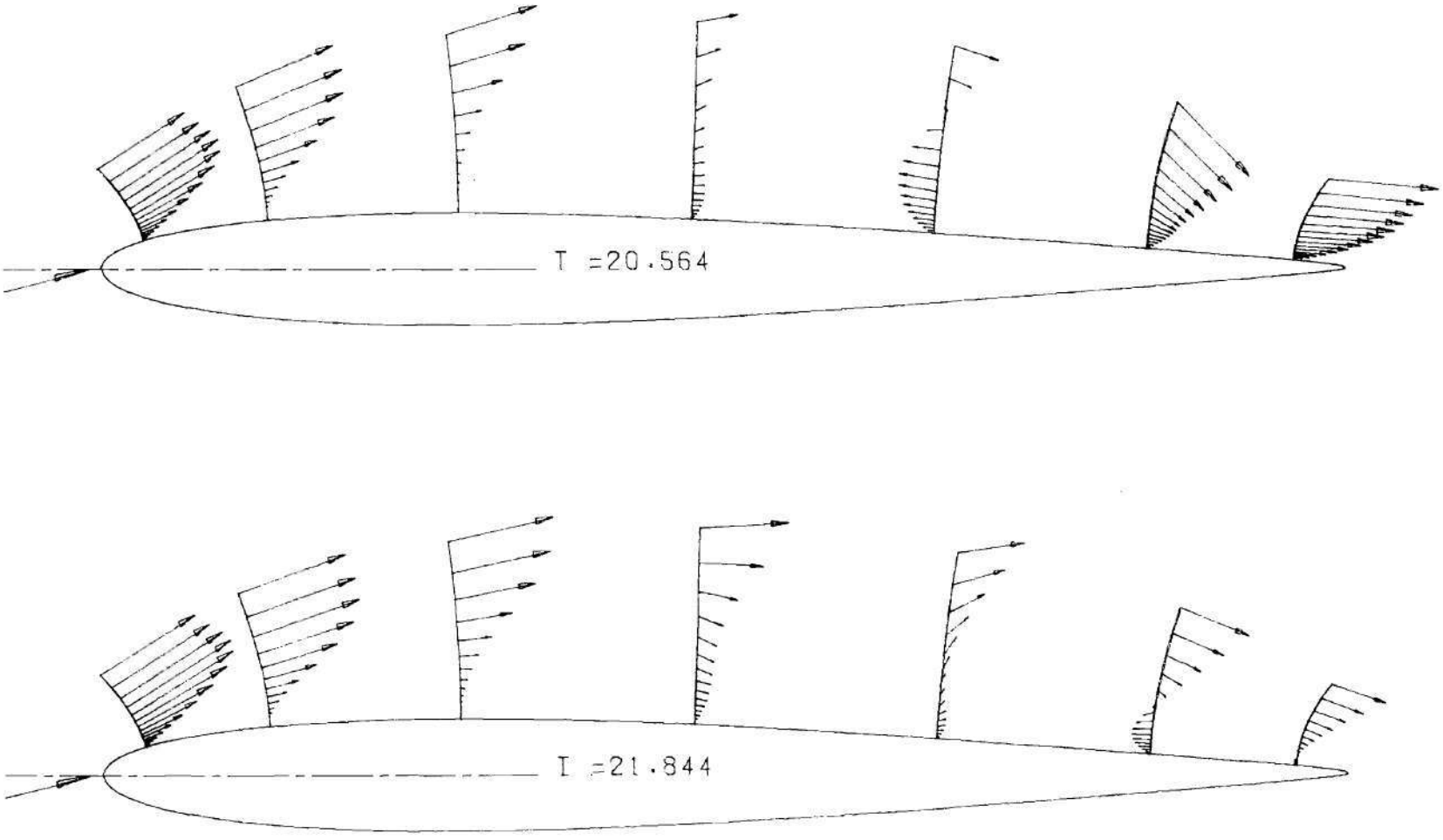

Figure 82. Velocity Profiles at t = 20.564 and t = 21.844

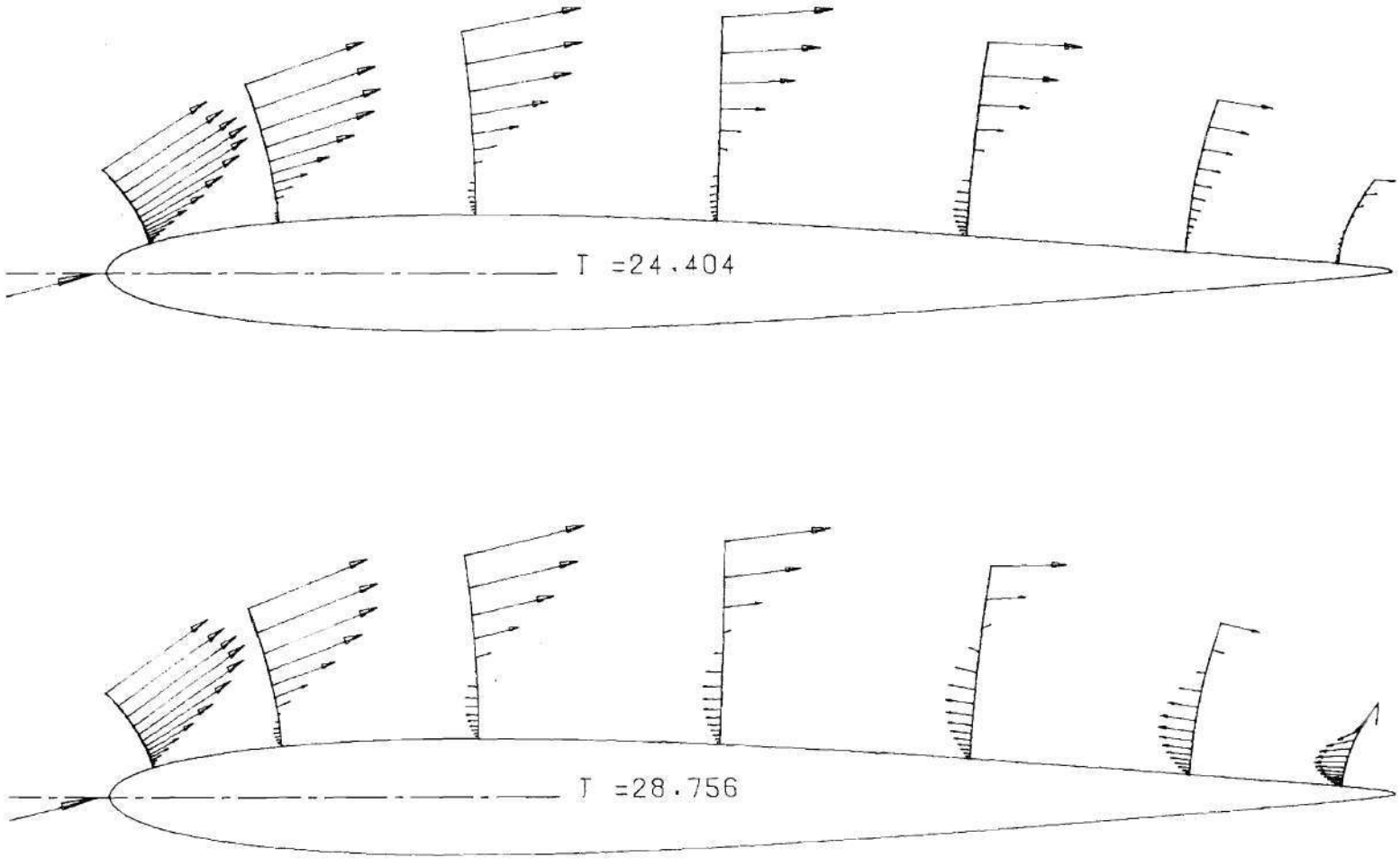

Figure 83. Velocity Profiles at t = 24.404 and t = 28.756

VITA

Sarangan Sampath was born on June 7, 1942. He received a Batchelor of Science degree in Physics from Annamalai University, Chidhambaram, India, in 1961 and a Diploma of Madras Institute of Technology in Aeronautical Engineering from M.I.T., Madras in 1964. He worked as a faculty member at the Madras Institute of Technology from 1964 to 1968 and as a faculty member at the Indian Institute of Technology, Madras from 1968 to 1972. He received a Master of Science degree in Aeronautical Engineering from I.I.T., Madras in 1972. In the Fall of 1972, he joined the Georgia Institute of Technology as a graduate student.